



Title	Studies on Energy Transport for Highly Efficient Laser Implsion
Author(s)	兒玉, 了祐
Citation	大阪大学, 1990, 博士論文
Version Type	VoR
URL	https://hdl.handle.net/11094/574
rights	
Note	

The University of Osaka Institutional Knowledge Archive : OUKA

<https://ir.library.osaka-u.ac.jp/>

The University of Osaka

**Studies on Energy Transport
for
Highly Efficient Laser Implosion**

Ryosuke Kodama

January 1990

Osaka University

Studies on Energy Transport for Highly Efficient Laser Implosion

(高効率爆縮を目的としたエネルギー輸送に関する研究)

Ryosuke Kodama

Course of Electrical Engineering

Osaka University

Osaka Japan

内 容 梗 概

本論文は筆者が、大阪大学大学院工学研究科電気工学専攻前期課程及び後期課程においてレーザー爆縮核融合の高効率化を目的として実施したエネルギー輸送に関する研究成果をまとめたものである。

レーザーによる爆縮核融合においては、高効率な燃料の圧縮と加熱が必須である。そのためには、レーザー光の高効率吸収、吸収エネルギーのターゲット内部への高効率輸送、爆縮過程における燃料層の低エントロピー保持高効率爆縮、燃料層における不純物の低減等が重要である。従ってエネルギードライバーとしては高い流体力学的効率が期待される短波長レーザー、また燃料ペレットとしては高い燃料密度、結合効率、及び爆縮効率の期待される噴出型での極低温固体DT燃料ターゲット(クライオターゲット)が考えられている。

このような観点に基づき、筆者はまず平面ターゲットを使用し、短波長レーザーによって生成されたプラズマ中でのX線によるエネルギー輸送の特性を明らかにし、エネルギー輸送でX線が重要な役割を果たすことを示した。また平面重水素充填フォームクライオターゲットを使用し、低密度・低原子番号固体ターゲット中での先行加熱機構を明らかにするとともに、世界に先駆け重水素充填フォームクライオシェルターゲットによる爆縮実験を行いその基礎特性を明らかにした。

本論文は7章より構成されている。

第1章は序論であり、本研究の意義を述べている。

第2章では、まずレーザー核融合高効率爆縮におけるエネルギー輸送の重要性について述べ、本研究の必要性を明らかにしている。更にレーザーにより励起されたプラズマ中で重要となる流体(衝撃波)、電子およびX線を媒体としたエネルギー輸送について概説している。

第3章では、短波長レーザーによって生成されたプラズマ中でのエネルギー輸送について述べている。まず短波長レーザー生成プラズマの特徴である高いX線変換効率に注目し、レーザープラズマからのX線発生の特長を実験的に明らかにするとともに、この特性を基に波長260nmのレーザー

照射実験により、短波長レーザー生成プラズマ中でのエネルギー輸送におけるX線の効果の重要性を示している。

第4章では、プラズマ中でのX線によるエネルギー輸送を、実験的に明らかにするため、レーザー励起されたプラズマ内に発生するX線とプラズマとの相互作用について明らかにしている。まずレーザープラズマX線により生成加熱されたプラズマのX線強度に対する温度の実験的比例則を示し、理論と比較検討している。また2重薄膜ターゲット法による透過X線の測定より電離バーンスルー現象を観測し、高密度プラズマ中でのX線の特定周波数領域においてX線の吸収再放出による異常透過現象が存在することを示している。

第5章では、微細構造をもった低原子番号、低密度フォームクライオターゲット中でのエネルギー輸送の基礎特性を明らかにしている。まず先行加熱の原因となる高エネルギー電子の生成機構の一つであるレーザーとターゲットとの非線形相互作用に関して、ターゲットの原子番号及び微細構造による影響を明らかにしている。またポーラス状の微細構造をもつターゲット中での衝撃波の形成及び伝搬特性を明らかにしている。さらに重水素充填フォームクライオターゲット中での高エネルギー電子によるエネルギー輸送と、これによる先行加熱の効果を明らかにしている。

第6章では、巨視的観点に立ち重水素充填フォームクライオシェルターゲットによる爆縮実験を行い、レーザー相互作用と爆縮特性の相関、爆縮に与える先行加熱の効果を明らかにしている。

第7章は結論であり、以上の研究により得られた結果をまとめ、本論文の総括としている。

Preface

This thesis is submitted in partial fulfillment of the requirement for the degree, Doctor of Engineering (KOGAKU HAKUSHI). The object of this thesis is to study the energy transport in laser produced plasmas for achieving efficient laser implosion in Inertial Confinement Fusion.

The research was conducted at the Institute of Laser Engineering in the Course of Electrical Engineering, Graduate School, Osaka University, Suita, Osaka, Japan.

Three categories are emphasized through fundamental experiments with planar targets and implosion experiments with spherical targets.

- (1) X-ray energy transport which is important in short wavelength laser-produced plasmas and/or high-atomic-number (high-Z) plasmas.
- (2) Laser-induced shock wave which causes fuel preheat in low-density target (solid deuterium).
- (3) Electron energy transport which becomes one of preheat sources in low atomic-number (low-Z) plasmas because of its long mean free path.

Chapter 1 is the introduction of this thesis.

In Chapter 2, the requirements of isentropic compression is theoretically described to explain the motivation of the studies on energy transport. Explanations about preheat source are presented reviewing the previous theoretical and numerical works.

In Chapter 3, the energy transport in UV-laser produced plasmas is experimentally studied. Characteristics of laser-plasma x rays are also studied to understand the laser-plasma x rays which may be important energy carrier in UV-laser plasmas.

In Chapter 4, radiative energy transport is shown by using intense x rays from laser produced plasmas. X-ray intensity dependence of electron temperature in x-ray heated plasmas is experimentally shown for the first time. The experimental evidence of ionization burnthrough and absorption

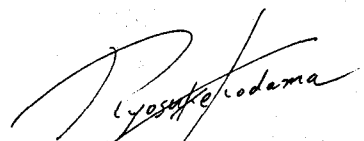
resonance by the successive process of absorption and reemission in radiative energy transport is presented.

In Chapter 5, presented is the energy transport in low-Z and low-density plasmas. Using x-ray backlighting method, the front and pile-up zone of laser-driven shock wave in low-density porous target is directly observed. Energy transport in low-Z plasmas is studied with cryogenically cooled deuterium filled foam target.

In Chapter 6, the first successful implosion is presented of cryogenically cooled deuterium filled shell target. Preheat effect to the implosion dynamics and thermonuclear fusion processes are discussed. Finally brief suggestion is also presented of future directions for cryogenic shell implosion.

In Chapter 7, we conclude with a summary of the thesis

The author hopes that these findings described in this thesis contribute to achieve the Inertial Confinement Fusion.



Ryosuke Kodama

Osaka, Japan

January, 1990

Table of Contents

Preface	i
Table of Contents	iii
 Chapter 1 INTRODUCTION	 1
 Chapter 2 GENERAL CONCEPT OF ENERGY TRANSPORT IN ICF PLASMAS	 5
§2-1. Energy Transport for Efficient Implosion	5
§2-2. Hydrodynamic Flow	7
§2-3. Electron Energy Transport	10
§2-4. X-ray Energy Transport	14
§2-4. Conclusion	18
 Chapter 3 ENERGY TRANSPORT IN UV LASER-PRODUCED PLASMAS	 20
§3-1. Introduction	20
§3-2. Characterization of UV Laser PlasmaX Rays	21
3-2-1. Experimental set up	22
3-2-2. Target atomic number dependence	22
3-2-3. Laser intensity dependence	26
3-2-4. Laser wavelength dependence	30
3-2-5. Laser pulse-duration dependence	36
3-2-6. Plasma scalelength dependence	40
3-2-7. Summary	47
§3-3. Energy Transport in UV Laser-Produced Plasmas	48
3-3-1. Experimental set up	49
3-3-2. Energy transport in medium-Z plasmas	51
3-3-3. Energy transport in high-Z plasmas	56
3-3-4. Summary	63
§3-4. Conclusion	63

Chapter 4 X-RAY ENERGY TRANSPORT IN HOT DENSE MATTER	67
§4-1. Introduction	67
§4-2. Laser Plasma X-ray Interaction with Solid Material	69
4-2-1. Experimental set up	69
4-2-2. Experimental results	71
4-2-3. Discussion	75
4-2-4. Summary	79
§4-3. Radiation Energy Transport in Hot Dense matter	80
4-3-1. Experimental set up	80
4-3-2. Experimental results	82
4-3-3. Discussion	86
4-3-3-1. ionization burnthrough	86
4-3-3-2. absorption resonance	92
4-3-4. Summary	94
§4-4. Conclusion	95
 Chapter 5 ENERGY TRANSPORT IN LOW-Z ($1 < Z < 4$) AND LOW-DENSITY ($0.1-0.2\text{g/cm}^3$) PLASMAS	 97
§5-1. Introduction	97
§5-2. Laser-interaction with Low-Z and Low-density Target	99
5-2-1. Experimental set up	100
5-2-2. Experimental results	103
5-2-3. Discussion	110
5-2-3-1. threshold intensity for SRS and TPD	110
5-2-3-2. damping of TPD	112
5-2-3-3. spectral shape of SRS	114
5-2-3-4. heating by SRS and TPD instabilities	118
5-2-4. Summary	120
§5-3. Laser-driven Shock wave in Low-density Porous Target	121
5-3-1. Experimental set up	121
5-3-2. Experimental results	124
5-3-3. Model for data analysis	128
5-3-4. Discussion	134
5-3-4-1. shock front property	134
5-3-4-2. pile-up zone property	137

5-3-4-3. energy transport in compressed wave	140
5-3-5. Summary	142
§5-4. Energy Transport in Cryogenically Cooled	
D ₂ Filled Foam Target	143
5-4-1. Experimental set up	144
5-4-2. Experimental results	146
5-4-3. Discussion	151
5-4-3-1. shock front property	151
5-4-3-2. anomalous energy transport	156
5-4-3-3. energy transport in	
tailored pulse produced plasmas	171
5-4-4. Summay	173
§5-5. Conclusion	174
 Chapter 6 IMPLOSION OF CRYOGENICALLY COOLED	
D₂ FILLED FOAM TARGET	178
§6-1. Introduction	178
§6-2. Experimental Set up	180
§6-3. Experimental Results	184
6-3-1. Laser interaction	184
6-3-2. Implosion dynamics	188
6-3-3. Thermo-nuclear fusion property	193
§6-4. Discussion	195
6-4-1. Implosion dynamics	195
6-4-2. Thermo-nuclear fusion property	200
6-4-3. Ideas of efficient implosion with CRYFAT	201
§6-5. Conclusion	204
 Chapter 7 CONCLUSION	207
 Acknowledgements	210
 List of Works	211

INTRODUCTION

What guideposts are there to promise the splendid 21st century for human? If we continue to depend on fossil fuels for energy source in this way, population growth and energy consumption with the growth will cause to be unable to expect a sustainable global energy system before the year 2100.^[1] Even though we can have a narrow escape from the exhaustion of fossil fuels, long before the exhaustion there may be disastrous global climate changes due to the greenhouse warming induced by CO_2 from the burning of fossil fuels.^[2] In view of the circumstances above, controlled thermonuclear fusion may provide a clean, safe, and abundant source of energy.

To achieve thermonuclear fusion energy we must solve two problems: (1) one is to produce and heat a plasma fuel to thermonuclear temperatures and densities, and (2) the other is to confine it long enough to produce more fusion energy than we have expended in heating and containing the fuel. These two requirements are usually quantified by a mathematical relation known as the *Lawson criterion*.^[3] To satisfy such requirements, various approaches and schemes have been suggested and studied. *Inertial confinement fusion* (ICF) with intense laser beam which is used to rapidly compress a tiny pellet of deuterium-tritium fuel is one of most effective schemes.^[4]

The intense laser light irradiates the pellet surface, ionizing this surface and ablating it off into the vacuum. As the outer surface of pellet blows away, an enormous pressure is generated (similar to a rocket exhaust) that compresses the core of fuel pellet to densities as high as 1000 to 10000 times

solid-state density. This compression raises also the temperature of the core of the pellet to fusion temperatures so that a thermonuclear burn is ignited. This burn would then propagate outward through the rest of the fuel pellet, igniting and burning it result in the explosive release of fusion energy. Various milestones have been suggested, such as high compression, scientific breakeven, and fuel ignition.^[5]

When one considers the pellet gain of laser fusion with some equations, these equations for the pellet gain assume that one can in fact reach the non-equilibrium state of a hot compressed ignitor surrounded by cold compressed fuel. To reach this state requires tow more concepts: a sufficient ablation pressure and an ignition concept for efficiently conversing the kinetic energy of the imploding shell into the correct mixture of hot and cold fuel region, with the cold region surrounding the hot region.

All of the above concepts and parameters can now be subsumed into five critical elements. These are

- (1) coupling efficiency
- (2) cold fuel isentrope
- (3) ablation pressure
- (4) implosion symmetry
- (5) ignitor concept

These five critical elements are fundamental. The values that can be achieved in the first four elements depend directly on the physics of laser-plasma coupling. Especially the energy transport is responsible to the first three elements. These three elements may be devided further by using short wavelength laser for driver and cryogenically cooled fuel target for pellet since the short wavelength creates high ablation pressure and the cryogenic target has initially low entropy.

Therefore this thesis presents the studies on energy transport in laser-produced plasmas under these circumstances. Especially following three categories are emphasized through fundamental experiments with planar targets and implosion experiments with spherical targets.

- (1) X-ray energy transport which is important in short wavelength laser-produced plasmas and/or high atomic-number (high-Z) plasmas.
- (2) Laser-induced shock wave which has a strong possibility of fuel preheat

in low-density target (solid deuterium).

- (3) Electron energy transport which becomes one of preheat source in low atomic-number (low-Z) plasmas because of the long mean free path.

In Chapter 2, the requirements of isentrope compression is theoretically described to explain the motivation of the studies on energy transport. Brief explanation about preheat source are presented reviewing the previous theoretical and numerical works i.e., shock propagation, electron transport, and x-ray transport in laser-produced plasmas.

In Chapter 3, the energy transport in UV-laser produced plasmas is experimentally studied. Characteristics of laser-plasma x ray are initially studied to understand the laser-plasma x ray which may be important energy carrier in UV-laser plasmas. Study on energy transport in 263nm-laser plasmas shows that x ray is an efficient energy carrier in high-Z plasmas. At the same time it is shown that the x ray may become a preheat source in the cold overdense region.

In Chapter 4, radiative energy transport is shown by using intense x ray from laser produced plasmas. X-ray intensity dependence of electron temperature in x-ray heated plasmas is experimentally shown for the first time with XUV spectroscopy. The experimental evidence of ionization burnthrough and absorption resonance by the successive process of absorption and reemission in radiative energy transport is presented using a double-foil technique.

In Chapter 5, presented is the energy transport in low-Z and low-density plasmas. Using x-ray backlighting method, the front and pile-up zone of laser-driven shock wave in low-density porous target is directly observed for the first time. Energy transport in low-Z plasmas is studied with cryogenically cooled deuterium filled target. Observed are nonlocal transport and preheat by high energy tail components in thermal electron distribution.

In Chapter 6, the first successful implosion is presented of cryogenically cooled deuterium filled shell target. A variety of observation is made to study laser-target coupling, implosion dynamics and thermonuclear fusion processes. Preheat effect on the implosion dynamics and thermonuclear

fusion processes is discussed considering the results from fundamental experiments on energy transport. Finally brief suggestion is also presented of future directions for cryogenic shell implosion.

In Chapter 7, we conclude with a brief summary of the thesis.

References

- [1] J. H. Nuckolls, Proc. 4th International Conference on Emerging Nuclear Energy Systems, Madrid (World Scientific Publishing Co. Pte. Ltd. 1986); W. Häfele and W. Jaek, Atomkernergie-Kerntechnik 43, 150 (1983).
- [2] W. C. Wang and G. Molnar, J. Geophys. Res, 90, 12971 (1985).
- [3] J. D. Lawson, Proc. Phys. Soc. London B70, 6 (1957).
- [4] J. L. Emmett, J. Nuckolls, and L. Wood, Sci. Am. 231, 24 (June, 1974); C. H. Stickley, Phys. Today 50 (May, 1978).
- [5] J. J. Duderstadt and G. A. Moses, Inertial Confinement Fusion, (Wiley-Interscience Publication, 1982).

Chapter 2

GENERAL CONCEPT OF ENERGY TRANSPORT IN ICF PLASMAS

§ 2-1. Energy Transport for Efficient Implosion

§ 2-2. Hydrodynamic Flow

§ 2-3. Electron Energy Transport

§ 2-4. X-ray Energy Transport

§ 2-1. Energy Transport for Efficient Implosion

Pellet gain

Several simple models of efficient ICF targets have been reported. Most of them are the central burning scheme which is composed of the central hot spot called the *ignitor* and the process of heating the rest of the fuel called *propagating burn*. For example, Kidder has shown the isochoric model (K model) ^{[1], [2]} which assumed constant density which led to a much higher pressure in the hot spot than in the cold fuel by homogeneous imploding. Meyer-Ter-Vehn isobaric (MTV) model ^[3] enforces a constant pressure throughout the assembled fuel. Anyway assuming the homogeneous imploding, the equation of the pellet gain satisfying these central burning concepts is given by

$$Q = A \eta \left[\frac{\eta E_L}{a^3} \right]^{0.3 \sim 0.4}, \quad (2-1)$$

where E_L is the driver energy, η the efficiency involved in reaching to this final, pre-burn state i.e. the ratio of the total internal energy of the

compressed fuel to an input driver energy, and α the ratio of the internal energy of the compressed fuel to that which would result from isentropic compression at minimum entropy. Here K model gives a gain five times higher than MTV model but in both cases isentropic fuel compression (α) is essential to the efficient pellet gain (Q).

Preheating parameter

With ideal gas relation, the specific internal energy ε and the pressure P of the compressed fuel are approximately given by

$$\varepsilon = \alpha \varepsilon_0 \left[\frac{\rho}{\rho_0} \right]^{2/3} \quad (2-2)$$

and

$$P = \alpha P_0 \left[\frac{\rho}{\rho_0} \right]^{5/3} = \left[\frac{2}{3} \right] \alpha \rho_0 \varepsilon_0 \left[\frac{\rho}{\rho_0} \right]^{5/3}, \quad (2-3)$$

where ε_0 and ρ_0 are the internal energy and density of the solid DT. Equation (2-2) also indicates the compression ratio for the function of preheating as $\rho/\rho_0 \propto \alpha^{3/2}$. It follows that the deposition of heat dq will result in an increase in the dimensionless parameter α as given by relation

$$dq = d\varepsilon + P d(1/\rho) = \varepsilon_0 \left[\frac{\rho}{\rho_0} \right]^{2/3} d\alpha \quad (2-4)$$

The integration of Eq. (2-4) using Eq. (2-1) and (2-3)

$$\alpha^3 = (1 + \beta)^5, \quad (2-5)$$

where

$$\beta = \frac{3}{5} \varepsilon_0 \int_0^q \left[\frac{P_0}{P} \right]^{2/3} dq \quad (2-6)$$

Equation (2-5) shows that a very small preheating say $q/\varepsilon_0 > 2$ increases the internal energy and the required laser energy given by Eq. (2-1)

significantly. For example the condition $\beta < 1$ can be adopted as the criterion for permissible preheat of the fuel. This criterion implies that the work required to compress the fuel should not exceed the minimum entropy value by more than the factor $2^{5/3} \approx 3$. For example when implosion velocity $V_i = 3.5 \times 10^7 \text{ cm/s}$ (60MJ/g), the criterion ($\beta < 1$) implies that the heating of fuel by electron and/or x rays during the implosion must be limited to roughly 1/100th the heating that from a single strong-shock acceleration to the final implosion velocity.^[2]

Therefor of great interest is the degree of preheat of the fuel preceding the final compression phase in ICF experiments. The preheat is due to a number of sources such as high energy electrons, strong shock (hydrodynamic flow), and x radiation. In following section we concretely present the transport mechanisms of such preheat factors (shock wave, electron and x ray) reviewing brief theory and previous work.

§ 2-2. Hydrodynamic Flow

The compression of fuel in an ICF target is driven by the ablation of the target surface using driver energy deposition. The velocity of the material ablating off of the surface is determined essentially by the local speed of sound in the high temperature ablation region. But the speed of sound in the cold fuel region ahead of the ablation front is quite low. Hence the inward motion of the pellet surface due to ablation pressure is supersonic with respect to the cold fuel material, and shock waves form. Such shock waves play an important role in the ICF pellet implosion process. In this section we study the general physics of laser-driven shock wave propagation, how the properties of the shock wave in a deflagration configuration, which is produced in laser fusion experiments, depend on parameters such as laser intensity, laser wavelength, and target density.

In the laboratory frame and the plane geometry, the Hugoniot relations^[4] describing the shock express conservation of mass and momentum across the shock front:

$$\rho_s v_{sh} = \rho_a (v_{sh} - u), \quad (2-7)$$

$$\rho_s v_{sh}^2 = \rho_a (v_{sh} - u)^2 + P_a, \quad (2-8)$$

where ρ_s is solid density, ρ_a shock compressed density, v_s shock front speed, u fluid speed, and P_a ablation pressure. In these equations the pressure in the solid has been neglected, which was assumed small compared to the ablation pressure P_a .

From Eq. (2-7) and (2-8), shock speed and the speed u of the fluid behind the shock can be determined to be

$$v_{sh} = \left\{ \left[\frac{P_a}{\rho_s} \right] \left[\frac{\chi}{\chi-1} \right] \right\}^{1/2}, \quad (2-9)$$

$$u = \left[\frac{\chi-1}{\chi} \right] v_{sh} = \frac{3}{4} v_{sh}, \quad (2-10)$$

where χ is simplified to be $\rho_a/\rho_s=4$ for a strong shock instead of using the adiabat of the Hugoniot curve to obtain the details of the shock energetics.^[4]

Here the ablation pressure depends on absorbed laser intensity I_a and its absorbed region (density ρ_c) or laser wavelength λ_L . The simple scaling of the ablation pressure is given from the well-known energy conservation for steady state flow and isothermal corona to be^[5]

$$P_a = 2\rho_c C_0^2 \approx 12 \text{ Mbar} \left[\frac{I_a}{10^{14} \text{ W/cm}^2} \right]^{2/3} \left[\frac{1 \mu\text{m}}{\lambda_L} \right]^{2/3} \left[\frac{A}{2Z} \right]. \quad (2-11)$$

Using Eq. (2-9) and (2-11), the shock speed is obtained to be

$$v_{sh} \approx 4 \times 10^6 \text{ cm/sec} \left[\frac{I_a}{10^{14} \text{ W/cm}^2} \right]^{1/3} \left[\frac{1 \mu\text{m}}{\lambda_L} \right]^{1/3} \left[\frac{1 \text{ g/cm}^3}{\rho_s} \right]^{1/2} \left[\frac{A}{2Z} \right]^{1/6} \quad (2-12)$$

Note the weak dependence of the shock speed on the laser intensity and wavelength.

Similarly, it is possible to determine the penetration speed v_a of the ablation front into the solid. The equations (mass, momentum, and energy conservation) for steady flow may be solved in the frame of the ablation front, which moves with a speed v_a in the laboratory frame. Then the mass ablation rate is given by ^[5]

$$\dot{m} = \rho_a (v_a - u) = 1.5 \times 10^5 \text{ g/cm}^2 \text{ sec} \left[\frac{I_a}{10^{14} \text{ W/cm}^2} \right]^{1/3} \left[\frac{1 \mu\text{m}}{\lambda_L} \right]^{4/3} \left[\frac{A}{2Z} \right]^{2/3} \quad (2-13)$$

It is also possible to solve for v_a as

$$v_a = v_{sh} \left\{ \left[\frac{\chi-1}{\chi} \right] + \left[\frac{\rho_c}{\rho_s} \right]^{1/2} \left[\frac{\phi}{0.6} \right]^{1/2} \frac{1}{\chi} \left[\frac{\chi-1}{2\chi} \right]^{1/2} \right\} \quad (2-14)$$

The movement of the shock into the solid material at speed v_{sh} increases the distance between the shock and the ablation front. The mass flux m across the ablation front has the effect of reducing the distance. In usual study of energy balance in the conduction zone, the energy flux Γ needed to maintain the shock was neglected, arguing that the great majority of the absorbed flux I_a was used to create thermal conduction and outward kinetic energy of the blow off. However, the energy flux Γ resulting from the work done by the ablation pressure P_a is $\Gamma = P_a u$, and it is straightforward to show that this energy flux Γ is large compared to that caused by m . The fraction F_s of Γ , relative to I_a is obtained ^[5]

$$F_s = \frac{\Gamma}{I_a} = \frac{1}{2^{1/2} F(\phi)} \left[\frac{\chi-1}{\chi} \right]^{1/2} \left[\frac{\rho_c}{\rho_s} \right]^{1/2} \left[\frac{\phi}{0.6} \right]^{3/2} \quad (2-15)$$

For $\chi=4$ this becomes

$$F_s = 3.7 \times 10^{-2} \left[\frac{1\mu m}{\lambda_L} \right] \left[\frac{A}{2Z} \right]^{1/2} \left[\frac{1g/cm^3}{\rho_s} \right]^{1/2} \left[\frac{\phi}{0.6} \right]^{1/2} \quad (2-16)$$

For example, for $\phi=0.6$, $F_s=1.9\%$ at $\lambda_L=0.5\mu m$ for $\rho_s=1g/cm^3$ is obtained and $F_s=33\%$ at $\lambda_L=0.25\mu m$ for $\rho_s=0.2g/cm^3$. Thus the fraction of energy dissipated in the shock is not more negligible when a short wavelength laser and low density target are used. This effect may be needed to take into account in experiments which attempt to measure hydrodynamic efficiency by accelerating foil targets of various thickness. In low density targets it is also necessary to shape the laser pulse carefully for pressure pulse tailoring in order to avoid the shell disassembly by strong shock heating.^[6]

§ 2-3. Electron Energy Transport

Electrons play an important role in the energy transport mechanisms in laser produced plasmas. The driver energy is deposited first into electrons. The absorbed energy is then conducted inward by electron thermal transport from the hot corona to the cold ablation surface. Then the electron transport strongly depends on its mean free path. The electron mean free path is given by

$$\rho \lambda_e = \rho \sqrt{\lambda_{ei} \cdot \lambda_{ee}} = 2.57 \times 10^{-3} \frac{A \epsilon^2}{\{Z(Z+Z^2)\}^{1/2}} \quad [mg/cm^2], \quad (2-17)$$

Where ϵ is electron energy (keV). Figure 2-1 shows the material dependence of the electron mean free path. It should be noted that the mean free path of the low-Z material is longer than the high-Z even at the same areal density.

Let us consider the kinetical analysis of electron heat transport. In the presence of small gradients we assume that the distribution function f has a

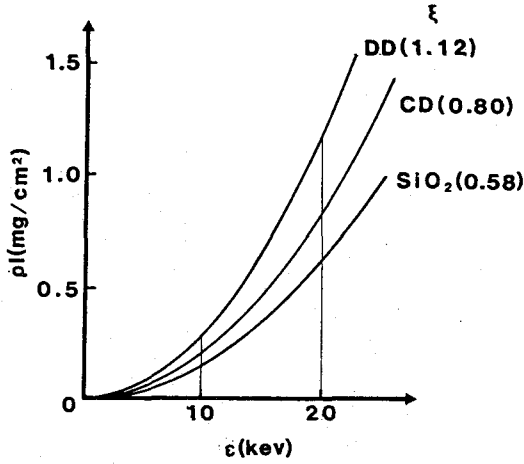


Fig. 2-1 Material dependence of the electron mean free path.
 $\xi = A/\{Z(Z^2 + Z)\}^{1/2}$ in Eq. 2-17.

weak angular dependence and can be expressed by $f = f_0 + \mu f_1$ (diffusion approximation), where f_0 and f_1 represent the local isotropic and unisotropic components, respectively. In the case of thermal equilibrium or small temperature gradient, f_0 is the local Maxwellian (spatially linearizing). An analytical expression for f_1 is obtained for Lorentz gas, in which the electron-electron collision terms are neglected and the ions are assumed at rest. The collisional mean free path is then $\lambda(v) = \lambda_e \cdot (v / v_{th})^4$, where v_{th} is the thermal velocity $(2kT/m_e)^{1/2}$. Using these assumptions one finds the ratio f_1/f_0 to be

$$\frac{f_1}{f_0} = \frac{\lambda_e}{L} \cdot \left(\frac{v}{v_{th}} \right)^4 \cdot \left[\left(\frac{v}{v_{th}} \right)^2 - 4 \right] \quad (2-18)$$

where the gradient length L is defined by $L = T/|dT/dx|$. Then in unmagnetized plasmas, the electron heat flux Q is given by

$$Q \equiv \frac{4nm_e}{6} \cdot \int_0^\infty v^5 f_1 dv = \frac{4nm_e}{6} \cdot v_{th}^4 \cdot \lambda_e \cdot \nabla T \cdot \int_0^\infty v_x^9 (v_x^2 - 4) f_0 dv_x \quad (2-19)$$

The integration of Eq. (2-19) becomes maximum at $2.7(kT/m_e)^{1/2}$ as shown in Fig. 2-2. Hence the electrons of which energy are approximately 7T contribute heavily to the electron heat flux. Since the electron-ion collision

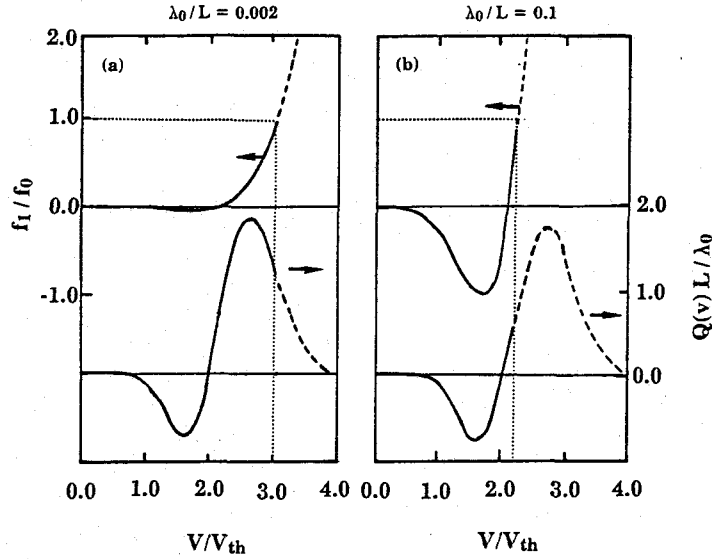


Fig. 2-2 Temperature gradient and mean free path dependence of heat flux $[Q(v)]$ and particle $[f_1/f_0]$. Solid lines are the region that f_1/f_0 does not exceed unity.

mean free path is proportional to the square of the energy, the mean free path of the heat carrier is about $25\lambda_e$. Furthermore, Eq. (2-19) indicates that the electrons of the energy higher than $15T$ (of which mean free path is $100\lambda_e$) can carry 1.5% of the total heat flux.

However above diffusion approximation should not be applied to steep temperature gradients compared with the electron mean free path. From Eq. (2-19), it can be seen that f_1/f_0 increases with λ_e/L at some velocity, depending on λ_e/L , becomes greater than unity. For $\lambda_e/L < 10^{-3}$, the violation of the diffusion approximation occurs at velocities above the range where significant part of the heat is carried, $2-3.5v_{th}$ as shown in Fig. 2-2(a). Contrarily as the gradient becomes steeper, λ_e/L increases, and the violation occurs at velocities at which a significant part of the heat is carried (for $\lambda_e/L = 0.1$, f_1/f_0 exceeds unity at about $2.1v_{th}$ as shown in Fig. 2-2(b)). For steeper gradients compared with the electron mean free path, the nonlocal contributions due to collisionless electrons will dominate the heat flow and the local theory is not adequate. Hence the classical expression

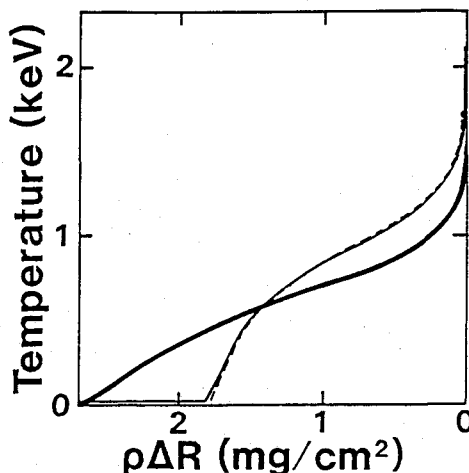


Fig. 2-3 Temperature profiles of laser heated plasmas at 1.45 nsec with solid DT ($\rho = 0.21 \text{ g/cm}^3$) from various simulations. $0.53\text{-}\mu\text{m}$ laser light is focused at the incident angle of 30° with intensity of $5 \times 10^{14} \text{ W/cm}^2$. Initial temperature is 20 eV. The scalelength in absorbed region is constant to be $40 \mu\text{m}$. Absorption is kinetically calculated with F-P simulation. Bold solid line is the result from F-P simulation. Broken line from S-H model (flux limiter $\alpha = 0.15$). Solid line from delocalization model.^[8]

overestimates the heat flux at the hot edge of the temperature front, while it underestimates the flux at the cold region.

When nonlocal transport is important, adequate modeling of the thermal electron transport requires a numerical solution of the fully kinetic Fokker-Planck equation. The first solution of the Fokker-Planck equation, as applied to the propagation of a heat front in a plasma, was given by A. R. Bell.^[7] Figure 2-3 shows that the spatial profiles of the temperature from numerical solutions of flux limited diffusion approximation (S-H)^[8] and full Fokker-Planck equation.^[9] At 500-eV region, the profiles from both solution is same. However in the hot part of the plasma and the heat front, the flux is less than S-H flux. At the foot of the heat front, the heat flow is actually higher than S-H flux because of the presence of long-mean-free-path electrons which came from the hot part of the plasma and have not lost their energy through collisions.

Therefore the high energy tail of the electron distribution is important as an energy carrier and can strongly preheat the cold dense region nonlocally. We have to pay attention to the preheating by thermal electrons even if there are not hot electrons generated by resonance absorption and/or various plasma instabilities.

§ 2-4. X-ray Energy Transport

Radiative processes and radiation energy transport play an important role in inertial confinement fusion. The hot and dense plasmas produced in an ICF target emit and reabsorb the radiation at soft x-ray wavelengths. This radiation represents a significant energy transfer mechanism and can strongly affect the implosion and thermonuclear burn dynamics of the target.

Radiation transport in laser-produced plasmas with steep temperature and density gradients are very complex in general. X rays with sufficient high energy photon is transported and shine through such plasmas without being affected by the temperature gradient. However x ray via low photon energy has complex processes e.g. transmission with ionization burn-through and repeating the absorption and re-emission over again.

Penetration of high energy photon^[10]

For photons to penetrate into target the ablation plasma is optically thin. X rays in an optically thin plasma transport with simple processes which depends on the photo-absorption cross section.

The specific heating rate $\dot{\epsilon}$ at depth x in the target with x ray of spectrum I_x can be written as

$$\dot{\epsilon} \approx \int_0^{\infty} I_x(h\nu) \cdot \exp[-\sigma(h\nu)x] \cdot \sigma(h\nu) d(h\nu) \quad (2-20)$$

where σ is the x ray mass absorption coefficient and ρx is the depth in units of mass per unit area. This is a simplified expression since the absorption coefficient also depends on the temperature i.e., ionization state and position x with temperature gradient. However this approximation is reasonable when the photon energy is sufficiently high and the absorption coefficient is not affected with the temperature gradient.

The temperature rise kT due to the x ray can be readily calculated for an ideal fully ionized plasma ($A \approx 2Z \gg 1$) without radiation loss to be

$$kT = \frac{4}{3} m_p \dot{\epsilon} \tau, \quad (2-21)$$

where m_p is the proton mass and τ the duration of radiation.

It is convenient, when evaluating kT from experimental data on $I(h\nu)$, to know which spectral regions are important. This can be achieved by introducing the "cut off" photon energy $h\nu_c$ defined by

$$\sigma(h\nu_c) \rho x = 1 \quad (2-22)$$

and by expressing the spectrum $I_x(h\nu)$ in the vicinity of $h\nu_c$ as

$$I_x(h\nu) = I_x(h\nu_c) \exp \left[\frac{h\nu_c - h\nu}{kT} \right] \quad (2-23)$$

and the mass absorption coefficient $\sigma(h\nu)$ as introducing the "cut off" photon energy $h\nu_c$ defined by

$$\sigma(h\nu) = \sigma(h\nu_c) (h\nu_c/h\nu)^3 \quad (2-24)$$

Then with the variable $a = h\nu/h\nu_c$ and introducing $b = kT/h\nu_c$ we have from Eqs. (2-20), (2-21), (2-22), (2-23), and (2-24)

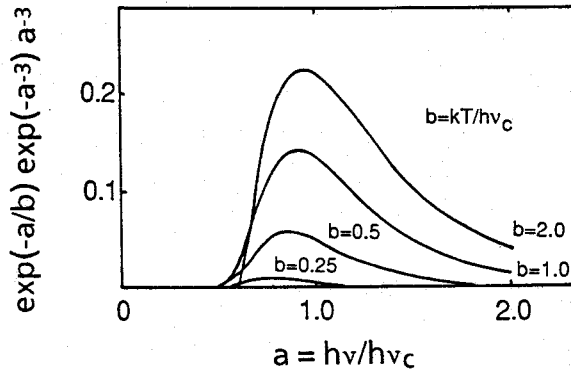


Fig. 2-4 X-ray frequency dependence of the integral in Eq. 2-25 for various values of the parameter $b = kT/hv_c$.

$$kT = \int_0^{\infty} \exp\left[\frac{1}{b}\right] \exp\left[-\frac{a}{b}\right] \exp(-a^{-3}) a^{-3} da \quad (2-25)$$

The frequency dependence of the integral in Eq. (2-25) is shown in Fig. 2-4 for various values of the parameter b . In all cases it peaks at $h\nu = hv_c$ and has a fairly narrow range about $h\nu_c$ showing that preheating is due to photons with $h\nu = hv_c$.

Recent reports of experiment and simulation have shown that the radiation was several order of magnitude more efficient in transporting energy past the ablation surface than the thermal conduction. However such situation cannot be explained with above treatment taking account of only constant photo-absorption cross section.

Ionization burn-through

In general the dense plasma which strongly attenuates photons via collisions with inner-shell is not neutral, and cross section must be adjusted as a function of ionization state as well as photon energy. For example a plot of the photo-ionization cross sections versus photon energy for the different ionization stages of aluminum is shown in Fig. 2-5. It should be noted that the edge of the cross section shifts with ionization state. Figure 2-6 shows the ionization state versus temperature in solid density aluminum from LTE

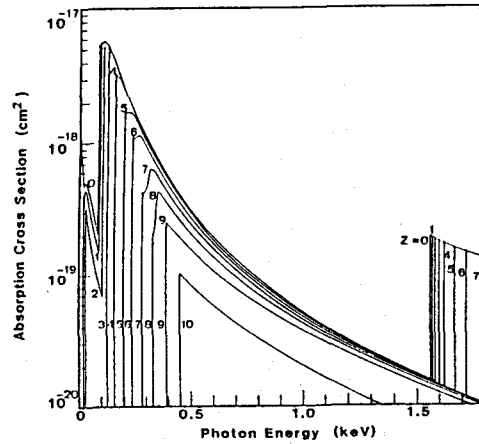


Fig. 2-5 X-ray photoabsorption cross sections at various ionization stages of aluminum.

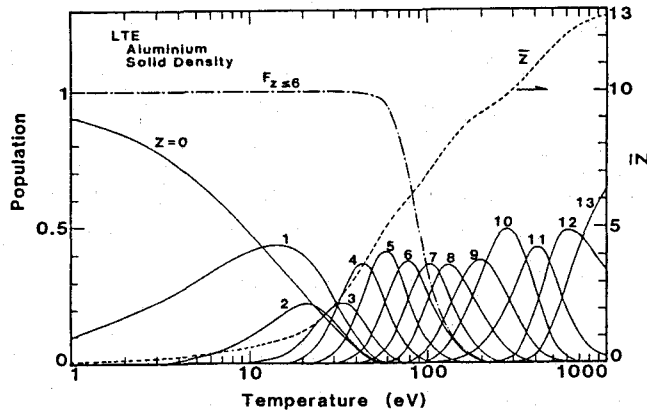


Fig. 2-6 Temperature dependence of ionization stages (Z) in solid aluminum from LTE model. Solid lines are population. Broken line is averaged Z .

model with Saha equation. These figures show that when temperature become 100eV in solid density, most of the ionization state is ≥ 7 and such plasma must be optically thin for the x ray of the photon energy of 200eV to 300eV. Then this transmitted radiation penetrates further into a colder and higher density region, resulting in increasing temperature and ionization in this cold region and shifting the absorption edges to higher photon energies. Here the heating in this region is caused by photo-ionization of inner-shell

electrons. This allows penetration of these photons deeper than the normal with time, resulting in moving ionization (or temperature) front toward the inner region. This "*ionization burn-through*" proved to be most important to radiative heating.^[11]

Down conversion

In above discussion considered is only absorption. In high Z plasma or not so much heated plasma i.e., partially ionizing plasma but exiting there may be different and complex processes (re-emission).

The matter heated by ionization burn-through will re-radiate much of its energy, but at lower photon energies corresponding to the dominant ionization stages of the colder material. This process continues with photons being absorbed and re-emitted at lower frequencies. Hence the radiation reaching the rear surface of the thin foil is comprised of a wide spectrum of photons, from front side soft x rays, which manage to penetrate the total extent of the foil, to transition and backside photons which have been born in the XUV range via progressive *down-conversion* in frequency of the incident soft x rays.^[11] It is this progressive down-conversion process which makes the radiational heating of the dense backside plasma such a complex process, and renders the simple technique of turning the measured forward spectrum back onto the cold dense plasma to obtain estimates the radiational heating, somewhat inaccurate.

§ 2-5. Conclusion

Preheat of the fuel preceding the final compression phase must be suppressed to achieve efficient laser implosion. Strong shock, x radiation, and high energy tail of thermal electron distribution may become an important factor of the preheat. In following chapter, we experimentally studied the energy transport i.e., shock wave, x ray, and electron energy transport.

References

- [1] R. E Kidder, Nucl. Fusion **16**, 405 (1976).
- [2] J. Meyer-Ter-Vehn, Nucl. Fusion **22**, 561 (1982).
- [3] R. E Kidder, Nucl. Fusion **21**, 145 (1981).
- [4] Y. Zeldovich and Y. Raiser, Physics of Shock Waves and High Temperature Hydrodynamic Phenomena (Academic, New York, 1966).
- [5] R. Fabro, C. Max and E. Fabre, Phys. Fluids **28**, 1463 (1985).
- [6] R. E. Kidder, Nucl. Fusion **19**, 223 (1979); S. M. Pollaine and J. D. Lindl, Nucl. Fusion **26**, 1719 (1986).
- [7] A. R. Bell, B. G. Evans and D. J. Nicholas, Phys. Rev. Lett. **46**, 243 (1981).
- [8] L. Spitzer and R. Härm, Phys. Rev. **89**, 977 (1953); L. Spitzer, Jr., Physics of Fully Ionized Gases, Wiley Interscience, New York (1962).
- [9] Y. Kihara, Master thesis, Osaka University, (1989) (unpublished).
- [10] M. H. Key :Energy transport in laser produced plasmas (Radiation in plasma Volume I, edited by McNamara, World Scientific, Singapore, 1984), p.478.
- [11] D. Duston, R. W. Clarc, J. Davis, and J. P. Apruzese, Phys. Rev. A **27**, 1441 (1983); D. Duston, R. W. Clarc, and J. Davis, Phys. Rev. A **31**, 3220 (1985).

Chapter 3

ENERGY TRANSPORT IN UV-LASER PRODUCED PLASMAS

§ 3-1. Introduction

§ 3-2. Characterization of Laser Plasma X Ray

§ 3-3. Energy Transport in UV laser Produced Plasmas

§ 3-4. Conclusion

§ 3-1. Introduction

A short wavelength laser ($<1\mu\text{m}$) is known to be advantageous for laser fusion because of its high-energy absorption and low hot-electron generation.^[1] The advantages of submicron wavelength lasers also include higher ablation rate and pressure.^[2] The rate at which mass is ablated from a directly driven, ICF target is ultimately responsible for the compression of that target. Many studies have been reported on the laser wavelength scaling of mass ablation rate and pressure for short wavelength laser (e.g., 1.05, 0.53, 0.35, and 0.26 μm).^{[3], [4]} For example the scaling by shown by T. Boehly et al are $m=\lambda^{-1.4}$ for mass ablation rate and $P_a=\lambda^{-0.9}$ for ablation pressure.^[3]

In addition, with the decrease in laser wavelength there is also an increase in soft x-ray generation.^{[4]-[6]} It thus becomes particularly important to understand the energy transport mechanisms highly weighted with x-radiation in targets irradiated by a UV laser. A number of experimental and theoretical studies ^{[5]-[12]} delineated details of energy transport in high-density plasmas. Duston et al.^[9] and Salzman^[10] et al. pointed out that x-radiation might explain some previously unexplained

experimental data with their simulation results. Ng's experimental study^[12] showed that data were consistent with x-radiation effect. However few experiments have been presented to study details of energy transport especially for high Z, thin targets irradiated by a 263 nm laser.

In this Chapter, energy transport in UV-laser produced plasmas are experimentally studied considering above circumstances.

Characteristics of x ray from short wavelength laser produced plasmas are initially shown in Section 3-2. Presented are experimental results on radiation spectra and conversion efficiencies of sub keV and keV emissions with different target materials, together with their dependence of laser intensity, laser wavelength, laser pulse. These results will provide quantitative bases for understanding the energy transport in short wavelength laser-produced plasmas.

In Section 3-3 experimental studies are presented on energy transport by x-radiation, shock, and electron thermal conduction through aluminum ($Z=13$) and gold ($Z=79$) thin foils irradiated with a frequency quadrupled Nd: glass ($\lambda=263\text{nm}$) laser beam. The measurement was conducted by observing the rear side emissions from the target with temporal resolution. For Al thin foils ($\leq 3\mu\text{m}$) emissions indicated that the energy transport mechanism could be mainly by radiation front propagating at slightly higher speed than the thermal conduction speed. Shock waves are clearly observed for Al targets thicker than $5\mu\text{m}$. For Au targets, a third peak could be distinctively observed in addition to the shock and thermal fronts, which was attributed to the radiation front.

§ 3-2. Characterization of Laser Plasma X Rays

Characterization of x-ray emission depends on the atomic structure, electron density, and temperature. Assuming the coronal equilibrium and

optically thin plasmas, the spectral intensity with $h\nu$ photon energy is given by [13], [14]

$$I_x(h\nu) = Z^{-3} \cdot \left(\frac{E_H Z^2}{h\nu} \right)^3 \cdot \left(\frac{E_H Z^2}{kT_e} \right)^{1/2} \cdot n_e \cdot n_i \cdot \exp \left[-\frac{h\nu}{kT_e} \right] \quad (3-1)$$

from the energy level of hydrogen-like ions, where $E_H = 13.6$ eV is the hydrogen ionization energy, Z is the ion charge state, n_e is the electron density and n_i is the total ion density for charge state necessary to produce the transition of interest.

3-2-1. Experimental setup

Experiments have been conducted with GEKKO IV glass laser system. X-ray spectra and energy from laser produced plasmas were measured by using a 10 channel x-ray diode set (XRD) and the transmission grating spectrometer (TGSM) coupled with a Kodack 101 film. Target plates were carefully handled and/or chemically cleaned in order to keep the surfaces free from oxidizable material was dissolved in hydrochloric acid or sulphuric acid.

3-2-2. Target atomic number dependence

Bound-bound and bound-free transitions are dominant factors to x-ray generation in the laser-produced plasmas unless the target is low-Z material. Thus we expect that the spectrum of laser plasma x rays depends on characteristic structure of electron orbits of ion. Here we present atomic number dependence of x-ray spectra and conversion efficiency where the conversion efficiency is defined as a ratio of the time-integrated x-ray spectral intensity per unit angle to the incident laser energy. Laser condition are and target materials are shown in Table 3-1.

Fig. 3-1 shows the obtained atomic number dependence of the spectrally resolved conversion efficiency ($J / \text{keV}/\text{sr}/E_L$), where the spectral range was from 0.1 to 3.0 keV. It should be noted that the x-ray spectra have several

Table 3-1. Experimental condition of atomic number dependence

Laser Wavelength (λ_L)	; 0.53 μm
Laser Intensity (I_L)	; $10^{14}\text{W}/\text{cm}^2$
Pulse Duration (τ_L)	; 1ns (400ps) (FWHM)
Spot Diameter (d)	; 150 ~ 200 μm
Incident Angle (θ_{in})	; 35°
Target Material (z)	; CH(6.5), Al(13), Ti(22), Cu(29), Ge(32), Nb(41), Mo(42), Ag(47), Sn(50), Gd(64), Ta(73), Au(79)

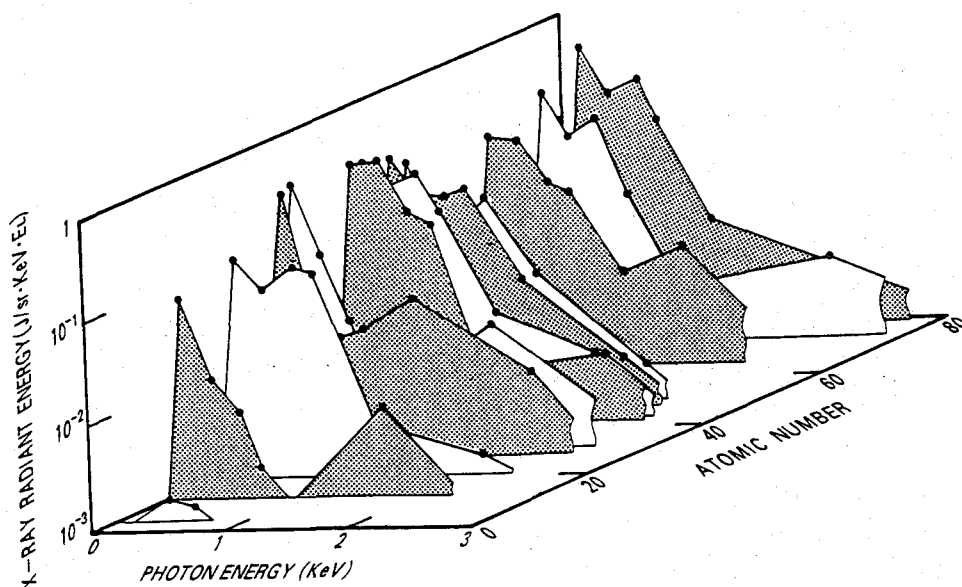


Fig. 3-1 Atomic number dependence of x-ray spectral intensity.
 $\lambda_L = 527 \text{ nm}$, $\theta = 35^\circ$, $I_L = 10^{14} \text{ W}/\text{cm}^2$, and $\tau_L = 1 \text{ nsec}$.

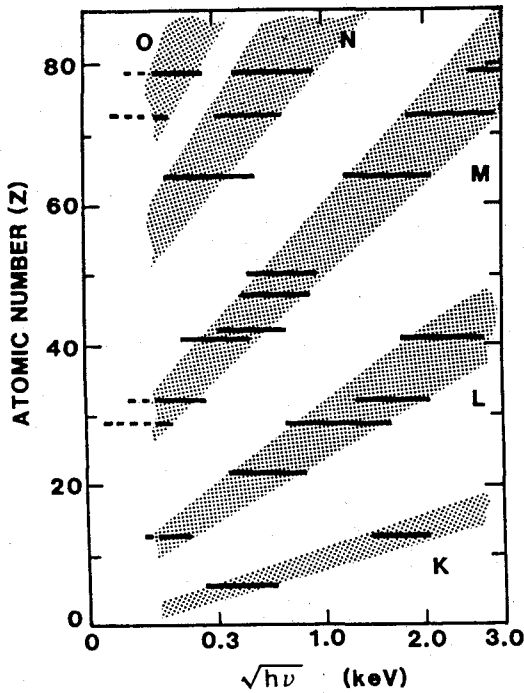


Fig. 3-2 Positions of x-ray spectral peaks (FWHM) as a function of atomic number Z . Solid bars show positions of the spectral peaks. Shaded zones correspond to the transitions in K, L, M, N, O shells of ions.

humps which move to the higher energy side as the atomic number (Z) of the target material increases. The square root of the photon energy at the spectral hump is found to be an approximately linear function of the atomic number (Z) as shown in Fig. 3-2. The solid line shows the photon energy bound which is defined as providing the intensity of more than a half of the hump maximum. These series of the spectral humps indicated by shaded zones in Fig. 3-2 are interpreted as the electronic transitions in K, L, M, N, and O shells of ions. These results indicate that a semi-Moseley's law i.e. $Z \propto \sqrt{h\nu}$ is valid in the laser-produced plasmas. Such atomic number (Z) dependence is due to the atomic structure. The height of these humps may change with the temperature and density distribution of produced plasmas but the position of the hump will not change so much ($Z \propto \sqrt{h\nu}$). From the obtained semi-Moseley's law we can easily anticipate the material which most strongly emits the radiation of desired photon energy.

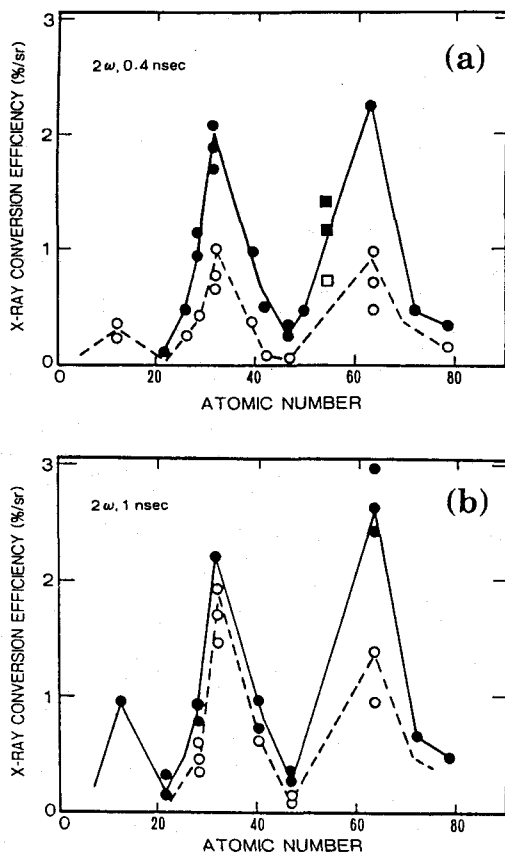


Fig. 3-3 X-ray conversion efficiency of $h\nu > 1$ keV. Atomic number dependence of solid and broken lines show efficiencies for the laser intensities of 10^{14} W/cm² and 10^{13} W/cm², respectively. $\lambda_L = 527$ nm, $\theta = 35^\circ$. (a) $\tau_L = 0.4$ nsec and (b) $\tau_L = 1$ ns.

Figure 3-3 shows the conversion efficiency to x-rays whose energies are more than 1.5 keV as a function of atomic number (Z). Solid and broken lines correspond to the cases of laser intensity of 10^{14} W/cm² and 10^{13} W/cm², respectively. These efficiencies were obtained by using a 45- μ m thick Be-filtered XRD. This XRD's spectral sensitivity composed of a sharp rising part at $h\nu$ 1.5 keV extending to about 3 keV and a gradually increasing but low level part from 1 keV to 1.5 keV as shown in Appendix B. In this figure the correspondence to the electronic shells of ions is seen more clearly than that in Fig. 3-1. The conversion efficiency decreases with the laser intensity but still has a tolerable level at 10^{13} W/cm². On the other hand, a shorter pulse produced a lower efficiency. These results are due to the electron

temperature and emission volume affected by the laser condition. Detailed studies are described in the following parts (3-2-4, and 3-2-5).

3-2-3. Laser intensity dependence

From Eq. (3-1), the emissivity is a function of temperature which depends on the laser intensity. Assuming that the inverse bremsstrahlung absorption is dominant and the plasma scale-length is equal to $C_s \tau_L$ for one-dimensional expansion, the electron temperature at the critical point is approximately given by^[15]

$$T_e = 0.55 \cdot (I_L \cdot \lambda_L)^{1/2} \cdot (Z \cdot \Lambda \cdot \tau_L)^{1/4} \cdot \mu^{-1/8} \quad (3-2)$$

where I_L is the incident laser intensity and $\mu = 2Z/A$, $\Lambda = \Lambda/6$ and T_e , I_L , λ_L and τ_L are normalized by the values of 100 eV, 4.8×10^{11} W/cm², 1.06 μ m, and 100 psec, respectively.

In this part we describe the intensity dependence or temperature dependence of the x-ray conversion efficiency. Diagnostics of x-ray measurements were same as the previous part. Laser condition and target material are shown in Table 3-2.

Table 3-2. Experimental condition of intensity dependence

Laser Wavelength (λ_L) ;	0.26 μ m	0.53 μ m
Laser Intensity (I_L) ;	$2.4 \sim 7 \times 10^{13}$ W/cm ²	$4 \times 10^{13} \sim 2 \times 10^{14}$ W/cm ²
Pulse Duration (τ_L) ;	400 ps	400 ps
Spot Diameter (d) ;	150 \sim 200 μ m	200 μ m
Incident Angle (θ_{in}) ;	22.5°	35°
Target Material (z) ;	Au(79)	Au(79), Cu(29), Ge(32), Gd(64)
Photon Energy (h ν) ;	0.1 \sim 1.6 keV	1 \sim 3 keV

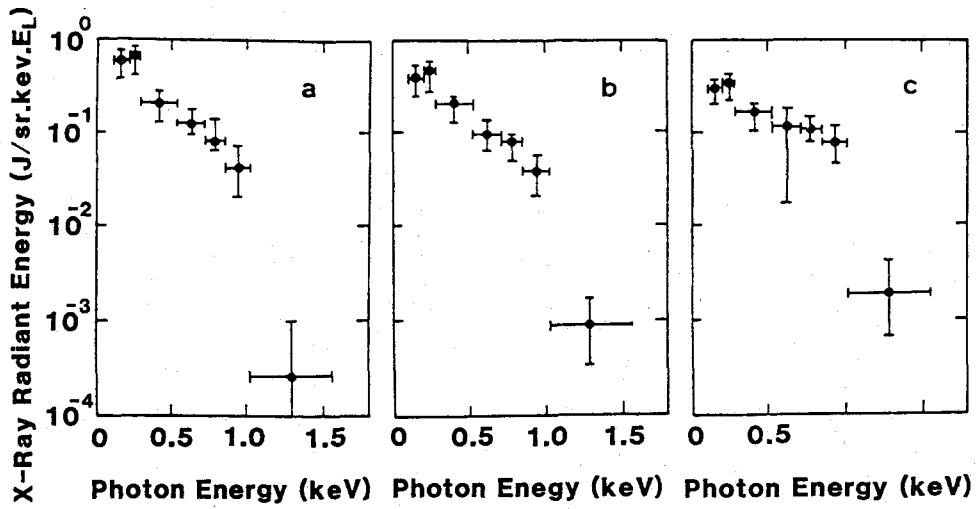


Fig. 3-4 Laser intensity dependence of soft x-ray spectra from Au plasmas produced by 263 nm laser light. (a) $I_L = 2.4 \times 10^{13} \text{ W/cm}^2$, (b) $I_L = 3.5 \times 10^{13} \text{ W/cm}^2$, and (c) $I_L = 6.5 \times 10^{13} \text{ W/cm}^2$.

Figures 3-4(a), 4(b), and 4(c) show the radiant energy spectra from Au targets with the 0.26- μm laser at intensities from $2.4 \times 10^{13} \text{ W/cm}^2$ to $6.5 \times 10^{13} \text{ W/cm}^2$. The laser intensity was varied by only changing the incident laser energy, not the focal spot size, in order to minimize the difference due to the lateral heat conduction. It is readily seen in Fig. 3-4 that the lower photon energy component ($\sim 200 \text{ eV}$) increases with decreasing the laser intensity. The higher energy photon component ($\geq 700 \text{ eV}$), however, decreases with decreasing the laser intensity. At laser intensity of 2.4×10^{13} , 3.5×10^{13} , and $6.5 \times 10^{13} \text{ W/cm}^2$, the ratio of the lower photon energy (100–300 eV) to the energy of 0.1–1.6 keV is about 55%, 45%, and 39%, respectively. Figure 3-4 indicates that the increasing rate of the lower photon energy component ($\approx 200 \text{ eV}$) for reducing laser intensity is higher than the decreasing rate of the higher photon ($\sim 700 \text{ eV}$).

Figure 3-5 shows the laser intensity dependence of the x-ray conversion efficiency obtained from Fig. 3-4. This efficiency varies from 63% at the laser intensity $6.5 \times 10^{13} \text{ W/cm}^2$ to 80% at $2.4 \times 10^{13} \text{ W/cm}^2$.

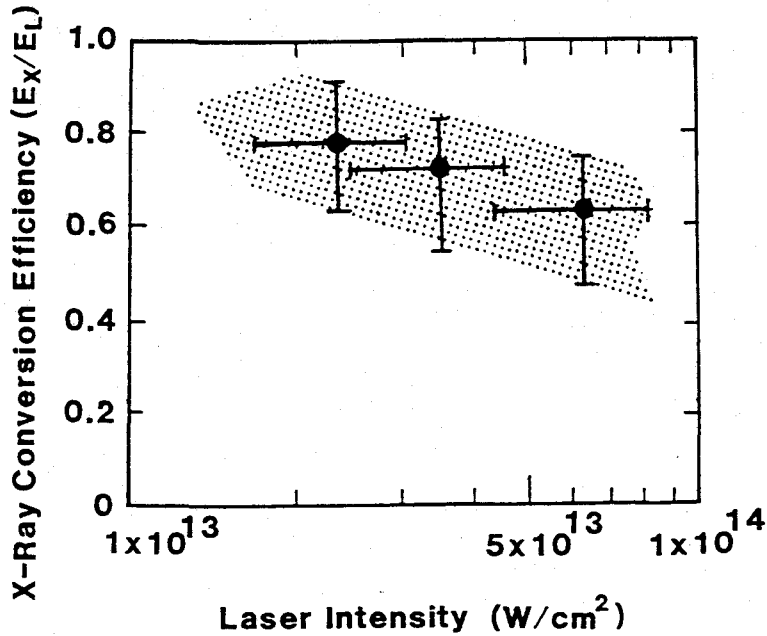


Fig. 3-5 Laser intensity dependence of x-ray conversion efficiency for Au plasmas at $\lambda_L = 263$ nm ($\tau_L = 400$ ps).

Here we consider the energy balance to check if we can obtain such high conversion efficiency. From charge collector signals, the thermal energy loss W_{th} is estimated to be $W_{th} < 0.16$ J at the intensity of 2.4×10^{13} W/cm². The ionization loss W_{ion} for gas ionize is estimated to be $W_{ion} < 0.18$ J. Radiation loss W_{rad} is 1.5 J from the x-ray conversion efficiency. The energy balance equation is realized to

$$W_L \eta_a = 1.9 \eta_a \cong W_{th} + W_{ion} + W_{rad} = 1.8 \text{ J} , \quad (3-3)$$

for which laser absorption η_a is about 95%. This absorption is in reasonable agreement with previous absorption data.

The increase in the conversion efficiency is not due to the increased laser absorption since the laser absorption for the 0.26- μ m light has been reported

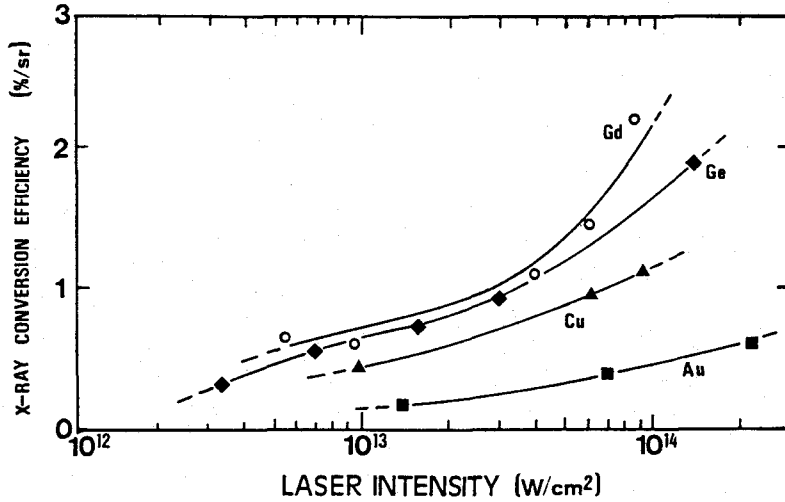


Fig. 3-6 Laser intensity dependence of keV x-ray conversion efficiency ($1 \leq h\nu \leq 3$ keV) at $\lambda_L = 527$ nm with $\tau_L = 400$ ps.

to be nearly 100%.^[16] Given the finite angle of incidence (45°), the absorption occurs at high density which should be two times higher than the critical density of the 0.53- μ m light. At such high density the absorption due to the inverse bremsstrahlung is expected to be dominating and nearly 100%. However the plasma temperature may decrease with decreasing the laser intensity. We consider that the temperature decrease, if any, works favorably to explain the results mentioned above. Lower photon energy (≈ 200 eV) and higher photon energy (≈ 700 eV) components are mainly from the bound-bound emission into the O-shell and N-shell, respectively. With the decrease of the plasma temperature, the electrons remaining in the O-shell orbits increase. Thus collisional excitations and emissions occur to produce more photons in 150~300 eV range. Such a condition may be satisfied at the lower laser intensity used in this experiment. However, at much lower intensity, lateral- and axial-thermal diffusions in the target are so dominant that the plasma temperature becomes too low to make sufficient collisional excitation of electrons.

Figure 3-6 shows the keV x-ray ($h\nu \approx 1 \sim 3$ keV) conversion efficiency as a function of laser intensity at the 0.53- μ m light for various target materials.

Here Gd and Cu or Ge conversion efficiencies correspond to the M- and L-shell from the experimental results shown in section 3-2-2. The conversion efficiencies of all materials increase with the laser intensity. It is considered that this increase in the conversion efficiency is due to the increased coronal temperature with the laser intensity as predicted by Eq. (3-2). X rays above 1 keV photon energy are generated near the coronal region^[17] and the emissivity strongly depends on the coronal temperature. Thus collisional excitations in M- or L-shell produces more photons in the 1~3keV range. However at much higher intensities, the electron temperature is so high that the population of each shell electrons decreases and the conversion efficiency originating in the bound-bound transitions of each shell electrons decreases.

3-2-4. Laser wavelength dependence

In general, laser-produced plasma has steep density and temperature gradients. At each temperature and density region, the ion charge state is different and the energy levels of electron orbits for each charge-state ion change in space. The emissivity of high energy photon (keV) or bound-bound transition is large in high temperature and underdense region (i.e., coronal region) near the critical density, while the radiation of lower energy photon (sub keV) or free-bound emission is dominant at a high density and low temperature region near ablation surface.^[17] On the other hand, the region of laser absorption strongly depends on the laser wavelength and

Table 3-3. Experimental condition of laser wavelength dependence

Laser Wavelength (λ_L) ;	1.05 μm	0.53 μm	0.26 μm
Incident Angle (θ_{in}) ;	22.5°	35°	45°
Laser Intensity (I_L) ;	10 ¹⁴ W/cm ² (10 ¹³ W/cm ²)		
Pulse Duration (τ_L) ;	400ps (FWHM)		
Spot Diameter (d) ;	150 ~ 200 μm		
Target Material (z) ;	Al(13), Cu(29), Ge(32), Gd(64), Au(79)		

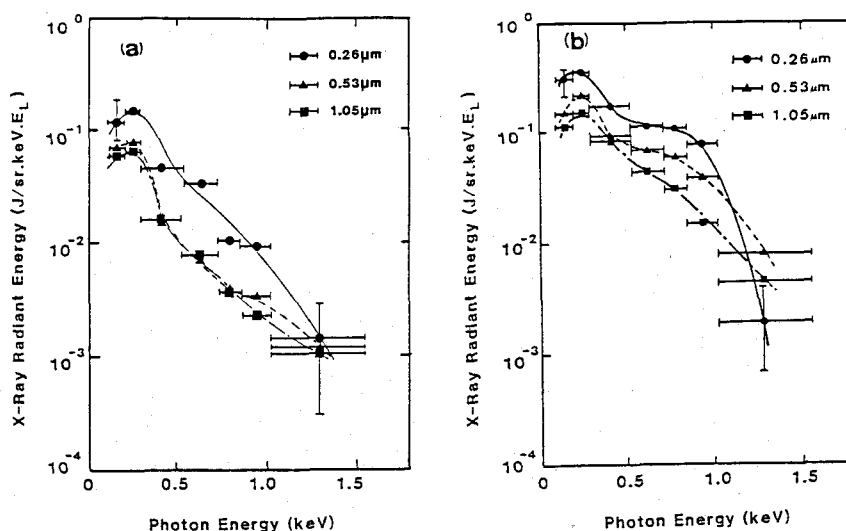


Fig. 3-7 Laser wavelength dependence of soft x-ray spectra from Al (a) and Au (b) plasmas produced by 0.26 μm (\bullet), 0.53 μm (\blacktriangle), and 1.06 μm (\blacksquare) laser lights at $I_L = 6.5 \times 10^{13} \text{ W/cm}^2$ with $\tau_L = 400 \text{ psec}$.

shorter wavelength laser deposits the energy into higher region more efficiently. From above reasons, the energy transport into the soft x-ray generation region depends on the laser wavelength.

In this part the laser wavelength dependence of the x-ray conversion efficiency ($h\nu \approx 0.1 \sim 1.6 \text{ keV}$) is described and discussed with respect to the energy transport into the x-ray generation region.^[17] The laser wavelength dependence of keV x-ray conversion efficiency ($h\nu \approx 1 \sim 3 \text{ keV}$) is also described.

The x-ray conversion efficiency is defined as the same as above section. Laser condition and target materials are shown in Table 3-3. X-ray spectra and energy were measured by same diagnostics as section 3-2-1. The electron temperature and hot electrons were evaluated with keV (1~25keV) x-ray spectra from 7 channel x-ray *p-i-n* diodes (XPIND). Ion expansion was monitored by using charge collectors.

Figure 3-7(a) and (b) show the wavelength dependence of the soft x-ray spectra from Al and Au planar targets, respectively. The laser intensity is $7 \times 10^{13} \text{ W/cm}^2$ at the pulse duration of 400psec. The horizontal bars indicate

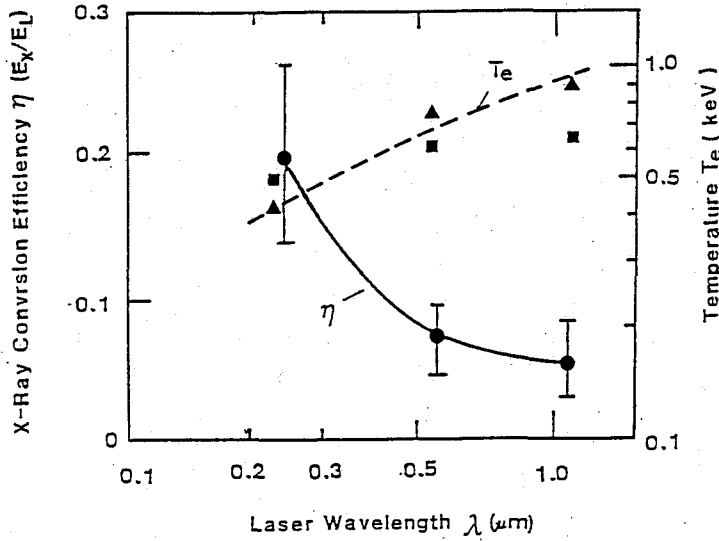


Fig. 3-8 Laser wavelength dependence of x-ray conversion efficiency and electron temperature for Al plasmas at $IL=7 \times 10^{13}$ W/cm² ($\lambda L=527$ nm, $\tau L=400$ psec). Broken line represents a theoretical scaling from Eq. 3-2.

the instrumental energy bands. Curve fitting was 50% response points. the vertical error bars are estimated from the filter response curve and filter thickness as mentioned in Appendix A. The emissivity of the lower-energy x rays increases with decreasing laser wavelength. For the 0.26- μm laser the emission from Au plasma around $h\nu=1.3\text{keV}$ appears to be reduced and most of the energy is confined to $h\nu < 1\text{keV}$. These results can be considered to be due to the decrease in electron temperature with laser wavelength which results in the decrease in high energy photon component.

Figure 3-8 and 3-9 show the x-ray conversion efficiency obtained from Fig. 3-7 for Al and Au plasmas, respectively, as a function of laser wavelength. Figure 3-8 also shows the wavelength dependence of electron temperature and the analytical prediction (broken line) from Eq. (3-2). The total emitted energy was calculated from the angular distribution of the emission. In the angular distribution measurements, the XRD signals through the parylen ($h\nu < 0.28\text{keV}$) and the nickel ($h\nu < 0.85\text{keV}$) filters showed roughly a cosine distribution for the 0.53- μm , and 1.05- μm lights.

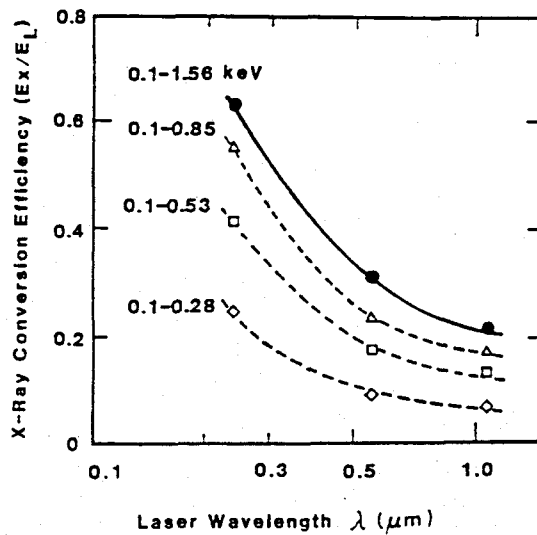


Fig. 3-9 Laser wavelength dependence of x-ray conversion efficiency for Au plasmas at $I_L = 7 \times 10^{13} \text{ W/cm}^2$ ($\lambda_L = 527 \text{ nm}$, $\tau_L = 400 \text{ ps}$).

The zinc channel ($h\nu > 0.85 \text{ keV}$) showed roughly a cosine^{1/2} distribution for these laser lights. The results have been reported for the 0.53- μm laser by W. C. Mead et al.^[6] For 0.26- μm light these three XRDs' signals showed the angular distribution of cosine^{1/2}. This observed difference in the angular distributions may come from the differences in the focal spot diameters and/or plasma scale lengths. At 90° to the target normal a zero flux was assumed to calculate the x-ray energies with the cosine or cosine^{1/2} distribution. Though there might be some x-ray flux at 90°, estimated errors for the total conversion efficiency are within 10%. One can see that the shorter wavelength laser shows a higher x-ray conversion efficiency in both cases of Al and Au materials.

For the 0.26- μm , 0.53- μm , and 1.05- μm laser produced Al plasmas, electron temperatures estimated from ion velocity distribution obtained with charge collector were 410 eV, 770 eV, and 890 eV, respectively. Electron temperatures estimated from keV bremsstrahlung x-ray spectra by the

XPIN were 500 eV, 610 eV, and 630 eV, respectively. Here we assumed that the electron distribution is Maxwellian. The temperatures from the ion distribution and the x-ray spectra show different values but have a similar trend; the shorter wavelength laser tends to produce the plasmas with lower electron temperature. The scaling from experiments is in good agreement with the theoretical scaling as shown in Eq. (3-2). Shorter wavelength laser is absorbed in higher density region and must heat higher density plasmas at same input energy. Thus from the energy conservation law, the electron temperature must decrease with decrease of laser wavelength.

Here we estimate the hot electron contribution to soft x-ray generation. The energy density for electrons is roughly proportional to $n_e \cdot (kT_e)^{3/2}$, where n_e and T_e are electron density and temperature. In this experiment n_e and T_e can be estimated from the results of the keV x-ray spectra (1~25keV) which are assumed to be due to the bremsstrahlung. The ratio of the heat flux by hot electrons to that by cold electrons is of the order of 10^{-3} for the 1.05- μm and 0.53- μm lights and 10^{-4} ~ 10^{-5} for the 0.26- μm light. These ratios are so small that the soft x-ray conversion efficiency is not affected by the flux of the hot electrons.

In the case of Au plasma the conversion efficiency for the 0.26- μm light is as high as 63% ($\geq 66\%$), while the 0.53- μm and 1.05- μm lights show 31% (43%) and 22% (31~34%), respectively. Here the conversion efficiency is the ratio of the total soft x-ray energy to the incident laser energy. The numbers in the parentheses are the conversion efficiencies calculated from the ratio of the x-ray energies to the absorbed energies. The absorbed energies are quoted from Ref. 6, 16, and 18. We took into account the differences of the incidence angles between our experiment and the references in these calculations. In Ref. 6, W.C.Mead et al. measured the conversion efficiency for 0.53- μm laser with Au target. At just below 10^{14} W/cm², the conversion efficiency using absorbed laser energy may be 50%, in reasonable agreement with our result within the experimental error bars. For Al plasmas the conversion efficiency was lower but showed the same tendency as the above Au case. The efficiencies were 20% ($\geq 22\%$), 9% ($\geq 11\%$), and 6% (12%) for the 0.26-, 0.53-, and 1.05- μm lights.

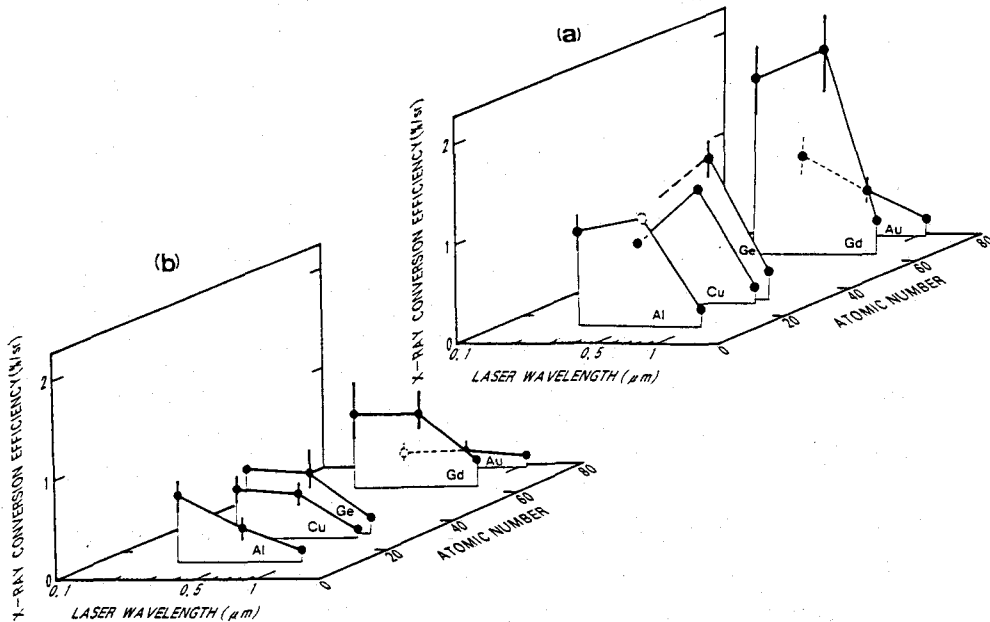


Fig. 3-10 Laser wavelength dependence for keV x-ray conversion efficiency (1~3keV) with variable targets at 400 psec. (a) $I_L = 10^{14} \text{ W/cm}^2$ and (b) $I_L = 10^{13} \text{ W/cm}^2$.

The x-ray conversion efficiency is about doubled for both cases of Au ($Z=79$) and Al ($Z=13$) at the 0.26- μm light compared to the cases at the 0.53- and 1.05- μm lights. This is due to the improved coupling of the energy from shorter wavelength light into the over-dense region. The length (X_c) of the heat conduction region between the ablation front and the critical surface depends strongly on the laser wavelength as $X_c \propto \lambda_L^{14/3}$.^[19] This distance is approximately the length between the laser absorbed region and the lower temperature and over-dense region which is responsible for most of the soft x-ray generation. We considered that the increased x-ray conversion efficiency for the shorter wavelength light is a direct result of the propagation of that light to higher densities thus creating a shorter conduction distance. Even if the absorption occurs near the turning point density, not the critical density, the turning point density of the 0.26- μm light is still three times higher than the turning point density of the 0.53- μm

light. Thus the finite incident angles in our experiment dose not affect the laser wavelength dependences of the conversion efficiencies.

Figures 3-10 (a) and (b) show the laser wavelength dependence of keV x-ray conversion efficiency ($h\nu \approx 1 \sim 3\text{keV}$), at laser intensities of (a) 10^{13} W/cm^2 and (b) 10^{14} W/cm^2 , respectively. At the laser intensity of 10^{13} W/cm^2 , the laser wavelength dependence is small. Shorter wavelength laser is absorbed in higher density region and the temperature is lower in the coronal region. The emissivity of about 1.5keV energy photons at the $0.26\text{-}\mu\text{m}$ light was almost at the same level as that at the $0.53\text{-}\mu\text{m}$. This is contrary to the soft x-ray ($h\nu < 1\text{keV}$) behavior. At the laser intensity of 10^{14} W/cm^2 , the conversion efficiency was maximum at the $0.53\text{-}\mu\text{m}$ except for the Au target.

keV x rays are generated near the critical region and depends on the critical density and temperature.^[17] From Eq. (3-1), higher temperature and higher density plasma produces higher emissivity. For the $1.05\text{-}\mu\text{m}$ light, the lower conversion efficiency is partly due to a lower laser absorption and partly due to the lower critical density. For the $0.26\text{-}\mu\text{m}$, the lower conversion efficiency than that for the $0.53\text{-}\mu\text{m}$ is due to the lower electron temperature. At the laser intensity of $\sim 10^{14}\text{ W/cm}^2$, the $0.53\text{-}\mu\text{m}$ light is most effective in generating x rays of $1 \sim 3\text{keV}$ photon energy.

3-2-5. Laser pulse duration dependence

It has been reported that the x-ray emission from laser-produced plasma was not a blackbody emission.^[17] Especially keV x-ray emission will be a volume emission in laser produced plasmas because of its low opacity by long mean free path.^[17] So the x-ray conversion efficiency will increase with a density scale length, where the plasma scale length is approximately equal to $C_0\tau_L$ for one-dimensional expansion, where τ_L is the laser pulse duration. Hence x-ray conversion efficiency will increase with a laser pulse duration τ_L .

This part shows the pulse duration dependence of the x-ray conversion efficiency. Diagnostics of x-ray measurements were same as the previous section. The laser condition and target materials are shown in Table 3-4.

Table 3-4. Experimental condition of laser pulse duration dependence

Laser Wavelength (λ_L) ;	0.53 μ m	0.53 μ m
Laser Intensity (I_L) ;	$0.7 \sim 2 \times 10^{14}$ W/cm ²	1×10^{14} W/cm ²
Pulse Duration (τ_L) ;	100ps \sim 1ns	130ps \sim 1ns
Spot Diameter (d) ;	150 \sim 300 μ m	250 \sim 300 μ m
Incident Angle (θ_{in}) ;	54.5°	35°
Target Material (z) ;	Au(79)	Cu(29)
Photon Energy (hv) ;	0.1 \sim 1.6keV	1 \sim 3keV

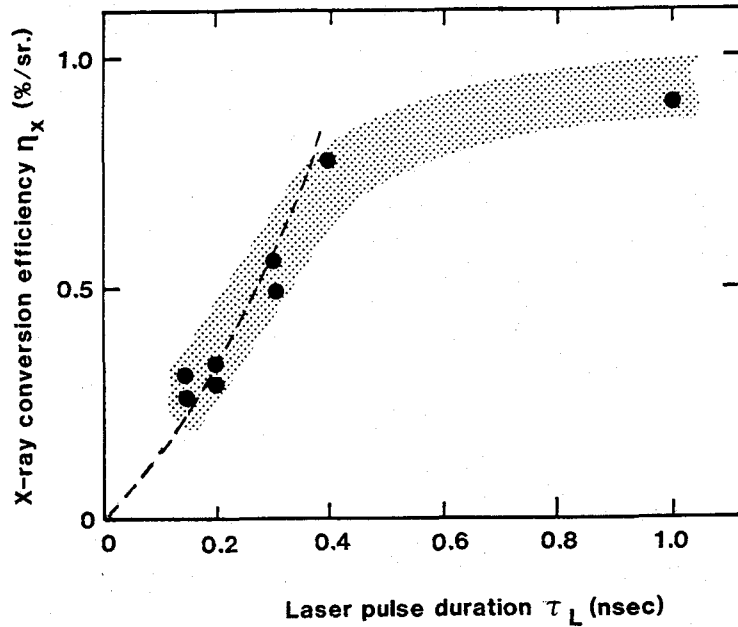


Fig. 3-11 KeV x-ray conversion efficiency as a function of laser pulse width at $I_L = 10^{14}$ W/cm² with a 527 nm laser. Dotted line shows ascaling of $\eta_x \propto \tau_L^{29/22} \exp(-3.86/\tau_L^{3/11})$ as presented by Eq. 3-4.

Figure 3-11 shows the keV x-ray conversion efficiency (η_x) as a function of full width at half maximum (FWHM) at a Gaussian laser pulse (τ_L) for a constant laser intensity of 10^{14} w/cm² with no pre-cursor pulse. Here the x-ray photon energy was 1~3keV. One can see that the longer the pulse duration the higher the conversion efficiency. For a 400 psec pulse the

conversion efficiency is 0.8 %/sr. which is about 2.5 times larger than that for a 130 psec pulse. For pulses less than 400 psec, the conversion efficiency scales as $\eta_x \propto \tau_L^{1.3}$. The observed increase of the conversion efficiency may be attributed to the increased emitting volume, simply because this volume is a function of the laser pulse duration. Detailed analysis of the emitting volume is given in the following paragraph. A longer pulse duration might increase the inverse bremsstrahlung absorption,^[20] which may also be another reason for the increased conversion efficiency. The absorption for an 80 psec pulse, however could reach as high as 75% at 0.53- μ m light at an intensity of 10^{14} W/cm².^[16] Thus the increased absorption is not enough to explain the above result.

The x-ray emissivity per unit volume (W/cm³) is a function of the electron temperature and the ion number density from Eq. (3-1). The electron temperature (T_e) increases with pulse duration increases. According to the self regulating model^[15] and assuming $Z \propto 2/3(AT_e)^{1/3}$ ^[21], it scales as $T_e \propto \tau_L^{3/11}$. Here Z is the ionization charge and A is the atomic number. The x-ray emitting volume is proportional to the density scale-length, assuming a planar plasma expansion. The density region responsible for the generation of x rays is assumed to be at critical region. The scale-length is inferred to be proportional to $C_s \tau_L$,^[22] where C_s is the sound speed. From these scalings, we can estimate that the conversion efficiency varies as

$$\eta \propto \tau_L^{29/22} \exp \left[\frac{-3.86}{\tau_L^{3/11} (\text{psec})} \right], \quad (3-4)$$

where τ_L unit is psec. In this estimation we also assume that the plasma is optically thin and the x-ray pulse duration is approximately equal to the laser pulse duration. This scaling is in reasonable agreement with the experimental results for durations less than 400 psec as shown in Fig. 3-11. The agreement indicates that the increase in the temperature and the emission volume are most responsible for the increase in the conversion efficiency.

The saturation at 1 nsec pulse duration could be explained by the effect of three-dimensional expansion. Since the three-dimensional expansion can be

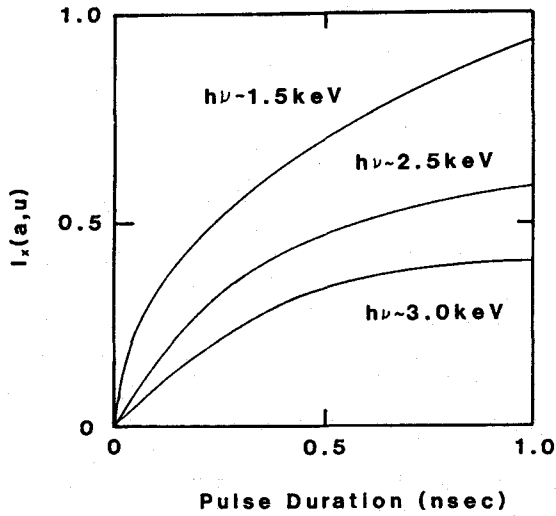


Fig. 3-12 Theoretical scaling of keV x-ray conversion efficiency as a function of laser pulse duration from Eq. 3-4.

dominant after $\tau_L \approx 800$ psec ($C_s \tau_L \approx$ focal spot diameter), the scale-length is limited to the focal spot size, causing the saturation.

Figure 3-12 shows the analytical scaling of conversion efficiency as a function of laser pulse duration neglecting the term of emission volume. Here the vertical axis is a relative value. This scaling suggests that the conversion efficiency saturates for long pulse duration. Such trend for long pulse duration is in good agreement with the experimental result.

Thus for the pulse durations the conversion efficiency increase with both temperature and emission volume and for long pulse durations emission volume i.e. the conversion efficiency.

Figure 3-13 shows the soft x-ray conversion efficiency ($h\nu = 0.1 \sim 1.6$ keV) at Au target as a function of FWHM of a Gaussian laser pulse (τ_L). We can see that the longer the pulse duration the higher the conversion efficiency becomes. The observed increase of the conversion efficiency at longer pulses will be attributed to the increased emitting volume and/or the increased laser absorption.^[23] However it is difficult to understand which is dominant mechanisms to increase the conversion efficiency, emitting volume or absorption. Soft x ray generated in the overdense and lower temperature region is reigned by a complex emission process.

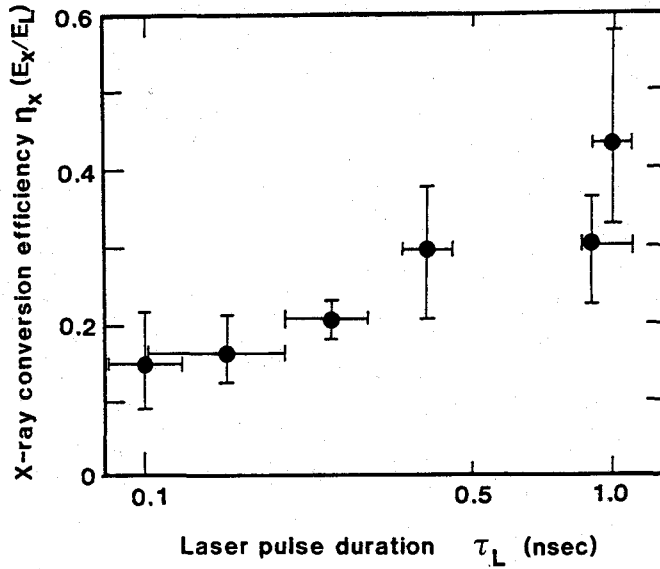


Fig. 3-13 Laser pulse width dependence of soft x-ray conversion efficiency for Au plasmas produced by 527 nm laser lights at $\tau_L = 400$ psec.

3-2-6. Plasma scale length dependence

In general, x-ray emission from laser-produced plasmas are not a blackbody radiation[]. Especially keV x-ray emissions are generated in a coronal region where the temperature is relatively high and the emission of bound-bound transition is dominant. Thus keV x rays from a coronal region depend on the emission volume as discussed on pulse duration dependence in section 3-2-5. Hence x-ray conversion efficiency can be controlled by changing the emission volume i.e. a plasma scale length.^[24] This characterization of x-ray emission from long scale-length plasmas is important for laser fusion; long scale-length plasma should be generated at the reactor target or in a cavity-type target.

Considering one-dimensional expansion of laser plasma, the scale length is inferred to be proportional to $C_s \tau$ where C_s is the sound speed and τ is the

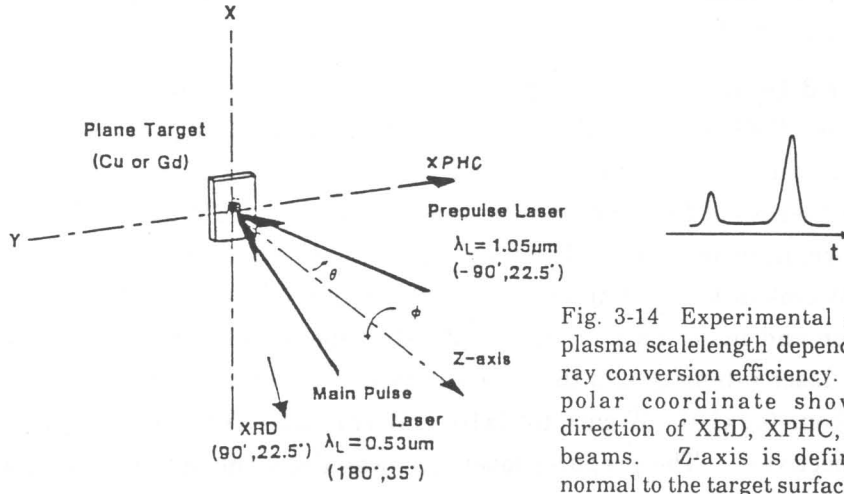
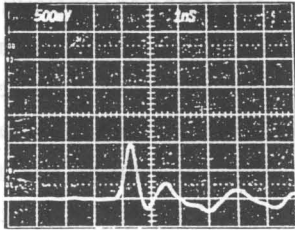


Fig. 3-14 Experimental set up for plasma scalelength dependence of x-ray conversion efficiency. (θ, ϕ) is polar coordinate showing the direction of XRD, XPHC, and laser beams. Z-axis is defined to be normal to the target surface.

Single pulse



Double pulse

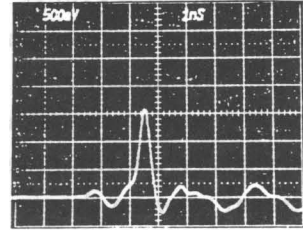


Fig. 3-15 Typical XRD signals for (a) single laser pulse and (b) double pulse. Time interval of two pulses is 1.8 nsec.

plasma expanding time. From Eq.(3-2) and $Z \propto T_e^{1/3}$ [21], the plasma scale length L scales as

$$L(I_a, \tau) \propto C_s \tau \propto I_a^{1/2} \tau, \quad (3-5)$$

where I_a is the absorbed laser intensity. In this section, we present the correlation of x-ray conversion efficiency with a plasma scale length when a

main pulse irradiates the preformed plasma and discuss the x-ray generation mechanisms.^{[25], [26]}

Figure 3-14 shows the experimental set up. A 0.53- μm main laser pulse of 200 psec (FWHM) preceded by a 1.05- μm prepulse (200psec) was used. The main and prepulses were focused onto a Cu ($Z=29$) target through aspherical lenses of $f/1.6$ and $f/8$ with incidence angles of 35° and 22.5° to the target normal, respectively. The intensity of the main laser pulse was fixed at 10^{14} W/cm² in the spot diameter of 250×300 μm (250×300 μm represents the minor and major axis of the elliptical shape of the focal spot). The prepulse laser intensity and the time interval between the two pulses were varied from 0.2×10^{13} W/cm² to 9×10^{13} W/cm² and from 1 nsec to 3.1 nsec, respectively. The prepulse laser spot was the same as the spot of the main laser pulse.

X-ray intensity measurements were performed by using an XRD with a 45- μm thick Beryllium filter which provided an overall spectral sensitivity of the photon energy range from 1.5 keV to 5.0 keV. The smaller sensitivity is down to a ~ 1 keV photon range which corresponds to the L-shell spectra of copper. As described in Appendix A, the overall time response of detection was 350 psec so that x-ray signal pulses corresponding to each laser pulse were easily discriminated in time as shown in Fig. 3-15 since the time interval between the pre and main pulses was at least 1.1 nsec. The x-ray conversion efficiency is defined as the ratio of the measured x-ray fluence only to the main laser energy per unit solid angle (%/sr.). One can obtain the total conversion efficiency by integrated with the angular distribution function over the solid angle which is well approximated to be semi spherical for keV x rays.

Time integrated images of the x-ray emission above the 1.3 keV-photon energy range were recorded on KODAK 2494 RAR film using an x-ray pinhole camera (XPHC) with a 31- μm thick beryllium filter and an pinhole of 10- μm diameter. The XPHC viewed the image from the right angle to the target normal.

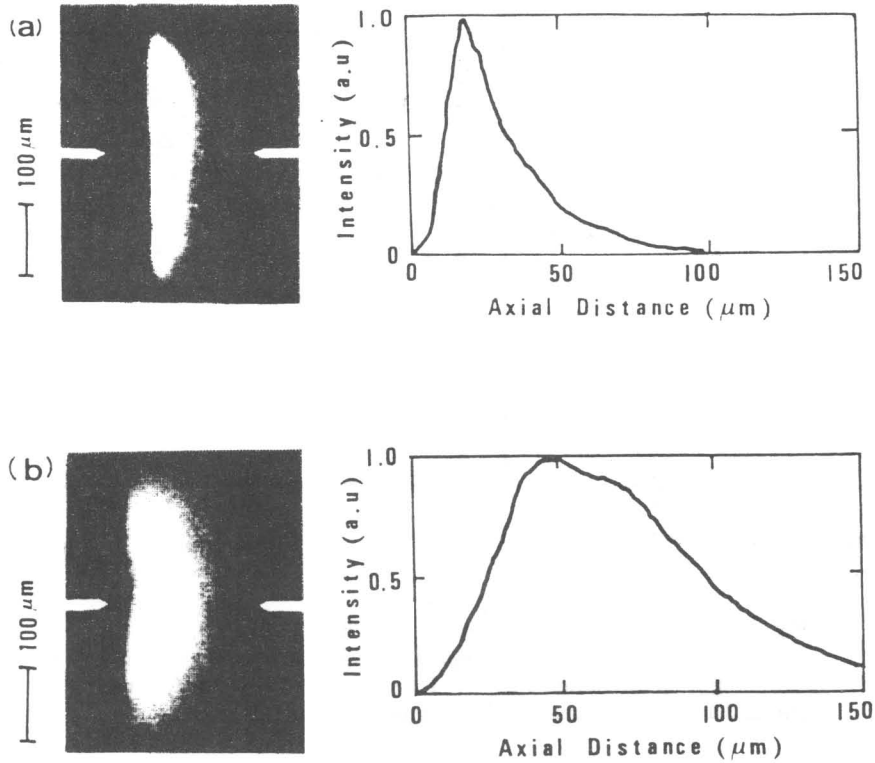


Fig. 3-16 Typical x-ray pinhole images and axial intensity scans for (a) the single pulse and (b) the double pulse. The images were taken perpendicular to the target normal direction. $I_L = 1 \times 10^{14}$ W/cm² and $\tau_L = 200$ ps.

Shown in Fig. 3-16(a) are typical pinhole image and its axial intensity scan for the single pulse and in Fig. 3-14(b) the same for the double pulse. Although the XPHC images are time-integrated and have a finite spatial resolution, these images clearly show that the emitting volume is extended by the prepulse laser. The intensity of the x-ray emission from the prepulse itself was found to be negligible in Fig. 3-14 as well as in the XRD signal measurement. The first x-ray pulse due to the prepulse was found to be as small as 13% of that from the main pulse even at the maximum prepulse intensity as shown in Fig. 3-13.

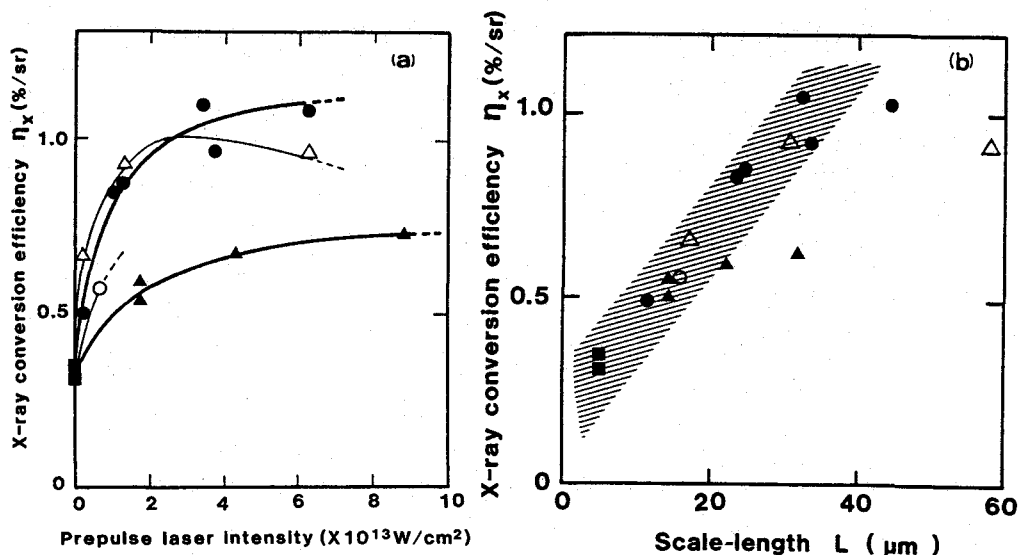


Fig. 3-17 X-ray conversion efficiency (η_x : $h\nu = 1 \sim 3 \text{ keV}$) from Cu target as a function of (a) prepulse intensity and (b) plasma scalelength for variable delays (\blacktriangle 1.1 nsec, \circ 1.3 nsec, \bullet 1.8 nsec, and \triangle 3.1 nsec). The main pulse intensity was at 10^{14} W/cm^2 .

Figure 3-17(a) shows the x-ray conversion efficiency as a function of the prepulse laser intensity at variable pulse delays of 1.1 nsec to 3.1 nsec. It is readily seen in Fig. 3-17(a) that the conversion efficiency increases with prepulse laser intensity and/or pulse delay. For a 1.8 nsec delay, the conversion efficiency is 0.85 %/sr. at the prepulse laser intensity of $1.2 \times 10^{13} \text{ W/cm}^2$. This efficiency is about three times larger than that without a prepulse. Such enhancement of the conversion efficiency can not be fully explained by the absorption increase because of the same reason given in section 3-2-5.

The conversion efficiency as a function of the preformed plasma scale-length is shown in Fig. 3-17(b). Here the plasma scale-length (L) at the turning point is evaluated from the hydrodynamic calculation taking account of spherical expansion in the XPHC images.^[27] The plasma extension at the peak of the main pulse evaluated from the numerical calculations agrees well with that from the XPHC images at the various pre-

pulse conditions. Thus the numerical calculation results can be used for guide lines of the scale-length.

The experimental result of the conversion efficiency is found to scale as $\eta_x \propto L$ (the emission volume) up to the plasma scale-length of about 50 μm . The XPHC images also show the increase in the emission volumes as already shown in Fig.3-16. As mentioned earlier part, the electron temperature is also essential to determine the keV x-ray conversion efficiency. However from the numerical calculation the electron temperature at the peak of main pulse is not influenced by the plasma scale-lengths of up to 50 μm , which are created by the prepulse. On the other hand the laser absorption length L_a is estimated to be 30-60 μm at the electron temperature $T_e \approx 0.6 \sim 1 \text{keV}$ from [23]

$$L_a = \frac{3 \cdot C_s}{4 \cdot \nu_c} \propto \frac{T_e^{3/2}}{n_c \cdot Z} , \quad (3-6)$$

where n_c is the critical density and ν_c is the electron-ion collisional frequency at the critical density. Here the absorption length is defined by that the spatially-integrated absorption becomes unity as []

$$\int_{n_e=0}^{n_e=n_c} \kappa_{ib} dx = \frac{4 \cdot \nu_c}{3 \cdot C_s \cdot L_a} = 1 , \quad (3-7)$$

where κ_{ib} is the inverse bremsstrahlung coefficient. At scalelengths less than the limit of the absorption length, the preformed plasma is heated sufficiently by the main laser. Thus the conversion efficiency increases linearly with the scalelength or the emission volume.

However the saturation of the conversion efficiency is found even at scalelengths less than the absorption length for certain prepulse conditions. The saturation begins with the prepulse laser intensity of about $4 \times 10^{13} \text{ W/cm}^2$ for the pulse delay of 1.1 nsec from Fig. 3-17(a) from the numerical calculation the electron temperature at the time of the main pulse increases with the prepulse laser intensity for the short time pulse delay such as 1.1 nsec. When the electron temperature is so high that the population of L-

shell electrons decreases in the preformed plasma, the L-spectra conversion efficiency originating in bound-bound transitions of L-shell electrons will saturate at the time of the main heating pulse.

There are some other possible mechanisms on the saturation of the conversion efficiency: the Brillouin backscattering and the condition of geometrical matching between the expanding volume of the preformed plasma and the focusing cone of the main pulse laser.

A theoretical threshold of the plasma scalelength for Brillouin backscattering^[28] is estimated to be about 100~200 μm in the turning point at the laser intensity of 10^{14} W/cm^2 with the electron temperature of 0.5~1 keV. The plasma scalelength inferred in the present experiment suggests that the Brillouin backscattering may be also responsible for the appearance of the saturation region in Fig. 3-17(b).

The opacity effect in the plasma which has a temperature gradient is also one of the factors to affect the conversion efficiency. In such experiment, the hot coronal region generating keV x-ray is surrounded by the relatively cold plasmas which have been cooled by expansion. Hence the surrounding plasma will absorb the x rays emitted at the inner hot plasmas.

It seems that the observed saturation for the longer scalelength has been caused by the complex form of these mechanisms described above. More detailed study is needed for the saturation mechanisms.

Figures 3-18(a) and (b) show the soft x-ray conversion efficiency as a function of the prepulse laser intensity and preformed plasma scalelength, respectively. Here the spectral ranges are 0.1~0.28 keV and 0.7~1.0 keV. Considering the x-ray spectrum of Cu plasma in section 3-2-1, the conversion efficiency of photon energy range of 0.7~1.0 keV is estimated to be about 10% of that of 0.1~0.2 keV. Hence Fig. 3-16 will show the soft x-ray conversion efficiency of 0.1~0.28 keV photon energy. It is found that soft x-ray conversion efficiency is also enhanced by the prepulse but the rate of increase is smaller than that of keV x ray. Such enhancement of the conversion efficiency is due to the same process as for keV emissions. However there is a negative factor to reduce the conversion efficiency to produce softer x rays with increase of scalelength. The conduction length

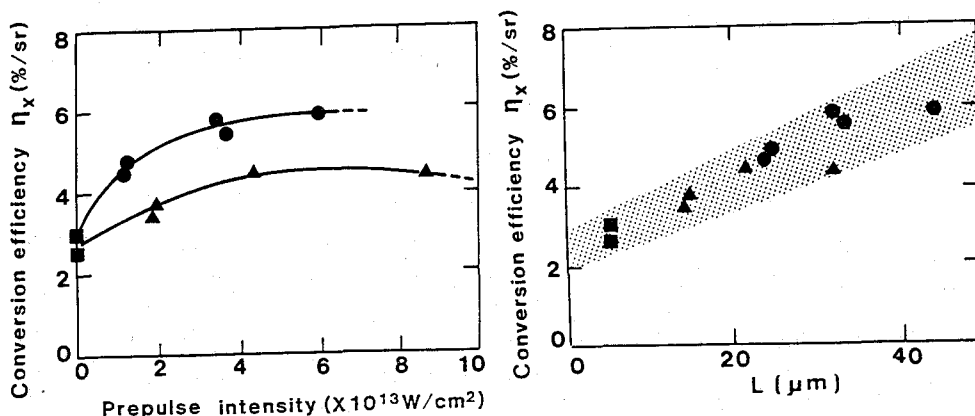


Fig. 3-18 X-ray conversion efficiency (η_x : $h\nu = 0.1 \sim 0.28 \text{ eV}$) from Cu target as a function of (a) prepulse intensity (b) plasma scalelength for variable delays (▲ 1.1ns and ● 1.8ns). The main pulse intensity was at 10^{14} W/cm^2 .

from the critical density region to the overdense region also increases with the preformed plasma scalelength, reducing a transportation of the absorbed energy into the overdense region which is responsible for the soft x-ray generation region. The enhanced keV x-ray emission in the coronal region may also transport a significant fraction of the absorbed energy into the overdense region. These complex mechanisms seem to dominate the soft x-ray generation.

3-2-7. Summary

Characterization of laser plasma x rays has been made experimentally. Spectral intensity and conversion efficiency have been obtained as a function of target atomic number, laser parameters, and plasma scale length.

From atomic number dependence, x-ray spectra from laser-produced plasmas have several humps corresponding to the electric transitions in K, L, M, N, and O shells of ions. These humps are found to be in accordance with a semi-Moseley's law.

The lower laser intensity i.e. lower temperature shows a higher conversion efficiency of soft x-ray and lower efficiency of keV x-ray. These results are due to the correlation between the electron temperature and collisional excitation process in characteristic shell structure of ions.

Soft x-ray conversion efficiency increases for shorter wavelength laser (to 80% for Au plasma produced by 263-nm laser). Shorter wavelength laser results in efficient energy transport into a lower temperature and overdense region which is most responsible for the soft x-ray generation.

The longer pulse duration shows a higher x-ray conversion efficiency, indicating that the emission volume and the electron temperature are essential.

By using a prepulse laser at weak intensity, we obtained the characteristics of x rays from long scale-length plasmas. The maximum enhancement of the conversion efficiency was observed to be as much as three times compared with that of only prepulse. We found the scaling of the conversion efficiency to preformed plasma scale length as $\eta_x \propto L$. This characterization may be important for future ICF experiments with reactor size target, when long scalelength plasmas will be produced.

§ 3-3. Energy Transport in UV Laser-Produced Plasmas

To study the energy transport in UV-laser produced plasmas, we observed rear side emission ^{[7], [13], [29]} of thin foil targets (Au and Al) irradiated by a 263nm laser. By using this method ^[29] not only shock wave propagation but also radiation heating and the thermal conduction wave could be observed. The growth and decay of shock waves were compared with a model of the shock formation.

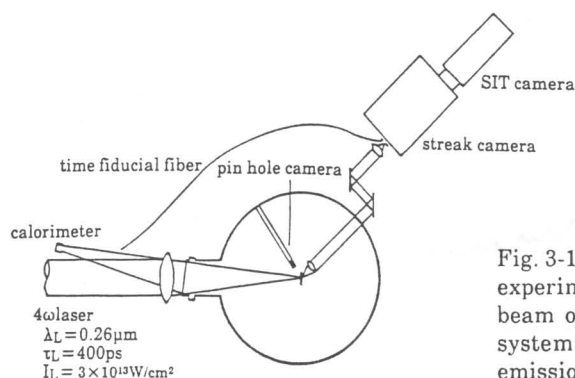


Fig. 3-19 Experimental setup for this experiment. Using one quadrupled beam of the GEKKO IV glass laser system ($\lambda = 263 \text{nm}$), the rear side emission of the target is observed by a streak camera.

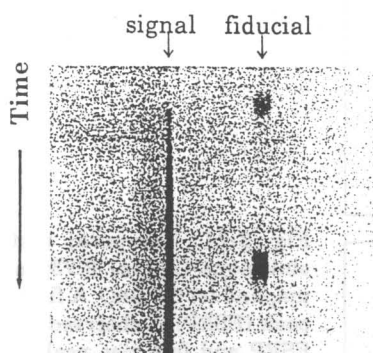


Fig. 3-20 Typical streak image of rear side emission with a time fiducial.

3-2-1. Experimental setup

Figure 3-19 shows the experimental setup for energy transport in UV-laser plasmas. One arm of the GEKKO IV four beam glass laser system (ω_0 ; $\lambda = 1.053 \mu\text{m}$) was quadrupled ($4\omega_0$; $\lambda = 0.263 \mu\text{m}$) with the use of two KDP (potassium hydrogen phosphate) crystals. The $4\omega_0$ energy was around 1J with a 400psec pulse full width at half maximum. Using a quartz lens whose focal length was 80cm, a typical spot size was 100 μm in diameter which contains 90% of the laser energy at 0° of incident angle. On target intensity was a few times 10^{13}W/cm^2 .

Thin aluminum and gold foils were used for targets whose thickness ranged from 0.7 μm to 20 μm and from 1 μm to 20 μm , respectively. Irradiating the front side of the target, the absorbed laser energy is transported through the target via several mechanisms, causing rear side

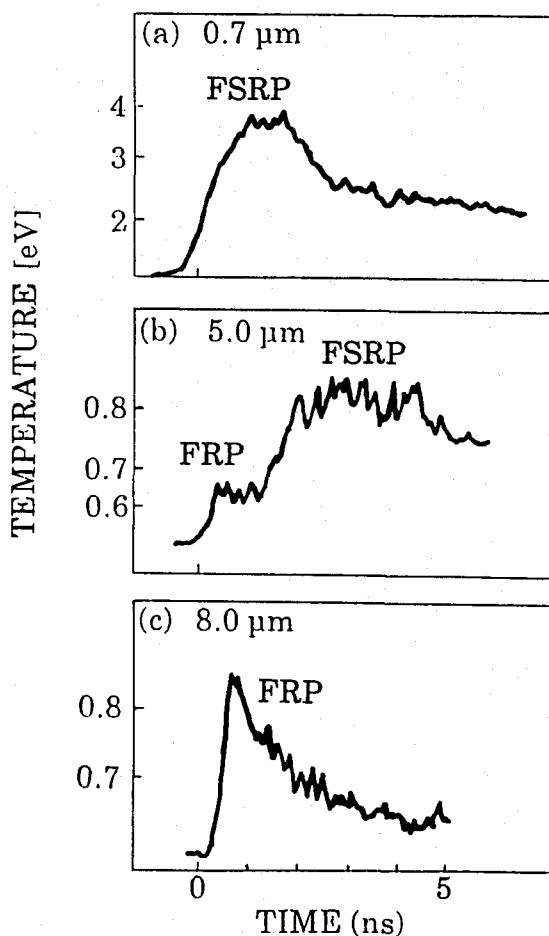


Fig. 3-21 Temporal histories of emissions (Al). (a) $0.73\mu\text{m}$, (b) $5.0\mu\text{m}$, and (c) $8.0\mu\text{m}$. A first slow rise peak (FSRP) is observed in (a). Both FSRP and fast rise peak (FRP) are observed in (b), while only the FRP (shock) is seen in (c). Time 0 ns corresponds to the laser intensity peak. The temperatures were obtained from emission intensities integrated over from 3000 \AA to 6000 \AA . The whole system was calibrated in situ with a tungsten lamp.

emissions. Emissions ($\lambda=300\text{-}600\text{nm}$) from the rear side were optically relayed onto a time streak camera (S-20) slit by quartz lenses at an observation angle of 45° to the target normal. The time resolution was 30psec . Figure 2-20 is typical streak image with a time fiducial. The time fiducial was introduced into the streak camera by an optical fiber which picked up a part of the incoming laser light. Using a tungsten lamp, the absolute sensitivity of this streak camera was calibrated in situ so that a black body temperature could be assigned for the rear side emission.

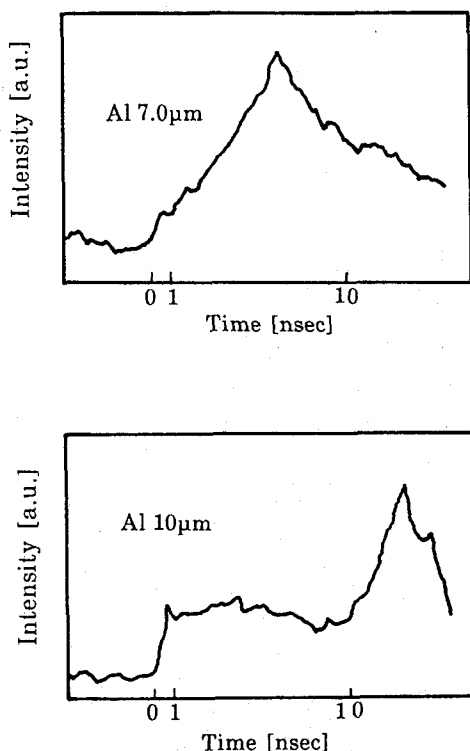


Fig. 3-22 Temporal histories of rear side emission with slow time unit in streak camera. Strong peak corresponds to the thermal front.

3-2-2. Energy transport in medium-Z plasmas

Figure 3-21(a)-(c) show temporally resolved emissions for Al foils of thickness of (a) 0.73 μm , (b) 5.0 μm , and (c) 8.0 μm , respectively. These data show absolute temperatures in the vertical axis, which were obtained numerically with the assumption of black body radiation, and comparing to the calibrated tungsten lamp measurement. The time is shown in horizontal axis. The time zero is the laser peak which was obtained absolutely by the optical fiber fiducial.

In Fig. 3-21(a), of the 0.73 μm Al case, the emission intensity was very strong and the peak temperature was around 4 eV. Since the rise time of the peak was rather slow ($\approx 1\text{nsec}$), we call this peak a first slow rise peak (FSRP) (Second slow rise peak will be appeared in following part when Au foils are used.). After the FSRP was over, there was no other emission peak observed as shown in Fig. 3-22. This was checked using a slower time unit

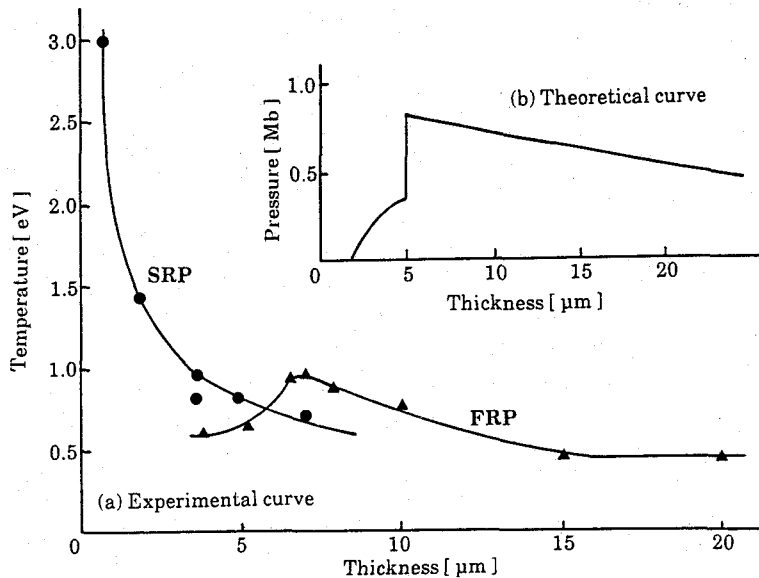


Fig. 3-23 (a) Temperature vs target thickness for SRP and FRP. There are two types of peaks : slow rise peak (SRP) and fast rise peak (FRP). The FRP have a peak temperature at the thickness of 7 μm Al. The intensity of the SRP decreases monotonically with target thickness. (b) Calculated pressure profile. We assume that a triangle temporal shape pressure is introduced for this calculation. The value of the pressure is 1 Mbar. The temporal width is 400 psec at the FWHM. The shock wave grows over some distance and reaches maximum pressure at the depth of 5 μm and decays.

in the streak camera. When 5 μm Al was used [Fig. 3-21(b)], the temporal structure of the emission shows two peaks: a fast rise (≤ 200 psec) peak (FRP) and FSRP. The FSRP was about 1 nsec delayed further and the full width of half maximum (FWHM) seems to be two times wider than that of the FSRP as shown in Fig. 3-21(a). For target thicker than 8.0 μm , [Fig. 3-21 (c)], only the FSRP could be observed within the time frame of the streak camera, and the SRP came much later in time, and the FSRP also decays with target thickness. Separation between the FSRP and SRP was 7 nsec, for example, for the 7 μm target as shown in Fig. 3-22.

In Fig. 3-23(a) the temperature of the observed FSRP and SRP are plotted as a function of the thickness. The thicker the targets, the lower the SRP

temperatures become. The FSRP temperature rises till 7 μm thickness and then the FSRP temperature decays. From both figures the FSRP and SRP appeared to be caused by different processes.

Absorbed energies may be transported from the front side of the target to the rear by several possible processes: direct heating by transmitted x rays, shock wave propagation, and thermal conduction. Heating by suprathermal electrons, which could usually result from nonlinear coupling of laser and plasmas, is excluded since the collisional absorption process is so dominant in $4\omega_0$ laser plasmas.^[30]

First we consider the heating by x rays. When a target is irradiated by the 4ω laser, the absorbed laser energy is converted to the x-ray energy with a relatively high conversion efficiency as shown in Sec. 3-2. And a part of this x-ray energy is transported through the target, and is reabsorbed at the rear side of the target (direct heating). The distribution of the x-ray deposited energy may be determined by the absorption cross section. The absorption distribution and the deposited energy is expressed as,

$$T_X(x_0) = \left. \frac{dT}{dx} \right|_{x_0} \cdot \Delta x = \frac{-2}{3kNx_0^2} \int (1 + N\sigma x_0) e^{-N\sigma x} E_f(h\nu) d h\nu, \quad (3-8)$$

where $E_f(h\nu)$ is the experimental x-ray emission spectrum, k is the boltzmann constant, N is the density of the target, σ is the absorption cross section, x_0 is the depth of the target, and $T_X(x_0)$ is the deposited energy at the depth $x = x_0$ of the heated target. From this calculation the rear side could be heated by direct x-ray heating up to a temperature as shown in Table 3-5 and Fig. 3-24. These estimated temperatures are too low compared with the observed rear side temperatures. Thus the observed rear side emission is not caused by x-ray heating.

Next we consider the thermal conduction including the ablation process. According to the rocket model the ablation speed is expressed as,^{[19],[29]}

$$\frac{d}{dt} a [\text{cm/s}] = 110 \times 10^3 \times \left\{ \frac{\phi_a [\text{W/cm}^2]}{10^{14}} \right\}^{1/3} \lambda [\mu\text{m}]^{-4/3} \frac{1}{\rho_0 [\text{g/cm}^3]} = 10^5 \text{ cm/sec} . \quad (3-9)$$

Table 3-5. X-ray deposited energy in the aluminum target. [see Fig. 3-24]

Target thickness x_0 (μm)	Deposited energy T_x (eV)
0.73	1.60
5.0	5.0×10^{-3}
6.5	1.8×10^{-3}
8.0	7.7×10^{-4}
20	9.9×10^{-4}

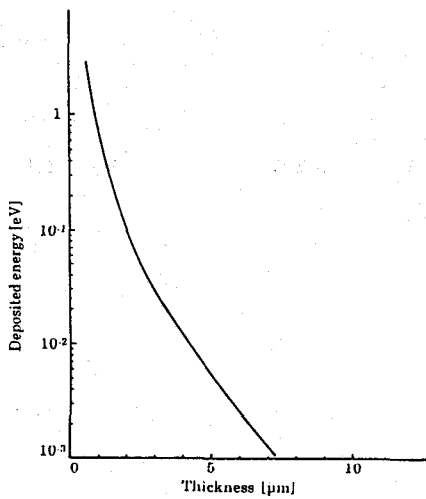


Fig. 3-24 X-ray deposited energy in the aluminum target is calculated using the experimental x-ray emission data and absorption cross section.

From this equation the quasi-burn through time τ_B can be estimated. These burn through times agree with the SRPs shown in Fig.3-23, 0.73 μm aluminum is about 0.7 ns for example. Figure 3-25 shows the target thickness dependence of burnthrough time. SRP speed is estimated to be about 3×10^5 cm/sec by about 1nsec after laser peak. So the SRP emissions could well be caused by the thermal conduction driven by the ablation. And in thicker than 5 μm target the SRP velocity slows down, since the front of thermal conduction loses its driving energy after the laser pulse. Thus the SRP observed for the target thickness less than 5 μm are consistent with the emissions caused by the ablation and thermal conduction.

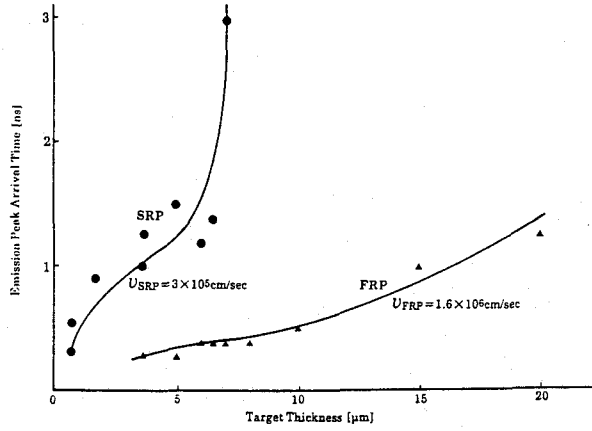


Fig. 3-25 Breakthrough time of shock front (FRP) and thermal front (SRP) vs target thickness.

Out of these possible mechanisms of energy transport in solid foils, the x-ray heating and the mass ablation have been discussed so far. The rest of this section is devoted to show the FSRPs are due to the shock heating.

At first one can simply estimate the shock speed from the Hugoniot relation and ablation pressure scaling as shown in Eq. (2-9). The estimated speed is about 2×10^6 cm/s at this experimental condition, which value is in good agreement with that of the FSRP from Fig. 3-25.

We next consider the shock amplitude and decay in Al target. The shock wave front grows and decays when it propagates. Assuming the incident temporal shape of pressure is a triangular pulse, the shock front grows because the shock velocity increases with its shock amplitude. The shock decay is expressed as^[31],

$$\frac{DP}{Dt} = -A \frac{\partial P}{\partial t} = A \left[\frac{\tau_p}{P_m} + \frac{x_i}{(C+u)_p^2} \left(\frac{du}{dP} + \frac{dC}{dP} \right) \right]^{-1}, \quad (3-10)$$

where P is the pressure, A is the coefficient for the material, τ_p is the incident laser pulse duration, P_m is the maximum pressure, C is the sound velocity and u is the particle velocity. Figure 3-23 (b) shows a calculated curve of the shock front pressure in an aluminum target using Eq.(3-10). This shock wave calculation gives us a profile of the shock front formation and decay. The shock front grows with the target thickness and reaches its maximum value of several Mbar at 7 μm , and then decays for the target thicker than that. From the Hugoniot relation in a target, the higher the shock amplitude is, the faster the shock velocity is. Thus the amplitude of the shock front increases with shock penetration. From our data the shock front reaches its peak value at about 7 μm depth. The shock speed for thickness more than 7 μm decreases and this is consistent with the temperature decay for thickness more than 7 μm as shown in Fig. 3-25. The burnthrough time for the 7 μm -thickness is about 400 psec which is same with laser pulse duration. For thickness more than 7 μm the shock starts decaying, since the rarefaction wave is usually much faster than the speed of the shock and catches the shock front.^[32] when laser pulse is turned off. Experimental points are plotted as dots (\blacktriangle) in Fig. 2-23 (a) and show a good agreement with the theoretical curve. At the decaying place, the model shows more gradual decay because a pure one dimensionality is assumed, while more three dimensional plasma expansion accelerates the rarefaction wave in the experiment.

3-3-3. Energy transport in high-Z plasmas

Observations for Au foil targets are shown in Fig. 3-26 (a)-(c). There are two components both of which have slow rises in Fig. 3-26 (a), where a 1 μm Au foil was irradiated. The peak of the FSRP is out of the temporal range of the figure. The second slow rise peak (SSRP) appears at 1 nsec after the laser peak. The rise time of the SSRP is again about 1 nsec. The rise time of the FSRP is much slower than those of the Al cases [e.g. Fig. 3-21(a)]. This thermal front (FSRP) of Au should be retarded and should be spread out,

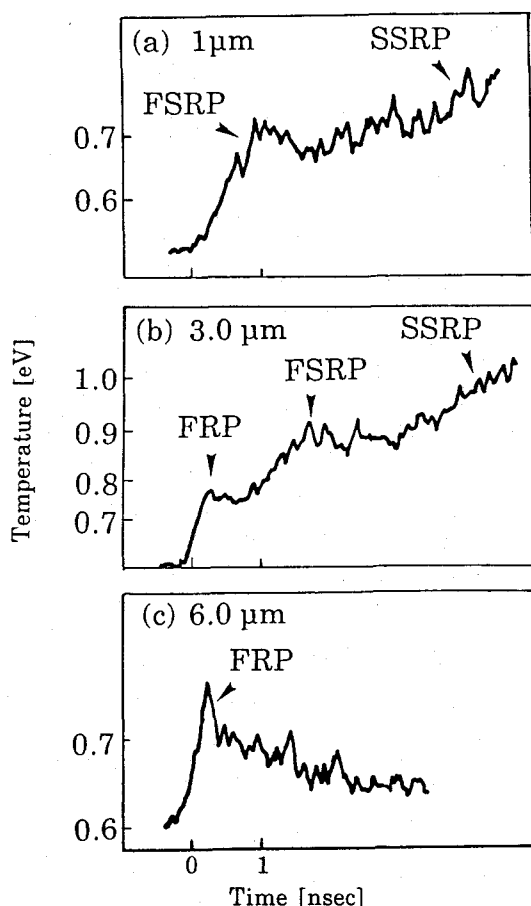


Fig. 3-26. Temporal histories of emissions (Au). (a) 1 μm , (b) 3.0 μm , and (c) 6.0 μm . Two components: FSRP and second slow rise peak (SSRP), both of which have slow rise time, are seen in (a). Three components: FRP, SSRP, and FSRP are observed in (b), while only the FRP (shock) is seen in (c).

since the areal mass density of Au is much larger (about seven times) than that of Al.

In Fig. 3-26(b), three components are clearly observed with a 3 μm Au foil. Right after the laser peak (~ 200 psec), there appears a third peak which has a fast rising slope. This corresponds to the FRP in the Al cases, and again only the FRP is observed when the thickness of the Au target is increased to 6 μm [Fig. 3-26(c)]. The SSRP also shows some relaxation compared to Fig. 3-26(a) and seems to be swallowed or absorbed by the FSRP.

There is a considerable difference between the emission structures from Al and Au targets. As shown in Fig. 3-26(b), the third peak (SSRP) is clearly observed only for Au targets, not for Al targets. For Au targets, most of the absorbed laser energy may be converted to soft x-ray energy ($\eta_x/\eta_{abs} \leq 80\%$) as shown in Section 3-2. This strong x-ray flux should have an important role in the energy transport. As a matter of fact, we ^[11] reported that soft x rays could be transferred efficiently through a Au target via absorption resonance, or down-conversion. When a strong flux of x rays enters into a solid Au target, the Au target is ionized and then ionization front may be formed. If the temperature in a front plasma increases, the absorption edges may shift to the high energy side and then an optically thick plasma might become optically thin for x rays generated in that region. This is called the ionization burnthrough as described in Section 2-4.^[33] At the same time re-emission of absorbed x rays may also occur. The efficiency of the re-emission may become high for certain discrete shells such as O and N shell transitions. Thus both ionization and re-emission processes may well enhance the radiation energy transport, resulting that x-ray energies could be transported for distances longer than the mean free path for a cold solid material. This kind of radiation front by an x-ray flux should be driven ahead of the ablation front and should only last for duration of laser pulse or slightly longer, since the x rays generated by a laser pulse should have a pulse width almost same as the laser pulse duration. After the laser pulse, the radiation front should decay losing its driving force and should be absorbed into a thermal front, which was first driven by the laser ablation and was then propagated by the heat conduction with its temperature cooling down. In Fig. 3-26(a) and (b), the observed SSRP could correspond to the radiation front which should be observable more clearly for high Z targets than for low to mid Z targets.

The ionization speed could be simply estimated by the equation of energy conservation to be ^[33]

$$v_{ion.} = \frac{3\eta_{ab} I A^{2/3} m_p}{4\rho T^{4/3}} = 1 - 2 \times 10^5 \text{ cm/sec} \quad (3-11)$$

Here η_{ab} is the absorption coefficient of the x-ray flux, I_x the effective x-ray flux, ρ the density of the target, m_p the proton mass, and T the electron temperature. For estimating the ionization speed, the electron temperature, the conversion efficiency of x radiation, and the absorption coefficient of the ionization front are taken to be 100eV, 80%, and 50 %, respectively.

In slightly different analysis, one can also similar result considering the mean free path λ_R of radiation. Taking account of an approximate relation $\lambda_R = \alpha T_R^{-7/4} / \{n_i^2 \cdot Z(Z+1)^2\}$ for bound-free radiation [32] we obtain the scaling law for ablation speed by radiation as

$$v_{rad} = 1.33 \times 10^6 \frac{\{I_x [10^{13} \text{ W/cm}^2]\}^{0.55}}{\rho [\text{g/cm}^3]} \left(\frac{A^2}{Z(Z+1)^2 \cdot \tau [\text{nsec}]} \right)^{0.4} = 2.4 \times 10^5 \text{ cm/sec} \quad (3-12)$$

where we assume that the x rays are near blackbody radiation in dense region. This assumption will be reasonable in high-Z plasmas because of its high re-emissivity and opacity. More detail discussion about such radiation energy transport is appeared in next Chapter.

In any case, above estimations are in reasonable agreement with the observed speed for the radiation front if the ablation speed is assumed to be smaller than the ionization front speed. Uncertainty of this estimated speed may vary within a factor of two. Since the ablation speed is proportional to $1/\rho$ (ρ : material density) the ablation speed in a Au target could be almost one-seventh the ablation speed in Al, which could be $\approx 2 \times 10^4 \text{ cm/sec}$. Thus the separation between the radiation and ablation fronts becomes more pronounced for high Z than for low to mid. Z targets, consistent with the observed data [Fig. 3-21 and Fig. 3-26].

The experimental results are analyzed by comparison with a one-dimensional Lagrangian hydrodynamic code HIMICO.[34] The simulation code includes the Thomas-Fermi EOS (Equation of State) calculated by Latter [35],[36], non-LTE atomic physics, multi-group radiation transport, and other conventional physics. For the opacity data, Kramer's formula was used with energy levels and populations calculated by a non-LTE average

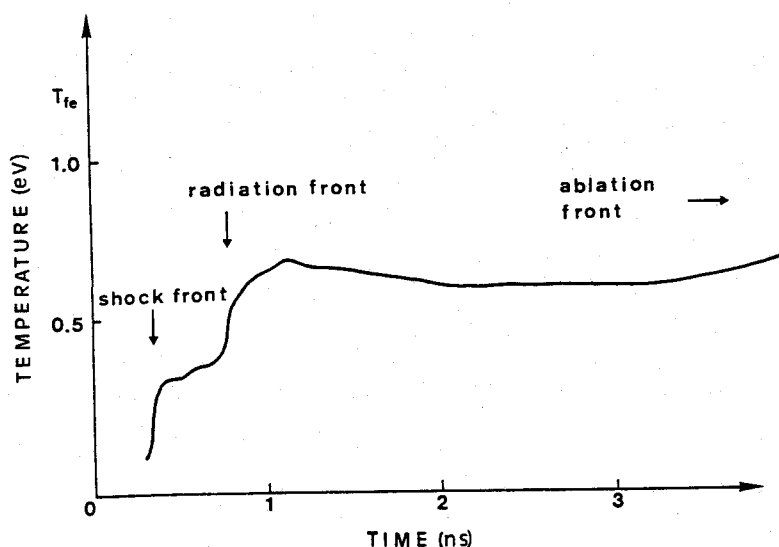


Fig. 3-27 Computer simulations by HIMICO. This simulation replicate well the observed rear emissions for Au targets. Clearly two (shock and radiation) fronts were observed.

ion model.^[38] This model has been proven^[39] to produce results very close to the SESAME library^[30] at high temperatures (≥ 100 eV) for xenon. Used was the data of cold Au for lower temperatures by Henke et al.^[40] Details were reported in Ref. 41, where the x-ray transmission through Au thin foils were compared with experiments by examining the opacity calculations and its sensitivity to the results. The simulation replicates the laser absorption, the subsequent x-ray generation, and the transport. Therefore the necessary inputs to the simulation are only the laser intensity, pulse shape, wavelength, and focusing angle, where other processes are self-consistently replicated in the code.

The simulation result given in Fig. 3-27 corresponds to Fig. 3-26, but the target thickness was $0.5 \mu\text{m}$. Three different phases are clearly seen in the figure: shock front, radiation front, and ablation front. If we increase the target thickness, both velocity and temperature of the radiation front increase in the simulation. Particularly at $0.75 \mu\text{m}$ the temperature increases up to 3 eV, which does not agree with the experimental result at $1 \mu\text{m}$. This could be attributed to the re-absorption of the relatively high

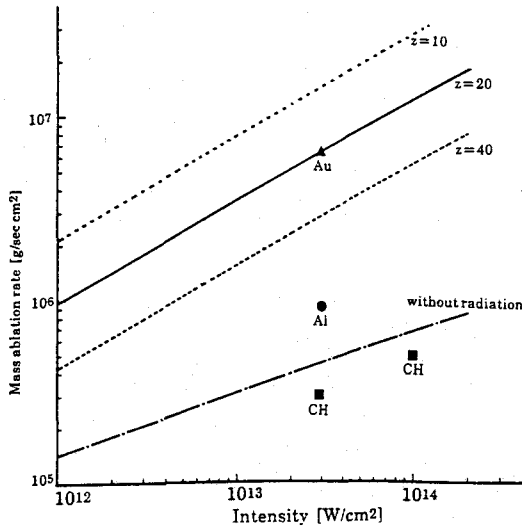


Fig. 3-28 Target material dependence of mass ablation rate. Upper three lines are from Eq. 3-12 for ionization state $Z=10, 20$, and 40 , which are radiation driven mass ablation rate. The lowest line is given by theoretical scaling without radiation effect.

energy radiation inside the target.^[42] In this sense the absolute value of the opacity used in this calculation may be slightly larger than the experimental one or a two dimensional effect may decrease the areal intensity of deposited laser energy. The latter effect for the small spot size experiment such as our case should be non-negligible. Temperatures from these visible emission may not represent the real blackbody temperature of the rear side plasma, since these visible emissions could only come from a very surface of the plasma where the temperature might be fairly low. This point was inferred from separate experiments, where both visible and x-ray rear emissions were observed of planar targets.^[43] In this experiment the observed spectral region was from 300 to 600 nm. Thus we estimate that a real temperature at the front could range from 1 eV to 10 eV.

Finally ablation rate and pressures may be estimated from the observed timing of the radiation (for Au) and the thermal (for Al) fronts for the given thickness of the targets.

Figure 3-28 shows the target material dependence of ablation rate for 263nm-laser produced plasmas from above results. Points for Au and Al targets are estimated from this experiment and points for CH target given by

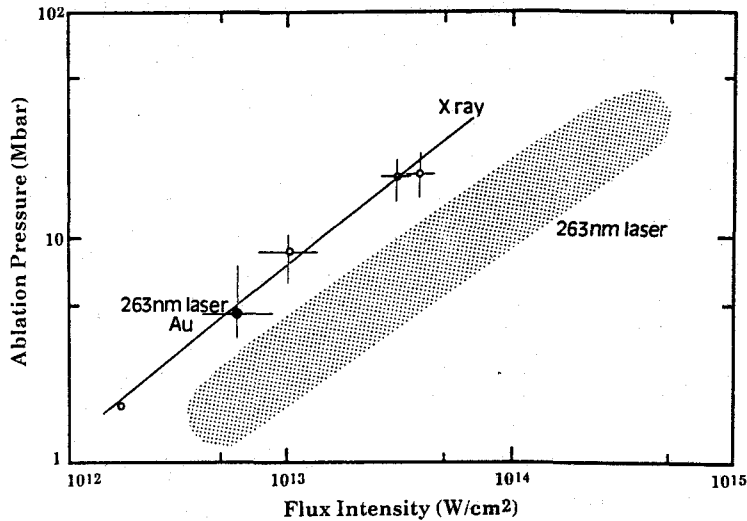


Fig. 3-29 Ablation pressure v.s. flux intensity (W/cm^2). Estimated pressure for Al falls into the hatched region where previously reported data are indicated for a 263 nm laser irradiation. The pressure for Au appears to be higher and con.

T. Boehly et al ^[3]. Upper three lines shown in this figure comes from Eq. (3-12) for ionization state $Z=10, 20$, and 40 which are radiation driven mass ablation rate. The lowest line in the figure is given by theoretical scaling without radiation effect ^{[19], [29]}. Higher Z plasmas show higher mass ablation rate and the rate for Au plasma ($Z=79$) is in good agreement with the radiation driven mass ablation rate for charge state of $Z=20$.

Figure 3-29 shows the ablation pressure from the experimental results and previously reported data by an x-ray flux driver ^{[42], [44]} and UV laser ($\lambda=263 \text{ nm}$) ^[3]. 4 Mbar is obtained for Au at $6 \times 10^{12} \text{ W}/\text{cm}^2$, and 1.5 Mbar for Al. While the ablation pressure for Al falls into the hatched region of UV laser data, the Au data fits onto the scaling by the x-ray driver. The results in the figure may indicate that the energy in a UV laser plasmas is predominantly transported by soft x rays especially for high Z target such as Au.

3-2-7. Summary

Energy transport was experimentally studied in Al and Au thin foils irradiated by a UV laser(263nm).

We observed the formation and the decay of a 4ω laser induced shock wave in the aluminum foil targets. The shock wave (FRP) had a peak value at the depth of 7 μm in the Al foil targets at the irradiation intensity of a few times 10^{13} W/cm^2 . Also observed were the temporally resolved emissions due to the transmission of the thermal conduction (SRP) in Al foil targets which was distinctively separated from the shock front.

Emissions from the rear side of Au target indicated that there was an emission peak due to soft x rays. The results were well replicated in the simulation calculation. Estimated ablation pressure was also consistent with that the energy being predominantly transported by soft x rays in the high Z targets. The pressure in Au plasmas ($Z=79$) was three times larger than that in CH plasmas ($Z=3.5$).

§ 3-4. Conclusion

Energy transport was experimentally studied in UV-laser produced plasmas.

In order to obtain quantitative bases for understanding the energy transport in short wavelength laser produced plasmas, studied was characteristic of x rays from laser-produced plasmas in various conditions (e.g. laser intensity, pulse duration, laser wavelength, target material, and plasma scalelength). Studies on this characterization in such various conditions must be also important guidance for future ICF experiments with reactor size targets because in that experiments long scalelength plasma may be produced with high laser intensity, long pulse duration, and short wavelength laser. Especially experimental results of keV x-ray enhancement in long scalelength plasmas will be important from a

viewpoint of fuel preheat. It should be also noted that shorter wavelength laser with higher atomic number targets more efficiently converts the laser energy to soft x-ray energy. For 263nm-laser light, the conversion efficiency of Au plasmas could be as high as 80%. Shorter wavelength laser results in efficient energy transport into a lower temperature and overdense region which is most responsible for the soft x-ray generation.

263nm-laser light irradiating Al and Au thin foils, the energy transport by x radiation, shock wave, and thermal conduction were experimentally studied. It was found that soft x rays were important factor in energy transport in UV-laser plasmas. Experiments with Al targets indicated that the energy transport mechanism could be primarily by the ablation front propagating at a slightly higher speed than the thermal conduction speed. For Au targets, the heating attributed to x radiation was clearly observed in addition to the heating by shock wave and thermal conduction. These results were reasonable with high x-ray conversion efficiency in higher atomic number plasmas produced by shorter wavelength laser. The ablation rate and pressure in high atomic number targets irradiated by UV laser were also consistent with that the energy being predominantly transported by soft x rays. The pressure in high atomic number plasmas (Au) was indicated to be about three times larger than that of low atomic number plasmas (CH).

However it should be noted that the more effectively converted x rays can preheat the cold high density region in high Z plasmas produced by UV laser. The choice for optional driver wavelength requires a trade off between the increases in ablation rate and pressure and preheating due to increased x-ray generation.

References

- [1] R. E. Turner, K. Estabrook, R. L. Kauffman, D. R. Bach, R. P. Drake, D. W. Phillion, D. F. Lasinski, E. M. Campbell, W. L. Kruer, and E. Williams, *Phys. Rev. Lett.* **54**, 689 (1985).

- [2] F. Amiranoff, R. Fabbro, E. Fabre, C. Garban, J. Virmont, and M. Weinfield, *Phts. Rev. Lett.* **43**, 522 (1979); R. Fabbro, E. Fabre, F. Amiranoff, C. Garban-Labaune, J. Virmont, M. Weinfield, and C. E. Max, *Phys. Rev. A* **26**, 2289 (1982).
- [3] T. Boehly, K. A. Tanaka, T. Mochizuki, and C. Ymanaka, *J. Appl. Phys.* **60**, 3840 (1986).
- [4]) H. Nishimura, H. Azechi, K. Yamada, A. Tamura, Y. Inada, F. Mitsuoka, H. Hmada, Y. Suzuki, S. Nakai, and C. Yamanaka, *Phys. Rev. A* **23**, 2011 (1981); M. H. Key, W. T. Toner, T. J. Goldsack, J. D. Kilkenny, S. A. Veats, P. F. Cunningham, and C. L. S. Lewis, *Phys. Fluids* **7**, 2011 (1983); C. E. Max, C. F. McKee, and W. C. Mead, *Phys. Rev. Lett.* **45**, 28 (1980); T. J. Goldsack, J. D. Kilkenny, B. J. MacGowman, P. F. Cunningham, C. L. S. Lewis, M. H. Key, and P. Y. Ramsby, *Phys. Fluids* **25**, 1634 (1982); B. Yalakobi, J. Delettrez, L. M. Goldman, R. L. McCrory, R. Majoribanks, M. C. Richardson, D. Shvarts, S. Skupsky, J. M. Soures, C. Verdon, D. M. Villeneuve, T. Boehly, R. Hutchinson, and S. Letzring, *Phys. Fluids* **27**, 516 (1984).
- [5] W. C. Mead, E. M. Campbell, K. G. Estabrook, R.E. Turner, W. L. Kruer, P. H. Y. Lee, B. Pruett, V. C. Rupert, K. G. Tirsell, G. L. Stradling, F. Ze, C. E. Max, M. D. Rosen, and B. F. Lasinski, *Phys. Rev. Lett.* **47**, 1289 (1981); H. Nishimura, F. Mitsuoka, M. Yagi, K. Yamada, S. Nakai, G. H. McCall, and C. Yamanaka, *Phys. Fluids* **26**, 1688 (1983).
- [6] W. C. Mead, P. H. Y. Lee, B. Pruett, V. C. Rupert, K. G. Tirsell, G. L. Stradling, F. Ze, C. E. Max, M. D. Rosen, and B. F. Lasinski, *Phys. Fluids* **26**, 2316 (1983).
- [7] E. A. McLean, S. H. Gold, J.A. Stamper, R.R. Whitlock, H. R. Griem, S.P. Obenschain, B. H. Ripin, S.E. Bodner, M.J. Herbst, S.J. Gitomer, and M.K. Matzen, *Phys. Rev. Lett.* **45**, 1246 (1980).
- [8] G. Thiell, B. Meyer, P. Aussage, and X. Fortin, *Opt. Commun.* **46**, 305 (1983).
- [9] D. Duston, R.W. Clark, J. Davis and J.P. Apruzese, *Phys. Rev. A* **27**, 1441 (1983).
- [10] D. Saltzmann, H. Szichman, and D. Krumbein, *Phys. Fluids*, **30**, 515 (1987).
- [11] T. Mochizuki, K. Mima, N. Ikeda, R. Kodama, H. Shiraga, K.A. Tanaka, and C. Yamanaka, *Phys. Rev. A* **36**, 3279 (1987).
- [12] A. Ng, D. Parfeniuk, L. DaSilva, D. Pasini, *Phys. Fluids*, **28**, 2915 (1985).
- [13] H. Griem, "Plasma Spectroscopy", (McGraw-Hill, New York, 1964).
- [14] D. L. Matthews, et al., *J. Appl. Phys.* **54**, 426 (1983).
- [15] P. Mora, *Phys. Fluids* **25**, 1051 (1982).
- [16] C. Garban-Labaune, E. Fabre, C. E. Max, F. Amiranoff, R. Fabbro, J. Virmont, and W. C. Mead, *Phys. Fluids* **28**, 2580 (1985).
- [17] T. Mochizuki, T. Yabe, K. Okada, M. Hamada, N. Ikeda, S. Kiyokawa, and C. Yamanaka, *Phys. Rev. A* **33**, 525 (1986).
- [18] J. F. Holzrihter, LLNL Report, No. UCRL-50021-81 (1981).
- [19] R. Fabro, C. Max and E. Fabre, *Phys. Fluids* **28**, 1463 (1985).
- [20] S. Sakabe, T. Mochizuki, and C. Yamanaka, *Jpn. J. Appl. Phys.*, **23**, 460 (1984).
- [21] D. Colombant and G. F. Tonon, *J. Appl. Phys.* **44**, 3524 (1973).
- [22] J. E. Crow, P. L. Auer, and L. E. Allen, *J. Plasma Phys.* **14**, 65 (1975); P. Mora and R. Pellat, *Phys. Fluids* **22**, 2300 (1974).
- [23] C. E. Max, "Physics of the Coronal Plasma in Laser Fusion Targets," in *Laser Plasma Interaction*, edited by R. Balian and J. C. Adam (Les Houches, Session XXXIV, North-Holland, 1982).
- [24] P. J. Mallozzi and H. M. Epstein, U. S. Patent No. 4053486 (15 Nov. 1977); D. J. Nagel, P. G. Burkhalter, G. A. Doscheck, C. M. Dozier, U. Feldman, B. M. Klein, and R. R. Witlock, NRL Report No. 7838, **92** (1974).
- [25] R. Kodama, T. Mochizuki, K. A. Tanaka, and C. Yamanaka, *Rev. Laser Eng.* **14**, 378 (1986).
- [26] T. Mochizuki, ILE Research Report ILE-8607P, 1986.

References

- [27] In this simulation, we used the laser spot diameter as the radius of a spherical target when C_{st} is greater than the spot diameter and otherwise we used the value of three times as large as the spot diameter. The hydrodynamic computer code we used is described in the literature by M. Murakami and K. Nishihara, ILE Quarterly Progress Report ILE. QPR-83-6 (1983), p.34.
- [28] K. A. Tanaka, Ph. D. thesis, Osaka University, (1983).
- [29] R. Fabbro, B. Faral, F. Cottet, and J. P. Romain, J. Appl. Phys. **56**, 3204 (1984).
- [30] A. G. Maaswinkel, K. Eidoman, and R. Sigel, Phs. Rev. Lett. **42**, 1625 (1979); W. Seka, R. S. Graxton, J. Delettrez, L. Goldman, R. Keck, R. L. McCrory, D. Shvarts, J. M. Soures, and R. Boni, Opt. Commun. **40**, 437 (1982).
- [31] F. Cottet and J. P. Romain, Phys. Rev. A **25**, 576 (1982).
- [32] Ya. B. Zel'dovich and Yu. P. Raiser, *Physics of Shock Waves and High Temperature Hydrodynamic Phenomena* (Academic, New York, 1966).
- [33] D. Duston, R. W. Clark, J. Davis, and J. P. Apruzese, Phys. Rev. A **27**, 1441 (1983).
- [34] T. Yabe and C. Yamanaka, Comments Plasma Phys. Contr. Fusion **9**, 169 (1985).
- [35] R. Latter, Phys. Rev. **99**, 1584 (1955).
- [36] A. R. Bell, New Equation of State for MEDUSA, Rutherford Laboratory Report, RL-80-091 (1981).
- [37] S. Kiyokawa, T. Yabe, and T. Mochizuki, Jpn. J. Appl. Phys. **22**, L772 (1983); M. Itoh, T. Yabe, and S. Kiyokawa, Phys. Rev. A, **35**, 233 (1987).
- [38] T. Yabe and B. Goel, Jpn. J. Appl. Phys. **26**, L296 (1987).
- [39] W. F. Huebner, A. L. Merts, N. H. Magee, Jr., and M. F. Argo, Astrophysical Opacity Library, Los Alamos Scientific Laboratory, report LA-6760 M (Aug. 1977).
- [40] B. L. Henke, P. Lee, T. J. Tanaka, R. L. Shimabukuro and B. K. Fujikawa, Atom. Data Nucl. Data Tables **27**, 1 (1982).
- [41] T. Yabe, S. Kiyokawa, H. Nishimura, and C. Yamanaka, Jpn. J. Appl. Phys. **24**, L439 (1985).
- [42] T. Yabe, S. Kiyokawa, T. Mochizuyki, S. Sakabe, and C. Yamanaka, Jap. J. Appl. Phys. **22**, L88 (1983).
- [43] R. Kodama and K. A. Tanaka, to be published.
- [44] T. Endo, H. Shiraga, K. Shihoyama, and K. Kato, Phys. Rev. Lett., **60**, 1022 (1988).

Chapter 4

X-RAY ENERGY TRANSPORT IN HOT DENSE MATTER

§ 4-1. Introduction

§ 4-2. Laser Plasma X-ray Interaction with Solid Material

§ 4-3. Radiative Energy Transport in X-ray Produced Plasmas

§ 4-4. Conclusion

§ 4-1. Introduction

As described in Chapter 3, a short wavelength laser converts its energy efficiently to x-ray energy. Especially in high-Z plasmas, the energy transport toward the overdense region from the laser-heated region was mostly carried by sub-keV x rays, driving a thermal radiative heat wave into the solid density. Radiative effect to the (ablation) pressure in high-Z plasmas produced by a short wavelength laser light was significantly large and the pressure was enhanced to be about three times compared with low-Z plasmas. However the temperature in the cold dense region which was the front of the ablation front was also enhanced by radiative preheat.

Yaakobi et al. experimentally showed that at a 0.35- μm laser light irradiance of 10^{15} W/cm^2 , 3% of the absorbed energy appeared as preheat, due almost entirely to x-ray radiation.^[1] Mclean et al. found that when even 1- μm laser heated the front surface of 4~12- μm -thick Al foils, x rays had a possibility of a major energy carrier to heat the rear surface up to several electron volts.^[2] Computational studies of the above experimental result were also reported. Duston et al. claimed that the ionization front driven by

the radiative preheat causes the reduction of the opacity, resulting in strong radiative energy transport to rear side of the foil ^[3], and they also pointed out that a cooperative work of radiation and thermal electrons dominated the hydrodynamics of a laser-heated plasma even if it is a low-Z element such as carbon ($Z=6$).^[4]

In addition to such energy transport processes in short wavelength laser produced plasmas and/or high-Z plasmas, a study of the radiative transport is also important for indirect driven scheme of ICF using intensive soft x ray. High hydrodynamic efficiency in the ablative compression in ICF requires a large mass ablation rate as described in Chapter 2. Thermal radiation with a temperature of an order of 100eV has higher characteristic frequency than that of the laser light and can deposit its energy in density region higher than the critical density. Then this leads to a larger mass ablation rate ^[5] and to expect high hydrodynamic efficiency. Thus the intensive soft x ray has one of the strong possibility to become an high efficient energy driver ^[6] at a viewpoint of energy transport if there is no strong preheat.

Therefore pure studies on the radiative energy transport in hot dense matter is important and unavoidable problem for search of high efficient implosion from a viewpoint of the energy carrier in short wavelength produced plasmas (especially high-Z plasmas) or energy driver of ICF. In this chapter we present the energy transport in intense x-ray generated plasmas in order to purely study the radiative transport in hot dense plasmas.

Section 4-2 shows the experimental study on x-ray intensity dependence of the electron temperature in x-ray heated aluminum plasmas in order to understand the x-ray interaction with a solid matter. Soft x rays penetrate into a higher-density region and heat up larger volume compared with a visible laser light because of its long penetration depth, resulting in lowering the temperature of heated plasmas (e.g., 100eV).^[7] By Al K-shell diagnostics we cannot measure such a relatively low temperature because it was shown that the line intensity ratios formed from lines from H-like and He-like ions provided plasma temperatures of more than about 300 eV.^[8] Even if some temperatures were measured by the line, often too weak, those temperatures could result from local hot spots. Here, we obtained

temperatures of x-ray-heated plasmas through extreme ultraviolet (XUV) spectroscopy which has measured L-shell line emissions and continuum emissions from Al plasma. The temperature scaling with x-ray intensities of 10^{12} to 6×10^{12} W/cm². This scaling was compared with a simple self-regulating model taking account of the x-ray mean free path.

In Section 4-3, we present the experimental evidence of ionization burnthrough and absorption resonance in radiative energy transport in hot dense matter using a double-foil technique, by which is possible to heat a rear foil only by x rays from a front foil. The experimental results show the evidence of the ionization burnthrough predicted by Duston for aluminum foil and the burnthrough speed. At a high-Z (gold) matter, the spectral structure of transmitted x rays indicates the formation of an x-ray heat conduction band via absorption resonance.

§ 4-2. Laser Plasma X-ray Interaction with Solid Material

4-2-1. Experimental setup

The experiments have been conducted by using two parallel-plate targets as shown in Fig. 4-1. 0.53- μ m laser light (one beam of Gekko IV laser system) was first focused onto a Au plate (50- μ m thickness) through an aspheric lens of $f/1.6$ in a pulse duration of 400 psec (full width at half maximum) with an incidence angle of 54° . The laser intensity on Au plate was fixed at $(1 \sim 2) \times 10^{14}$ W/cm² in an effective spot diameter of 200 μ m. An Al square plate (500 \times 700- μ m side length and 50- μ m thickness) was used as a target irradiated by x rays from Au plasma and was placed parallel to the Au plate. The Al plate was positioned such that neither the incident laser light nor the specularly reflected light was allowed to heat it directly. An x-ray pinhole camera was used to monitor if the incident laser light directly heated Al plate. The gap distance between the parallel plates was varied from 300 μ m to 700 μ m in order to control the x ray intensity.

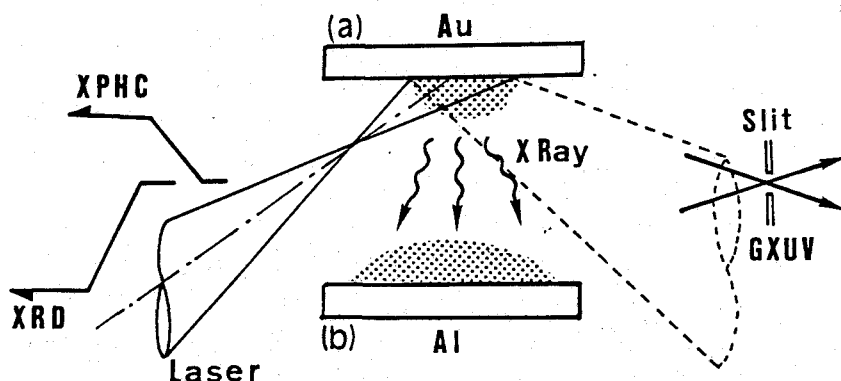


Fig. 4-1 Experimental setup: Au and Al plates are used as an x-ray emitter and a target irradiated by x-rays. XPHC: x-ray pinhole camera. XRD: a set of filtered x-ray x-ray diodes. GXUV: flat-field grazing incidence XUV spectrometer.

X-ray spectral measurements were performed using a flat-field grazing incidence XUV spectrometer with a grating of 1200 grooves/mm average pitch whose spectral range was from 45 Å to 250 Å.^[9] The spectrometer has a 50-μm entrance pinhole and a spectral resolution of 0.3 Å for the incidence wavelength of 60 Å. The spatial resolution was about 50 μm. The spectrometer was mounted at the right angle to the normal direction of the parallel plates and spatially resolved perpendicular to the target plane (see Fig. 4-1). The time-integrated XUV spectrometer was recorded on a Kodak-type 101 film.^[10]

A temporal behavior of soft-x-ray emissions was monitored by using two-channel Al photocathode biplanar x-ray diodes (XRD) with a 2-μm-thick parylene and 1-μm Al filters which provided spectral sensitivities in the photon energy range of 0.1~0.3 keV and 0.6~1.0 keV, respectively.^[11] The XRD's were mounted at a right angle to the normal of the parallel plates (see Fig. 4-1).

Time-integrated soft-x-ray spectra and the energy from Au plasmas were measured separately by 10-channel XRD's at the same laser condition as the one in this experiment but without the lower Al plate. The conversion efficiency defined as the ratio of a measured x-ray energy to the incident laser energy was 20~30 % in 0.1 to 1.6 keV for the cosine distribution of the

emission. The spectrum was same as the one shown in Section 3-2. The x-ray intensity on the Al plate was controlled by the distance between the x-ray emitter (Au) and Al plate and was determined by the illumination geometry. The x-ray spectra and intensity at Au plasmas were kept fixed through this experiment in order to avoid any change in the x-ray absorption processes.

Other energy fluxes such as (1) plasma ion particles, (2) hot electrons from Au plasma, and/or (3) radiation from the stagnated plasma between the parallel plates may heat the Al plate. However, the first two kinds of components (1 and 2) were estimated to be four or more orders of magnitude less than the radiative energy flux from charge collector and x-ray *p-i-n* diode signals.^[11] Moreover, effects of ion components will be reduced by the plasma stagnation between the parallel plates. From the spatially resolved XUV spectra, it was observed that the Au plasma was not stagnated directly on the Al plate but halfway to the Al plate. X-ray emissions from the stagnated plasma were monitored by the XRD's and x-ray intensity was small (typically <20 % of the x-ray intensity from the laser-heated Au plate is a major heating flux to the Al plate.

4-2-2. Experimental results

An example of XUV spectra of 50~100 Å from x-ray heated Al plasmas obtained with two different x-ray intensities is shown in Fig. 4-2. It should be noted that the continuum spectral peak shifts to a higher-energy side with increase of incident x-ray intensity. These observed characteristics are caused by the change of the averaged ionization state with the increased electron temperature since the free-bound spectrum is a function of the ionization state. For a Boltzmann distribution of free electrons in a Z-times ionized plasma, the spectrum of free-bound radiation vary as^[12]

$$\frac{dP_{fb}}{d(h\nu)} \sim \exp \left[\frac{X_{Z-1} - h\nu}{\theta} \right], \quad h\nu > X_{Z-1} \quad (4-1)$$

Here X_{Z-1} and θ are ionization potential and electron temperature.

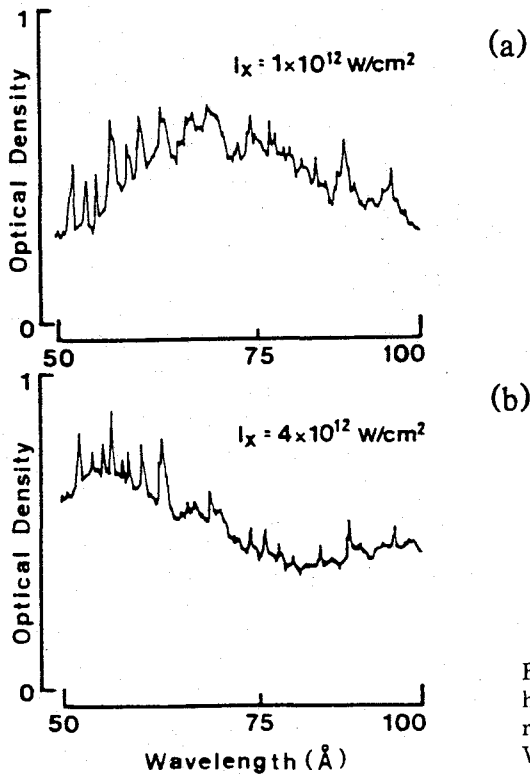


Fig 4-2 XUV spectra from x-ray-heated Al plasmas with different x-ray intensities I_x . (a) $I_x = 1 \times 10^{12} \text{ W/cm}^2$. (b) $I_x = 4 \times 10^{12} \text{ W/cm}^2$.

Figure 4-3 shows the x-ray intensity dependence of the electron temperature in x-ray heated Al plasmas from XUV spectra. Bold bars in Fig. 4-3 show the temperatures from the continuum spectra or average ionization state. The correlation of the electron temperature and the average ionization state by the hybrid-atom model (HAM)^[13] were shown in Fig. 4-4 and used in order to determine the electron temperature. This model is combination of the collisional-radiative model and the averaged-ion model. The correlation also depends on the ion density which was estimated to be $0.1 \sim 1.0 \times 10^{19} \text{ cm}^{-3}$ from the intensity ratio of the L-shell line emissions. In these L-shell emissions, the transitions of $\text{Al}^{18+} 2s^2 2p^2(3P) - 2s^2 2p^3 d(3D)$ and $\text{Al}^{18+} 2s^2 2p^3(5S) - 2s^2 2p^3 d(5P)$ were used.^[14] Such line ratio vs ion density are shown in Fig. 4-5(a). Debye screening of the ion potential may be displaced the energy levels, resulting in a continuum lowering. The red shift of the edge is described as^[15]

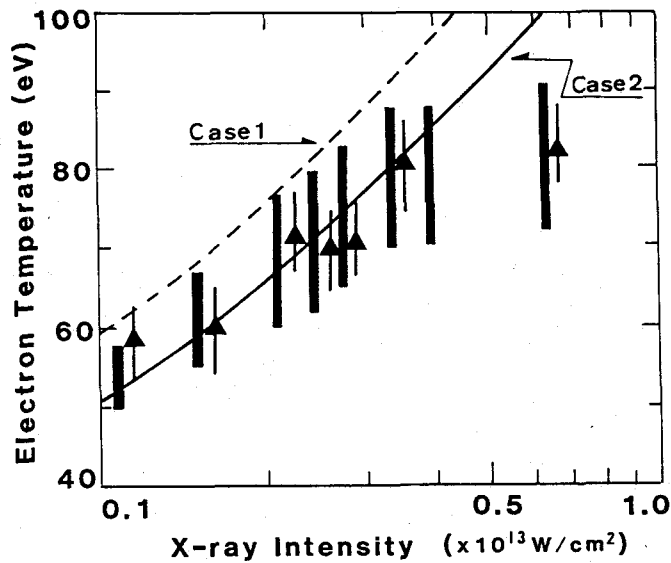


Fig. 4-3 Temperature vs x-ray intensity for x-ray-heated Al plasmas. Bold bars and triangles show the temperatures estimated from continuum spectra and line ratio. Dashed (case 1) and solid (case 2) lines are temperature scalings from analytical models. Case 2 includes the ionization loss into case 1.

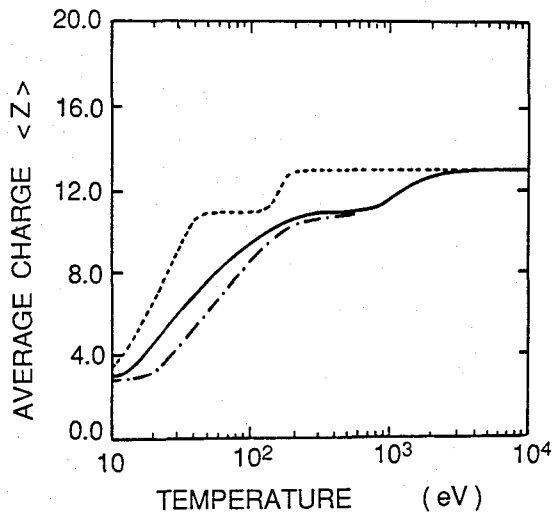


Fig. 4-4 Temperature dependence of the averaged charge state of Al. Ion number density: 10^{18} cm^{-3} . The solid, the broken, and the dot-solid lines denote the results of the HAM, LTE and the corona models, respectively. [see Ref. 13].

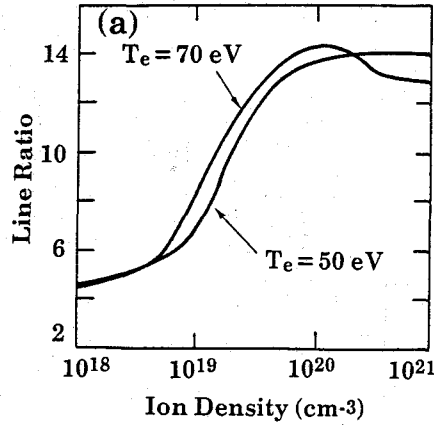


Fig. 4-5 (a) Line intensity ratio for the $2s^22p^2(3P)$ - $2s^22p3d(3D)$ / $2s2p^3(5S)$ - $2s2p^23d(5P)$ transitions vs ion density, for several electron temperatures (optically thin approximation). [see Ref. 14].

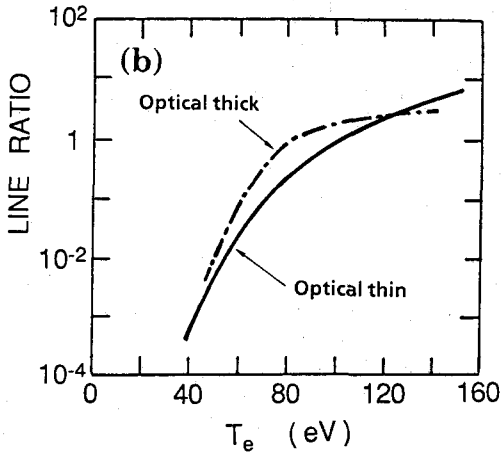


Fig. 4-5 (b) Line intensity ratio for the $2p-3s/2s^2-2s3p(1P)$ transitions for densities of 10^{19} ions/cm³ (optically thin approximation) and a plasma cylinder at 10^{19} ions/cm³ (with opacity effects) for radii of 500 μ m. [see Ref. 14].

$$\Delta E \sim -3 \frac{Z \cdot e^2}{2R_i} \quad (4-2)$$

where Z is the average charge of ions and R_i an ion-sphere radius defined by the relationship $4\pi R_i^3 N_e / 3 = Z$. In these ion density ($0.1 \sim 1.0 \times 10^{19}$ cm⁻³), the edge shift due to the density is negligibly small to estimate the temperature

and the shift is estimated to be $\Delta\lambda \sim 1.2 \text{ \AA}$ (6eV). The width of the temperature value in Fig. 4-3 is due to the uncertainty of the ion density.

Triangles in Fig. 4-3 show the electron temperatures obtained from a temperature-sensitive L-shell ratio [Al+10 $2s^2-2s3p(1P)$ and Al+11 $2p-3s$].^[14] The line intensity ratio depends only slightly ($\leq \pm 20\%$) on the plasma density between 10^{17} and 10^{21} ions/cm³ whose magnitude is consistent with experimental data. However, the opacity effects to the L-shell line emissions in such a density region may not be neglected so that radiation transport should be taken into account for determining the temperature. We assumed that an Al plasma with radius of 50~500 μm was produced along the viewing axis of XUV spectrometer in order to consider the opacity effect. Fig. 4-5(b) shows the temperature and opacity dependences of this line ratio. The vertical bars are due to the difference of plasma volume or optical thickness.^[14]

The result from the line ratio is in good agreement (within 20%) with that from the ionization state. It is readily seen in Fig. 4-3 that the electron temperature increases with the x-ray intensity. The scaling suggested by our data is

$$T_e = 53 \times I_x (10^{12} \text{ W/cm}^2)^{0.29} \quad (\text{eV}), \quad (4-3)$$

where I_x is incident x-ray intensity on Al plate.

4-2-3. Discussion

If we assume a steady state for x-ray heated plasmas, the electron temperature could be estimated by considering a self-similar isothermal expansion from the Chapman-Jouguet (C-J) point.^{[15],[16]} Let us imagine the process depicted in Fig. 4-6. The radiation comes from the vacuum and is absorbed at some point. In this model, incident x-ray flux I_x satisfies the condition,

$$I_x = 4 m_i n_{is} C_s^3 + U_r + U_i, \quad (4-4)$$

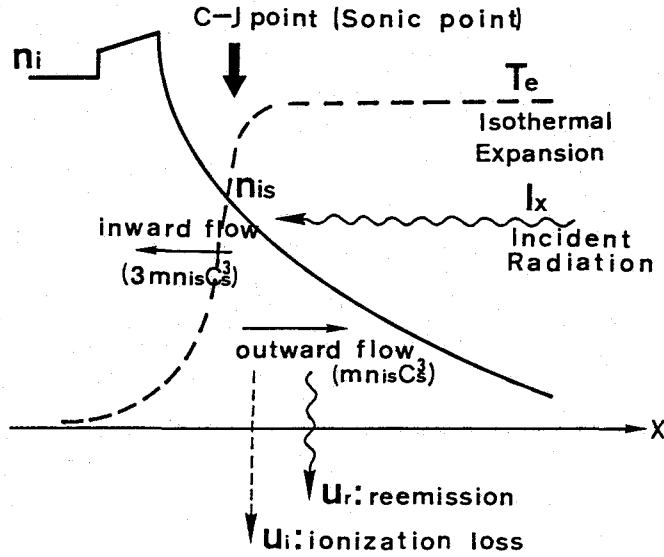


Fig. 4-6 Schematics of self-regulating flow model.

where U_r , U_i , and C_s are the radiative loss (reemission in the deflagration region), the ionization loss, and the sound speed $C_s \approx \sqrt{ZT_e/m_i}$, respectively. m_i and n_i are the ion mass and density. $4m_i n_{is} C_s^3$ is the heat flux necessary to maintain a self-similar isothermal expansion in which case the outward heat flux is $m_i n_{is} C_s^3$ and the inward flux is $3m_i n_{is} C_s^3$.^[16]

At first approximation (case 1), we neglected the ionization loss and the radiation loss as $I_x \approx 4m_i n_{is} C_s^3$. The inward energy flux of reemission U_r' is assumed to be less than the energy flux necessary to form the deflagration as $U_r' < 3m_i n_{is} C_s^3$. The structure and thickness of the ablation region are approximated by a radiation mean free path L_r . It is reasonable assumption that the electron thermal conduction is neglected in the deflagration region, comparing the mean free paths of thermal electron to that of x-ray radiation. L_r is assumed to have a form

$$L_r(x) = f(T_e) \cdot g(n_i) = \frac{f(T_e)}{n_i(x)^2}, \quad (4-5)$$

where $n_i(x) = n_{is} \exp(-x/C_s \tau)$. Moreover, the energy density of reemission in the deflagration region is assumed to be negligibly small compared to that of the incident radiation. Introducing the optical thickness $d\tau = dx/L_r$, we can obtain the radiation flux q_r in deflagration region from radiative diffusion approximation^[17] as

$$q_r = I_x \cdot \exp(-3|\tau|), \quad (4-6)$$

where τ is the opacity. Then Eqs. (4-5) and (4-6) give the following equations, respectively.

$$\sqrt{3} \int d\tau = \ln\left(\frac{I_x}{\int q_r dx}\right) = \ln\left(\frac{4m_i n_{is} C_s^3}{3m_i n_{is} C_s^3}\right) = \ln(4/3), \quad (4-7)$$

and

$$\sqrt{3} \int d\tau = \sqrt{3} \int_0^\infty \frac{dx}{L_r} = \frac{\sqrt{3} n_{is}^2 C_s t}{f(T_e)} \cdot \frac{C_s t}{2}, \quad (4-8)$$

where t is the duration of the radiation pulse. The ion density at the C-J point is given from diffusion approximation for the radiation flux as^[16]

$$n_{is} = \left[\frac{2 \ln(4/3) f(T_e)}{\sqrt{3} C_s t} \right]^{1/2}, \quad (4-9)$$

In the absorption process of radiation, the plasma is assumed to be in equilibrium condition ($T_e \approx T_r$). But in the emission process, the plasma may be out of the equilibrium condition, namely, the emissivity of reemission is much smaller than that in the case of the blackbody condition ($I_r < \sigma T_R^4$). A quasi-equilibrium condition such as this might be reasonably assumed as long as x-ray pulse continues, since the x-ray produced plasma at the C-J point will have a low temperature and high density. Then a simple

scaling of the temperature is obtained from Eqs. (4-4) and (4-9) taking account of the relation of $L_r = \alpha T_e^{3/2} T_r^2 / [n_i^2 Z(Z+1)^2]$ with $\alpha = 4.4 \times 10^{22} \text{ cm}^5 \text{ deg}^{7/2}$ for bound-free radiation^[17] as

$$T_e = 1.36 \times 10^{-1} [I_x^{12/35} (W/cm^2)] [(\tau^2 A A')^{1/3}]^{3/35} \quad (\text{eV}), \quad (4-10)$$

where we assume the relation of $Z = 2/3(A'T_e)^{1/3}$ ^[18]. Here, A and A' are the atomic weight and the atomic number, respectively. This scaling as shown in Fig. 3-3 for dashed line is about 30% higher than the experimental results. Such a result may stem from the neglect of the ionization loss U_i and/or radiation loss U_r in Eq. (4-4).

Next (case 2), we considered the ionization loss and the thermal energy is written from Eq. (4-4) as

$$I_x - U_i = 4m_i n_{is} C_s^3 = I_x \frac{3/2 k T_e (Z+1)}{3/2 k T_e (Z+1) + \sum \chi_n} = (0.6 \sim 0.7) I_x, \quad (4-11)$$

where χ_n is the ionization potential.

The scaling with ionization loss is shown as a solid line in Fig. 4-3. This scaling is in good agreement with the experimental result over the x-ray intensity of 10^{12} to $4 \times 10^{12} \text{ W/cm}^2$. This comparison implies that the incident radiation over such intensity will be quasi-equilibrated with the plasma.

It should be also noted that the saturation of temperature is found at a x-ray intensity of more than $5 \times 10^{12} \text{ W/cm}^2$. There are some possible mechanisms for the saturation. Considering the temperature at the ion density of 10^{19} cm^{-3} , the radiation loss is one of the important factors used to determine the electron temperature. Al plasma has a peak of emissivity by L-shell emission at the electron temperature of about 100 eV as shown in Fig. 4-6 from calculation^[14]. Thus, the effect of radiation losses through L-shell emission will be essential to the temperature scaling near 100 eV and the temperature may be saturated around 100 eV^[19].

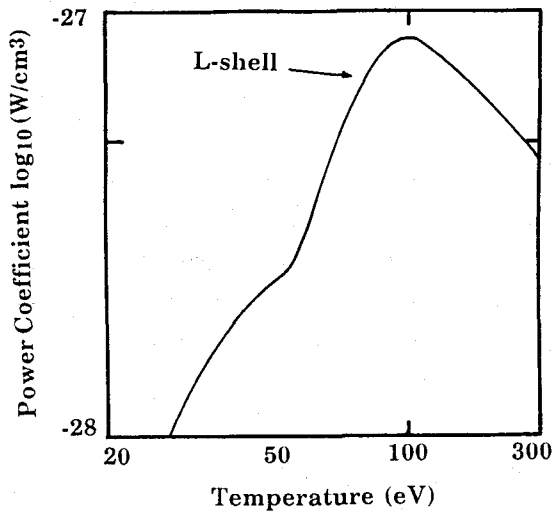


Fig. 4-7 Total radiative cooling power coefficient for aluminum and carbon plasmas versus electron temperature, at a density of 10^{20} ions/cm³. [see Ref. 14]

The ionization burnthrough^{[3],[7]} in the x-ray absorption process may also be one of the factors saturating the electron temperature. The photon energy of 100~300 eV of incident radiation is a component which forms about 30% of incident x-ray energy, and is mainly absorbed through the Al L-absorbed edge. However, temperature rise shifts the ionization front. Thus, incident radiation with the same energy flux penetrates further into a higher density region and heats a rather large volume, resulting in the temperature saturation. Details of the ionization burnthrough are appeared in next section(4-3).

4-2-4. Summary

We have measured the electron temperature of intense x-ray-heated Al plasma through XUV spectroscopy. The temperature scaled with x-ray intensity as $T_e = 53 \cdot I_x (10^{12} \text{ W/cm}^2)^{0.29} \text{ (eV)}$ over the range of intensity of 10^{12} to $4 \times 10^{12} \text{ W/cm}^2$. Temperature scaling is also obtained with a simple-self-regulating model taking account of the x-ray mean free path. Good agreement is found when we assume that the radiation is quasi-equilibrated with plasma considering the ionization loss. Saturation of temperature at

around $T_e \sim 100$ eV suggests a radiation loss by L-shell emission and/or ionization burnthrough in the absorbed region.

Above study is important to understand the x-ray interaction with a solid matter. In addition to such basic physical processes, a study of x-ray heating of solid matter is also practically important for various applications using intense x rays such as x-ray backlighting, x-ray lithography, and x-ray laser with a photo-pumping scheme. In such application, there are unavoidable problems in that the x-ray-irradiated objects are heated by the x rays of unnecessary photon energy components.

§ 4-3. Radiative Energy Transport in X-ray Produced Plasmas

4-3-1. Experimental set up

The experiments have been carried out by using double foil targets as shown in Fig. 4-8. The first layered foil, which is used for an x-ray emitter, consists of typically 500-Å-thick gold and 0.2- μm parylene (CH) layers. The first foil is heated by a 0.53- μm Gaussian laser pulse (one beam of Gekko IV laser system) through an aspheric lens of $f/1.6$ at an intensity of 2×10^{14} W/cm² with an incidence angle of 54° .

Either Al or Au foil is used for the second foil. Intense soft x rays emitted from the rear side of the first foil irradiates the second foil. The second foil thickness is changed from 0 to 0.3 μm . All the foils used were supported by a 0.2- μm parylene layer, except for a 0.3- μm Al foil which was free standing. The foils are mounted on 390- μm -thick brass washers whose inner and outer diameters were 2.1 and 4.2 mm, respectively. The second foil was electrically insulated. The vacuum gap distance between the first and second foils was fixed at 150 μm . This distance is long enough to minimize the effect to the second foil of the hydrodynamic shock wave and heated thermal electrons produced at the place where the laser deposits its energy.

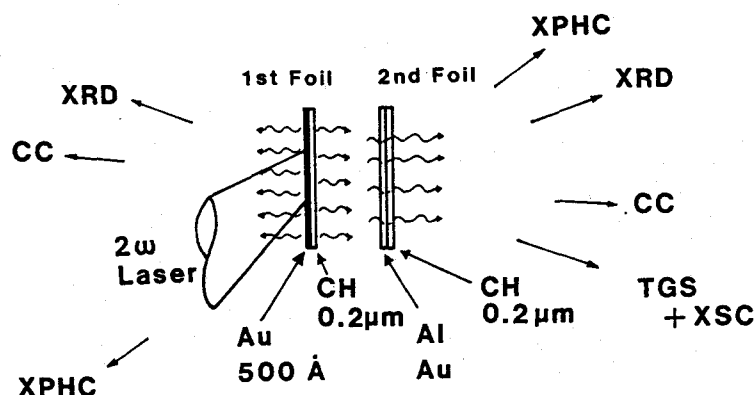


Fig. 4-8 A schematic view of the experimental setup. Laser: 0.53 μm wavelength Gaussian pulse with an intensity of $2 \times 10^{14} \text{ W/cm}^2$ in 350 psec. XRD: A set of ten channel-filtered x-ray diodes. XPHC: X-ray pinhole camera. CC: charge collector. TGS: transmission grating spectrometer. XSC: soft-x-ray streak camera. The first foil is used as an x-ray emitter. CH is a parylene layer.

Time-integrated soft x-ray spectral intensities towards the front and rear sides of the first foil were measured by a set of ten channel filtered biplanar x-ray diodes (XRD). The laser spot was monitored by 45- μm -thick Be-filtered x-ray pinhole cameras at both sides. A transmission grating spectrometer coupled with a soft x-ray streak camera was mounted at the rear side of the foils to measure time-resolved spectra in the range of 100eV to 1keV with a spectral resolution of 4 \AA . The photo cathode of streak camera was 300- \AA gold on 1000- \AA parylene and has a 80 $\mu\text{m} \times 10\text{mm}$ slit. The time scale of the streak camera was calibrated by a double laser pulse technique. The time resolution was estimated to be typically about 30 psec. The overall spectral response was indirectly estimated by comparing with a time-integrated spectrum obtained from the XRD signals. Charge collector were mounted at the both front and rear sides near the target normal to monitor the ion time-of-flight spectrum.

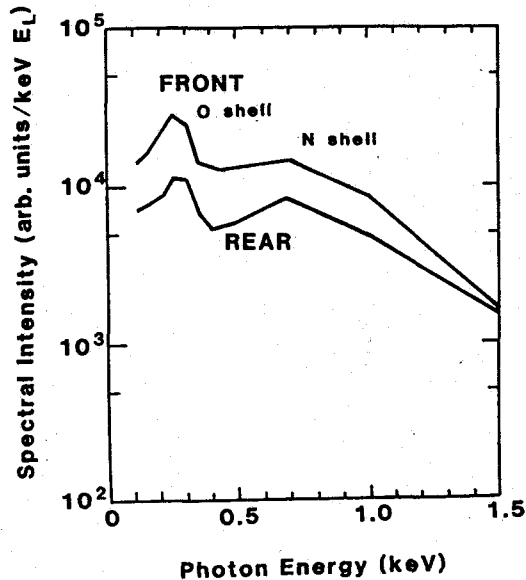


Fig. 4-9 Time-integrated spectral intensities of the front and rear emissions from a 500-Å-thick Au foil. Laser parameters are described in Fig. 4-8. E_L is the laser energy.

4-3-2. Experimental results

First we measured the rear emission from the first foil by the XRD as a function of gold-layer thickness without mounting the second foil. The signal of parylene-filtered XRD which corresponds to 150~280-eV x rays increased with Au-layer thickness up to 500Å and decreased at 1000Å by about 10% of the value at 500Å. The optimum thickness of 500Å is in reasonable agreement with the mass ablation depth which is estimated by the experimental result^[19] at several micrometers thick Au foils.

Figure 4-9 shows time-integrated spectral intensities of the front and rear emissions which were obtained by the ten-channel XRD for a 500-Å-thick Au layer. It should be noted that the rear emission spectrum has a more prominent structure due to O-shell and N-shell emissions, a deeper valley about 400 eV, than the front emissions, while the front emission has a spectral shape similar to that from an Au block target as shown in Chapter 3. In order to evaluate the effect on the observed rear emission spectrum by the 0.2-μm-thick parylene (CH) substrate, another 0.2-μm-thick CH foil was

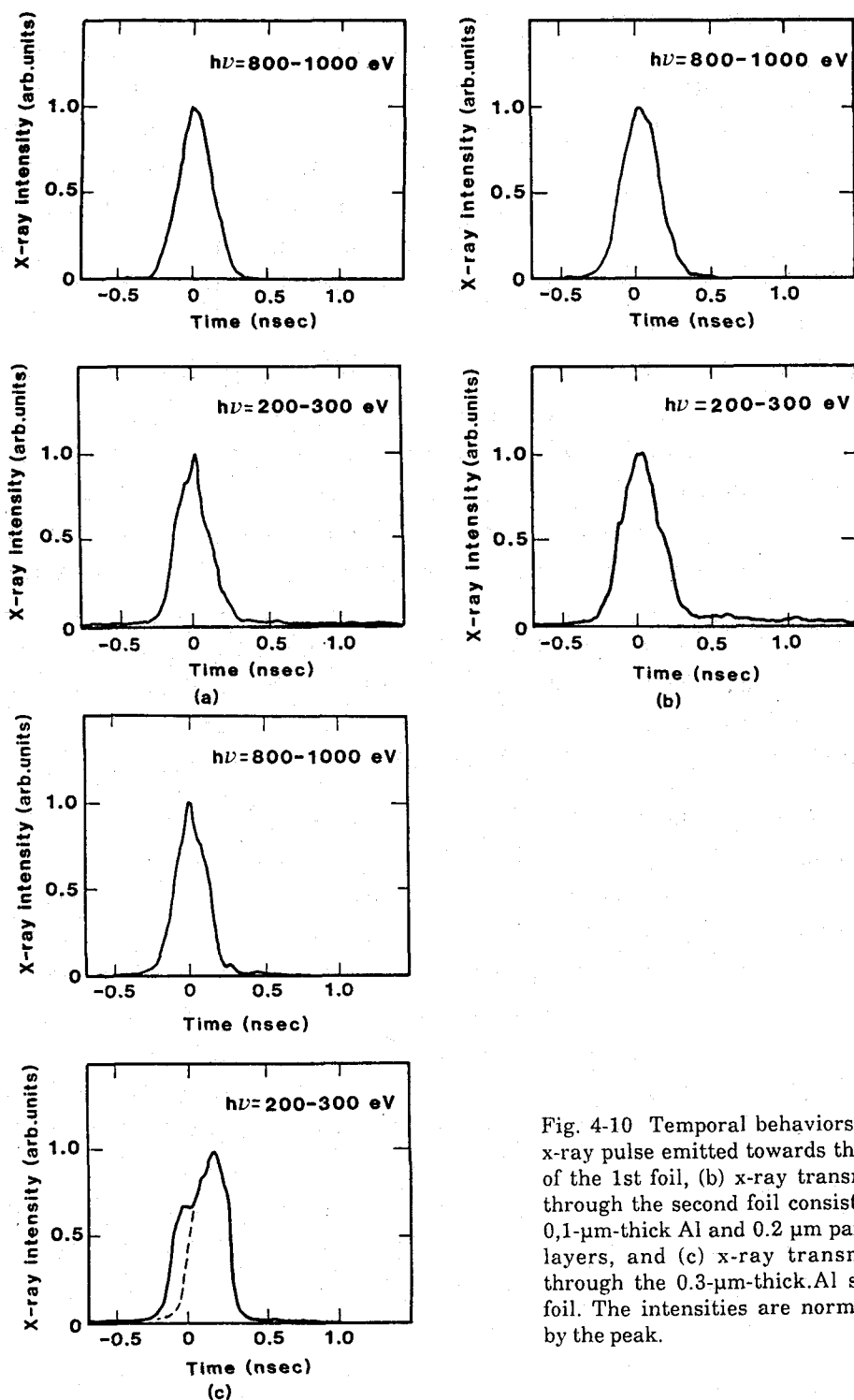


Fig. 4-10 Temporal behaviors of (a) x-ray pulse emitted towards the rear of the 1st foil, (b) x-ray transmitted through the second foil consisting of 0.1- μ m-thick Al and 0.2 μ m parylene layers, and (c) x-ray transmitted through the 0.3- μ m-thick Al second foil. The intensities are normalized by the peak.

placed as the second foil, but the observed spectrum was identical within $\pm 10\%$ to that obtained without the second CH foil. The x-ray conversion efficiency in 0.1 to 1.6 keV which is defined as the ratio of a time-integrated x-ray flux to the incident laser energy was 25% towards the front and 15% towards the rear; a total of conversion efficiency was 40%. Typical x-ray signal in the streak camera shows that the radiation is emitted towards the rear in a 320 psec full width at half maximum for 200 eV and a little shorter for 1000 eV as shown in Fig. 4-10(a).

From the above results, the intensity of the rear emission (we call it primary x ray hereafter) is determined to be 7.4×10^{12} W/cm² at the second foil taking account a geometrical reducing factor 0.35 which originates in a finite size of the x-ray emitter and a distance of the two foils, and also taking into account a spatial distribution of the primary x-ray intensity at the second foil. We averaged over the primary x-ray intensity in the spot area on the second foil whose diameter is the same as the laser spot on the first foil. The average intensity is $0.7 I_{x,0}$ where $I_{x,0}$ is the intensity at the center of the spot area. We could not measure directly the intensity distribution at the second foil. When the x-ray transmission through the second foil was measured, we always used 500-Å-thick Au foils as the x-ray emitter.

The charge collector signals showed very smooth velocity distributions to the rear and front directions, both of which had a peak at about 3×10^7 cm/s. The front signal had a additional precursor peak which is inferred to be due to fast protons. The observed ion velocity to the rear direction corresponds to an electron temperature of about 500 eV assuming an isothermal expansion of the foil. Hydrodynamic code calculation shows that the electron density is maintained during the laser heating at a significantly higher level than the density of the laser turning point due to slow hydrodynamic expansion of heavy Au ions, indicating that the transmission of the laser light is negligible for the 500-Å Au on 0.2-μm CH foil. This conclusion is also supported indirectly in an x-ray pinhole image through the second foil; the keV x-ray pinhole image would otherwise contain a much larger hot area heated by the leaked laser light in the second foil than that in the first foil.

Other energy fluxes into the second foil may be divided into the following several components: (i) plasma ion particles, (ii) hot electrons, and (iii) radiation from the plasma trapped between the two foils. The intensity of the plasma ions is estimated to be less than $8 \times 10^8 \text{ W/cm}^2$ from the charge collector signal. Their arrival to the second foil was confirmed to be only after the laser pulse in this experiment. Heat flux by the hot electrons (ii), which is generated at the laser-heated region is estimated to be less than 10^{-3} of that by cold electrons.^[21] In addition the flux reaching the second foil would be much less since vacuum insulation is effective for stopping the hot electrons^[22]. Hence these two components are four or more orders of magnitude less than the radiative energy flux. The x-ray emission from the stagnated plasma was observed only 0.5 nsec after the laser heating pulse, but the intensity was negligible. Therefore only radiative energy flux to the second foil during the laser heating phase.

Figure 4-10(b) shows an x ray transmitted through the second foil consisting of 0.1- μm -thick Al and 0.2- μm CH layers. Figure 4-10(c) shows an x ray transmitted x rays have a pulse shape similar to that of the incident primary x rays except for lower energy photons (200~300 eV) which show a long lived low level emission for the 0.1- μm Al and a delayed peak for the 0.3- μm Al. The positions of the time origins for Figs. 4-10(a), (b), and (c) are not identical because of the trigger jitter in the streak camera. However, the signal peak of transmitted high-energy x rays, say 800~1000 eV photons should correspond to the maximum intensity of the primary x rays, i.e., the laser intensity peak, because these x rays easily shine through the second foil. So we can use the time of the appearance of these signal peaks as the time reference in each shot. The long lived emission is inferred to be due to the afterglow during radiative cooling phase after the x-ray heating and/or due to the emission from the stagnated plasma. Therefore we concentrate on the x ray transmitted at the heating phase and evaluate the amount of spectrally resolved transmitted, i.e., rear emitted, radiation by integrating the intensity in the time period of the x-ray heating pulse.

4-3-3. Discussion

4-3-3-1. ionization burnthrough

Figure 4-11 shows the spectrally resolved x-ray intensities which were obtained as described above as a function of Al thickness. Dashed lines correspond to the x-ray attenuation due to photo-ionization absorption^[23] in a cold Al. The x-ray intensity is normalized to that obtained with no Al layer. The emissivity of the 0.2- μm CH layer is two orders of magnitude lower than that of Au^[21], so its fluorescence is negligible in the observed radiation. It is clearly seen that the transmission of 100~300 eV photons gradually decreases as the Al layer thickness increases, but its level is significantly higher than the transmission for a cold Al up to 0.3- μm thickness. The observed transmission rate η_{tr} of 100~300 eV photons decreases with the foil thickness d_0 linearly as

$$\eta_{tr} = 1 - 0.28 \left[\frac{d_0}{0.1 \mu\text{m}} \right], \quad (4-12)$$

rather than exponentially. On the other hand the attenuation of the intensities of 500~1000 eV photons approximately follows the dashed lines. If three dimensional (3D) expansion dominated the hydrodynamic motion of the radiatively heated foil, it would cause the opacity reduction in the whole photon energy range, resulting in the enhanced transmission also in the higher-energy range. The observed anomalous transmission at 100~300 eV in the time of concern suggests that the 3D expansion of the heated foil is not the case. The change of transmission behavior at 500 to 200 eV is considered to be due to the drastic change of opacity in lower- and higher-energy sides of the L absorption edge (100~400 eV) of aluminum ions, especially when their charge states are +5 to +8.

The above result is best explained by the ionization burn-through process predicted in Chapter 2; absorbed radiation is collisionally quenched, resulting in increased temperature and ionization of Al layer, while the temperature rise shifts the L-absorption edge -100 eV to the higher energy 300 eV, i.e., the blue shift of edge occurs, as shown in Fig.2 of Ref. 3, so the opacity decreases behind the ionization front. Finally shine-through

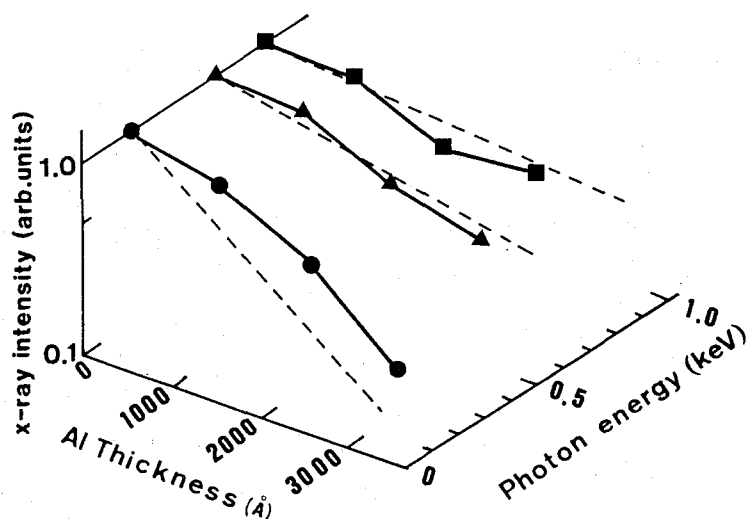


Fig 4-11 Spectrally resolved intensities of the x-rays transmitted through the Al second foil as a function of Al thickness. The intensity normalized to that obtained with no Al layer. Dashed lines correspond to the x-ray attenuation due to the photoionization absorption in a cold Al.

radiation comes out from the rear side of the foil with an enhanced transmission of 100~300 eV x rays as shown in Fig. 4-11. This indicates that most of the aluminum ions were ionized up to the charge state $+7$ whose L absorption edge was about 300 eV. Local thermodynamic equilibrium (LTE) calculation shows that Al^{+7} is mostly populated at the electron temperature of about 100 eV at solid density as shown in Fig. 2-6 on Chapter 2. So it is likely that the present primary x ray flux heated the Al foil up to about 100 eV.

In the dense plasmas discussed above, the energy levels are displaced by Debye screening of the ion potential, resulting in a continuum lowering. A red shift of the edge is estimated from Eq. (4-2) to be ~ 90 and ~ 40 eV for the ion density $5 \times 10^{21} \text{ cm}^{-3}$, respectively, assuming that the average charge of ions is ~ 7 at $T_e = T_i = 100$ eV. Thus the red shift described above compensates the blue shift (300 eV) only in a so small fraction that the

ionization burn-through process is maintained to be effective in the present experiment.

The rear surface may be preheated instantaneously by shine-through high-energy photons of $500\text{ eV} \sim 1\text{ keV}$ and then may reemit lower-energy photons via frequency down-conversion process^[3]. Their contribution to the observed flux of lower-energy x ray would be only in a negligible fraction except for the $0.3\text{-}\mu\text{m}$ Al foil because the absorbed energy of $500\text{ eV} \sim 1\text{ keV}$ photons in the foil is one or two orders of magnitude smaller than that of $100\sim 400\text{ eV}$ photons. For $0.3\text{-}\mu\text{m}$ Al foil it is found that the signal level of lower-energy photons is about one fifth reemitted lower-energy photons described above may be comparable in this case to that of the lower-energy photons which shined through after the ionization burn-through front reached the rear side.

Significant differences were not seen in time of appearance and temporal shapes of x-ray pulses at $100\sim 300\text{ eV}$ and $700\sim 1000\text{ eV}$ for the foil thickness up to $0.2\text{ }\mu\text{m}$. This fact may be partly due to the finite time resolution of the streak camera, but more intrinsically would be due to a two-dimensional distribution of the primary x ray intensity on the foil surface which blurs the arrival time of ionizing front, and/or due to a diffused structure of the ionizing front.

However, it is found that lower-energy photons ($200\sim 300\text{ eV}$) for $0.3\text{-}\mu\text{m}$ foil appear in the streak camera with a pulse shape which is composed of two parts as shown in Fig. 4-10(c). One is a smaller hump at earlier time and the other the signal peak at later time. The two-dimensional distribution of the primary x-ray intensity at the second foil is a smooth function that gradually decreases towards the peripheral part of the heated area. Therefore it is unlikely that the two-dimensional distribution caused the stepwise variation in the spatially integrated x ray streak signal as shown in Fig. 4-10(c). The first hump corresponds to the appearance of high energy photons ($800\sim 1000\text{ eV}$), thus seems to be due to the instantaneous heating by the high-energy photons as discussed previously. The second peak tends to delay by about 100 psec compared to the $800\sim 1000\text{ eV}$ photons and is inferred to have a rising part as shown by a dashed line in Fig. 4-10(c). This indicates that the

delayed appearance of lower-energy photons is caused by the time period of traveling of the ionization burn-through front.

The ionization burn-through depth defined as the foil thickness at $1/e$ transmitted x ray intensity is determined from Fig. 4-11 to be about 6×10^{-5} g/cm². The nominal average velocity of the ionization front is thus estimated to be about 6×10^5 g/cm²/sec by dividing the depth by the time delay.

The ionization burn-through speed $V_{IB} = \rho dx/dt$ is evaluated by the equation of energy conservation,

$$\rho E_Z dx = I_X \eta_{ab} dt - \dot{E}_{exp}(t) dt, \quad (4-13)$$

assuming that the opacity is reduced to a negligible level after the absorption edge is blue shifted via x-ray heating, i.e., the plasma becomes transparent to the incident x ray coming thereafter. E_Z is the energy loss per unit mass consisting of the ionization energy loss and the thermal energy of plasma,

$$E_Z = M^{-1} \left[\sum_{i=0}^{Z^*} I_i + \frac{3}{2} (Z^* + 1) k_B T_e \right], \quad (4-14)$$

where I_i is the ionization energy of the i th multiple ion and Z^* is the average ion charge which is achieved at a LTE state of plasma. M is the ion mass. \dot{E}_{exp} is the cooling rate by the hydrodynamic expansion of the plasma. I_X , η_{ab} , and ρdx are the incident x-ray intensity, the effective absorption in the foil of the spectrally integrated primary x rays, and the areal mass density, respectively.

Here as the most probable value to explain the result in Fig. 4-11, we adopt $T_e = 100$ eV at which an Al atom is ionized up to Al^{+7} in the LTE condition and thus the blue shift of the edge to 300 eV occurs. We neglect \dot{E}_{exp} at the first step. From Fig. 4-9 and the absorption cross section, η_{ab} is estimated to be about 0.35 for the photon energy range of interest. Then the average ionization burn-through speed V_{IB} is found to be 4×10^5 g/cm²/sec; 1.5×10^5 cm/sec for a solid density Al, at the x-ray absorbed intensity $I_X \eta_{ab}$ of

2.6×10^{12} W/cm². This value is in reasonable agreement with the experimental result if it is taken account that the model is not a completely self-consistent one. For example, the effect of hard x ray (500~1000 eV) preheating is neglected here.

After the ionization burn-through crosses the Al foil, the hydrodynamic expansion becomes a dominant cooling mechanism. When the absorption edges shift to below 300 eV due to the expansion cooling, the soft x rays are absorbed efficiently to heat up the plasma. As the result the average ionization state Z^* is kept constant, 7. During the x-ray pulse, the Al plasma expands to the thickness of $d \approx C_s \tau_x$. When $Z^* = 7$ is required, the LTE ionization relation gives

$$k_B T_e \text{ (eV)} \approx 100 \left[\frac{n}{n_{\text{solid}}} \right]^{0.2}, \quad (4-15)$$

according to the average ion model ^[13] where n is the ion number density. $n/n_{\text{solid}} = d_0/d$ gives $k_B T_e = 39$ and 48 eV at $d_0 = 0.1$ and 0.3 μm , respectively, and $n \approx 6 \times 10^{20} (d_0/0.1 \text{ } \mu\text{m}) \text{ cm}^{-3}$. When Z^* is assumed to be constant during the expansion, the temperature depends weakly on the density as shown by Eq. (4-17). Therefore the cooling rate \dot{E}_{exp} is approximately evaluated by using a self-similar solution of one-dimensional isothermal expansion of the foil which is uniformly heated by the x-ray pulse. From the self-similar analysis the expansion energy \dot{E}_{exp} is obtained as

$$E_{\text{exp}} = \frac{\dot{R}^2 \rho_0 d_0}{2} = \rho_0 d_0 C_s^2 \ln \left[\frac{R}{R_0} \right], \quad (4-16)$$

where ρ_0 and d_0 are the initial mass density and foil thickness, respectively, and the initial density profile is assumed to be $\rho_0 \exp(-x^2/2R_0^2)$ and $R_0 = d_0/\sqrt{2\pi}$. C_s is the sound speed in the x-ray heated plasma and $R(t)$ is determined by Eq. (A10) in the Appendix of Ref. 24.

By integrating the energy balance equation over the x-ray heating time τ_x , we obtain the energy necessary for ionization burn through and keeping the average ionization state constant during expansion as follows ^[24]:

$$E_{tot} = \rho_0 d_0 E_z + E_{exp} , \quad (4-17)$$

Note that E_z is the value for the expanding rarefied plasma. Thus E_{tot} of the expanding plasma is evaluated to be

$$E_{tot} = 248 \left[\frac{d_0}{0.1 \mu m} \right] (J/cm^2) . \quad (4-18)$$

On the other hand, the total plasma energy at $k_B T_e = 11 \text{ eV}$ and the solid density where $Z^* \sim +7$ was

$$E_{tot} = \rho_0 d_0 E_z = 187 \left[\frac{d_0}{0.1 \mu m} \right] (J/cm^2) . \quad (4-19)$$

The energy required to keep Z^* in the expanding plasma constant is about $61[d_0/0.1 \mu m] J/cm^2$. Namely, about 1/4 of the total plasma energy of the expanding plasma is considered to be absorbed after the ionization burnthrough. Note that the total plasma energy is proportional to d_0 when Z^* is kept constant and the transmission rate of the x rays, η_{tr} , is given by

$$\eta_{tr} = \frac{E_{x,0} - 248 d_0 / (0.1 \mu m)}{E_{x,0}} = 1 - 0.30 \left[\frac{d_0}{0.1 \mu m} \right] , \quad (4-20)$$

which reasonably agrees with the experimental data represented by Eq. (4-12), where $E_{x,0} = 822 J/cm^2$ is the primary x-ray flux.

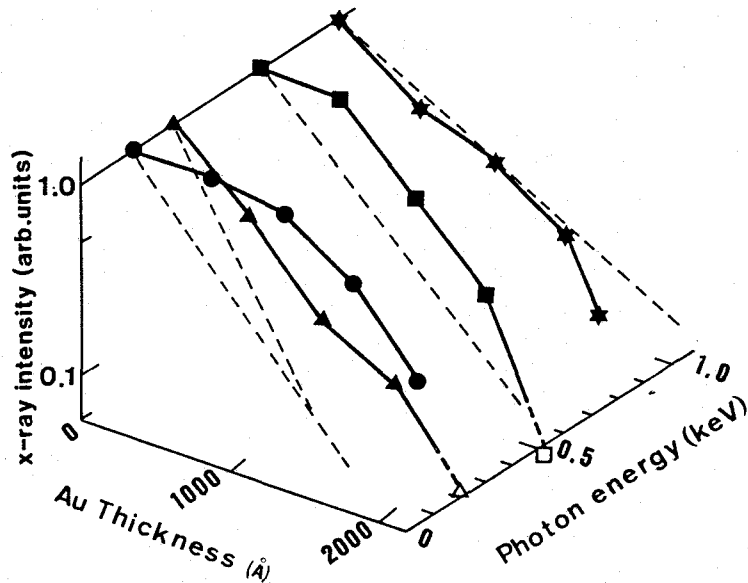


Fig. 4-12 Spectrally resolved intensities of the x-rays transported in the Au second foil as a function of Au layer. Dashed lines correspond to the x-ray attenuation in a cold Au.

3-3-3-2. absorption resonance

Similar experiments have been made using the Au second foil. Figure 4-12 shows the results obtained in the same way as for Fig. 4-11. Lowest-energy channel had a more prominent fluorescence signal level as shown in Fig. 4-13 after the heating laser pulse than that for Al, whereas higher-energy photons produced a pulse shape similar to the incident x rays shown in Fig. 4-9(a). It should be noticed that 150~250 and 600~700 eV photons are emitted more strongly than 350~450 and 900~1000 eV photons which are monotonically attenuated according to the photo-absorption (dashed lines) for a cold Au with the Au thickness. The transmitted radiations are enhanced not only by the shine through which has been discussed previously, but also by the reemission from the x-ray heated second foil because a significant fraction of high-energy x rays is absorbed in such high- Z matter. the second process is seen as equivalent to the effective energy transmission through the Au layer. The enhanced energy transports at 150~250 and

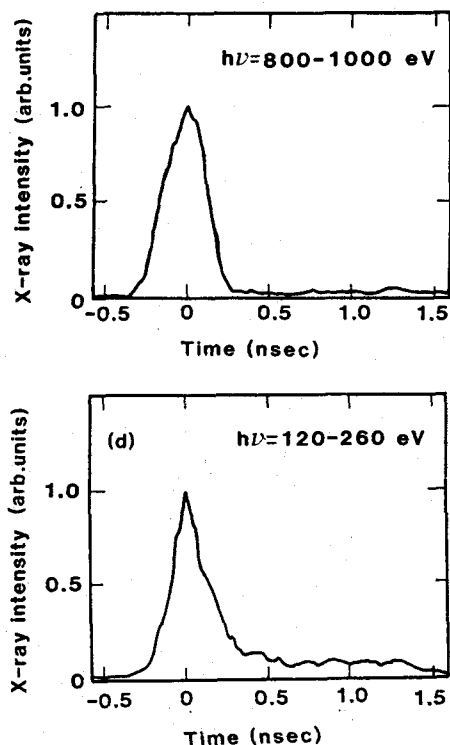


Fig. 4-13 X-ray transported in the second foil consisting of 0.1- μm -thick Au and 0.2- μm CH layers. The intensities are normalized by the peak.

600~700 eV channels correspond to the electric transitions in O shell and N shell of gold ions, respectively, as seen in the emission spectrum at a laser-heated Au plasma ^[21]. We consider a possibility that the energy levels in these orbital shells are so dense that the strong reemission process forms the effective heat conduction band in x-ray frequency domain via *absorption resonance*.^[24] This has similarity to the electron conduction band in semiconductor. The existence of absorption resonance has been only indirectly suggested by the anomalous optical constants of Au derives from the diffraction measurements of an Au transmission grating ^[25]. The frequency of the photons incident to the second foil would be strongly down converted during energy penetration as described in Chapter 2. Thus the energy transport should be concentrated on the conduction bands described above. However the radiative cooling and the ionization energy loss limit the radiative energy-transport depth in the Au foil. In the present case, an

effective x-ray mass penetration depth (g/cm^2) is found to be 3~4 times larger than that in Al layer.

Finally we consider the limited value $I_{x,\text{limit}}$ of incident radiation the hydrodynamic deflagration wave can never catch up with the radiation-driven ionization front. Using Eq. (4-13) and $V_{\text{IB}}(I_{x,\text{limit}}) > C_s$, we obtain

$$I_{x,\text{limit}} = 9 \times 10^{14} \frac{n_0^{16/7}}{A^{8/7}} \quad (\text{W/cm}^2) \quad , \quad (4-21)$$

where n_0 is the density in $5 \times 10^{22} \text{ cm}^{-3}$ and A is the atomic mass number. Hence we assumed a blackbody radiation with a radiation temperature T_r , as the incident x ray and $T_e \approx T_r$, and E_z is given as $2Zk_B T_e/M$ by the approximate estimation of $\Sigma I_i \sim ZI_z/2 \sim Zk_B T_e/2$. For example $I_{x,\text{limit}} = 2 \times 10^{13}$ and $5 \times 10^{13} \text{ W/cm}^2$ for $A=27$ (Al) and 12 (C) at $n_0=1$ (solid density), respectively. Practically other many factors will have to be considered, i.e., absorption by free-free transition and weak bound-free transitions behind the ionization front and hydrodynamic motion.

4-3-4. Summary

Radiative energy transport has been investigated using double foil targets in the sub-keV region. This target separates the energy transport by laser-heated bulk thermal electrons from radiative energy transport. In a midium-Z matter (Al), ionization burn through has been clearly observed. Burn-through speed in Al is estimated to be $6 \times 10^5 \text{ g/cm}^2/\text{sec}$ at the x ray intensity of $7.4 \times 10^{12} \text{ W/cm}^2$. In a high-Z matter (Au) with strong reemission and reabsorption, radiative energy has been transported for a long distance (mass penetration depth was 3-4 times larger than the case of Al). The spectral structure of rear emission indicates the formation of x-ray heat conduction band via absorption resonance.

§ 4-4. Conclusion

Radiative energy transport was experimentally studied in hot dense plasmas.

In order to give a basis of x-ray absorption for understanding the energy transport in x-ray heated plasmas, we obtained the experimental scaling of the electron temperature to x-ray intensity ($10^{12} \sim 10^{13}$ W/cm²) through XUV spectroscopy. The obtained scaling as $T_e = 53 \cdot I_x (10^{12} \text{ W/cm}^2)^{0.29}$ (eV) was in good agreement with the simple self-regulating model taking account of the x-ray mean free path and ionization loss over the range of intensity of 10^{12} to 4×10^{12} W/cm². Saturation of temperature was found above the intensity of 5×10^{12} W/cm², which will be caused by radiation loss by L-shell emission and/or ionization burnthrough in the absorbed region.

Using double foil targets, we measured the temporal resolved x-ray spectra transmitted through the second foil and radiative energy transport was studied in intense soft x-ray heated plasmas. In midium-Z plasmas (Al), ionization burn through has been clearly observed. Burn-through speed in Al was estimated to be 6×10^5 g/cm²/sec at the x ray intensity of 7.4×10^{12} W/cm². In high-Z plasmas (Au) radiative energy has been transported for a long distance with strong reemission and reabsorption. Penetration depth ($\rho \Delta R$) of radiative energy transport in Au is found to be 3-4 times larger than that in Al.

The obtained results and the discussion suggest that low-Z and midium-Z elements will easily become transparent to intense soft x rays by the ionization burn-through process. In a high-Z element strong radiative energy transport may take place through the process which is similar to the self-induced transparency process in laser interaction with nonlinear optical medium. Both processes operate to that the inner part of the matter so efficiently that they may produce some difficulty in laser fusion scheme; the preheating of the fuel pellet may easily occur with intense soft x rays.

References

- [1] B. Yaakobi, I. Pelah, and J. Hoose, *Phys. Rev. Lett.* **37**, 836 (1976).
- [2] E. A. McLean, S. H. Gold, J. A. Stamper, R. R. Whitlock, H. R. Griem, S. P. Obenschain, B. H. Ripin, S. E. Bodner, M. J. Herbst, S. J. Gitomer, and M. K. Matzen, *Phys. Rev. Lett.* **45**, 1246 (1980).
- [3] D. Duston, R. W. Clark, J. Davis, and J. P. Apruzese, *Phys. Rev. A* **27**, 1441 (1983).
- [4] D. Salzman, H. Szichman, and A. D. Krumbein, *Phys. Fluids* **30**, 515 (1987).
- [5] R. Docoste, S. E. Bodoner, B. H. Ripin, E. A. Mclean, S. P. Obenschain and C. M. Armstrong, *Phys. Rev. Lett.* **42**, 1673 (1979).
- [6] S. L. Bogolyubski, B. P. Gerasimov, V. I. L
- [7] T. Mochizuki, K. Mima, N. Ikeda, R. Kodama, H. Shiraga, K. A. Tanaka, and C. Yamanaka, *Phys. Rev. A* **36**, 3279 (1987).
- [8] H. J. Kunze, A. H. Gabriel, and H. R. Griem, *Phys. Rev.* **65**, 267 (1968); U. Feldman, G. A. Doschek, D. K. Prinz, and D. Nagel, *J. Appl. Phys.* **47**, 1341 (1976); D. Duston and J. Davis, *Phys. Rev. A* **21**, 1664 (1980).
- [9] T. Kita, T. Harada, N. Nakano, and H. Kuroda, *Appl. Opt.* **22**, 512 (1983); N. Nakano, H. Kuroda, T. Kita, and T. Harada, *ibid.* **23**, 2386 (1984).
- [10] B. L. Henke, S. L. Kwok, J. Y. Uejio, H. T. Yamada, and G. G. Young, *J. Opt. Soc. Am. B* **1**, 818 (1984).
- [11] R. Kodama, K. Okada, N. Ikeda, M. Mineo, K. A. Tanaka, T. Mochizuki, and C. Yamanaka, *J. Appl. Phys.* **59**, 3050 (1986); T. Mochizuki, T. Yabe, K. Okada, M. Hamada, N. Ikeda, S. Kiyokawa, and C. Yamanaka, *Phys. Rev. A* **33**, 525 (1986).
- [12] H. Griem, *Plasma Spectroscopy* (McGraw-Hill, New York, 1964); R. W. P. McWhirter and F. Stratton, in *Plasma Diagnostic Techniques*, edited by R. H. Huddleston and S. L. Leonard (Academic, New York, 1965); D. Mosher, *Phys. Rev. A* **10**, 2330 (1974).
- [13] M. Ito and T. Yabe, *Phys. Rev. A* **35**, 233 (1987); M. Ito, Masters thesis, Osaka University, 1987 (unpublished).
- [14] D. Duston and J. Davis, *Phys. Rev. A* **23**, 2602 (1981).
- [15] J. Stewart and K. Pyatt, *Astrophys. J.* **144**, 1203 (1963).
- [16] K. Nozaki and K. Nishihara, *J. Phys. Soc. Jpn.* **48**, 993 (1980); K. Nishihara, *Jpn. J. Appl. Phys.* **21**, L571 (1982); T. Yabe, S. Kiyokawa, T. Mochizuki, S. Sakabe, and C. Yamanaka, *ibid.* **22**, L88 (1982).
- [17] Ya. B. Zel'dovich and Yu. P. Raiser, *Physics of Shock Waves and High Temperature Hydrodynamic Phenomena* (Academic, New York, 1966).
- [18] D. Colombant and G. F. Tonon, *J. Appl. Phys.* **44**, 3524 (1973).
- [19] S. K. Goel, P. D. Gupta, and D. D. Bhawlikar, *J. Appl. Phys.* **53**, 223 (1982).
- [20] H. Nishimura, F. Matsuoka, M. Yagi, K. Yamada, S. Nakai, G.H. McGall, and C. Yamanaka, *Phys. Fluids* **26**, 1688 (1983).
- [21] T. Mochizuki, T. Yabe, K. Kodama, M. Hamada, N. Ikeda, S. Kiyokawa, and C. Yamanaka, *Phys. Rev. A* **33**, 525 (1986).
- [22] H. Shiraga, S. Sakabe, K. Okada, T. Mochizuki, and C. Yamanaka, *Jpn. J. Appl. Phys.* **22**, L383 (1983).
- [23] B. L. Henke, P. Lee, T. J. Tanaka, R. L. Shimabukuro, and B. K. Fujikawa, *At. Data Nucl. Data Tables* **27**, 1 (1982).
- [24] T. Mochizuki, K. Mima, N. Ikeda, R. Kodama, H. Shiraga, K. A. Tanaka, and C. Ymanaka, *Phys. Rev. A* **36**, 3279 (1987).
- [25] R. Tatchyn, I. Lindau, E. Kälin, and E. Spiller, *Phys. Rev. Lett.* **53**, 1264 (1984).

Chapter 5

ENERGY TRANSPORT IN LOW-Z ($1 < Z < 4$) AND LOW-DENSITY ($0.1\text{-}0.2\text{ g/cm}^3$) PLASMAS

§ 5-1. Introduction

§ 5-2. Laser-interaction with Low-Z and Low-density Target

§ 5-3. Laser-driven Shock Wave in Low-density Porous Target

§ 5-4. Energy Transport in Cryogenically Cooled D₂ Filled Foam Target

§ 5-4. Conclusion

§ 5-1. Introduction

Recently for high-gain ICF reactor's targets a new approach to sustain a thick layer of fuel in a hollow foam sphere has been proposed, tested and asked for the implosion experiments.^[1] The foam, which defines the spatial location of the fuel (DT or D₂) acts like a sponge and which holds the fuel by surface tension. The cryogenic foam target, which is composed of a low-density foam shell saturated with a liquid fuel, provides a thick and uniform fuel layer without introducing a high-Z element for fuel containment. This cryogenically cooled foam target (CRYFAT) has many advantages in ICF reactors such as relatively easy control of the fuel layer uniformity and inner gas pressure for hot spark burning, and reduction of fuel-pusher mixing. Detailed explanation of this CRYFAT will be presented in next chapter.

Instead of such advantages of CRYFAT, little experimental data about energy transport have been reported yet. CRYFAT is much different from previously studied target, namely low atomic number ($Z \approx 1$) and low density ($\rho \approx 0.2\text{ g/cm}^3$) with microscopical structure such as porous in target. In low

density target, laser-driven shock wave can be one of the important factors to preheat the overdense cold region as shown in Section 2-2. Section 2-3 indicates that the Maxwellian tail of thermal electrons may be directly or nonlocally transported into cold region in low-Z plasmas and preheat that region because of their long mean free path. In addition it is critical for deciding the implosion dynamics to study the shock formation and propagation in the target with micro structure.

In the previous chapters we studied the energy transport especially by radiation in short wavelength laser-produced plasmas which becomes important energy carrier in such plasmas from a view point of energy driver for efficient laser implosion. We have to study the energy transport in low-Z and low density target from a view point of efficient target such as CRYFAT for ICF.

In this Chapter, we studied the energy transport by the shock wave and electrons in low-Z and low-density target using mainly planar CRYFAT ($Z=1.2$, $\rho=0.2\text{g/cm}^3$).

In Section 5-2 we studied the nonlinear laser interactions such as stimulated Raman scattering (SRS) and two plasmon decay (TPD) instabilities which have possibility to create energetic electrons. In low-Z plasmas it is important to study energetic electron production by nonlinear interaction because of its long mean free path. In addition, in the target with structure such as CRYFAT the filamentation of laser beam and other instabilities could take place in the corona region. Such target properties may enhance nonlinear laser interactions.

In Section 5-3 the properties of laser-driven shock wave in porous target were studied. We observed directly the shock wave propagation in low-density foam target with an x-ray streak shadowgraphy. This method provides the measurement of the shock compressed region with temporal resolution between shock front and ablation front (pile-up zone). From experimental result we could estimate the time dependent of shock parameters such as the pressure, the temperature, and the compression in shock front and pile-up zone. The energy transport in shock compressed region from pile-up zone to shock front was also discussed.

In Section 5-4 the energy transport in low-Z plasmas ($Z \approx 1$) was studied with planar CRYFAT. Measurements were conducted by observing the rear side emissions from the target with temporal resolution. We obtained the temporal history of rear side temperature. Observed were shock heating and electron preheat preceding the shock heating. By over-coating of higher-Z material on CRYFAT or laser pulse shaping, we also obtained some solutions to reduce this electron preheat.

§5-2. Laser-interaction with Low-Z and Low-density Target

SRS is a parametric instability in which the beating of the incident laser-light wave with a scattered-light wave drives a plasma wave and the beating of the plasma wave with the pump drives the scattered-light wave. SRS scattered radiation can originate in the coronal at electron densities $n_e \leq n_c/4$, where n_c is the critical density at which $\omega_{pe} = \omega_0$. In this region the incident electro-magnetic (EM) wave may decay into a scattered EM wave and an electron plasma wave following the energy and momentum conservation laws and the relevant dispersion relations

$$\omega_0 = \omega_s + \omega_{epw}, \quad (5-1)$$

$$\mathbf{k}_0 = \mathbf{k}_s + \mathbf{k}_p, \quad (5-2)$$

$$\omega_0^2 = \omega_{pe}^2 + c^2 k_0^2, \quad (5-3)$$

$$\omega_s^2 = \omega_{pe}^2 + c^2 k_s^2, \quad (5-4)$$

$$\omega_{epw}^2 = \omega_{pe}^2 + 3v_{th}^2 k_{epw}^2. \quad (5-5)$$

Here ω_0 , ω_s , ω_{epw} , and ω_{pe} are the incident laser and scattered light frequencies, the plasma-wave frequency, and the plasma frequency,

respectively. The k 's are the corresponding wave vectors; c and v_{th} are the speed of light and the electron thermal speed.

When the incident laser decays into two electron plasma (EP) waves in a three wave parametric process, the instability is called two plasmon decay instability (TPD instability). The instability grows in time (absolute mode) at $n_c/4$ where the two EP wave frequencies (ω_{epw1} , ω_{epw2}) equally match with the natural mode frequency ($\omega_{epw1} = \omega_{epw2} = \omega_0/2$). The energy and momentum among the waves are conserved to be $\omega_0 = \omega_{epw1} + \omega_{epw2}$ and $k_0 = k_{epw1} + k_{epw2}$. This instability, like SRS, may produce supra-thermal electrons through wave breaking or Landau damping, and has the lowest threshold among parametric instabilities. TPD instability emits three-half harmonic scattered light following the energy and momentum conservation laws as

$$\omega_{3/2} = \omega_0 + \omega_{epw1, ep2} , \quad (5-6)$$

$$k_{3/2} = k_0 + k_{epw1, ep2} . \quad (5-7)$$

In consequence of SRS and TPD instabilities, supra-thermal electrons may be generated. The instability could accelerate electrons through Landau damping or wave breaking of the excited EP waves. The wave energy is converted to the energy of electrons. These suprathermal electrons may affect to the preheating of fuel. Then in this section we describe the experimental results of the scattered lights whose wavelength was 527~1000 nm and 352 nm at pump wavelength of 527 nm for SRS and TPD, respectively

5-2-1. Experimental set up

Experimental configurations for back and side-scatter measurements are shown in Fig. 5-1(a) and (b). Measurements were made at 143° and 180° with respect to the wave vector of the incident beam k_0 (side scatter was collected at 143°).

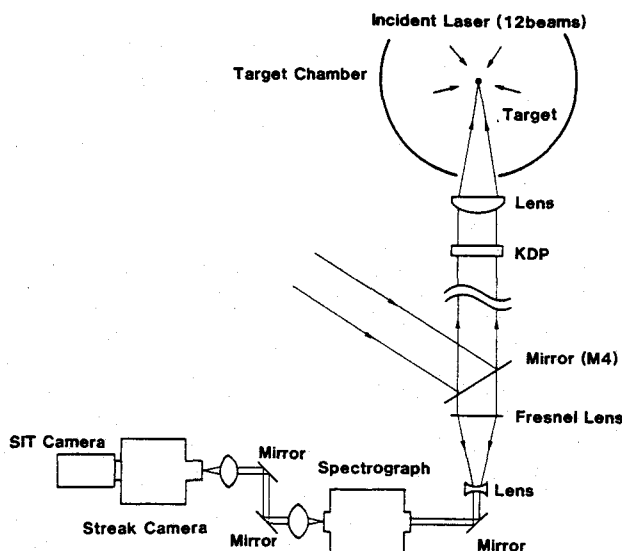


Fig. 5-1(a) Experimental configuration for back-scattered measurements. Back-scattered SRS was collected by the focusing lens.

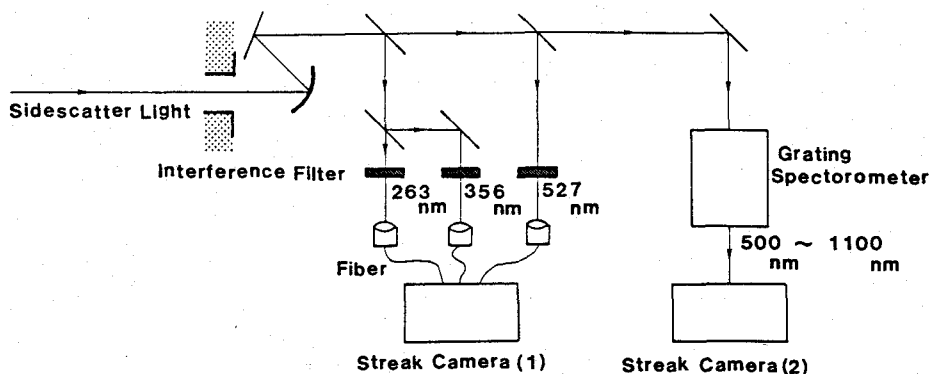


Fig. 5-1(b) Experimental configuration for side-scattered measurements. Side-scattered SRS was collected by a concave aluminum mirror at the angle of 143° to the wave vector of the incident beam.

The SRS light was dispersed in wavelength by a 0.25m grating spectrometer, temporally resolved with an optical streak camera (S-1 photocathode) and was recorded on SIT camera. Covered spectral range was from 500nm to 1000nm. Colored-glass filters (orange) were used to

attenuate a reflection of pumping light (527nm) and to block the high orders. The spectral calibration was done with a standard mercury lamp.

Back-scattered SRS was collected by the focusing lens as shown in Fig. 5-1(a). The green (527nm) reflection from target was monitored with a calibrated biplanar photodiode. The over-all spectral response, taking account of S-1 photo cathode response, filters, and relay lenses, was near flat between 600nm to 1000nm. The absolute fraction of SRS was estimated from the reflected green energy considering the spectral response of the system. The spectral and temporal resolutions were less than 10nm and 50psec, respectively. The 527nm-light reflected from a vacuum window was used for the time marker, which was led to the streak camera through an optical fiber. The relative timing of the scattered light to the laser pulse was determined by using shots with a 100psec laser pulse. Then the time accuracy is about 100psec.

Side scattered SRS was collected by a concave aluminum mirror to the optical streak camera coupled with the spectrometer as shown in Fig. 5-1(b). The spectral and temporal resolutions were 16nm and 90 psec, respectively. The spectral range was from 500nm to 1100nm. The absolute SRS was attenuated with HA(heat absorber) filter. The spectral response of this system was not flat and the spectrum was converted considering the spectral response of the system.

Three-half harmonic scattered light was measured with S-20 streak camera coupled with optical fiber and recorded on a CCD camera. A light collector was same with the collection system of the side SRS as shown in Fig. 5-1(b). Collected lights were split with a quartz glass and transferred to the collecting lens of the optical fiber through the interference filter (351nm $\Delta\lambda$ (FWHM)=15nm). Green and second harmonic scattered lights were also monitored with the same system. The system composed of four channels for 527-nm, 351-nm, 263-nm scattered lights and time fiducial. Time fiducial and its calibration was same with SRS measurements.

The experiments were carried out by GEKKO XII laser system. 527-nm light converted with KDP crystal was focused onto the targets by an f/3 lens. In most cases, the cryogenically cooled foam targets(CRYFAT) were used. The spherical target was irradiated with 12 beams at the focus condition of

$D/R = -5$. Planar targets were irradiated with 2 beams at the incident angle of 32° . The spot diameter was monitored with an x-ray pinhole camera to be an oval shape of $600 \times 700 \mu\text{m}$. Mostly the laser pulse was temporally near Gaussian profile and the pulse width (FWHM) was 900 psec.

5-2-2. Experimental results

One might have misgivings that very strong nonlinear interactions may occur for CRYFAT, since the surface of this target has many fine structures by porous materials, which could work as initially-imposed density perturbations.

Figure 5-2 shows the target material dependence of time-resolved Raman back scattered light with spherical targets [(a)CRYFAT, (b)CD plastic, and (c)plastic foam without D_2]. At the same laser intensity SRS from CRYFAT [5-2(a)] was same or even lower compared with the CD plastic targets [5-2(b)] whose surface was almost ideally smooth. However SRS from a plastic foam target without dipping into D_2 [5-2(c)] was 4-5 times stronger than that from CRYFAT. We also observed that the back-scattered light from the foam target without D_2 was strongly modulated in both time and spectrum. The temporal modulation was strongly correlated with both the spectral broadening and the spectrum of SBS, which can be seen in Fig. 5-2(c). The observed broadening from the pump laser wavelength exceeded actually $\Delta\lambda \geq 1000 \text{\AA}$. This was almost white light generation in laser plasmas ^[2]. Such a strong correlation might only be possible when laser light is broken up into many filamentats which could be initiated with the foam structure. When CRYFAT was filled only partly with D_2 , we observed larger SRS and some modulation in spectrum. These experimental results suggest that unless CRYFAT is filled completely with D_2 , structures in the target works as initially-imposed density perturbations and enhance SRS fraction with the spectral modulation.

Figure 5-3 shows the time-integrated spectra of Raman back scattered lights from CD plastic (dotted line) and CRYFAT (solid line). While spectral peak for both targets was same to be about 870 nm, spectral shape was clearly different. Short wavelength cutoff of SRS spectrum was same to be

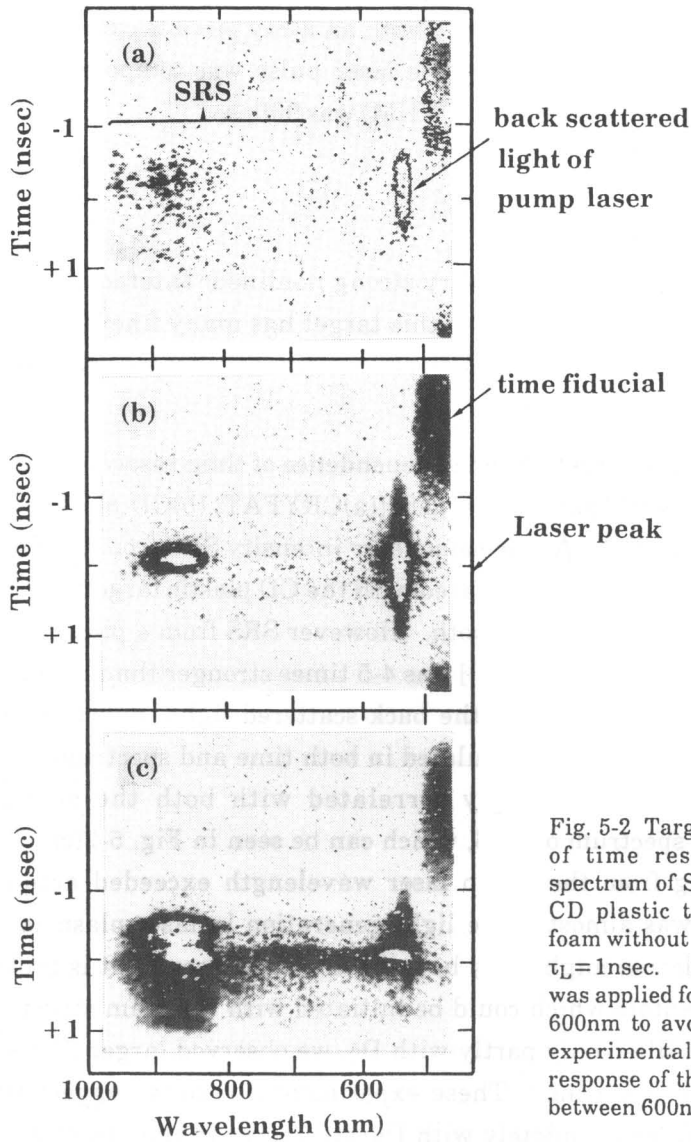


Fig. 5-2 Target material dependence of time resolved backscattered spectrum of SRS. (a) CRYFAT, (b) CD plastic target, and (c) plastic foam without D₂. $I_L = 3 \times 10^{14}$ W/cm², $\tau_L = 1$ nsec. Heavy filtering ($1/10^3$) was applied for the wavelength below 600nm to avoid any damage on the experimental set-up. The spectral response of the system was near flat between 600nm to 1000nm.

about 820 nm but long wavelength cutoff of SRS spectrum for CRYFAT (980nm) was longer than that for CD plastic target (940nm).

Figure 5-4 shows the laser intensity dependence of Raman back scattered light from CRYFAT. Spectral intensity increased with laser intensity but the spectral peak for both laser intensity of 3×10^{14} W/cm² and 5×10^{14} W/cm²

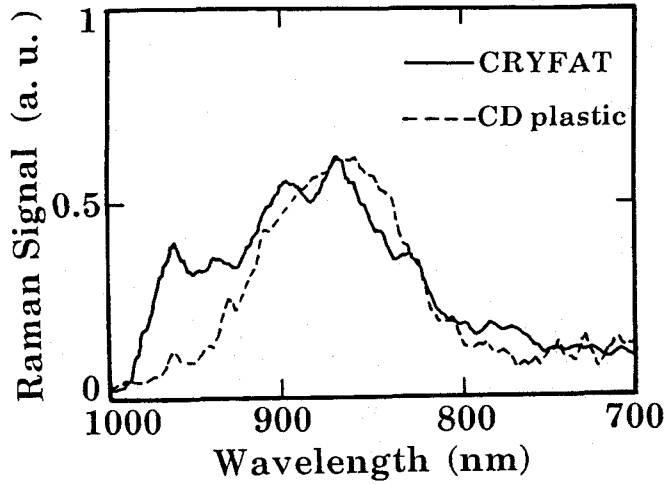


Fig. 5-3 Time integrated spectra of SRS from CD plastic (dotted line) and CRYFAT (solid line). $I_L = 3 \times 10^{14} \text{ W/cm}^2$.

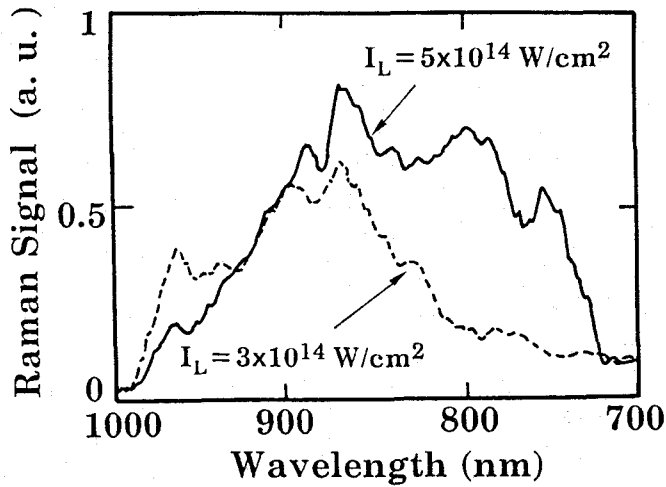


Fig. 5-4 Laser intensity dependence of SRS spectra from CRYFATs. Solid line; $I_L = 5 \times 10^{14} \text{ W/cm}^2$, and dotted line; $I_L = 3 \times 10^{14} \text{ W/cm}^2$.

stayed at about 870 nm. Spectral width for higher laser intensity was wider than that for lower intensity. While long wavelength cutoff of SRS was same for both laser intensity, short wavelength cutoff for higher laser intensity (720 nm) was 100 nm shorter than that for lower laser intensity (820 nm).

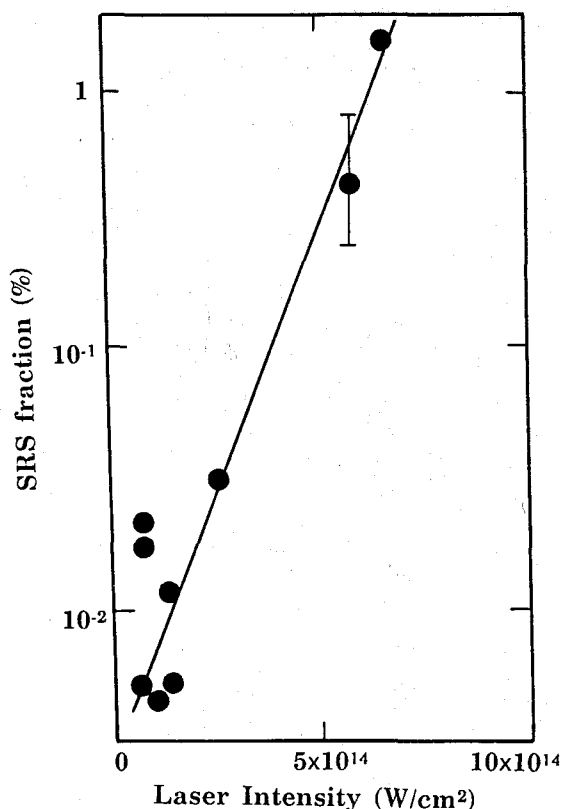


Fig. 5-5. SRS fraction v.s. laser intensity. Spectrally and temporally resolved data of both pump laser backscattered light and SRS. Since the energy of the pump laser backscattered light was monitored separately, scattered light energy of SRS could be estimated. Nonlinear growth of SRS reaches as much as 1% of the incident laser energy at laser intensity of $6 \times 10^{14} \text{ W/cm}^2$.

These target material and laser intensity dependence of spectral shape may be affected by the wave damping such as collision and/or Landau damping. Detailed discussions will be appeared in following part.

Time history and fractional energy of SRS for spherical target were also monitored. Figure 5-5 shows a nonlinear growth of SRS for CRYFATs versus the pump laser intensity. Fractional energy of SRS was estimated by time-integrated SRS spectrum and comparing then this integrated value to the 527nm (pump beam) back-scattered value, since the energy of the 527nm back-scattered value was measured separately with a calorimeter. At below laser intensities $4 \times 10^{14} \text{ W/cm}^2$, the amount of SRS energy becomes less than 0.1% of incident laser energy and should have negligible effect for

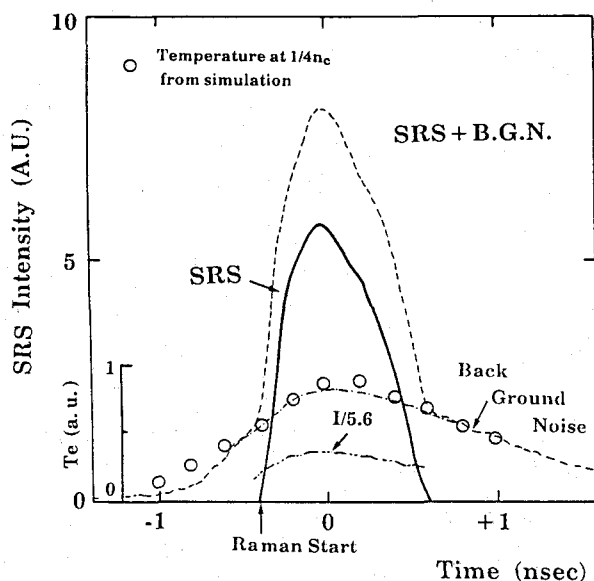


Fig. 5-6 Temporal history of SRS and background noise from planar CRYFATs at $I_L = 4 \times 10^{14} \text{ W/cm}^2$. Real SRS is shown for bold line supposed by subtracting the back ground noise from overall signal. Open circles are relative electron temperatures at the quarter critical density point from 1-D simulation.

implosion performance^[3]. The observed threshold intensity of the laser for SRS was consistent with measurements at different institutions^[4].

Temporal histories of background noise and Raman side scattered light rising from the noise were also observed for planar CRYFAT as shown in Fig. 5-6. At a laser intensity of $4 \times 10^{14} \text{ W/cm}^2$ there were two different temporal slopes were observed (i) slow rise signal whose rise time was about 1nsec and decay time was extremely long and (ii) fast rise signal which rise at 400psec before laser peak. Slow rise signal was spectrally continuum and increases exponentially with decrease of the wavelength. As the laser intensity decreased ($I_L = 7 \times 10^{13} \text{ W/cm}^2$), only slow rise signal was observed not fast rise signal as shown for double-dot-dashed line in Fig. 5-6. Hence the slow rise signal is due to thermal emissions (background noise) from plasmas and the fast rise signal is due to SRS.

From the temporal behavior of SRS rising from background noise, the threshold laser intensity was about 2×10^{14} W/cm². This value is reasonable compared with the threshold obtained from time integrated signals as shown in Fig. 5-5. This background noise may represent a blackbody emission and depend linearly on the thermal electron temperature. Open circles in this figure show relative electron temperatures at quarter critical density point for the laser intensity of 4×10^{14} W/cm² from 1-D hydrodynamic simulation. Temporal history of this background noise is similar to the temperature behaviors from the simulation. At lower laser intensity (7×10^{13} W/cm²) this signal magnitude was about 1/2.5 times lower than that at 4×10^{14} W/cm². From theoretical scaling as described in Eq. 3-2 ^[5], temperature difference between these laser intensities are estimated to be about a factor of 2.38 corresponding to the same times intensity difference of blackbody emission. However we should note that the observed thermal emission may not always come from only laser spot area. In low-Z target thermal emission area may be larger than laser spot area by lateral energy transport which also depends on the laser intensity.^[6]

Figure 5-7 shows the time histories of three-half harmonic scattered light from planar CRYFATs at the laser intensity of 4×10^{14} W/cm² (solid line) and 7×10^{13} W/cm² (dashed line). At the high laser intensity the scattered light rises from about 700 psec before laser peak and begins to saturate at 400 psec before laser peak. These rising point and saturation point corresponds to the incident laser intensity at quarter critical point of 1×10^{14} W/cm² and 2×10^{14} W/cm² from simulation, respectively. Increasing the laser intensity by factor 5.6, the scattered light intensity increases nonlinearly by factor about 40 with laser intensity. In the saturation region there are some intensity modulations, most of which well correspond to the temporal intensity modulation of incident laser light. At the low laser intensity the rising point is about 300 psec before laser peak corresponding to the laser intensity of 5.5×10^{13} W/cm². Here we observed the signal barely above the detection level but even by extending the temporal slope to lower level each rising point will be different.

The level of energetic x rays produced by electrons heated by various laser-plasma coupling processes was measured with a multichannel filter-

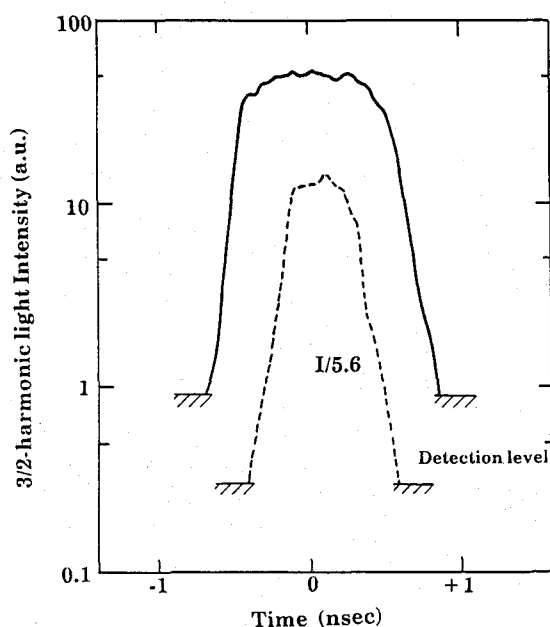


Fig. 5-7 Time histories of three-half harmonic scattered light from planar CRYFAT at $I_L = 4 \times 10^{14}$ W/cm² (solid line) and $I_L = 7 \times 10^{13}$ W/cm² (dashed line).

fluorescer x-ray spectrometer (FFX)^[7]. Used filter-fluorescer sets are Zn-Fe, Mo-Y, Sn-Pd, Yb-Dy, and Pb-Ta, which correspond to the energy bands of 7-10 keV, 17-20 keV, 24-29 keV, 54-61 keV, and 67-88 keV, respectively. Figure 5-8 shows the suprathreshold x-ray spectrum with planar CRYFAT. If we assume that the x rays are produced by Maxwellian electrons,^[8] the data indicate that super-hot electron temperature is about 12 to 14 keV and hot electron temperature 6 keV. By using Brueckner's model^{[9],[10]}, the ratio of the energy corresponding super-hot electron distribution to hot component is estimated to be about one tenth. However it should be noted that determining the hot electron temperature (~ 5 keV), the spectrum in the corresponding photon energy region (about 5-10 keV) are affected by thermal electron distribution such as 1 keV. Relatively small error in the determination of temperature will result in a significant error in the corresponding energy density. Then we had better consider only super-hot component (12-14 keV) here, which may be produced by nonlinear laser interactions such as two-plasmon decay and/or SRS instabilities.

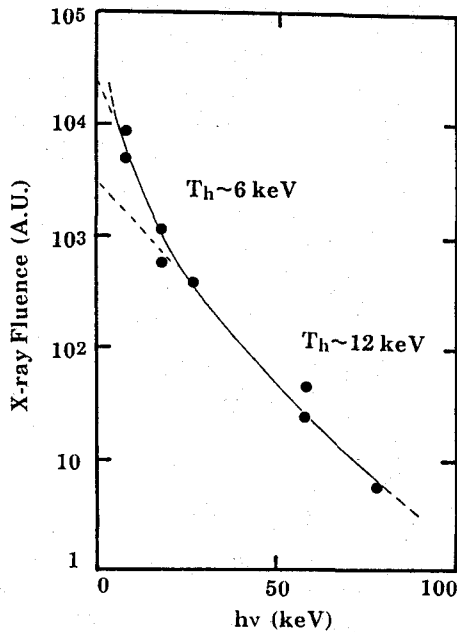


Fig. 5-8 Supra thermal x-ray spectrum from planar CRYFATs with FFX spectrometer.

5-2-3. Discussion

5-2-3-1 threshold intensity for SRS and TPD

The threshold intensity for convective back SRS in inhomogeneous plasma^[4] is simply estimated to be order of 10^{15} W/cm² at this experimental conditions. However Fig. 5-5 shows much lower laser intensity for the threshold. This discrepancy may be explained by the density modulations and /or filamentation of laser produced by the ponderomotive force.^[11] Another possibility is that observed signal includes not only back scatter component but side scattered lights. The twelve focusing lenses are arranged symmetrically so that the some side scattered light comes into the collecting lens.

The theoretical threshold for the convective Raman side scattering instability in an inhomogeneous plasma is given by^[12]

$$I_{SRS} > 1.2 \times 10^{17} \frac{f(\theta, \omega_{epw})}{\lambda_p^{2/3} L_p^{4/3}} \quad (\text{W/cm}^2) \quad , \quad (5-8)$$

where λ_p and L_p is the pump light wavelength and plasma scalelength in the unit of μm . $f(\theta, \omega_p)$ is threshold parameter as a function of density and angle of the incidence in vacuum for S-polarized pump wave. For example when θ is 0° and 30° , $f(\theta, \omega_p)$ values are about 0.4 and 0.25 at $0.1 n_c$, respectively. Then the threshold is about $1.2 \times 10^{14} \text{ W/cm}^2$ for the plasma scalelength of about $100 \mu\text{m}$. This estimated value is in good agreement with the experimental result of side scattered SRS as shown in Fig. 5-6.

The threshold intensity of TPD instability for a linear density profile is given by ^[13]

$$I_{TPD} > 5 \times 10^{15} \frac{T_e}{\lambda_p L_p} \quad (\text{W/cm}^2) \quad , \quad (5-9)$$

where T_e is the thermal electron temperature in the unit of keV. The threshold of TPD instability is lower than that of SRS at $n_c/4$ unless the plasma temperature is several ten keV. The threshold is 10^{14} W/cm^2 and is in good agreement with the above estimation at high laser intensity ($4 \times 10^{14} \text{ W/cm}^2$) estimating from temporal rising point of three-second harmonic light from detection level. The threshold is derived to be about $6 \times 10^{13} \text{ W/cm}^2$ at low laser intensity ($7 \times 10^{13} \text{ W/cm}^2$) if we assume the temperature and scalelength given by the scaling of Eqs. (3-2) and (3-5). Experimental results in Fig. 5-7 suggest the threshold of $5.5 \times 10^{13} \text{ W/cm}^2$ in good agreement with the estimation value.

Figure 5-9 shows the temporal behaviors of threshold intensity for side SRS and TPD taking account of plasma scalelength and electron temperature from 1-D hydrodynamic simulation. Laser intensity at the quarter critical point is also presented from simulation (absorption is mostly due to inverse bremsstrahlung). When the laser intensity crosses each threshold, each instability (SRS and TPD) will occur. These estimations are

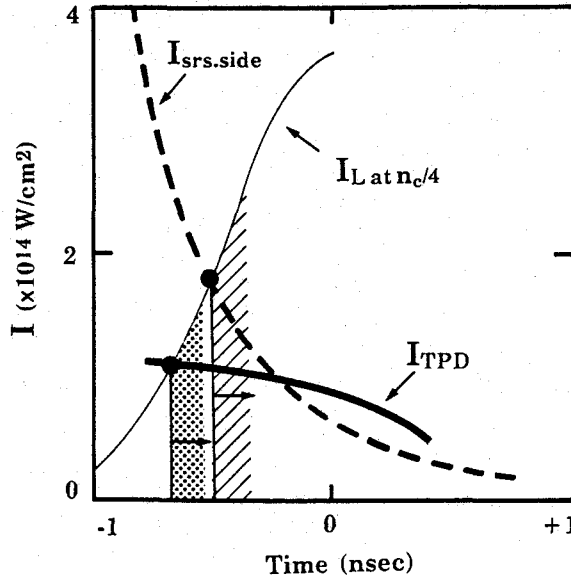


Fig. 5-9 Temporal histories of threshold intensity for SRS (Eq. 5-8) and TPD (Eq. 5-9) taking account of plasma scalelength and temperature from 1-D simulation. Broken line is laser intensity at the quarter critical density point from simulation.

in good agreement with experimental results of temporal behaviors of side SRS and three-second harmonic scattered lights.

5-2-3-2 damping of TPD

Between the unstable region of TPD instability and harmonic generation region, the electron plasma waves are damped due to collisional or Landau damping or both, depending upon their wavenumbers.

The temporal, collisional damping rate $(\Gamma_p)_c$ of electron plasma wave is expressed as $(\Gamma_p)_c = v_{ei}/2$ ^[14], where v_{ei} is the electron-ion collisional frequency and can be evaluated from the equation ^[15]

$$v_{ei} = 9 \times 10^{-11} \frac{n_e Z \ln \Lambda}{T_e^{3/2}}, \quad (5-10)$$

where Z is the effective ion charge, n_e is the electron density in cm^{-3} , T_e is the electron temperature in keV, and $\ln \Lambda$ is the Coulomb logarithm of approximately $[31 - \ln(n_e^{1/2}/T_e)]$. Landau damping rate $(\Gamma_p)_L$ of the electron plasma wave is approximated as ^[16]

$$(\Gamma_p)_L = (n/8)^{1/2} \omega_{pe} (k_{epw} \lambda_D)^{-3} \exp \left[-\frac{1}{2k_{epw}^2 \lambda_D^2} - \frac{3}{2} \right], \quad (5-11)$$

in which λ_D is the Debye length given by v_{th}/ω_{pe} . Using conservation laws and dispersion relations we can estimate each dumping rate. Then in low temperature region TPD instability is dominated by mainly collisional dumping which decreases with electron temperature. At high electron temperature the instability is mostly limited by Landau dumping which increases with electron temperature. In this experimental condition Landau dumping is expected to be negligible.

From Fig. 5-7, the saturation level of three-half harmonic scattered lights in pulse increases with incident peak laser intensity due to the electron temperature from Eq. 3-2 ($T_e \propto I_L^{1/2}$). For example the threshold intensity of the saturation is $2.8 \times 10^{14} \text{ W/cm}^2$ for peak laser intensity of $4 \times 10^{14} \text{ W/cm}^2$ and $6-7 \times 10^{13} \text{ W/cm}^2$ for $7 \times 10^{13} \text{ W/cm}^2$. Then the collisional damping rate $(\Gamma_p)_c$ of electron plasma wave is estimated to be 7×10^{11} and 2.3×10^{12} for 1 keV and 0.4 keV, respectively assuming that the electron temperature is 1 keV at the laser intensity of $4 \times 10^{14} \text{ W/cm}^2$.

Figure 5-10 shows the incident laser intensity dependence of harmonic light obtained in Fig. 5-7. Closed and open triangles correspond to the points before the laser peak and after the laser peak, respectively. The points are following hysteresis locus and the scattered light intensity is lower before the laser peak than that after laser peak at the same laser intensity. If this may be also due to the collisional dumping, electron temperature before the laser peak is lower than that after the laser peak. Then the collisional damping rate before laser peak will be higher than that after laser peak.

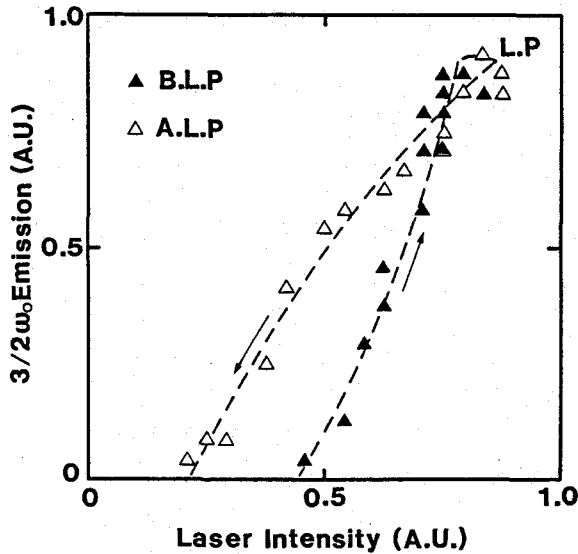


Fig. 5-10 Incident laser intensity dependence of three-half harmonic light obtained in Fig. 5-7. Closed and open triangles correspond to the points before and after the laser peak, respectively. The points are following hysteresis locus.

We also obtained the target material dependence of three-half harmonic lights. The scattered light intensity from CRYFAT ($Z=1.2$) was about 2 times higher than that from plastic target ($Z=3.5$). While Landau damping rate dose not depend on the atomic number, collisional damping rate increases with atomic number; $(\Gamma_p)_c = 7 \times 10^{11}$ for $Z=1.2$ and $(\Gamma_p)_c = 2.0 \times 10^{12}$ for $Z=3.5$ at 1 keV electron temperature.

From the above experimental results and discussion we can conclude that in this experimental condition collisional damping dominantly affects the TPD instability.

5-2-3-3 spectral shape of SRS

The threshold for convective SRS in a plasma where damping dominates the effect of inhomogeneity is ^[17]

$$\gamma_{oi}^2 / v_1 v_2 > 1, \quad (5-12)$$

in which γ_0 is the homogenous growth rate of SRS and is given by

$$\gamma_{0i} = \frac{1}{4} \cdot v_{osc} k_{epw} \left(\frac{\omega_{pe}^2}{\omega_s \omega_{epw}} \right)^{1/2}, \quad (5-13)$$

where v_{osc} is the oscillating velocity of an electron in the laser light. In practical units, $v_{osc}/c = 0.01(I_{14}\lambda_\mu^2/1.35)^{1/2}$, where I_{14} and λ_μ are the intensity and wavelength of the laser light in units of 10^{14} W/cm² and microns. The damping rates of the scattered-light wave and the plasma wave are ν_1 and ν_2 , respectively, where $\nu_1 = (\Gamma_p)_c(\omega_{pe}^2/\omega_s^2)$ and $\nu_2 = (\Gamma_p)_c + (\Gamma_p)_c$. If Eq. (5-13) is not satisfied, then SRS will not grow, independent of the actual density profile. Once Eq. (5-13) is satisfied, the amplitude and scaling of SRS will depend upon the actual density profile and upon the consequent absolute or convective character.

From Eq. (5-11) the collisional damping rate decreases substantially as density decreases or scattered light wavelength increases. As a result, collisional damping can produce an upper limit to the density at which SRS grows, which would correspond to a long wavelength limit on the observed spectrum. Collisional damping can limit SRS in two other ways. First, the scattered-light wave may be significantly absorbed before it escapes the plasma. The second additional effect of collisions is absorption of the laser light wave before it reaches the resonant point for SRS. Landau damping affects only the electron-plasma wave produced by SRS. Then the shorter-wavelength cutoff in the Raman spectrum is generally attributed to Landau damping.

Concerning the long wavelength cutoff of SRS spectra in the experimental results (980nm for CRYFAT 940nm for CD plastic target) in Fig. 5-3, we introduce the collisional damping. In such density region (980nm) Landau damping is smaller than collisional damping. The threshold is estimated for collisional damping of convective amplification by SRS in a uniform plasma^[18] to be

$$\frac{v_{ei}}{\gamma_0} = 2 \left(\frac{\omega_s}{\omega_{pe}} \right) = 3.3, \quad (5-14)$$

for 980nm wavelength and electron temperature of 1 keV at the laser peak using Eqs. (5-1)-(5-5). If the damping is above the threshold given by Eq. (5-14), then no SRS amplification will occur, as the SRS is damped within one gain length. For CRYFAT ($Z=1.2$) the damping (v_{ei}/γ_0) is estimated to be 1.72 and 5.03 for CD plastic target ($Z=3.5$) using Eqs. (5-1)-(5-5), (5-10), and (5-13). The damping of higher-Z material is larger than that of lower-Z material. Then the damping for CD target is higher than the threshold(3.3) but the damping for CRYFAT is lower than the threshold. Hence we could not observe SRS signal for CD target while obtained the signal for CRYFAT at the wavelength of 980 nm.

Next we consider the short-wavelength cutoff of SRS spectra in the experimental results. If only Landau damping affects the short-wavelength limit as temperature or laser intensity increases, the cutoff wavelength increases by Landau damping.^{[5], [19]} However our results are contrary results as shown in Fig. 5-4, namely the cutoff wavelength increases with decrease of laser intensity. Similar results were obtained in one pulse; short wavelength cutoff was minimum at laser peak as shown in Fig. 5-2. When Landau damping dominantly affects the entire SRS, the spectral peak should also shift to the longer wavelength with increase of electron temperature.^{[5], [19]} However the spectral peak was almost constant even with the laser intensity changing from 3×10^{14} W/cm² to 5×10^{14} W/cm² or target materials (CD plastic or CRYFAT). These experimental results indicates that in this experimental condition temperature is not a drastically changing parameter so as the Landau damping.

Then we introduce the alternative explanation by enhanced incoherent Thomson scattering^{[20], [21]}. In this model by A. Simon et al.^[20], transient pulses of hot electrons are produced by a local instability elsewhere; such as TPD instability or the absolute SRS instability at the quarter critical point. These pulses then move through the rest of the corona. The resultant transient electron velocity distribution, which will have a positive slope near

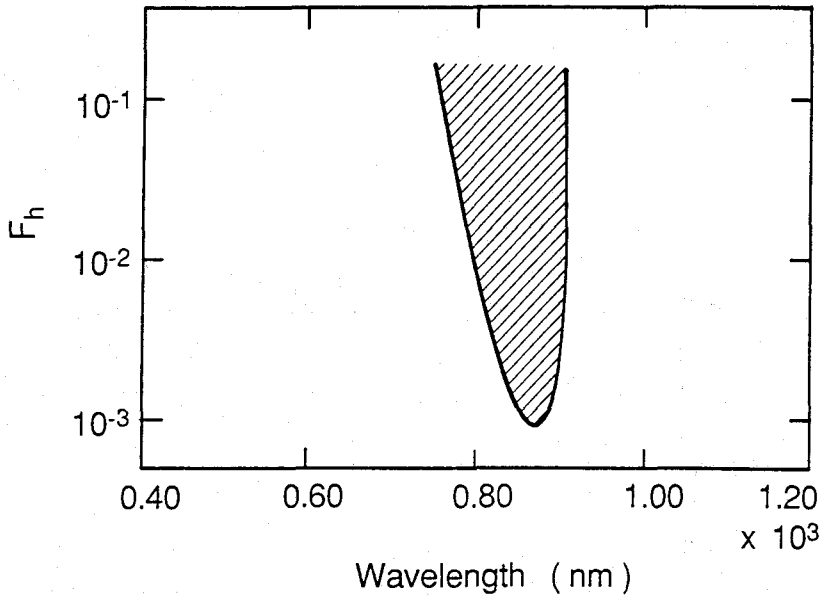


Fig. 5-11 The wavelength bands of enhanced scattered SRS as a function of F_h , the ratio of the number density of fast electrons to the number density of the background plasma. $T_e = 2\text{keV}$, $\lambda_0 = 527\text{nm}$, and target atomic number $Z = 3$. [see Ref. 21]

the directed velocity of the pulse, can then give rise to greatly enhanced Thomson scattering.

Figure 5-11 shows the variation of wavelength bands for enhanced convective SRS with fraction of hot electrons produced by a local instability^[21]. The width of SRS spectra increases with hot electron fraction decreasing of only short-wavelength cutoff. Although we should note that the spectral region and its width also depend on the hot electron temperature, we assume that hot electron temperature does not change so much. When the laser intensity increases hot electrons by TPD instability also increase because three-half harmonic scattered light strongly increases as shown in Fig. 5-7. Hence the spectral width for slightly high laser intensity would be wider than that of lower laser intensity. In comparison of long wavelength cutoff of SRS spectrum between CD and CRYFAT, SRS for CRYFAT occurs at higher density than CD target because of its lower collisional damping. From three-half harmonic measurements, TPD

instability in CRYFAT tends to be occurred compared with plastic target because of collisional damping. These result may imply that hot electron fraction from near the quarter critical point in CRYFAT is larger than that in CD target. Thus spectral width for CRYFAT may be wider than that of CD target.

5-2-3-4 heating by SRS and TPD instabilities

From hard x-ray spectrum in Fig. 5-8, high energy electrons are produced with temperature of about 12-14 keV. One of important mechanisms to produce such hot electron may be resonance absorption. When electric field of laser light resonant with electron plasma waves, the large electric fields produce accelerated electrons. Previous works on this energetic electron through resonantly excited plasma waves have presented the laser parameter scaling of hot electron temperature with particle simulations. From this scaling we can roughly estimate the temperature of hot electron by resonance absorption to be about 3.5-4.3 keV at this experimental condition. This value is too low to explain the experimental result on super-hot component (12-14keV) by resonance absorption.

Both TPD and SRS instabilities produce electron plasma waves and can create for fast electron production. Whether produced by wavebreaking or trapping, the temperature T_{SH} of the electrons would be expected to be crudely:

$$T_{SH} = \frac{1}{2} m_e v_\phi^2, \quad (5-15)$$

where m_e is the electron mass and v_ϕ is the phase velocity of the plasma wave ($v_\phi = \omega_{epw}/k_{epw}$).

Using Eqs. (5-1)-(5-5) and (5-15), the temperature of energetic electrons by SRS is estimated. Figure 5-12 shows the SRS heated electron temperature and scattered light frequency versus plasma density for thermal electron of 1 keV.^[23] Taking account of experimental results on spectra, SRS would produce the energetic electron of the temperature above 10 keV in this experiment.

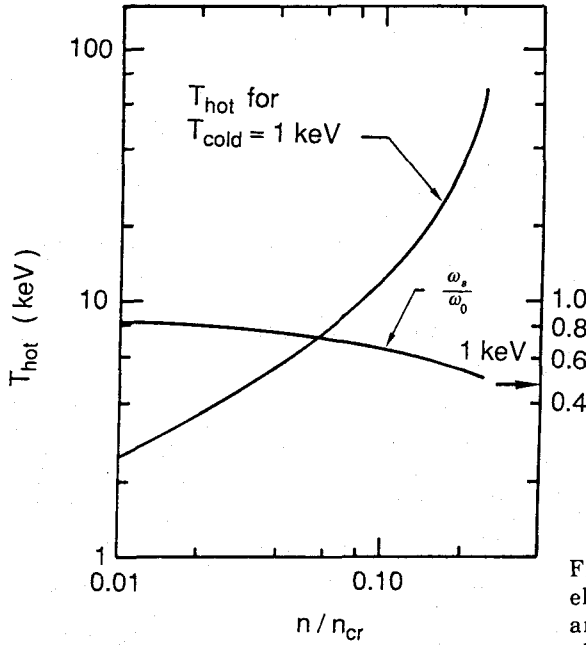


Fig. 5-12 Raman-backscatter-heated electron temperature from Eq. 5-15 and scattered light frequency vs plasma density for the cold electron temperature of 1 keV.

The temperature of energetic electron due to TPD instability is also similarly derived from Eq. (5-15) to be 7-10 keV for thermal electron temperature of 1 keV. The temperature scaling of hot electron by TPD from simulation have been previously presented as

$$T_{SH} = 90 (I_L \lambda_L^2)^{1/3} (T_e / 3)^{1/2} \quad (\text{keV}) \quad , \quad (5-16)$$

where I_L , λ_L , and T_e are in the units of 3×10^{14} W/cm², μm , and keV, respectively. From this scaling the temperature is estimated to be 8-17 keV when we assume $T_e = 0.5$ keV at 1×10^{14} W/cm² corresponding to the start point of harmonic light and $T_e = 1$ keV at 4×10^{14} W/cm² corresponding to the laser peak as shown in Fig. 5-7.

The above estimation indicates that hot electron with 12-14 keV temperature was produced by SRS and/or TPD in this experimental condition.

5-2-4. Summary

We studied nonlinear laser-interaction with low-Z and low-density target with CRYFAT. Measurements are side and back-SRS and three-half harmonic scattered light due to TPD instability.

TPD and SRS thresholds in CRYFAT were reasonable compared with simple theoretical scaling. At laser intensities below 4×10^{14} W/cm², the amount of SRS energy become less than 0.1% of incident laser energies and should have a negligible effect for implosion performance. Unless CRYFAT is enough to be filled with D₂, fine foam structures in target work as initially-imposed density perturbations and enhance SRS fraction with drastic spectral modulation. Energetic electrons with 12-14 keV temperature were also measured with hard x ray spectra, which was produced by SRS and/or TPD.

From intensity and target material dependence of three-half harmonic scattered light, TPD was affected mainly collisional damping in this experimental conditions. The scattered light intensity from CRYFAT ($Z=1.2$) was about 2 times higher than that from plastic target ($Z=3.5$).

SRS spectral width increased as the target atomic number decreases and the laser intensity increases. Long-wavelength cutoff (high density region) in spectra was controlled by the collisional dumping. Short-wavelength cutoff in SRS spectra was not explained fully by Landau damping. Enhanced Thomson scattering may explain the short wavelength cutoff. This scattering is due to the hot electrons produced by a local instability elsewhere such as TPD instability and/or the absolute SRS instability at the quarter critical point.

§5-3. Laser-Driven Shock Wave in Low-Density Porous Target

In low density porous targets proposed especially for an ablator and/or a follow shell in inertial confinement fusion, ^{[1],[24]} it is crucial for a high gain implosion to reveal details of shock waves. In this section we present an extensive study of the laser-driven shock wave in CD porous targets by using an x-ray streak shadowgraphy.

When the absorbed intensity changes in time, the ablation pressure changes accordingly. The time dependent pressure generates successive shock waves during the laser irradiation, resulting to create two parts in the shock compressed region: (i) a pile-up zone in the rear portion of the shock wave where the incoming shock waves from the ablation surface pile up, and (ii) a steep shock front portion which is the front part of the shock wave propagating into the solid material ahead of the pile-up zone.^[25]

There have been many experimental studies on the laser-driven shock waves, which were carried out using a visible-shadowgraph method with transparent targets ^[26] and shock break-through measurements with thin foil targets.^{[27],[28]} Most of them were based on the measurements of only shock front and were not possible to measure the pile-up zone. Even with the thin foil techniques, it is difficult to investigate the pile-up zone without a rarefaction effect since after the shock break through the rarefaction wave overtakes the pile-up zone from the target rear side and the temperature and the density must be changed.^[29] There are few experimental studies of the transient shock waves including the pile-up zone. Such detailed shock study ours gives assessments of the preheat in the shell as well as the shell dynamics depending on the time of shock break through in ICF.

5-3-1. Experimental set up

The experiments were carried out with use of the Gekko XII twelve beam laser system. The second harmonic (527nm) of Nd-doped glass laser light was used with a temporally Gaussian pulse of 900 psec full width at half maximum (FWHM). The temporal profile of the incident second harmonic light was monitored with an optical streak camera.

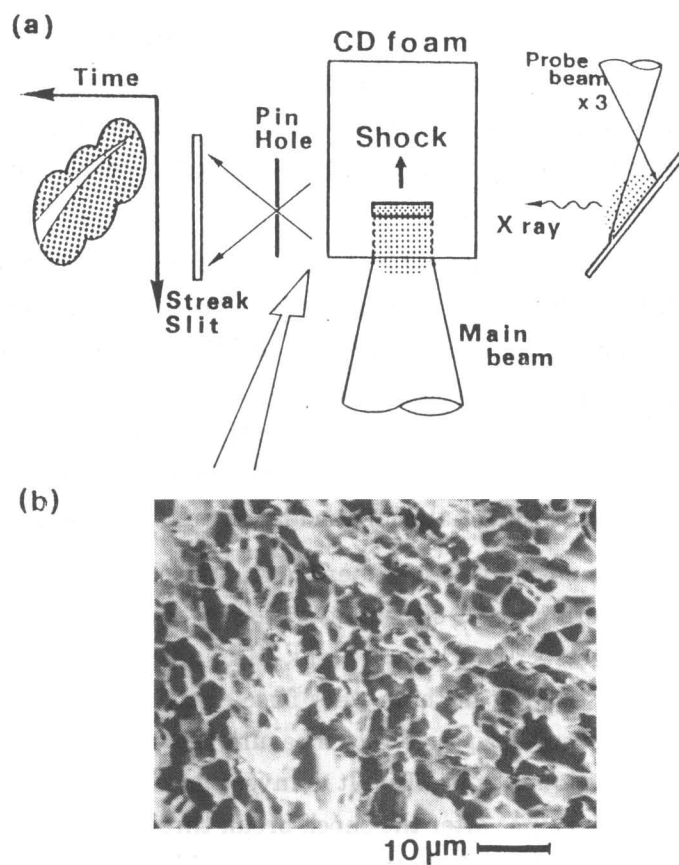


Fig. 5-13 (a) Experimental configuration for measuring shock trajectories. Main beam was focused on CD porous targets with the averaged-mass density of 0.1g/cm^3 and 0.2g/cm^3 at a laser intensity of $3.3 \times 10^{14}\text{W/cm}^2$. Only one backlighting beam is shown in the figure, while three beams were used at slightly different timing and positions. Probe x rays were imaged onto the entrance slit of an x-ray streak camera such that the shock propagation was along the slit direction. (b) A typical SEM picture of used CD porous target. Each cell size is several microns.

In Fig. 5-13(a) shown is the experimental arrangement directly to measure a shock trajectory in a solid target with x-ray streak shadography. One beam of the Gekko XII was focused on a surface of CD($[\text{C}_8\text{D}_8]_n$) foam slab target ($1.2 \times 1.2 \times 2.0\text{ mm}$) at normal incidence in order to drive a shock

wave. The incident laser intensity was 3.3×10^{14} W/cm² at a spot diameter of 500 μ m. Other three beams were focused on a palladium(Pd) plate at the intensity of 10^{15} W/cm² to produce x-ray sources for the backlighting. Each beam was temporally delayed (-0.5, 0, and +1 nsec delay) compared to the main beam and was focused at slightly different positions to diagnose the moving shock trajectory in the foam target.

X rays from Pd plasmas illuminated a foam target in the direction perpendicular to the main beam axis. The transmitted probe x rays were imaged onto the entrance slit of an x-ray streak camera through a 10 μ m pinhole such that the shock propagation was along the slit direction. The temporal resolution of this system was 80 psec. A gold photo cathode was used for the x-ray streak camera with a 20 μ m Be filter. Taking account of the effective quantum efficiency of the streak photo cathode and Pd x-ray spectrum, the main photon energy of the detected x ray was about $3.1 \text{ keV} \pm 0.3$ which was emitted mostly from L-shell ions of Pd plasmas. The x-ray spectra from Pd plasma was monitored with a time-integrated crystal spectrograph.

Figure 5-13 (b) shows a picture of a typical CD foam target taken with a scanning electron microscope (SEM). 0.1 g/cm³ and 0.2 g/cm³ mass-density targets were used in the experiments. The targets were fabricated by a freeze-dry method.^[30] The average-mass density was estimated from the initial concentration of the CD polystyren in a solvent taking account of the volume shrinkage rate of 10% during the freeze-dry process. In this way the accuracy of the mass density should be within about 20 %.

Considering the temporal behavior of the shock wave induced by the ablation, it is important to know the time history of the absorbed laser intensity which should be coupled to the ablation pressure. The laser absorption was inferred from the difference between the incident and the scattered light energy. Time histories of back- and side-scattered light collected by the focusing lenses were measured with an optical streak camera in different shots, but at the same experimental conditions. The energies of the back- and side-scattered light were monitored with biplanar photo diodes at the same time. The total non-absorbed energy, by integrating the

scattered light energy over the solid angle, gives a target absorption of $70 \pm 10\%$ for both cases of the target mass density (0.1 and 0.2 g/cm^3).

In order to compare the experimental results, we used the one-dimensional Lagrangian hydrodynamic code HISHO which used LTE model and EOS (equation of state) with an averaged atom model.^[31] The code includes multi-group electron and radiation transport and other conventional physics. The electron thermal energy was transported using a flux-limited diffusion flux and the free-streaming flux. The initial density of a porous target was treated as a homogeneous mass density.

5-3-2. Experimental results

Figure 5-14 shows a typical streak shadowgraph of the target with the mass density of 0.1 g/cm^3 . The bright white region indicates the probe x rays transmitted through the target, whereas the oblique dark scar indicates the region where backlighting x rays have been absorbed in the high density region created by a shock and a compression wave via the laser ablation. The dark-scar (DS) region propagates into the target and the width broadens with time, indicating that well-defined planar shock wave is created by the laser ablation in the porous target. The bright (B-1) region in the front of the DS region is the unperturbed area. Assuming negligibly small preheat, about 80% of the probe x ray (3 keV) should be transmitted through the B-1 region over the distance comparable to the laser spot diameter. The rear bright (B-2) region is the ablated region via the electron thermal conduction where the electron temperature is above 100 eV and the x-ray transmittance should be about 100% in the laser spot area.

Figure 5-15 (a) shows the scanned intensity along the spatial axis of the streaked data [Fig. 5-14] at three different times (-250 , laser peak; 0 , $+250$ psec). When the relative x-ray intensities are evaluated, the degradation of the original intensities due to the finite pinhole size ($10 \text{ }\mu\text{m}$ in diameter) are considered. By a simply image transformation scheme, the the contrast of the image is corrected and is typically 1.5 times higher than the observed. From the 1-D simulation results spatial distributions of the relative x-ray intensity and the density compression ratio in the shock compressed region

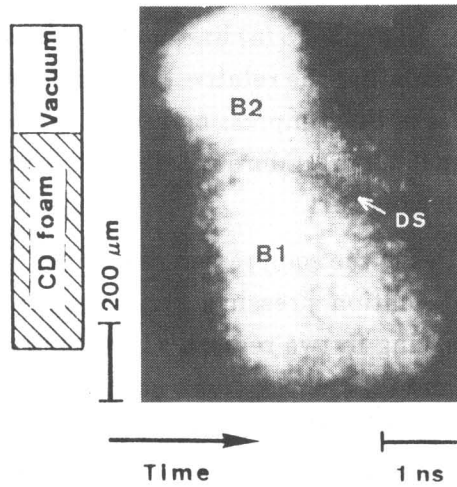


Fig. 5-14 Streak photograph (shadowgram) showing the shock-wave propagation in CD porous target with the mass density of 0.1g/cm^3 . Dark scar (DS) in a line corresponds to high density regions due to the shock wave. B1 and B2 means the bright regions at the front and the rear of the DS region, respectively.

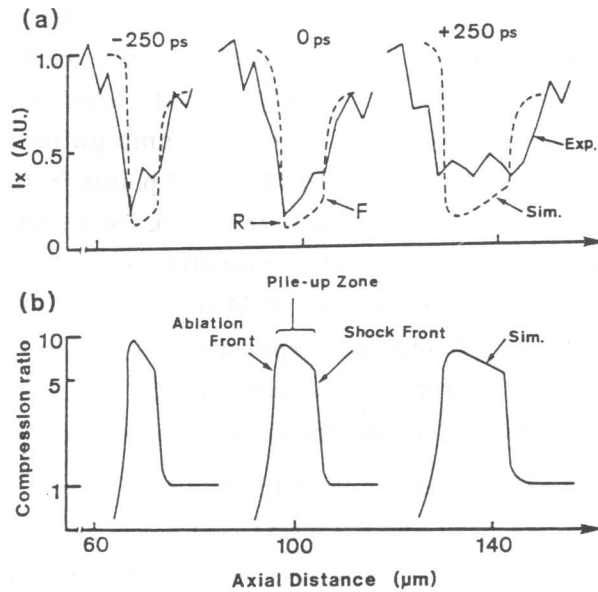


Fig. 5-15 (a) Cross cuts of the relative x-ray intensity at the DS region in Fig. 5-14 along the spatial axis at three different times (-250 , laser peak; 0 , $+250$ psec). F and R mean the front point rising sharply and the rear bottom point of the profiles, respectively. Solid line is from experiment, while dashed line from Simulation. (b) Spatial distributions of the density compression ratio at -250 , 0 , and $+250$ psec from simulation.

are shown as the dashed in Fig. 5-15 (a) line and as the solid line in Fig. 5-15 (b), respectively. In calculating the relative x-ray intensity, it was assumed that the lateral distance of the compression region in the target is equal to the laser spot diameter (500 μ m). More details of the simulation condition will be presented in following part.

The simulated profiles of the compressed region indicates that the shock wave induced by the ablation pressure arrives at the rear side of the compression wave, resulting in two regions : (1) a multiple shock or pile-up zone at the rear side, and (2) a shock front propagating into the material ahead of the pile-up zone. In the x-ray intensity profiles [dashed lines in Fig. 5-15 (a)] from the calculation, the front portion rising sharply (F) and the rear bottom point (R) correspond to the shock front and the density maximum in the pile-up zone in Fig 5-15 (b), respectively in each time step. The opacity near the R point (ablation region) changes abruptly where the density drops and the temperature increases rapidly.

Compared the experimental intensity profiles to the calculation, the experimental ones are quite close to the calculation except the intensities. The profile from the experiment is broadened with time as well as the ones by the calculation. Though there are some ambiguity of the absolute intensities, it is quite possible that the F and R points in the experiment [solid lines in Fig. 5-15(a)] correspond to the shock front and the rear part of the pile-up zone, respectively. The intensity profile due to the finite resolution in the imaging system may affect the intensities to be reduced as mentioned earlier. A 3-dimensional expansion of a shock wave may also be responsible since the discrepancy increases of the width of the intensity profile between the calculation and the experiment with time lapse.

Figure 5-16 shows the positions of the F and R points versus time for targets with densities of 0.1 and 0.2 g/cm³. At early time of the laser pulse the F and R points are accelerated but after about laser peak the F point become a steady state for both target density. At early time of the laser pulse, the ablation pressure is increased with laser intensity and time, resulting that the compression wave is accelerated.

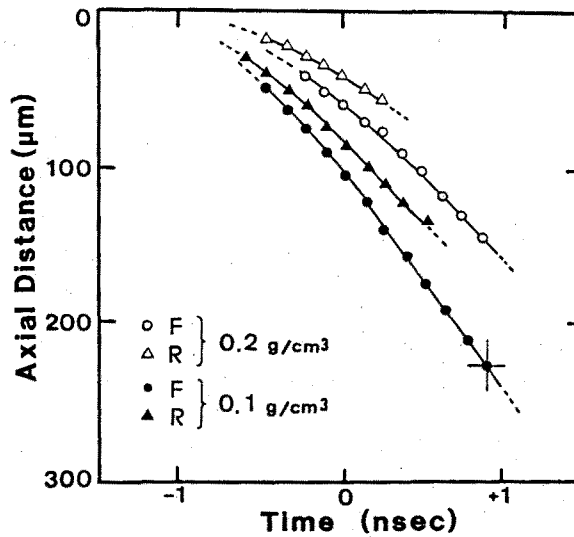


Fig. 5-16 Shock wave positions (F and R points) vs. time for two different mass-density target of 0.1g/cm^3 and 0.2g/cm^3 . Open circles and triangles are R and F points for 0.2g/cm^3 -density targets. Closed circles and triangles are R and F points for 0.1g/cm^3 -density targets.

The distance between the R and F points is expanded as they propagate deeper into the target (this expansion is also seen in Fig. 5-14 and Fig. 5-15). The velocity of the F point is higher than the R point. When the ablation pressure increases (case A), the virtual piston (say ablation front) creates the pile-up zone by multiple shock waves and the density should be highest in front of the piston. The shock front runs ahead of the pile-up zone, its speed being typically higher than the piston. After the maximum of the ablation pressure i.e. after laser peak (case B), the shock-front velocity becomes steady until the rarefaction wave catches up. At this time the rear of the pile-up zone begins decelerating because of the rarefaction. In either case of A or B, the velocity of the rear part of the pile-up zone is generally lower than the shock front.^[33] Consequently the difference of the velocities between the shock front and the pile-up zone causes the broadening of the compression wave. From these propagation characteristics (Fig. 5-16) and the intensity

profiles (Fig. 5-15), the R and F points are identified with the rear part of the pile-up zone and the shock front, respectively.

At the steady states, the shock front velocities of 0.1g/cm³- and 0.2g/cm³-targets are 1.5×10^7 and 1.1×10^7 cm/s, respectively. Here the absorbed laser intensities for the different mass-density targets were same within $\pm 8\%$. From these experimental results the dependence of the shock-front velocity (v_f) on the target mass density (ρ_0) is deduced to be $v_f \propto \rho_0^{-0.6}$. Theoretical scaling of a shock front velocity at a steady state is simply from the equation of mass and momentum conservation across the shock front as

$$v_f = \left(\frac{P_f}{\rho_f - \rho_0} \right)^{1/2} \cdot P^{1/2} \cdot \rho_0^{-1/2}, \quad (5-17)$$

where P , ρ_0 , and ρ_f are the pressure, the initial density, and the compressed density by the shock wave, respectively. The scaling from the 1-D simulation was same as the theoretical one. These results prove also that a fairly planar and uniform shock wave within the focal spot is created in the porous target and can be treated as a fluid based on the average density at our experiment.

5-3-3. Model for data analysis

With the above x-ray shadowgram, we can obtain the opacity and the velocity of the shock front and the pile-up zone. In general, the opacity(τ) is a function of temperature (T_e) and density (ρ) as $\tau = f(T_e, \rho)$. Inferring the temperature, we can estimate the density with some function of the opacity and the pressure (P) by applying an EOS such as a relation of $P = g(T_e, \rho)$.

A pure shock wave satisfies the Hugoniot relation in a steady state. With an acceleration of a shock front, the front may not completely satisfy the Hugoniot relation. However considering an infinitesimal time interval abrupt changes of the shock front parameters are small during the short interval. Then we can treat the shock front with an acceleration in a quasi-steady state. Between ahead and behind the shock front, the pressure jump is large enough ($P_f/P_0 \gg 1$) and the entropy changes suddenly. Further more

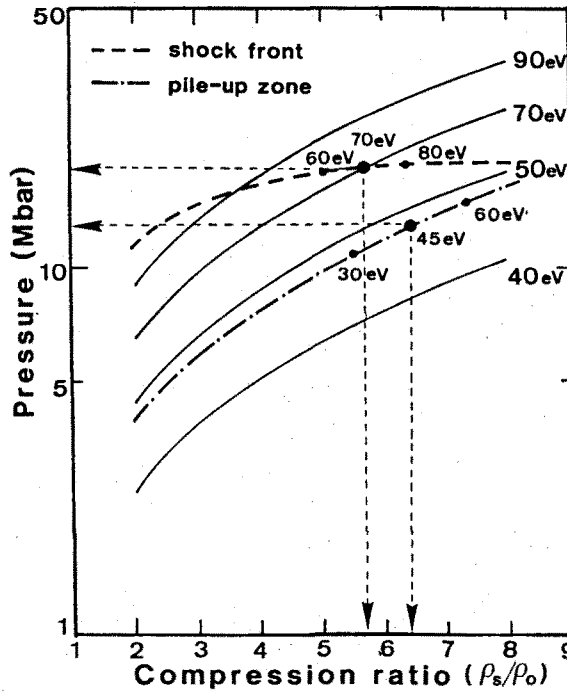


Fig. 5-17 Thermodynamic trajectories (lines) with various temperatures from AAM for CD material with 0.1g/cm³-mass density. Dotted and dot-dashed lines are given by Eq.(5-17) and Eq.(5-33), respectively. The temperatures expressed on the bold dotted and dot-dashed lines are obtained from the experiment (opacity).

the shock front here is always facing and propagating into the unperturbed region of solid material unless there is any anomalous energy transport before the shock. Then thermodynamic trajectory in the P - ρ plane of the front part is generally quite close to the Hugoniot condition. Thus we may apply the Hugoniot relation $P = h(v_f, \rho_f)$ of Eq.(5-17) for a quasi-steady state to the shock front (quasi-steady model). The five parameters (v_f , T_f , P_f , ρ_f and τ_f) in the shock front portion are related by the above three functions (f , g , and h). From the experiment we can obtain two parameters (v_f and τ_f). Using the above functions, we can estimate the other three parameters (T_f , P_f , and ρ_f).

Figure 5-17 shows the calculated results of EOS (lines) with various temperatures obtained from the well-known averaged atom model (AAM)^[32] for CD material with 0.1 g/cm³ mass density. Dotted line indicates a trajectory according to Eq.(5-17) for the shock velocity obtained with the experiment (In this case $v_f = 1.5 \times 10^7$ cm/s is used for example). The temperatures expressed on the dotted line are given by the obtained opacity.

On this dotted line frame, the temperature increases with the compression ratio, since the opacity depends on the density. Assigning the cross point of the two curves with the same value of temperatures as the temperature, we have a unique solution for the pressure and the compression.

The rear portion, namely the pile-up zone, of the compression wave behaves quite differently compared to the shock front. The pressure and the density in the pile-up zone change successively in space and the entropy change is smaller than that of the shock front. The thermodynamic trajectory in a P-p plane of the pile-up zone should be somewhere between the Hugoniot and an adiabatic conditions and can be described as ^[25]

$$P(t) = P_0 \left(\frac{\rho(t)}{\rho_0} \right)^\alpha \quad (5-18)$$

For an adiabatic condition, α is equal to the adiabatic constant γ which is 5/3 for an ideal gas and Eq. (5-18) is the Poisson adiabatic equation.^[33] In the pile-up zone, α becomes larger than γ .

When a compression wave's motion has a constant acceleration, the time evolutions of the pressure and the density in the pile-up zone have been solved as shown in Ref. 25, 33. If the thermodynamic trajectory of the discontinuity from one Hugoniot curve to another, the instantaneous shock velocity is found as

$$v_s^2(t) = V^2(t-\Delta t) \frac{P(t) - P(t-\Delta)}{V(t-\Delta t) - V(t)} \quad (5-19)$$

where v_s , V , P are the shock velocity, the volume, and the pressure, respectively. For $\Delta t \rightarrow 0$, Eq. (5-19) is modified to

$$v_s^2(t) = -V^2(t) \frac{P(t)}{V(t)} = \frac{P(t)}{\rho(t)} \quad (5-20)$$

When compression wave motion has a constant acceleration , Eq.(5-20) is described

$$\frac{dP}{dt} = (at+v_0)^2 \frac{dp}{dt} \quad (5-21)$$

Substituting Eq. (5-18) into Eq. (5-21), we obtain the time evolution of the pressure and density

$$\rho(t) = \rho(0) \left[1 + \frac{at}{v_0} \right]^{\frac{2}{a-1}}, \quad (5-22)$$

$$P(t) = P(0) \left[1 + \frac{at}{v_0} \right]^{\frac{2a}{a-1}}, \quad (5-23)$$

Equations (5-22) and (5-23) yield

$$P(t) = \frac{P(0)}{\rho(0)} v_0^{-2} (v_0 + at)^2 \rho(t) \quad (5-24)$$

Assuming a thermodynamic relation $P = p[\rho(t)]$, the time derivatives satisfy $\dot{P} = (\delta p / \delta \rho) \cdot \dot{\rho}$, and Eq. (5-21) yields

$$\frac{\delta p}{\delta \rho} = (at+v_0)^2 \quad (5-25)$$

Partially differentiating Eq. (5-18), Eq. (5-25) is modified to

$$a \frac{P_0}{\rho_0^a} \rho(t)^{a-1} = (at+v_0)^2 \quad (5-26)$$

Using Eqs. (5-18) and (5-26) for $t=0$ we obtain the relation

$$\frac{P(0)}{\rho(0)} v_0^{-2} = \frac{1}{\alpha} \quad (5-27)$$

Above treatment is not satisfied for a deceleration phase of the velocity. However assuming that the velocity of the pile-up zone v_s is equal to a piston velocity U_p which creates shock wave or rarefaction wave, above results can be extended to deceleration condition. In the piston model the change of the piston velocity creates the discontinuity of the pressure and the density at a front of piston as

$$U(t) - U(t-\Delta t) = j \left\{ [P(t) - P(t-\Delta t)] \left[\frac{1}{\rho(t-\Delta t)} - \frac{1}{\rho(t)} \right] \right\}^{\frac{1}{2}} \quad (5-28)$$

where $j = \pm 1$ i.e. positive or negative. When $j = +1$, Eq. (5-28) indicates that a piston is accelerated and a compression wave is created. When $j = -1$, a piston is decelerated and rarefaction wave is created. Anyway for $\Delta t \rightarrow 0$, Eq. (5-28) is modified to

$$\left(\frac{dU}{dt} \right)^2 = \rho(t)^{-2} \frac{dP}{dt} \frac{d\rho}{dt} \quad (5-29)$$

Using Eqs. (5-18) and (5-29), we obtain

$$\frac{dU}{dt} = A \rho(t)^{\frac{\alpha-3}{2}} \frac{d\rho}{dt} \quad (5-30)$$

Equation (5-30) gives similar results on the time evolution of the pressure and the density compared to Eq. (5-22) and Eq. (5-23) as

$$\rho(t) \propto U(t)^{\frac{2}{\alpha-1}}, \quad (5-31)$$

$$P(t) \propto U(t)^{\frac{2\alpha}{\alpha-1}}. \quad (5-32)$$

Then even in the piston model we can obtain the same function among the pressure, the density, and the velocity as Eq. (5-24). Whereas one can obtain the temporally changing pressure of the pile-up zone as a function of the density and the velocity as

$$P(t) = \frac{P(0)}{\rho(0)} v_0^{-2} (v_0 + at)^2 \rho(t) = \frac{1}{\alpha} v(t)^2 \rho(t), \quad (5-33)$$

where $P(0)$, $\rho(0)$, and v_0 are the pressure, the compressed density, and the velocity at a given time $t=0$. This feature is satisfied not only at the pile-up zone but also at the shock front portion at an acceleration phase.

If we take $v(t)$ in Eq. (5-33) as the shock-wave velocity, Eq. (5-33) is satisfied only for an acceleration phase and not for a deceleration phase or a rarefaction wave. However as shown in Fig. 5-15 the R point in the pile-up zone is quite close to the ablation surface which works as a piston producing a shock wave. Then it is reasonable to assume that the velocity of the R point is almost equal to the piston velocity. In this assumption Eq. (5-33) is extended also to a deceleration phase extensively as above discussion. Therefore even if the portion follows with a variable acceleration or deceleration, we are able to use Eq. (5-33) for quasi-constant acceleration or deceleration within an infinitesimal-time interval (quasi-constant acceleration model). Using Eq. (5-33) and EOS we can estimate the pressure, the temperature, and the compression of the R point from the obtained velocity and the opacity data for a quasi-acceleration model.

Dot-dashed line in Fig. 5-17 is given by Eq. (5-33) for definite velocity and α . As shown in Fig. 5-17 the temperature can be given uniquely within 10% accuracy from the obtained opacity for the same reason as the above.

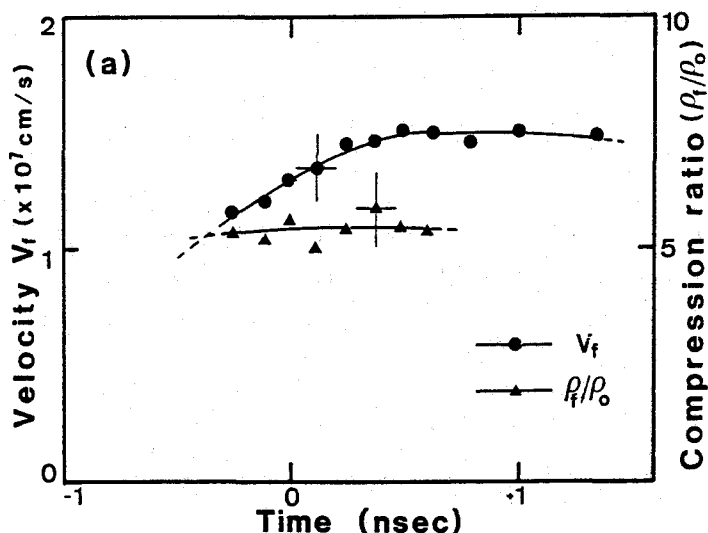


Fig. 5-18 (a) Temporal behaviors of F-point (shock-front) velocity (v_f) and compression ratio (ρ_f/ρ_0) to the initial density for 0.1 g/cm³ density target. Closed circles and triangles are v_f and ρ_f/ρ_0 .

5-3-4. Discussion

5-3-4-1. shock front property

Figure 5-18(a) shows the temporal behaviors of the shock front velocity and the compression ratio of the shock front density ρ_s to the initial density ρ_0 for 0.1 g/cm³ density target. The time histories of the temperature and the pressure at the shock front are shown in Fig. 5-18(b). These parameters are evaluated with the quasi-steady model.

Two phases are clearly seen in Fig. 5-18(a) or in the time history of the shock front velocity: (i) a phase of acceleration, and (ii) a phase of constant velocity. The acceleration of 5×10^{15} cm/s² develops until about 500 psec after the laser peak and finally the velocity of 1.5×10^7 cm/s is attained during the constant-velocity period. If the shock front would behave as a single shock wave satisfying the Hugoniot relation, there should be no acceleration of the shock front. Thus we have to deduce the shock parameters of an acceleration

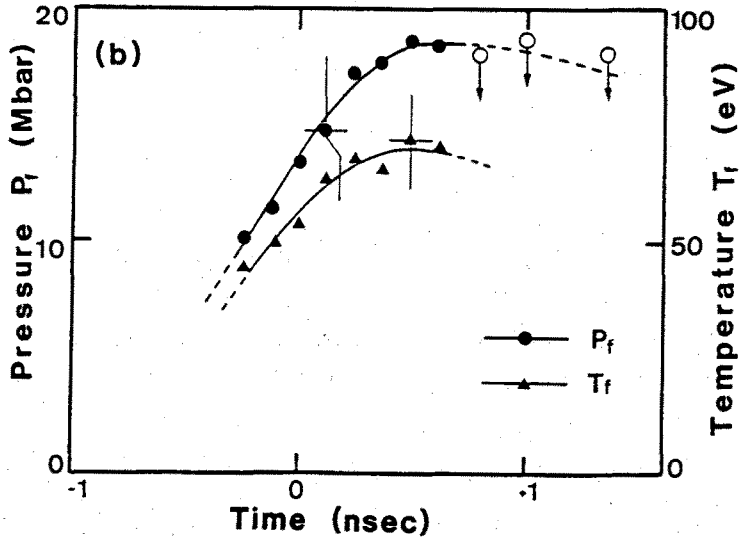


Fig. 5-18 (b) Time histories of the temperature (T_f) and the pressure (P_f) of F point. Closed circles and triangles are P_f and T_f . Open circles are implied for the compression ratio of 5.5 and indicate the maximum limit.

phase from the quasi-constant acceleration model. However the pressure deduced from the quasi-constant acceleration model [Eq. (5-33)] is similar to that from the quasi-steady one [Eq. (5-17)] within 10 %. Then the exponent α in Eq. (5-18) which indicates the thermodynamic property in P - ρ plane was more than 7. Here α can be estimated by Eq. (5-27). Time history of the compression ratio indicates that the compression ratio is almost constant to be about 5.5 in the acceleration. Even during an acceleration phase, the thermodynamic condition in of the shock front is close to the Hugoniot curve in the thermodynamic trajectories and is near the limitation of the strong shock condition ($P_s/P_0 \gg 1$). Thus the results of the pressures from both models and the time history of the compression ratio indicate that it is reasonable to apply the quasi-steady model in the shock front portion to this experimental condition.

The temperature and pressure at the shock front increase during the shock acceleration as shown in Fig. 5-18(b). The maximum pressure and

temperature become 19 Mbar and 72 eV, respectively at 500 psec after laser peak. In general the ablation pressure also increases with laser intensity but reaches its maximum at the laser peak. Such time delay of the peak pressure at the shock front is due to the finite traverse time from the ablation front to the shock front. More detail of this delay will be presented in the following discussion.

To show the applicability of the EOS model in our data processing, we estimate here the temperature using an EOS for ideal plasmas. In the observed temperatures and densities, the plasma at the shock front should be nondegenerate since the Fermi temperature is estimated to be about 10 eV, much smaller than the estimated electron temperature (50-70 eV) at the shock front.^[33] The ion coupling parameter Γ , which is the ratio of the screening energy to the thermal energy,^[35] is estimated to be $\Gamma \leq 1$ for the temperature $T_e \geq 50$ eV. These results may imply that the plasma at the shock front is close to the ideal plasma condition.^[34] For the ideal plasma approximation, the pressure is given by EOS in a partially ionized gas as,

$$P = P_e + P_i + P_r \approx n_i kT_i + n_e kT_e \approx \rho_s \left[\frac{(z+1)}{Am_p} \right] kT, \quad (5-34)$$

where P_e , P_i , and P_r are the electron, ion and radiation pressure, respectively. The radiation pressure is dropped here because the value is negligibly small (only 0.006% of the total plasma energy is estimated to be used for the radiation). Combining Eqs. (5-17) and (5-34), the temperature is given by the shock velocity as

$$kT = \left[\frac{Am_p}{(z+1)} \right] \frac{1 - 1/K}{K} v_s^2, \quad (5-35)$$

where $K = \rho_f / \rho_0$ (compression ratio). For $K=4$ ($\gamma=5/3$) the velocity of 1.5×10^7 cm/s leads us to estimate the temperature to be 77 eV at the average charge state of $Z=3$. If K is larger (for example 5.8, which corresponds to the maximum points of the compression ratio in Fig. 5-18(a)), the temperature becomes lower (59 eV) than the above value. This level of the temperature

(59~77 eV) is estimated with the assumption of the ideal plasma condition. The temperature above is quite consistent with the peak temperature (72 eV) in Fig. 5-18(b) where the information of the opacity is included. Thus it is proved that at this experimental condition the shock front is close to an ideal plasma condition.

5-3-4-2. Pile-up zone property

Figure 5-19 shows the temporal behaviors of the velocity, compression ratio, pressure, and temperature estimated from the quasi-constant acceleration model at the R point for 0.1 g/cm³-density target. It is found that there are two different phases in the time history of the velocity before and after about laser peak: (i) a phase of acceleration, and (ii) a phase of deceleration.

At the phase of acceleration, the compression[Fig. 5-19(a)], the temperature[Fig. 5-19(b)], and the pressure[Fig. 5-19(b)] increase with time. Though the compression at the shock front portion is almost constant to be 5.5 at the acceleration phase as in Fig. 5-18(a), the compression ratio at the R point changes from 5.7 to 7 and is larger than the value in the shock front region. At the R point, multiple shock waves are created where the incoming shock waves from the ablation surface pile up. This part has there a higher compression than the shock front portion. The exponent α in Eq. (5-18) indicating the thermodynamic property is from 2.5 to 4, whose magnitude is smaller than that of the shock front portion (≥ 7) and larger than adiabatic constant γ (5/3 for ideal gas). The compression at the pile-up zone is closer to an adiabatic condition than that in the shock front region and satisfied the approximate Hugoniot condition. The maximum temperature (57 eV) at the R point is lower than that (72 eV) of the shock front in spite of same magnitude of the maximum pressure in both region. This is also consistent with the adiabatic condition. At the pile-up zone, the successively increasing ablation generates weak shock waves and multiple shock waves piles up. Then the pressure at the pile-up zone gradually changes in an infinitesimal spatial interval and R point is compressed in small change of the entropy.

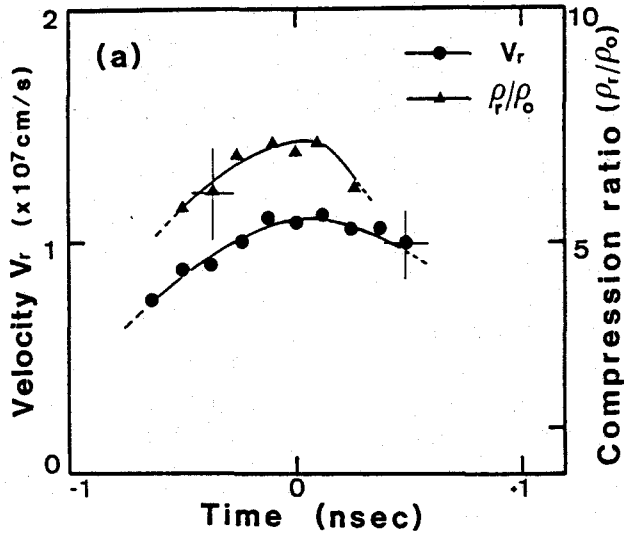


Fig. 5-19 (a) Temporal behaviors of R-point (pile-up zone) velocity (v_r) and compression ratio (ρ_r/ρ_0) to the initial density for 0.1g/cm³ density targets. Closed circles and triangles are v_r and ρ_r/ρ_0 .

At a deceleration phase, the density, the temperature, and the pressure decrease. Upon the decrease of the absorbed laser intensity, the pressure at the ablation surface drops. Then the rarefaction wave propagates into the target, eventually overtaking and attenuating the shock wave in the pile-up zone.

The pressure behavior at the R point in the pile-up zone is temporally different from that of the shock front. The temporal profile of the R-point pressure should be close to that of the ablation pressure since the R point is spatially close to the ablation front until 250 psec after laser peak as shown in Fig. 5-15. The ablation pressure generally depends on the absorbed laser intensity and is simply described as the scaling of $P_a \propto I_a^\beta$ where β is a constant and depends on the ablation model.^{[28], [36]-[38]} Absorbed laser intensity profile obtained from the experiment is shown also in Fig. 5-19(b) as a dot-dashed line. The first half of the absorbed laser intensity can be approximated with Gaussian 750 psec FWHM as

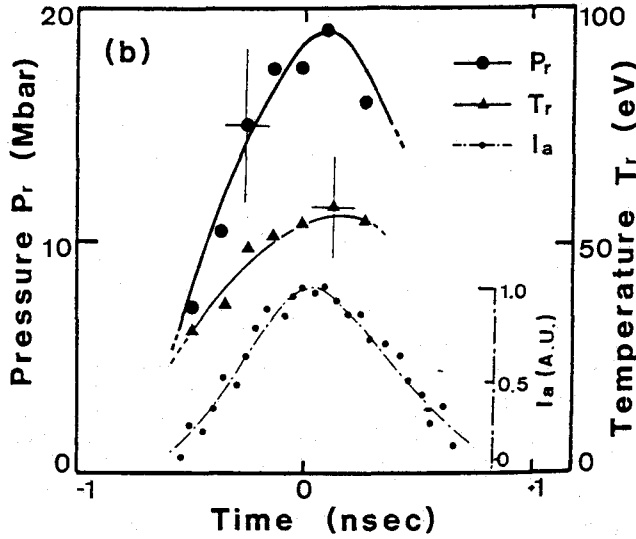


Fig. 5-19 (b) Time histories of the temperature (T_r) and the pressure (P_r) of R point. Closed circles and triangles are P_r and T_r . Small closed circles are relative absorbed laser intensity (I_a). The profile of dot-dashed line at first half is approximated with 750psec near Gaussian. Pressure profile of the solid line is given by Eq. (7) for $\beta = 0.55$ or $P_r(t) \propto I_a^{0.55}$.

$$I(t) = I_0 \exp \left[-4 \ln 2 \left(\frac{t(\text{psec})}{750} \right)^2 \right]. \quad (5-36)$$

Thus the pressure at the pile-up zone will be given by

$$P(t) = P_{\max} \exp \left[-4 \ln 2 \beta \left(\frac{t(\text{psec})}{750} \right)^2 \right]. \quad (5-37)$$

The data points are fitted with Eq. (5-37), using $\beta = 0.55$ as shown in Fig. 5-19(b) for a solid line drawn on the closed circles. The intensity dependence of the pressure is obtained to be $P \propto I_a^{0.55}$ from the figure. This scaling is in good agreement with the ablation pressure scaling reported in the previous

experimental results with plane targets.^[37] Thus we could conclude that the pressure characteristics at the R point reflect those of the ablation front.

5-3-4-3. energy transport in compressed wave

From the above data analysis of the shock front and the pile-up zone, 19 Mbar of the ablation pressure is attained. However 1-D simulation gives a peak pressure of 29 Mbar for the experimental condition here with the flux limiter $f=0.6$, where the predicted absorption in the simulation is in agreement with the measured one within the experimental error. Even with very limited flux of $f=0.03$, the predicted ablation pressure drops only to 26 Mbar, still much larger than measured one. The ambiguity of the observed x-ray intensity which stems from the degradation due to the finite spatial resolution may underestimate of the density and the pressure. Suppose that the observed x-ray intensity through the shock perturbed region is twice lower than the original transmitted intensity, the observed pressure rises to 25 Mbar. However this forced reduction of the x ray is beyond the experimental error. The reported scalings of the ablation pressure including lateral energy loss with planar targets or from small spot diameter experiments give a range of pressures from 12.4 Mbar to 18.5 Mbar at our experimental condition.^[37] The lateral heat loss is likely to be one of important factors to explain the discrepancy of the peak pressure between the experiment and 1-D simulation, though we have not checked this using 2-D simulations. If the code is run at 74% of the absorbed energy (namely the other 26% is assumed for the lateral energy loss), the shock trajectory from the simulation becomes in good agreement with the experiment. At this simulation condition, the peak pressure and compression ratio at the R point are 20~21 Mbar and 8.3~8.8, respectively, when the temperature is 55~60 eV. The simulated temperature is close to the experimental one (57 eV) while the compression from the experiment (7) is lower than the simulation.

From Fig. 5-18(b) and Fig. 5-19(b) the pressure profile of the F point is delayed compared with one of the R point and the time lag increases with time. The pressure at the F point maximizes at 500 psec after laser peak but the peak pressure at the R point appears only at 100 psec after laser peak. Such time lag of the peak pressure indicates the finite traverse time for the

shock propagation through the compression region. The temporal change of the time lag is due to the increase of the distance between the R point and the F point with time as shown in Fig. 5-15 and Fig. 5-16. In a moving frame of the shock compressed region between the F and R points, each one of multiple shock waves travels successively and adiabatically from the R to F points. Then the pressure information created at the ablation surface is transported to the shock front region with an order of the sound speed since in the limit of a weak shock the entropy change approaches zero $(P_1 - P_0)/P_0 \rightarrow 0$ and the wave speed is equal to the sound speed in the moving frame (between the R and F point).^[33] For this time lag (400 psec) and the traverse distance (25 μm) between F and R points, the corresponding speed is estimated to be 6×10^6 cm/s. This value is equivalent to the plasma temperature of 65 eV for a plasma with an average charge state $Z=3$. This averaged temperature between the F and R points at from +100 psec to +500 psec is in good agreement with the estimation of the temperatures as shown in Fig. 5-18(b) and 5-19(b). This agreement indicates that in the compressed region (pile-up zone) from the R to F points the entropy change is small and the thermodynamic condition is closer to the adiabat than the Hugoniot condition.

Finally we consider the fraction F_s of the absorbed energy used to sustain the shock wave. The energy flux I' resulting from the work done by the shock pressure P is $I' + PU$, where U is the fluid velocity behind the shock front which is deduced from the conservation of mass and momentum across the shock front as $U = (1 - 1/K)V_s$. Then F_s is identified with I' relative to absorbed laser intensity I_a as,

$$F_s = \frac{I'}{I_a} = \left(1 - \frac{1}{K}\right) \frac{P v_s}{I_a}. \quad (5-38)$$

For our measured conditions ($P=18\text{Mbar}$, $V_s=1.5 \times 10^7\text{cm/s}$, $K=5.5$, and $I_a=2.1 \times 10^{14}\text{W/cm}^2$), we obtain $F_s=10\%$. Other energy flux of the absorbed flux will be used for creation of axial thermal conduction, outward kinetic energy, and lateral heat loss.

5-3-5. Summary

Laser-induced shock wave propagation in CD porous targets was observed with an x-ray streak shadowgraphy.

The final shock-wave velocities were 1.5×10^7 cm/s and 1.1×10^7 cm/s for the targets with average-mass densities of 0.1 g/cm^3 and 0.2 g/cm^3 , respectively. The density scaling of the velocity was $v_s \propto \rho^{-0.6}$, which was in good agreement with a simple scaling from the Hugoniot relation. Such a result indicates that a pure shock wave was created in the CD porous target at our experimental condition.

The x-ray shadowgraphy shows clearly a shock formation in the porous targets, which is composed of two parts: a shock front and following a pile-up zone of multiple shock waves. Temporal histories of the temperature, the pressure, and the compression ratio at two different points were estimated from the measured shock velocities and the opacities using a quasi-steady model for shock front region and a quasi-constant acceleration model for the pile-up zone.

Maximum temperature and pressure at the shock front for 0.1 g/cm^3 target were estimated to be 70 eV and 19 Mbar, respectively. Maximum pressure in the pile-up zone was attained to the same magnitude (19 Mbar) as that of the shock front but the compression ratio (ρ/ρ_0) and the temperature (T_e) were higher and lower in the pile-up zone ($\rho/\rho_0 = 5.7 \sim 7$ and $T_e = 57 \text{ eV}$) than at the shock front ($\rho/\rho_0 = 5.5$ and $T_e = 72 \text{ eV}$).

Temporal profile of the pressure at the shock front differed from that of the pile-up zone. The pressure at the pile-up zone reached its maximum at about peak of the absorbed laser intensity. The profile indicated the absorbed laser intensity scaling as $P \sim I_a^{0.55}$ same as the reported ablation pressure scaling. However the pressure at the shock front was delayed and reaches its maximum at 400 psec after the peak of the pile-up zone pressure. This time delay was due to the finite traverse time of the shock from the ablation to the shock front. The time lag of the peak pressure between the shock front and the pile-up zone had a temperature information in the shock compressed region. Assuming small entropy change in the compressed region (pile-up zone), the temperature (65 eV) deduced from this time lag was

consistent with the result (57~72 eV) from the shock velocity and the opacity.

Comparing the shock parameters and the temporal profiles of the shock front and the pile-up zone, it is concluded that the pile-up zone followed a thermodynamic condition closer to the adiabat than the shock front.

§5-4. Energy Transport in Cryogenically Cooled D₂ Filled Foam Target

As shown in Chapter 2, preheat by high energy components of thermal electron distribution and shock wave may become important in low-Z and low-density targets: cryogenically cooled D₂ foam target (CRYFAT) ($Z=1.2$, $\rho=0.2\text{g/cm}^3$). In this section, energy transport in CRYFAT is studied by temporal resolved observation of the rear side emission with planar targets. This studies are not important only for ICF application but also for understanding the nonlocal electron transport in laser-produced plasmas as purely physical point of view.

Previous experimental studies ^[38] on nonlocal electron transport have been in a high temperature region (between ablation front and coronal region) and have been compared with flux limited diffusion model i.e., heat reduction by nonlocal effect. Little experimental study have been presented on preheat in cold dense region by nonlocal transport. It has been experimentally difficult to separate the preheat by shock wave and high energy electron with single foil technique. Even if shock heating is delayed using thick target, electron mean free paths in a target of Maxwellian tail ($2-3v_e$) are not long enough compared with the target thickness to heat the rear side of the target upto the observation level.

Using CRYFAT (low-density and low-Z target), it become easy to temporally separate the heating by high energy electron and shock heating. With the same areal density target, shock break-through time in a lower-

density target is longer from Eq. 2-9 and the electron mean free path in lower-Z target is longer as in Eq. 2-17 compared with medium-Z, high-Z and high-density targets. Then it becomes possible to separate the preheat by shock wave and electrons.

5-4-1. Experimental set up

Energy transport in low-Z and low density material was studied by illuminating the 527nm-laser light onto planar CRYFATs. Two beams of GEKKO XII laser system was used and the second harmonic (527nm) of Nd: glass laser light was focused on the target with a temporally Gaussian pulse of 900 psec full width at half maximum (FWHM). The incident energy was usually 650 J per beam and the average incident laser intensity on the target was 4×10^{14} W/cm² in the oval area of 600x700 μ m. The incident angles of both beams to the target normal was 32° at center axis of the laser light in the perpendicular plane. The polarization of two beams was different with 45°.

Figure 5-20 shows the schematic diagram of experimental arrangement. The visible emission from the rear side of the target was measured using a visible streak camera (S-20) with a schwarzschild microscope at an observation angle of 32° in the horizontal plane. The spatial resolution of the microscope was less than 2.5 μ m. Dichroic mirror (transmission was 80-90% and spectrally flat within $\pm 15\%$ between 250nm to 480nm) was set on the front of the microscope to cut the specular reflection of incident laser light (527nm). When spectrally resolved data were obtained, the relayed image with microscope was spatially collimated to be about 200 μ m ϕ in the center on target size and relayed to the spectrometer (F/250mm) slit by aluminum concave mirror. The spectral range and the spectral resolution was from 250nm to 400nm and several nm, respectively. Obtaining spatially resolved data, the images with the microscope was directly relayed onto the streak slit through the interference filter. The transmission response of the interference filter was 400 nm \pm 10nm (FWHM). The system spatial resolution was checked to be less than 5 μ m. The time resolution was

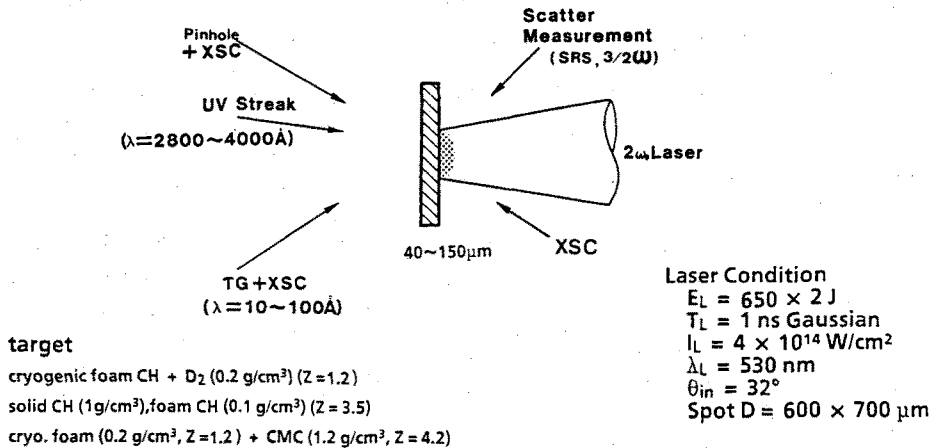


Fig. 5-20 The schematic diagram of experimental configuration. The rear side UV emission was measured with a visible streak camera coupled with a schwarzchild microscope at an observation angle of 32° in the horizontal plane. Side scattered measurements are the same with that in Sec. 5-2. XSC; x-ray streak camera, XSC+TGS; x-ray streak camera with a transmission grating spectrometer.

less than 50 psec. A time fiducial was introduced into the streak camera by an optical fiber which picked up a part of the other damped beam before the focusing lens. The spectral and intensity response of the system including the S-20 streak camera, microscope, filters and/or spectrometer were calibrated with a standard tungsten lamp so that a blackbody temperature could be assigned for the rear side emission.

In order to evaluate the x-ray contribution to the energy transport in low-Z plasmas, x-ray emissions from both sides of the target were monitored with x-ray streak camera. Side scattered light of SRS, and three-half harmonic scattered light were also measured to monitor the nonlinear laser interaction which may produce suprathermal electrons. Detail explanations of these scattered lights measurements are presented in Section 5-2.

The thickness of planar CRYFAT was changed from 40 μm to 150 μm . The thickness was controlled by varying the thickness of the polystyrene planar foam target which works as a supporting matrix. The planar foam

target was dipped into liquid deuterium and was then frozen in cryogenic shroud. Dipping the foam target in the liquid deuterium, extant bubbles in the porous target were driven out by boiling method.^{[30], [39]} Detailed explanation about cryogenic system is reported.^{[30], [39]} The foam targets were fabricated by freeze-dry method mentioned in Section 5-3. The average-mass density of the foam target was measured with the chemical balance and was typically 70 mg/cm³. The average-density of CRYFAT was estimated to be 0.21-0.23 g/cm³. The average atomic number and mass number were 1.2 and 2.39, respectively.

5-4-2. Experimental results

Figure 5-21 shows the typical time-resolved spectra from the rear side of CRYFAT with UV ($\lambda = 250\text{nm} \sim 400\text{nm}$) and soft x-ray streak ($\lambda = 90\text{\AA} \sim 10\text{\AA}$) cameras. Here the spectral responses for both emissions were not constant on these images. Time zero corresponding to the laser peak of the incident pulse was determined with a separate time fiducial for UV images. X-ray streak camera did not have time fiducial and emission peak of the 0th order was taken as the laser peak.

Both images of UV and soft x ray show the similar temporal history of intensity. The emissions strongly rose at near the laser peak and low intensity emission existed in the front of the strong emission. These temporal changes are explained in the next figure. The spectral profile in UV region was different with x-ray spectra.

Concerning x-ray spectra there were two components. A high energy component appeared at the time before laser peak and even higher component appears in earlier time. A low energy component appeared at near the laser peak. Spectral intensity was stronger at lower photon energy. These data suggest that the higher energy component is due to the transmitted x rays from the laser irradiated region and the observed x-ray intensity is the attenuated one through the target. While softer x-ray components from the front side are absorbed before the shock front because of its shorter mean free path. Then observed spectra will come from the shock

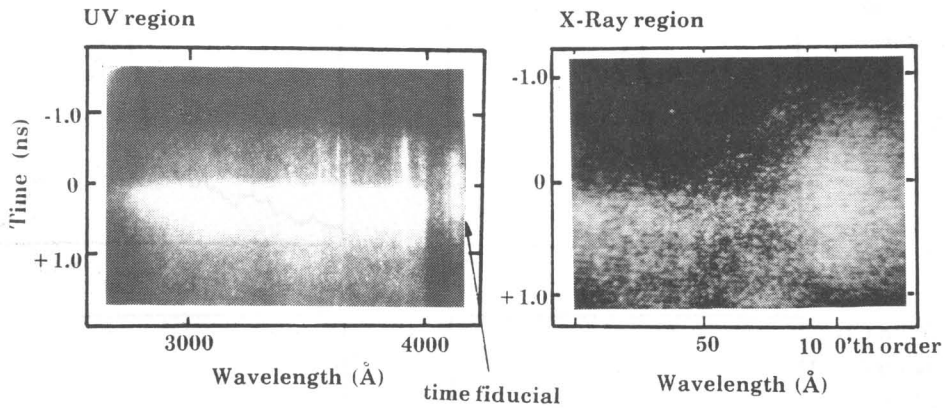


Fig. 5-21 typical time-resolved spectra from the rear side of CRYFAT with UV ($\lambda=250\text{nm}\sim400\text{nm}$) and soft x-ray streak ($\lambda=90\text{\AA}\sim10\text{\AA}$) cameras. Time zero corresponding to the laser peak of the incident pulse was determined with a separate time fiducial for UV images. X-ray streak camera did not have time fiducial. The emission peak of the 0th order was taken as the laser peak.

heated region and the spectral peak may exist at softer region. The shock heated temperature is implied to be several ten eV from such soft x-ray spectra.

UV spectra was fundamentally constant with time though in early time till about 500 psec before laser peak the spectra were slightly changed with time. Assuming the blackbody emission the spectra must be near constant above 4 eV between 250nm to 400 nm and the intensity increases linearly with temperature above 1 eV. In the visible emission region the opacity is large enough that blackbody emission is assumed. Then UV spectra indicate that the rear side temperature before several hundred psec of laser peak is several eV and the strong emission corresponds to several ten eV from UV intensity in this figure.

Figure 5-22 shows the temporal behaviors of visible (250-400nm) and soft x-ray (80Å) emissions from rear side of the CRYFAT ($\rho=0.23\text{g/cm}^3$) and normal density polystyrene target ($\rho=1.1\text{g/cm}^3$) with the same areal mass

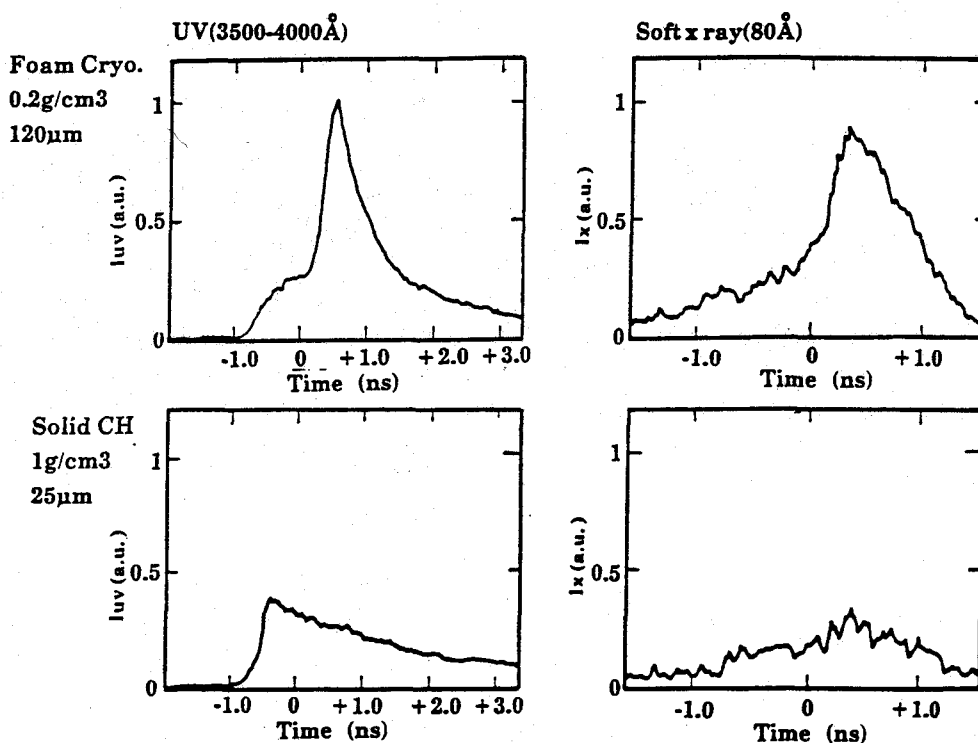


Fig. 5-22 Target material dependence of the temporal behaviors of visible (250-400nm) and soft x-ray (80Å) emissions. Used were CRYFAT ($\rho=0.23\text{g/cm}^3$) and normal density polystyrene target ($\rho=1.1\text{g/cm}^3$) with the same areal mass density ($\rho l=2.5\text{mg/cm}^2$).

density ($\rho l=2.5\text{mg/cm}^2$). The detection sensitivity was same for both cases. Both emissions of strong peak in visible and x-ray regions from CRYFAT were stronger than those from the polystyrene target by about factor 3 to 4.

CRYFAT signals of both visible and x-ray emissions showed the two separated signals; one was the first slow rise signal (FSR signal) at the front of the strong emission. Another was the second fast rise signal (SFR signal) whose rise time was about 150 psec in visible emission. However in normal density plastic targets we could not distinguish two signals but only observe slight fast rise signal with rise time of about 500 psec in visible light. Two components might be temporally combined.

For x-ray emissions from CRYFAT, the rise time of SFR signal was about

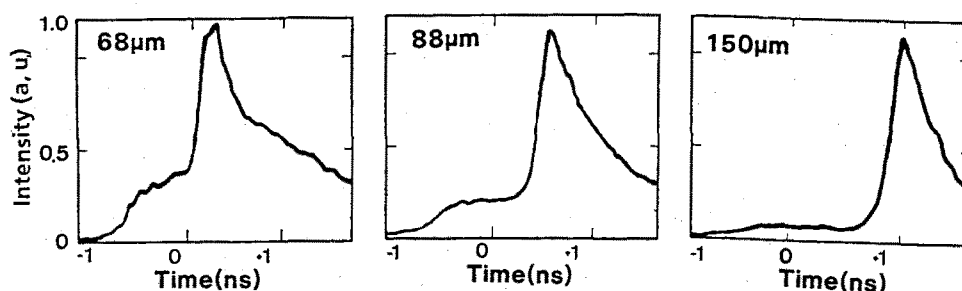


Fig. 5-23 Target thickness dependence of the temporal histories of the rear side UV emission from CRYFATs.

400 psec and longer than that for the visible emissions. This would be caused by effect of transmitted x ray. X-radiation has longer mean free paths than that of visible one. We observed the transmitted emission from inner region before heated region arrived the rear surface of the target. Then it may be misleading to estimate the temperature applying the blackbody emission to x-ray FSR signals.

In any way SFR signal clearly indicates that the rear side temperature of CRYFAT is about three or four times higher than that of plastic target because of the emissivity for both visible and soft x-ray region ($\lambda=80\text{\AA}$). Such temperature difference for SFR signals should stem from the initial density difference of factor 5. If the same energy is deposited and the ionization energy losses are neglected, the temperature will be different by the factor same as the density difference. Here we have to consider the ablation pressure difference by the absorption difference depending on the target atomic number. Absorption of normal density plastic target was measured to be about 1.5 times higher than that of CRYFAT with plasma calorimeters. Then the temperature by shock heating will be 3.8 times larger in CRYFAT than that in normal density plastic target.

Figure 5-23 shows the target thickness dependence of the temporal histories of the rear side UV emission from CRYFATs. The SFR signals

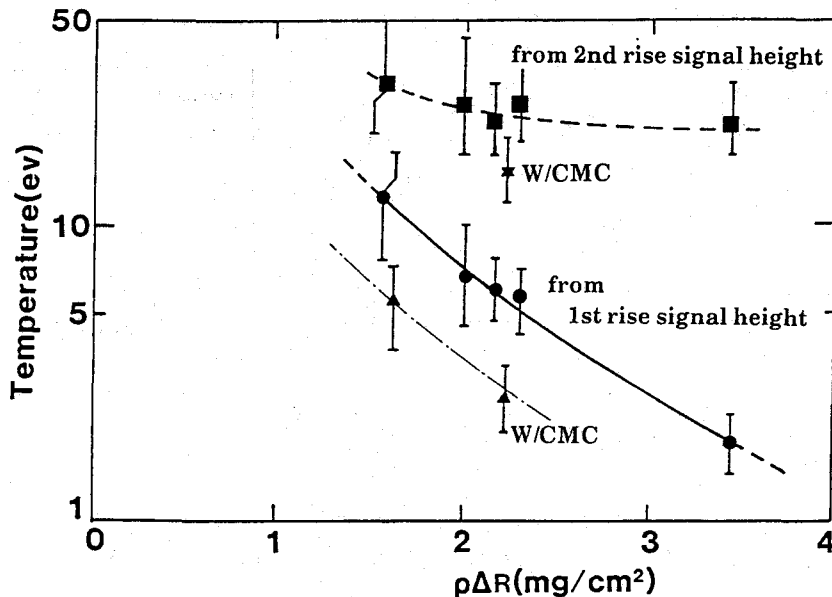


Fig. 5-24 The areal mass density dependence of the target rear temperatures from the FSR signals and the SFR signals. The temperature was estimated assuming blackbody radiation. (●) and (■) are results from the FSR and the SFR signals with bare CRYFATs, respectively. (★) and (▲) are results from the FSR and the SFR signals with CMC over-coated CRYFATs.

were retarded with the target thickness while the signal intensity stayed almost constant. However the start point of the FSR signals was independent of the target thickness while the signal intensity decreased with target thickness. Time histories of the FSR signals and start point may imply that the FSR signal is coupled with the laser pulse.

Figure 5-24 shows the brightness temperatures of the target rear by the FSR and the SFR signals as a function of the areal mass density. The temperature was estimated assuming blackbody radiations. The temperature for the FSR signal is the value at the laser peak. Here the SFR signal did not appear before the laser peak for 0.9 mg/cm² thickness target and could not be separated from the FSR signal. The temperature estimated from the FSR signal depends strongly on the target thickness and increases exponentially with the target thickness. While the temperature from the SFR height dose not change so much even if the target thickness increases.

These results indicate that the SFR signals are mainly caused by the shock heating and the FSR signals are due to the preheating by electrons and/or x rays.

The data with CMC is obtained using CRYFAT coated with sodium carboxyl-methyl-cellulose (CMC) on the irradiated side. CMC thickness was constant to be about 5 μm which would be almost ablated at the end of the laser pulse. CMC density and averaged atomic number are 1.2g/cm³ and 4.2, respectively. It should be noted that the temperatures for both FSR and SFR signals of CMC over coated targets were half times lower than that of bare CRYFATs. These results are very important to understand the mechanisms of shock heating and preheating corresponding to the FSR signals and may give some ideas to suppress the shock heating and preheating in CRYFAT.

5-4-3. Discussion

5-4-3-1. shock front property

Target thickness dependence of temperature and its break through time indicates that the SFR signals are due to the shock heating. Temporal history (rise time ≤ 150 psec) is also consistent with the strong change of entropy by shock wave at SFR signal. In this part we discuss about the shock heating in CRYFAT.

Figure 5-25 shows the experimental points of the SFR peak time versus target thickness with bare CRYFATs and over-coated CRYFATs for closed circles and triangles, respectively. Error values on time in the figure mainly comes from ambiguity of absolute time from the time fiducial and rise time of shock front which were usually larger than temporal resolution (≤ 50 psec) and spatial modulation at shock front. Open square in the figure is the data of bare CRYFAT at low laser intensity (7×10^{13} W/cm²). The lower intensity was varied by only changing the incident laser energy, not focal spot diameter and pulse duration, in order to minimize the difference due to

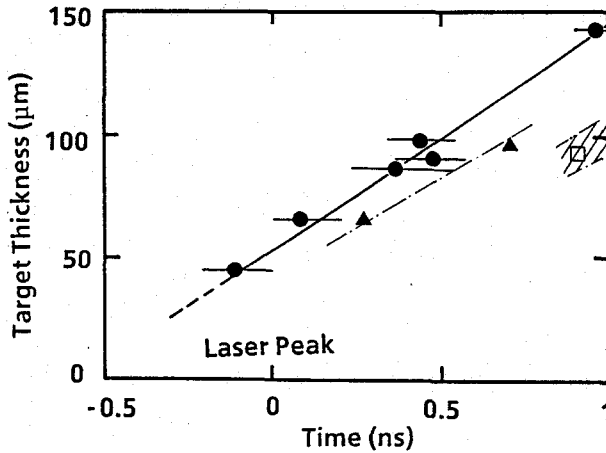


Fig. 5-25 Shock breakthrough time versus target thickness with bare CRYFATs (●) and over-coated CRYFATs (▲) at the laser intensity of 1×10^{14} W/cm². (□) is the data of bare CRYFAT at low laser intensity (7×10^{13} W/cm²).

lateral heat conduction. Shock propagation in plastic foam target with the density of 0.2 g/cm³ from x-ray backlighting method as shown in Fig. 5-16 is also presented for dotted line.

From this break through time, the shock front speed in the bare CRYFAT is estimated to be 1×10^7 cm/s. The shock speed at steady state in plastic foam target with same density was measured to be 1.1×10^7 cm/s. Although the incident laser intensity for plastic foam target was different by factor two (2×10^{14} W/cm² for foam target and 4×10^{14} W/cm² for CRYFAT experiment at same laser pulse duration), taking account of difference of the absorption (the absorption of plastic target was about 1.5 times larger than that of bare CRYFAT from plasma calorimeter), the shock speed in CRYFAT is reasonable compared with the speed in same mass density plastic target. Here we should also note that the shock speed does not so much depend on absorbed laser intensity as described in Eq. 2-12 ($v_s \propto I_a^{1/3}$).

From the shock speed, the pressure is simply calculated to be about 17 Mbar in CRYFAT at the laser intensity of 4×10^{14} W/cm² using Eq. 2-11 for strong shock wave. One-dimensional hydrodynamic simulation (HISHO) shows that the peak ablation pressure is 18-20 Mbar for the same shock

propagation speed at half the laser intensity (2×10^{14} W/cm²) of experimental condition. Here the simulation is composed of diffusion model and run with averaged density target and without strong preheat by hot electrons. Some difference between experimental and simulation results at the same shock speed may be caused by ambiguity of the equation of state in CRYFAT in which there are some micro structures (porous effect) and/or by simple calculation with assumption of shock compression (4 times compressed with initial density) for strong shock relation. The discrepancy of the incident laser condition may be due to lateral energy losses and/or difference of temporal behavior of absorption. In the simulation the temporal history of absorbed laser intensity was similar to the incident laser pulse shape but the absorption rate at the first half of laser pulse was lower on experiment than that at the latter half supposed from scattered light measurements.

Figure 5-26 shows the temperature of shock heated plasma on the rear side versus target thickness from Fig. 5-24. Here in order to estimate pure shock heating, we subtract the temperature of the FSR signals from that of the SFR peak signals. This estimation may give some error for pure shock heating. We have no bases about preheating property in the shock compressed region by anomalous energy transport corresponding to the FSR signals. Especially in 0.9 mg/cm² thickness target, the shock break through time is before laser peak when preheat is temporally changing so much. It is difficult to assume the pure shock heating only from the data.

The point of 0.9 mg/cm² in Fig. 5-25 is estimated by subtracting the temperature extrapolated from the temperature slope for the FSR signals at thicker targets (1.5 mg/cm² ~ 2.5 mg/cm²) from the temperature of maximum intensity. Bold dotted line in this figure presents the shock heating induced at the ablation pressure of 18-20 Mbar without preheat by 1-D simulation (HISHO). The point for the 0.9 mg/cm² is in agreement with the simulation result. This target thickness dependence of shock heating is also consistent with the experimental results as shown in Fig. 2-23 and behavior supposed from the temporal history of shock front heating in plastic foam target as shown in Fig. 5-18(b).

The peak temperature of the shock front at steady state is about 27 eV

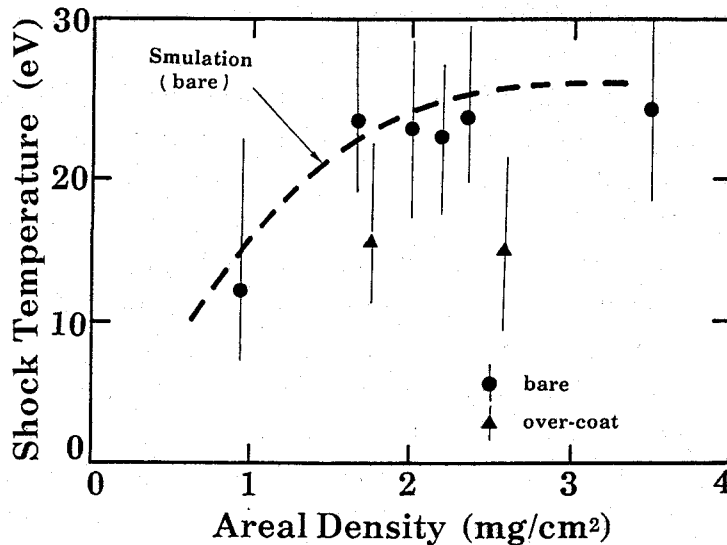


Fig. 5-26 Shock temperature versus target areal mass density. Circles and triangles are the results of bare CRYFATs (●) and over-coated CRYFATs (▲) at the laser intensity of 1×10^{14} W/cm². The temperature was estimated by subtracting the FSR signals from that of the SFR peak signals. Bold dotted line presents the shock heating induced at the ablation pressure of 18-20 Mbar without preheat by 1-D simulation (HISHO).

which corresponds to the pressure of 19 Mbar and the shock speed of 1.05×10^7 cm/s for ideal condition. These values are in good agreement with ones estimated from shock break through time. In thinner region the shock front grew with target thickness and reaches at the steady state.

Next we consider the intensity dependence of shock wave in CRYFAT. From Eq. 2-12 the shock speed at low laser intensity (7×10^{13} W/cm²) is estimated to be about $5.6 \sim 7.1 \times 10^6$ cm/s for strong shock wave assuming that the laser absorption at low laser intensities is same or 2 times larger than that of high intensity (4×10^{14} W/cm²). For low laser intensity the shock break through time in bare CRYFAT with near 90 μ m thickness is shown as the shaded zone in Fig. 5-25 applying above estimation, which is in good agreement with the experimental result. Temperature for lower laser intensity is also theoretically estimated to be about 8~13 eV. From experimental result of visible luminosity the temperature is about 15 eV.

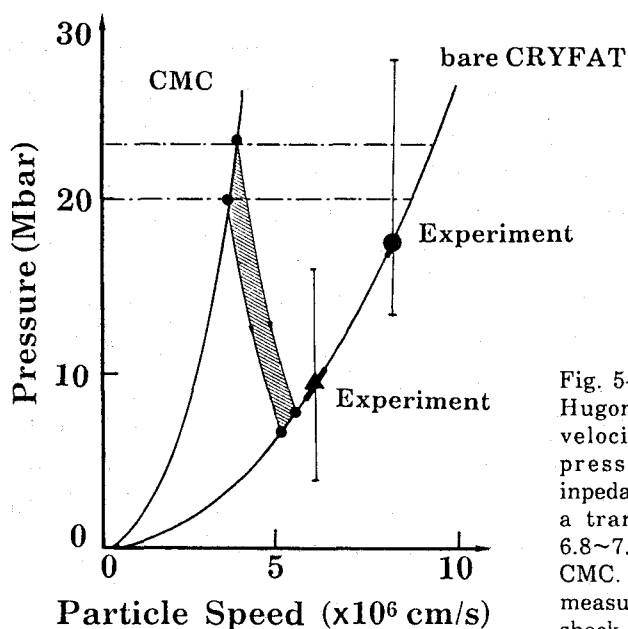


Fig. 5-27 CMC and bare CRYFAT Hugoniot in the pressure-particle velocity plane. For an incident pressure of 20~23Mbar the impedance-match technique leads to a transmitted shock pressure of 6.8~7.6Mbar in bare CRYFAT from CMC. For the same conditions the measured shock pressure from the shock speed and the temperature are 8.3~10.4 Mbar.

Considering the ambiguity of EOS in CRYFAT, laser absorption, and/or measurable error, the estimated temperature is in reasonable agreement with experimental result.

Finally it should be noted that shock strength in the over coat CRYFAT is weaker than that in the bare CRYFAT; shock speeds were 7×10^6 cm/s for over coated CRYFAT and 1×10^7 cm/s for bare CRYFAT as in Fig. 5-25 and temperatures were 12 eV and 27 eV, respectively as in Fig. 5-26. Here we have to note that only the laser side was coated with higher initial density plastic (1.2 g/cm^3) compared with bare CRYFAT and not on the rear side (observation side was always same 0.23 g/cm^3). Laser absorption for over-coated CRYFAT is improved because the atomic number of the CMC ($Z=4.2$) is higher than that of bare CRYFAT ($Z=1,2$), resulting in that collisional absorption becomes higher. Practically the experimental result from plasma calorimeters showed that the absorption of plastic is 1.3-1.6 times

higher than that of bare CRYFAT, which is in reasonable agreement with the simulation result.

The transmitted shock pressure from the front material (CMC) into the second one (CRYFAT) can be theoretically predicted by CMC and bare CRYFAT Hugoniot in a pressure-particle velocity plane in Fig. 5-27. Considering difference of absorption, the ablation pressure in CMC is calculated to be from 20 Mbar to 23 Mbar from the experimental results of the pressure in CRYFAT. Then the transmitted shock pressure [33], [40], determined by the intersection of the symmetrical curve of the CMC principal Hugoniot with the bare CRYFAT Hugoniot, is attenuated to be 6.8~7.6 Mbar. From experimental results of shock speed and temperature, attenuated pressure is estimated to be 8.3~10.4 Mbar. These experimental results are in good agreement with the above calculation results from shock attenuation model in boundary. Some discrepancy between the estimation and experimental results may be due to the ambiguity of EOS in CMC and CRYFAT and pressure in CMC.

5-4-3-2. anomalous preheat

It is important to understand the preheat mechanisms for the FSP signals as shown in Figs. 5-22 and 5-23. There are some possible mechanisms to cause such preheat in low-atomic number plasmas e.g., x rays and electrons due to its long mean free path in low-Z plasmas as shown in Chapter 2.

5-4-3-2-1 X-ray heating

First we estimate the relative x-ray preheating level using the measured x-ray emissions from the front and rear sides of bare and over-coated CRYFATs. If we assume that x rays from laser irradiated side mainly cause the preheat, the main contributed photon energy is estimated from Fig. 5-24 to be about 1 keV for both kinds of targets (bare and over-coated CRYFATs). Target thickness dependence of preheat temperature gives the energy deposition rate on axial distance in target, assuming the ionization energy loss is negligibly small and satisfied the ideal condition.

Figure 5-28 shows the relative x-ray intensity for the photon energy of 0.8 keV to 1.6 keV from front side of various targets such as bare CRYFAT

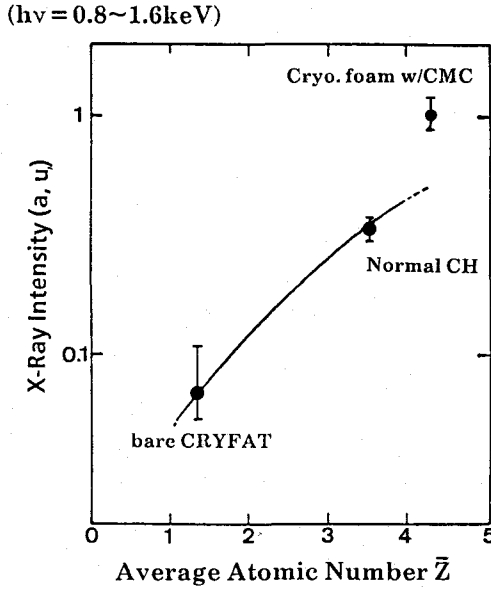


Fig. 5-28 Target material dependence of relative x-ray intensity from the front side for the photon energy of 0.8~1.6 keV. Solid line is the theoretical scaling from Eq. 5-41.

($Z=1.2$), CH plastic ($Z=3.5$), and CMC ($Z=4.2$) coated CRYFAT. The intensity increases with average atomic number Z of the laser irradiated side. X-ray emission with photon energy of 0.8 keV to 1.6 keV from low- Z plasmas ($Z=1-3.5$) will be mostly due to free-free transition because the carbon emission peak by bound-bound and bound-free transition will be about 0.3 keV at this experimental condition from Fig. 3-2 in Chapter 3. Emissivity of free-free transition in $\Delta h\nu = 0.8 \sim 1.6$ keV is simply described for Maxwellian distribution of electron as^[33]

$$\begin{aligned}
 J_v(x) &= \left(\frac{1}{kT_e} \right)^{1/2} Z^2 n_i n_e \int_{0.8}^{1.6} \exp\left(-\frac{h\nu}{kT_e} \right) d\nu \\
 &= (kT_e)^{1/2} Z^2 n_e^2 \left[\exp\left(-\frac{0.8}{kT_e} \right) - \exp\left(-\frac{1.6}{kT_e} \right) \right] \quad , \quad (5-39)
 \end{aligned}$$

where T_e , n_e , n_i , and x are temperature, electron density, ion density, and point in emission region. The emission region for such photon energy is assumed to be under critical point and isothermal expansion of coronal

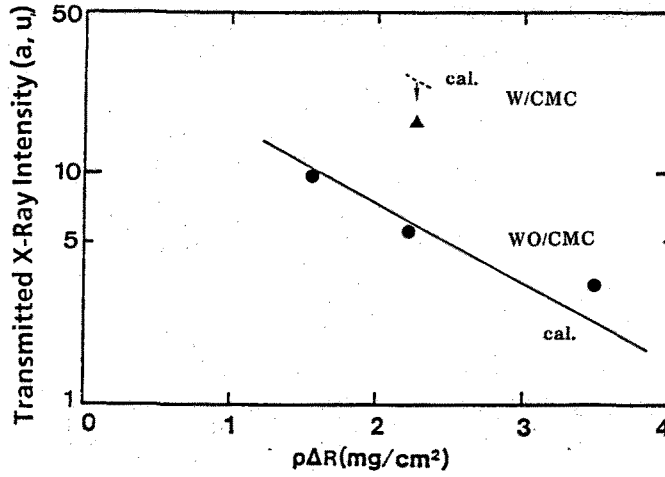


Fig. 5-29 Target areal mass density dependence of transmitted x-ray intensity for 0.8~1.6 keV photon energy. Circles and triangles are in the cases of bare CRYFAT and CMC over-coated CRYFAT, respectively. Solid line and dashed lines correspond to the transmitted x-ray intensity estimated by x-ray attenuation due to the photoionization absorption for bare CRYFAT and CMC over-coated CRYFAT, respectively.

plasmas is also assumed. From self similar solution the density profile is described as $n_e = n_c \exp(-x/L)$ where L is the plasma scale length. Then x-ray intensity from such plasma is estimated to be

$$I_v = \int_0^\infty J_v(x) dx \propto (kT_e)^{1/2} Z L n_c^2 \left[\exp\left(-\frac{0.8}{kT_e}\right) - \exp\left(-\frac{1.6}{kT_e}\right) \right] \quad (5-40)$$

Assuming that plasma scalelength is $L = C_s \tau \propto kT_e^{1/2}$ and temperature is $T_e \propto Z^{1/3-1/2}$ from Eq. 3-2 or simulation, atomic number dependence of free-free transition x-ray intensity is obtained to be

$$I_v \propto Z^{4/3-3/2} \left[\exp\left(-\frac{0.8}{kT_e}\right) - \exp\left(-\frac{1.6}{kT_e}\right) \right] \quad (5-41)$$

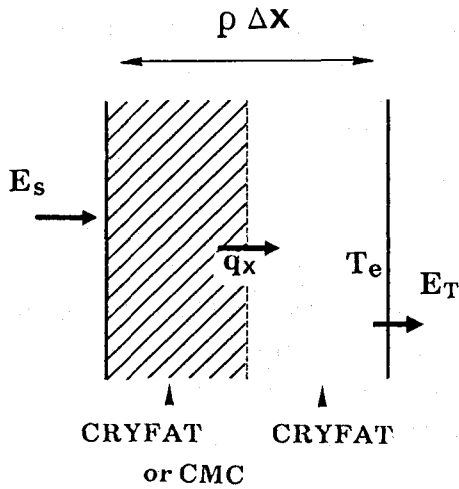


Fig. 5-30 Schematic diagram for calculation of deposited energy. E_s ; source energy, E_t ; transmitted energy, q_x transmitted flux through the boundary between CMC or the same areal mass density CRYFAT and the rear side bare CRYFAT.

Solid line in Fig. 5-28 is from Eq. 5-41 for electron temperature of 1 keV and fit to the experimental point of bare CRYFAT. X-ray intensity from CH plastic target is in good agreement with this scaling but for CMC is slightly higher than this scaling because the bound-free emission from sodium and/or oxygen may contribute to x ray with photon energy of 0.8~1.6 keV.

Figure 5-29 shows the target areal mass density dependence of transmitted x-ray intensity for 0.8~1.6 keV photon energy. Circles and triangle are in the cases of bare CRYFAT and CMC over-coated CRYFAT, respectively. Solid line and dashed lines correspond to the transmitted x-ray intensity estimated by x-ray attenuation due to the photoionization absorption for bare CRYFAT and CMC over-coated CRYFAT, respectively. Here calculating the relative transmitted x-ray intensity, the experimentally obtained front side emissivity is taken into account. Calculated relative transmitted x-ray intensity is in good agreement with experimental values for both targets. This agreement suggests that anomalous transport as shown in Chap. 4 is not seen here by the x rays with photon energy of 0.8~1.6 keV which will mainly contribute to preheat if preheat is mostly due to x ray.

From the above x-ray attenuation (see Fig. 5-29), the relative deposited energy in rear side (CRYFAT) can be calculated as shown in Fig. 30. We

experimentally obtained the source energy E_s and transmitted energy E_t . Then relative flux q_x transmitted through the boundary is calculated by

$$\frac{E_t(bare)}{E_t(CMC)} = \frac{q_x(bear) \cdot \exp(-\alpha \rho \Delta x_1)}{q_x(CMC) \cdot \exp(-\alpha \rho \Delta x_1)} = \frac{q_x(bare)}{q_x(CMC)} \quad (5-42)$$

Thus neglecting the ionization loss the temperature of preheated plasma by x ray for over-coated CRYFAT would be 3.3 times higher than that in bare CRYFAT. This relative temperature is clearly different with experimental results ($T_{CMC} / T_{bear} = 0.49$). Hence the x-ray preheating level must be extremely lower than observed preheat level (several eV).

5-4-3-2-2 Electron heating

Next we consider preheating by energetic electrons. The temperature of high energy electrons contributing to preheat can be also estimated from the slope of the areal mass density dependence of the preheat temperature.

Given an incident Maxwellian distribution of energetic electrons of total energy E_H and temperature T_H , the specific heat ϵ is given by [41], [42]

$$\epsilon(x) = \frac{E_H \left(\frac{x}{l}\right)^{-0.1}}{l \cdot S \cdot \rho} \exp \left[-1.9 \left(\frac{x}{l}\right)^{1/3} \right] \quad (J/g) \quad , \quad (5-43)$$

where l is electron mean free path (cm), S is the heated area (cm²) and ρ is the density of energy deposited region (g/cm³). The mean free path of monoenergetic electron is described as

$$l = 9 \times T_H^2 \left(\frac{10^{21}}{n_i (1/cm^3)} \right) \frac{10^{-4}}{[Z(Z+Z^2)]^{1/2}} \quad (cm) \quad , \quad (5-44)$$

from Eq. 2-17. In this simple calculation we neglect ionization energy losses.

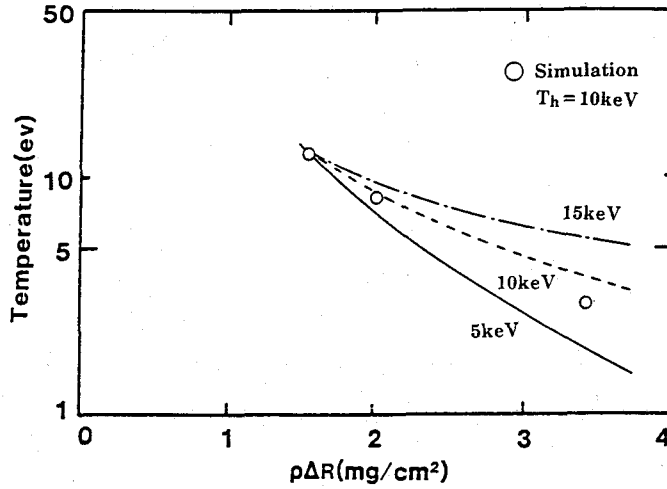


Fig. 5-31 Source temperature dependence of relative preheat temperature (slope) versus target thickness from Eq. (5-44). The relative temperature for various source temperatures are fixed at the point of 1.5 mg/cm². Open circles are simulation results with 10 keV source temperature.

Assuming the ideal condition, the temperature scaling to the axial distance (target thickness) is given by $T_p \propto (x/l)^{0.1} \exp\{-1.89(x/l)^{1/3}\}$.

Figure 5-31 shows the source temperature dependence of relative preheat temperature (slope) versus target thickness from Eq. (5-44). Here the relative temperature for various source temperatures are fixed at the point of 1.5 mg/cm² areal density in order to consider only the source electron temperature dependence of slope. Preheat temperatures with 10 keV source temperature from simulation (HISHO) are also presented for open circles. This simple estimation is in good agreement with the simulation results.

Thus the source temperature is estimated to be about 6 keV from target thickness dependence of preheat in Fig. 5-24. For $\rho = 0.2 \text{ g/cm}^3$ and $S = 600 \times 700 \mu\text{m}$ corresponding to the laser spot, the total source energy E_H of energetic electron is also estimated to be $10 \pm 5\%$ of absorbed laser energy. In 1-D hydrodynamic simulation (HISHO) forcing 20% of classically absorbed energy to high energy electron with Maxwellian distribution by resonance absorption, the preheat temperature of target rear side becomes

close to the experimental level. Here the source temperature of electron in simulation changes with laser intensity and average temperature is 5 keV.

We estimated the relative preheat levels by electron for various targets (bare CRYFAT and over-coated CRYFAT). The relative source energy E_H of high energy electron for both targets was determined by measuring relative hard x ray intensity I_x from FFX. Order of magnitude estimation of the amount of energy in high energy electrons that would produce the hard x-ray fluence can be made by assuming that the radiation is produced by bremsstrahlung radiation from Maxwellian energetic electron distribution. The x-ray fluence is simply given by ^{[9], [10]}

$$I_x \propto Z E_H , \quad (5-45)$$

in which the electrons are slowing down. In this simple estimation we neglect loss of hot electron energy to hydrodynamic plasma expansion.

Electron energy flux $q(x)$ at point x is described by ^[42]

$$q(x) \propto \left(\frac{x}{l}\right)^{9/10} \exp\left[-1.89\left(\frac{x}{l}\right)^{1/3}\right] , \quad (5-46)$$

from Eq. 5-44. Then the flux across the boundary point between CRYFAT and CMC or same areal density point of CRYFAT with CMC is estimated taking account of source energy E_H which is determined Eq. 5-45 and experimental result of hard x rays as shown in Table 5-1. Thus the relative deposition energy or temperature at the rear surface of over-coated CRYFAT is 60% of that in bare CRYFAT whose magnitude is in agreement with the experimental result (49%) as shown in Fig. 5-32 or Table 5-1.

These agreement between the experimental results and estimation of electron preheat (see Fig. 5-32) indicates that the preheat corresponding to the FSR signal is mainly caused by energetic electron whose source temperature and energy are about 6 keV and $10 \pm 5\%$ of absorbed energy.

Table 5-1. Energy deposition rate in the rear side from calculation.

relative comparison	E_s (source) (Exp.)	q_x (Cal.)	T_e (Cal.)	T_e (Exp.)
CRYFAT	1	1	1	1
overcoat	0.9	0.7	0.6	0.49

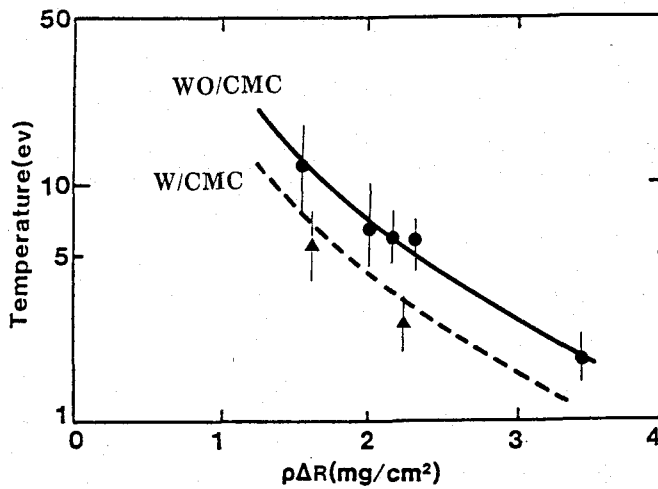


Fig. 5-32 Relative electron preheat temperature from calculation with Eq. 5-46 versus target areal mass density. Solid and broken lines are the results for bare CRYFAT and over-coated CRYFAT, respectively.

5-4-3-2-2 Origin of preheating electron

Considering ICF we have to understand where such high energy electrons (6 keV) are produced in order to reduce the preheat. There several possible mechanisms to produce such energetic electrons e.g., hot electrons by resonance absorption, nonlocally transported high energy tails of thermal

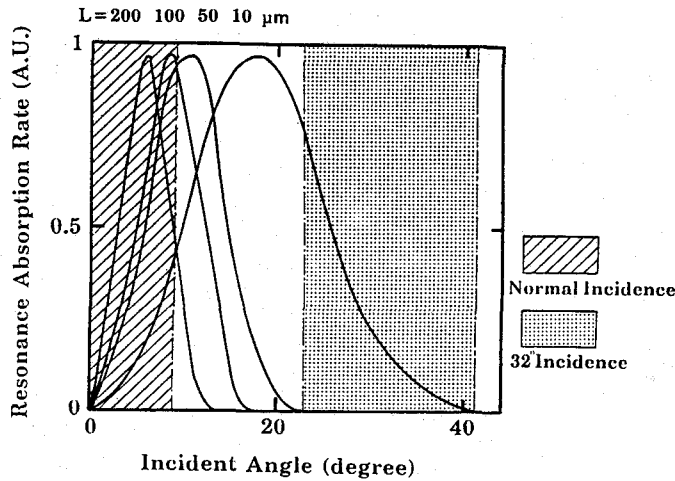


Fig. 5-33 The efficiency of resonance absorption versus laser incident angles for 527nm laser light with P polarization from Ginzburg function ^[17]. L is the plasma scalelength near critical point. Netted and shaded zones are the angles of experimental conditions.

electrons, and super hot electron produced by nonlinear laser interaction such as SRS and TPD instability.

Figure 5-33 shows the efficiency of resonance absorption versus laser incident angles for 527nm laser light with P polarization from Ginzburg function ^[17]. L is the plasma scalelength near critical point. Above 50 μm scalelength the resonance absorption will be neglected for 527 nm lights below 20° incident angle because of its long distance between the laser turning point and critical point in near which the resonance absorption tends to occur. The incident angle in this experiment was $32 \pm 9^\circ$ taking account of focusing cone, which is shown for a netted zone in Fig. 5-33. From 1-D hydrodynamic simulation the plasma scalelength are about 25 μm at 500 psec before laser peak and about 90 μm at laser peak. Thus in this experimental condition the resonance absorption would be too small to produce the energetic electron with $10 \pm 5\%$ of laser absorbed energy affecting to preheat.

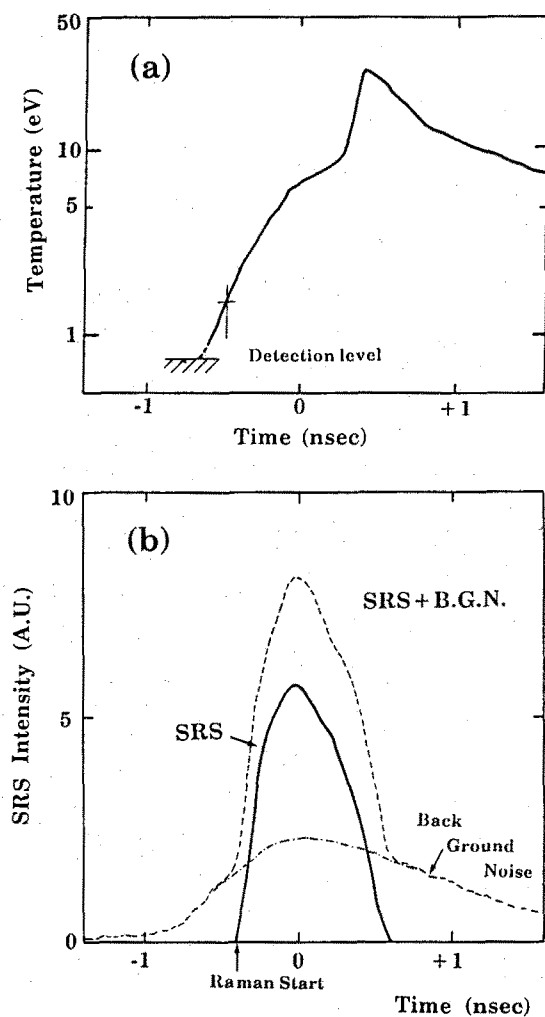


Fig. 5-34 Temporal correlation between the rear side temperature and side SRS light. Solid line in Fig. 5-34 (b) is determined by subtracting the background noise from overall signal.

We also measured the rear side temperature at normal incidence, when resonance absorption will be efficiently occurred as shown for hatched zone in Fig. 5-33. If energetic electrons produced by resonance absorption preheat the target rear, preheating level would be temporally and absolutely changed with different laser incident angles. However we could not observe such expected change of preheat.

For possibility of preheat by high energy electrons due to resonance absorption without depending on incident angles, there may be

filamentation of laser light which can raise the local intensity, resulting that the resonance absorption may be enhanced because CRYFAT initially has density modulation. However x-ray pinhole picture and Brillouin backscattered lights measurements showed no evidence of filamentation as long as plastic foam contains sufficient deuterium. For other possibility to increase the resonance absorption we consider the density steepening near critical point. If strong density steepening happens near the critical point, the effective scalelength will change, resulting that the distance between critical point and turning point become short and resonance absorption may increase. More detail studies may be necessary on the resonance absorption with density steepening.

Figure 5-34 shows the temporal correlation between the rear side temperature and side SRS light. Rear side temperature profile as shown in Fig. 5-34(a) is the data of CRYFAT with 90 μm thickness. Temporal history of SRS as shown in Fig. 5-34(b) is same with Fig. 5-6 whose detail is discussed in Section 5-2. Time history of the back ground noise was clearly observed and start point of SRS was proved in this figure. Real SRS is shown for bold line suppose by subtracting the back ground noise whose detail is also mentioned in Section 5-2. Then the start point of SRS was about 500 psec before laser peak for target thickness of 40 μm as shown in Fig. 5-34 and about 300 psec before laser peak for 90 μm thick target. SRS start was delayed relative to the preheat start point from the detection level which is about 800 psec before laser peak as shown in Fig. 5-34(a). Therefore we conclude that the preheat dose not temporally correlate with SRS.

Besides the temperature of energetic electron produced by SRS instability is 12 keV from hard x-ray spectra in Fig. 5-8 and is above 10 keV from simple theoretical estimation discussed in Section 5-2. Even if down conversion of high energy (from 12 keV to 6 keV) is occurred through collision in plasma, the energy flux which was less than 0.2% for planar CRYFAT is too small to heat the rear side of target upto the level of observed preheat temperature (several eV). Hence the high energy electrons produced by SRS instability exert little influence on preheat in this experimental condition.

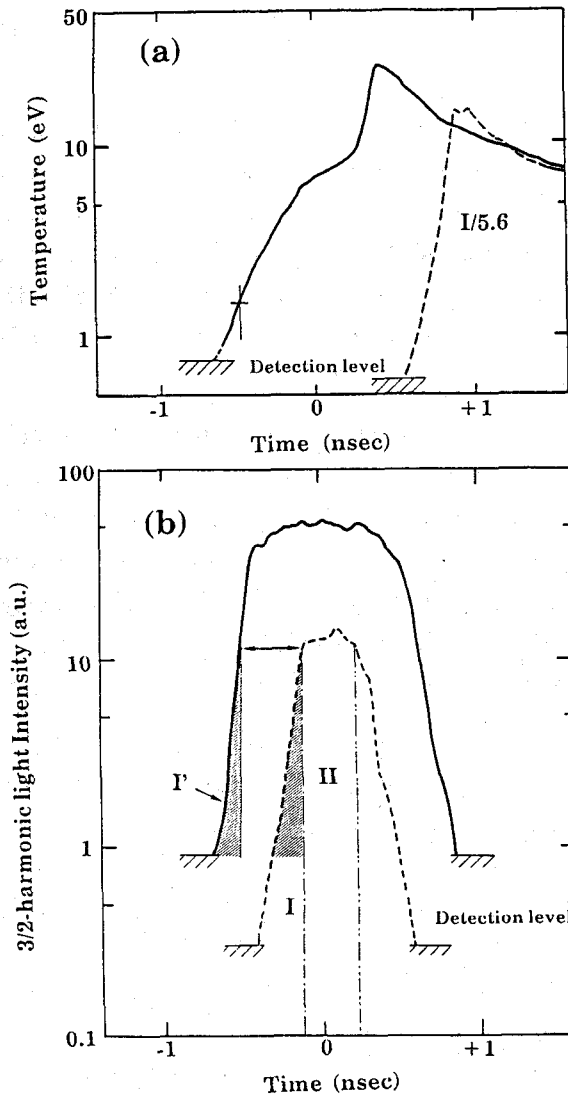


Fig. 5-35 Temporal correlation between the rear side temperature of bear CRYFAT [5-35(a)] and three-half harmonic scattered light [5-35(b)] at two different laser intensities. Solid line in the figure is at $4 \times 10^{14} \text{ W/cm}^2$ and dotted line at $7 \times 10^{13} \text{ W/cm}^2$.

Figure 5-35 shows the temporal correlation between the rear side temperature of bear CRYFAT [5-35(a)] and three-half harmonic scattered light [5-35(b)] at two different laser intensities. Solid line in the figure is at $4 \times 10^{14} \text{ W/cm}^2$ and dotted line at $7 \times 10^{13} \text{ W/cm}^2$. Three-half harmonic scattered light depends on TPD instability and detailed explanation about Fig. 5-35(b) is mentioned in Section 5-2 for Fig. 5-7. Here we discuss the

correlation between preheat and TPD instability assuming that the three-half harmonic scattered light and hot electron correlates linearly with TPD instability.

At high laser intensity (4×10^{14} W/cm²) preheat starts from the detection level at 800 psec before laser peak and the harmonic scattered light rises from detection level in 700 psec before laser peak. Here we could not obtain the back ground level and then it is impossible to compare the time original correlation between both start point. However intensity dependence of both signals may suggest the correlation between the preheat and TPD instability.

At low laser intensity (7×10^{13} W/cm²) the preheat at the front of the shock heating was reduced to below the detection level, where we changed the sensitivity of streak camera at high and low intensity cases in order to obtain lower preheat level at low laser intensity. The preheat reduction rate was more than ten. Then the fraction of the harmonic light at low laser intensity was also reduced to be one fifth of that for high laser intensity at laser peak. Thus the preheat temperature depends nonlinearly on or be independent of TPD instability.

At high laser intensity the temporal history and intensity of the harmonic light till 500 psec before laser peak (region I') is same with those at low laser intensity till 100 psec before laser peak (region I). We are able to assume that the same hot electron fraction is created by TPD instability in region I and I'. Then the rear side of of target was preheated to be 1.6~1.8 eV for high laser intensity case. Therefore if the hot electron temperature is same between both cases (i.e., hot electron penetration rate is same for both laser intensity cases) the target rear side for low laser intensity would be preheated up to be 1.6-1.8 eV at 100 psec before laser peak. However we could not observe such preheat level at low laser intensity.

Here it should be noted that the thermal electron temperature is also different with each laser intensity, resulting that the hot electron temperature for low laser intensity case is low compared with that for high intensity case. Using Eqs. 5-16 and 3-2, in high laser intensity case hot electron temperature at 500 psec before laser peak (2×10^{14} W/cm²) is estimated to be 10 keV and for low laser intensity case 5 keV at 100 psec

before laser peak ($6.8 \times 10^{13} \text{ W/cm}^2$), whose relative penetration depth are shown in Fig. 5-31. Then preheat temperature is extrapolated from preheat temperature (1.6~1.8 eV) in high laser intensity case to be about 0.6~0.8 eV at 100 psec before laser peak in the low laser intensity, whose level is same with or lower than the detection level at low laser intensity case. After that (region I) the harmonic light intensity level was kept till about 200 psec after laser peak (region II), resulting that the hot electron created by TPD instability will continue to deposit into the rear side and the temperature will keep increasing in region II. Here we have no bases on energy production rate to time in region I or I' but we under-estimate the preheat temperature at 200 psec after laser peak in low laser intensity case assuming the energy production rate in region I is same with that in region II. The preheat temperature is expected to be $\geq 1.3 \sim 1.6 \text{ eV}$ whose level is clearly above the detection level. However we could not also observe such preheat above detection level (0.6 eV).

Although the detail of absolute intensity correlation between three-half harmonic scattered light and TPD instability are not well understood, experimental results and above estimation indicate that the hot electron due to TPD instability dose not mainly contribute to preheat. Hot electron temperature due to TPD instability is also estimated to be about 10-20 keV as mentioned in Section 5-2 whose value is higher than that from target thickness dependence of preheating temperature (see Fig. 5-32).

Finally we discuss the contribution of nonlocally transported high energy tail in thermal electron distribution with kinetical simulation.^[43] Figure 5-36 shows the temporal history of rear side temperature for bare CRYFAT with 90 μm thickness from experimental result and 1-D Fokker-Planck (F-D) simulation^[43]. F-D simulation was with a spherical target of 600~700 μm diameter. This code dose not include nonlinear laser interactions such as SRS and TPD instabilities. Resonance absorption can beartificially controlled. Rear side temperature is derived considering the Fermi degenerate effect under Fermi temperature (about 5 eV for solid CRYFAT). Under Fermi temperature bulk electron obey Fermi-Dirac distribution, resulting that the temperature tends to increase compared with that at same temperature Maxwellian distribution.

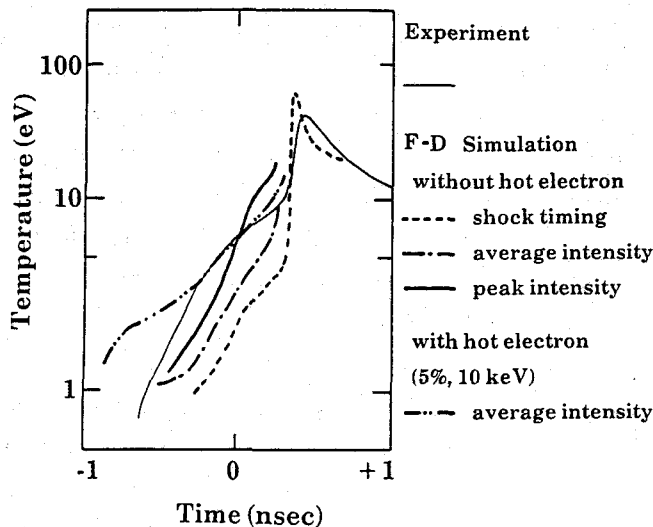


Fig. 5-35 Temporal history of rear side temperature for bare CRYFAT with 90 μm thickness from experimental result and 1-D Fokker-Planck (F-D) simulation^[43]. Dotted line is a result by reducing the input energy to fit the shock timing to the experimental result. Dot-dashed line and solid line are results at average intensity and peak laser intensity considering the real laser intensity pattern. Double dot dashed line is a result when with 5% of the laser energy is forced to resonance absorption with 10 keV hot electron temperature at average laser intensity.

Simulation was run with four kinds of laser conditions. Dotted line in Fig. 5-36 is a result by reducing the input energy to fit the shock timing to the experimental result. Dot-dashed line and solid line are results at average intensity and peak laser intensity considering the real laser intensity pattern. Dot-dot dashed line is a result when with 5% of the laser energy is forced to resonance absorption with 10 keV hot electron temperature at average laser intensity. Preheat of several eV appeared clearly at the front of shock heating. From this simulation, the preheat at the front of shock heating is mainly due to nonlocally transported high energy components of thermal electron distribution and other hot electron by nonlinear laser interaction and/or resonance absorption may affect to the preheat with several %.

5-4-3-3. energy transport in tailored pulse produced plasmas

We show the temporal history of rear side temperature of bare CRYFAT using tailored laser pulse. Tailored pulse has been expected for efficient ICF target implosion in order to achieve low entropy compression and high implosion velocity by additional acceleration.

Experimental conditions were same with above experiments without tailoring of the laser pulse. Fig. 5-37 shows the temporal shape of used laser pulse which was produced by combining two kinds of Gaussian pulses. Two pulses were generated by two synchronized oscillator. One was 400 psec FWHM and another 2.8 nsec FWHM. Short pulse was delayed by 170 psec to the long pulse. The short pulse peak intensity was 6×10^{14} W/cm² on target for main pulse and 4×10^{13} W/cm² at the long pulse peak for foot pulse.

Figs. 5-38 (a) and (b) show the temporal behaviors of the rear side temperature of CRYFAT of 43 μ m and 130 μ m thickness. For 43 μ m thickness target there were several heating components (peak; 36 ± 7 eV, shoulder at laser peak; 22 eV, foot heating; several eV). In 130 μ m thickness target we observed two components (peak; 19 ± 5 eV, foot at laser peak; 3 eV). Peak signals are due to the shock heating by main pulse because they were retarded by increasing of target thickness. The components at laser peak may be due to the high energy electron preheat. The intensity decreased and temporal point was not changed with target thickness. Foot part appeared in thin target is foot pulse effect. Taking a shot with only foot pulse or without main pulse, we obtained similar temporal history with foot part in Fig. 5-38(a) in 40 μ m target. Peak temperature of foot pulse heating by thermal conduction or shock wave was 8.7 eV. Thus in 40 μ m thickness target foot pulse heating, high energy electron preheat, and shock heating by main pulse were temporally combined whose temperatures were estimated to be 8.7 eV, 13 eV, and 14 eV, respectively. Using tailored pulse, we obtained lower level preheat for each component while peak preheat temperature was higher compared with that of single pulse. From target thickness dependence of preheat temperature, the high energy electron temperature is also estimated to be about 10 keV which is higher than that in single pulse experiments (6keV). Using foot pulse, the plasma

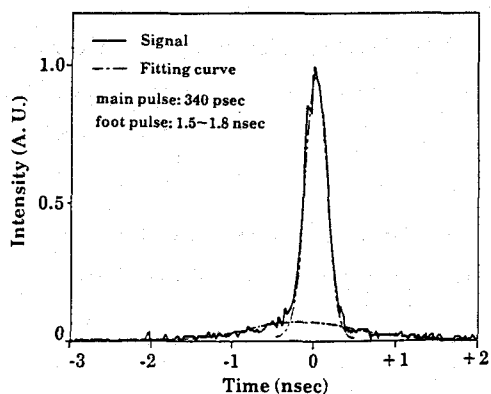


Fig. 5-37 Temporal shape of used laser pulse which was produced by combining two kinds of Gaussian pulses. Two pulses were generated by two synchronized oscillator. One was 400 psec FWHM and another 2.8 nsec FWHM. Broken lines are fitting curves.

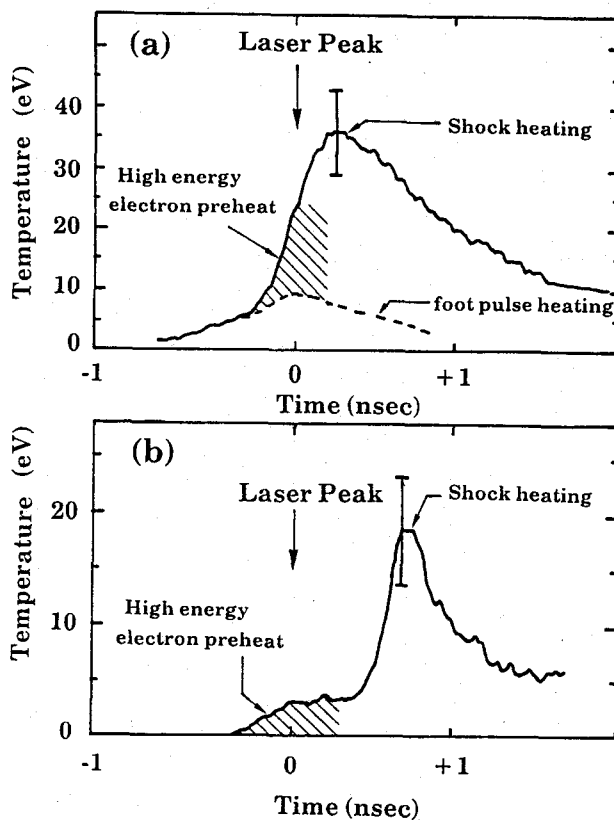


Fig. 5-38 Temporal behaviors of the rear side temperature of CRYFAT of 43 μm (a) and 130 μm (b) thickness with tailored laser pulse as shown in Fig. 5-37.

scalelength increases and TPD and/or SRS instabilities may be enhanced. Peak laser intensity increase may enhance the thermal electron temperature increases, resulting that the high energy component of thermal electrons may increase.

We have to study about foot pulse effect in more detail to exactly understand the energy transport in tailored pulse produced plasmas.

5-4-4. Summary

We have studied energy transport in low-Z plasmas using cryogenically cooled D₂ filled foam targets (CRYFAT $Z=1.2$ $\rho=0.2$ g/cm³). Measurements were made on time-resolved rear side temperature of targets. We distinguished the shock heating and preheat at the front of shock heating.

Shock speed was 1×10^7 cm/s and the temperature of shock heating was about 30 eV at laser intensity of 4×10^{14} W/cm² in bare CRYFAT. Such shock heating level was 3-4 times larger than normal density plastic target. The temperature of shock heating in high density plastic overcoated CRYFAT was lower than that of the without coating. This reduction of shock heating in layered target was explained by simple shock attenuation model at boundary layer.

The preheat at the front of shock heating was due to high energy electron whose source temperature and energy were 6 keV and $10 \pm 5\%$, respectively. The preheat was also reduced to 50% by overcoating of higher-Z material on the laser iside. The high energy electron which caused the preheat was mainly due to the nonlocal effect i.e, high energy tail of thermal electrons. SRS and three-half harmonic scattered light were also measured at the same time and we studied the correlation between the preheat and SRS and TPD instabilities. The preheat was not directly correlated with these instabilities but several % of preheat might be caused by hot electrons produced by these instabilities and/or resonance absorption.

Extensionally studied was energy transport in tailored pulse produced plasmas using bare CRYFAT. For 43 μ m thickness target there were several

preheating components (shock heating by main pulse; 14 eV, electron preheat; 13 eV, foot pulse heating; 8.7 eV) and in 130 μm target two components was observed (shock heating by main pulse; 16 eV, electron preheat; 3 eV). Using tailored pulse, we obtained lower level preheat for each component while peak preheat temperature was higher than that of single pulse. However high energy electron temperature was about 10 keV which was higher than that in single pulse experiments (6 keV).

§ 5-5. Conclusion

We studied the energy transport by shock wave and electron in low-Z and low-density target using mainly planar CRYFAT ($Z=1.2$, $\rho=0.2\text{g/cm}^3$).

In order to obtain the bases about high energy electrons which may become preheat source in low-Z plasmas, we studied nonlinear laser-plasma interactions such as stimulated Raman scattering (SRS) and two plasmon decay (TPD) instabilities in CRYFAT. Below laser intensities $4\times 10^{14}\text{ W/cm}^2$, the amount of SRS energy become less than 0.1% of incident laser energies and should have negligible effect for implosion performance. Unless CRYFAT was enough to be filled with D_2 , some structure in target worked as initially-imposed density perturbations and enhanced SRS fraction with some spectral modulation.

Laser-driven shock wave in porous and low density material was studied using plastic foam target. We directly observed the shock wave propagation with an x-ray streak shadowgraphy. The x-ray shadowgram showed clearly a planar shock formation in the porous targets, which was composed of two parts: a shock front and following a pile-up zone of multiple shock waves. The pressure at the shock front was delayed and reached its maximum at 400 psec after the peak of the pile-up zone pressure. The pile-up zone followed a thermodynamic condition closer to the adiabat than the shock front.

The energy transport in low-Z and low-density target was studied with planar CRYFAT. It was found that low-density and low-Z target such as

CRYFAT was sensitive to the preheating by high energy electrons and also shock heating. Shock heating was about 30 eV at laser intensity of 4×10^{14} W/cm² in bare CRYFAT whose level was 3-4 times larger than normal density plastic target. The preheat preceeding the shock heating was due to high energy electrons whose temperature and energy were 6 keV and $10 \pm 5\%$, respectively. The high energy electrons which caused the preheat were mainly due to the nonlocal effect i.e, high energy tail of thermal electrons. The preheatings by shock and high energy electrons were suppressed to 50% by overcoating of higher-Z and higher-density material on laser irradiated side.

In low-Z and low-density target, strong electron preheat and shock heating may produce some difficulty in efficient laser implosion; preheating of the fuel may easily occur. These preheat effect to implosion are studied in next chapter.

References

- [1] R. Mason, Nucl. Fusion 15, 9 (1975); A New Direct-Drive ICF Capsule, LLNL Annual Report, Livermore (1985); R. A. Sackes and D. H. Darling, Nucl. Fusion 27, 447 (1987); T. Yamanaka, K. Nishihara, K. A. Tanaka, T. Norimatsu, M. Murakami, R. Kodama, Y. Kato, T. Jitsuno, M. Nakatsuka, S. Nakai, M. Nakai, and C. Yamanaka (Implosion Experiment of Cryogenic foam targets), IQEC, Tokyo 1988 (unpublished).
- [2] K. A. Tanaka, B. Boswell, R. S. Craxton, L. M. Goldman, F. Gaglielmi, W. Seka, R. W. Short, and J. M. Soures, Phys. Fluids 28, 2910 (1985).
- [3] R. P. Drake, R. E. Turner, B. F. Lasinski, K. G. Estabrook, E. M. Campbell, C. L. Wang, D. W. Phillion, E. A. Williams, and W. L. Kruer, Phys. Rev. Lett. 53, 1739 (1984); N. M. Ceglio, D. T. Attwood, and J. T. Larsen, Phys. Rev. A 25, 2351 (1982).
- [4] K. A. Tanaka, L. M. Goldman, W. Seka, M. C. Richardson, J. M. Soures, and E. A. Williams, Phys. Rev. Lett. 48, 1179 (1982); D. W. Phillion, D. L. Banner, E. M. Campbell, R. E. Turner, and K. G. Estabrook, Phys. Fluids 25, 1434 (1982); H. Figueroa, C. Joshi, H. Azechi, N. A. Ebrahim, and K. G. Estabrook, Phys. Fluids 27, 1887 (1987).
- [5] W. Seka, E. A. Williams, R. S. Craxton, L. M. Goldman, R. W. Short, and K. A. Tanaka, Phys. Fluids. 27, 2181 (1984); J. M. Dawson, in Advances in Plasma Physics, edited by A. Simon and W. R. Thompson (Interscience, New York, 1968), Vol. 1.
- [6] S. P. Obenshain et al., in 18th Annual Anomalous Absorption Conference, L'Estérel, Quebec, 1988 (unpublished).
- [7] H. Nishimura, H. Niki, N. Miyanaga, K. Okada, H. Azechi, T. Yabe, R. Tsuji, S. Ido, M. Yamanaka, T. Mochizuki, K. Nishihara, T. Yamanaka, and C. Yamanaka, rev. Sci. Instrum. 56, 1128 (1985).

References

- [8] A. H. Compton and S. K. Allison, *X Rays in Theory and Experiment* (Van Nostrand Reinhold, New York, 1935).
- [9] K. A. Brueckner, *Nucl. Fusion* **17**, 1257 (1977).
- [10] R. L. Keck Ph. D. thesis, University of Rochester (1983).
- [11] R. P. Drake, R. E. Turner, B. F. Lasinski, E. A. Williams, D. W. Phillion, K. G. Estabrook, W. L. Kruer, E. M. Campbell, K. R. Manes, and J. S. Hildum, *Phys. Fluids* **31**, 3141 (1988).
- [12] B. B. Afeyan and E. A. Williams, *Phys. Fluids* **28**, 3397 (1985).
- [13] B. F. Lasinski, A. Langdon, K. G. Estabrook, and W. L. Kruer, LLNL Laser Program Annual Report No. UCRL-50021-80, 3-, 1980 (unpublished).
- [14] J. A. Bittencourt, *Fundamentals of Plasma Physics* (Pergamon Press, Oxford, 1986).
- [15] T. W. Johnston and J. M. Dawson, *Phys. Fluids* **16**, 722 (1973).
- [16] J. D. Jackson, *J. Nucl. Energy Part C1*, 171 (1960).
- [17] W. L. Kruer, *The Physics of Laser Plasma Interaction* (Addison-Wesley Publishing Company, Inc. 1988).
- [18] Kent. Estabrook, and W. L. Kruer, *Phys. Rev. Lett.* **53**, 465 (1984); R. P. Drake, E. A. Williams, P. E. Young, Kent. Estabrook, W. L. Kruer, H. A. Baldis and T. W. Johnston, *Phys. Rev. A* **39**, 3536 (1989).
- [19] C. L. Shepard, J. A. Tarvin, R. L. Berger, Gar. E. Bush, R. R. Johnson, and R. J. Schoroede, *Phys. Fluids* **29**, 2217 (1986); R. P. Drake, E. A. Williams, P. E. Young, Kent. Estabrook, W. L. Kruer, H. A. Baldis and T. W. Johnston, *Phys. Fluids B* **1**, 2217 (1989).
- [20] A. Simon and R. W. Short, *Phys. Rev. Lett.* **53**, 1912 (1984); S. H. Batha, R. Bahr, L. M. Goldman, W. Seka, and A. Simon, *Phys. Fluids* **31**, 3667 (1988); A. Simon and R. W. Short, *Phys. Fluids B* **1**, 1073 (1989).
- [21] A. Simon, W. Seka, L. M. Goldman, and R. W. Short, *Phys. Fluids* **29**, 1704 (1986).
- [22] Kent. Estabrook, and W. L. Kruer, *Phys. Rev. Lett.* **40**, 42 (1978).
- [23] Kent. Estabrook, W. L. Kruer, and B. F. Lasinski, *Phys. Rev. Lett.* **45**, 1399 (1980).
- [24] K. Okada, T. Mochizuki, S. Sakabe, H. Shiraga, T. Yabe, and C. Yamanaka, *Appl. Phys. Lett.* **43**, 231 (1983).
- [25] D. Saltzman, S. Eliezer, A. D. Krumbein, and L. Gitter, *Phys. Rev. A* **28**, 1738 (1983).
- [26] C. G. M. van Kessel, and R. Sigel, *Phys. Rev. Lett.* **33**, 1020 (1974); D. Billon, D. Cognard, J. Launspach, C. Patou, D. Redon, and D. Scirmann, *Opt. Commun.* **15**, 108 (1975); F. Amiranoff, R. Fedosejevs, R. F. Shmalz, R. Sigel, and Y. L. Teng, *Phys. Rev. A* **32**, 3535 (1985); A. Ng, P. Celliers, and D. Parfeniuk, *Phys. Rev. Lett.* **58**, 214 (1987).
- [27] L. R. Veaser and J. C. Solem, *Phys. Rev. Lett.* **40**, 1391 (1978); R. J. Trainor, J. W. Shaner, J. M. Auerbach, and N. C. Holmes, *Phys. Rev. Lett.* **42**, 1154 (1979); E. A. MacLean, S. H. Gold, J. A. Stamper, R. R. Whitlock, H. R. Griem, S. P. Obenschain, B. H. Ripin, S. E. Bodner, M. J. Herbst, S. J. Gitomer, and M. K. Matzen, *Phys. Rev. Lett.* **45**, 1246 (1980); F. Cottet, J. P. Romain, R. Fabbro, and B. Faral, *Phys. Rev. Lett.* **52**, 1884 (1984); A. Ng, D. Parfeniuk, L. DaSilva, and D. Pasini, *Phys. Fluids* **28**, 2915 (1985).
- [28] R. Fabbro, B. Faral, J. Viromont, F. Cottet, P. Romain, and H. Pepin, *Phys. Fluids* **28**, 3414 (1985).
- [29] L. DaSilva, A. Ng, and D. Parfeniuk, *J. Appl. Phys.* **58**, 3634 (1985).
- [30] T. Norimatsu, H. Katayama, T. Mano, M. Takagi, R. Kodama, K. A. Tanaka, Y. Kato, T. Yamanaka, and S. Nakai, *J. Vac. Sci. Technol. A* **6**, 3144 (1988).
- [31] M. Murakami and K. Nishihara, *ILE Quart. Prog. Rep.* **6**, 34 (1983).
- [32] T. Yuchi and K. Nishihara, *Technol. Repts. Osaka Univ.* **32**, 295 (1982); G. B. Zimmerman and R. M. More, *J. Quant. Spectrosc. Radiant. Transfer* **23**, 517 (1980); R. M. More, *J. Quant. Spectrosc. Radiant. Transfer* **27**, 345 (1982); C. W. Cranfill

- and R. M. More, Los Alamos Scientific Labo. Rept. LA-7313-MS (1978); S. Atzeni, A. Caruso, and V. A. Pais, *Laser and Part. Beams* **4**, 393 (1986).
- [33] B. Ya. Ze'ldovich and Yu. P. Raizer, *Physics of Shock Waves and High Temperature Hydrodynamic Phenomena* (Academic Press, New York, 1966).
 - [34] R. M. More, *Proceedings of the 29'th Scottish Univ. Summer School in Phys.* **157** (The Camelot Press, Southampton, 1985).
 - [35] S. Brush, H. Sahlin and E. Teller, *J. Chem. Phys.* **45**, 2102 (1966); J. P. Harsen, *Phys. Rev. A* **8**, 3096 (1973); M. Baus and J. P. Harsen, *Physics Reports* **59**, 1 (1980).
 - [36] R. E. Kidder, *Nucl. Fusion* **8**, 3 (1968); B. J. Gitomer, R. L. Morse, and B. S. Newberger, *Phys. Fluids* **20**, 234 (1977); C. E. Max, C. F. Mokee and W. C. Mead, *Phys. Fluids* **23**, 234 (1980); P. Mora, *Phys. Fluids* **25**, 1051 (1982); R. Fabbro, C. E. Max, and E. Fabre, *Phys. Fluids* **28**, 1463 (1985).
 - [37] M. H. Key, W. T. Toner, T. J. Goldsack, J. D. Kilkenny, S. A. Veats, P. F. Cunningham, and C. L. S. Lewis, *Phys. Fluids* **26**, 2011 (1983); T. Boehly, K. A. Tanaka, T. Mochizuki, and C. Yamanaka, *J. Appl. Phys.* **60**, 3840 (1986).
 - [38] R. C. Malone, R. L. McCrory, and R. L. Morse, *Phys. Rev. Lett.* **34**, 721 (1975); F. C. Young, R. R. Whitlock, and S. E. Bodner, *Appl. Phys. Lett.* **30**, 45 (1977); B. Yaakobi, J. Dellett, L. M. Goldman, R. L. McCrory, R. Marjoribanks, M. C. Richardson, D. Shvarts, S. Skupsky, J. M. Soures, C. Verdon, D. M. Villeneuve, T. Boehthly, R. Hutchinson, and S. Letzring, *Phys. Fluids* **27**, 516 (1984).
 - [39] H. Katayama Ph. D. thesis Osaka University (1990).
 - [40] F. Cottet, M. Hallouin, J. P. Romain, R. Fabbro, B. Faral, and H. Pepin, *Appl. Phys. Lett.* **47**, 678 (1985).
 - [41] M. D. Rosen, R. H. Price, E. M. Campbell, D. W. Phillion, K. G. Estabrook, B. F. Lasinski, J. M. Auerbach, S. P. Obenschain, E. A. McLean, R. R. Whitlock, and B. H. Ripin, *Phys. Rev. A* **36**, 247 (1987).
 - [42] K. Mima, H. Takabe, A. Nishiguchi, K. Nishihara, T. Yabe, H. Totsuji, Y. Furutani, Y. Kihara, C. Yamanaka, and S. Nakai, *Proc. 12th Int. Conf. on Plasma Physics and Ccontrolled Nuclear Fussion Research, France, IAEA-CN-50/B-3-2*.
 - [43] A. Nishiguchi and K. Mima (private communication, 1989).

IMPLOSION OF CRYOGENICALLY COOLED D₂ FILLED FOAM TARGET

- §6-1. Introduction
- §6-2. Experimental Set up
- §6-3. Experimental Results
- §6-4. Discussion
- §6-5. Conclusion

§6-1. Introduction

In order to obtain efficient compression of an ICF target, the fuel should be initially at solid state and be compressed adiabatically. If enough fuel is compressed in this way and heating of the fuel occurs at the final stage of the implosion, then ignition of the fuel and successive fusion process take place.^[1] A simple way to achieve high compression of fusion fuel is to cool the target cryogenically so that the fuel is initially a solid layer inside the pusher. In addition to the low initial temperature, another advantage is to make shocks impossible to propagate through the fuel layer to reach the center and to rebound. Gaseous fuel would suffer serious preheat by the shock propagation. Other requirements to keep a low adiabat could be performed using a shaped laser pulse and suppressing preheating of fuel.^[2]

A new approach ^{[3],[4]} to sustain a thick layer of fuel in a hollow foam shell has been proposed for a high-gain ICF reactor's target as shown in Fig. 6-1. The foam, which defines the spatial matrix of the fuel (DT or D₂) acts like a sponge and holds to the fuel by surface tension.

Cryogenic targets with either a solid or a liquid fuel layer on the inside wall of a glass microballoon (GMB) fuel capsule have been developed and

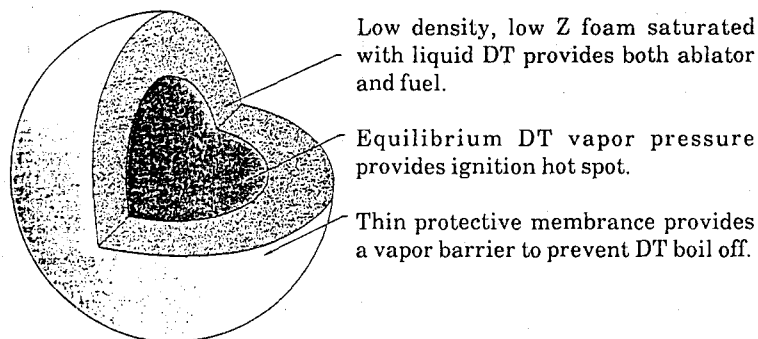


Fig. 6-1 The use of low-density, low-Z foam to define and hold the DT shell, proposing attractive single shell high gain ICF target design. [see Ref. 3]

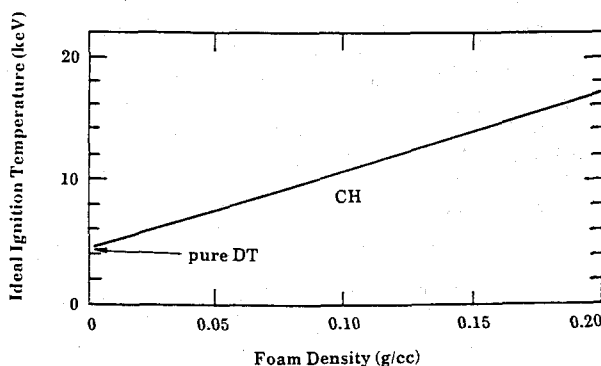


Fig. 6-2 The ideal ignition temperature for DT wetted foam depends primarily on the foam and composition.

used for high-density compression experiments.^[5] In comparison to these cryogenic GMB target, a cryogenic foam target composed of a low-density foam shell saturated with a liquid fuel, provides a thick and uniform fuel layer without introducing a high-Z element for fuel containment. Cryogenically cooled D₂ filled foam targets (CRYFAT) have many advantages of ICF reactors such as relatively easy control the fuel layer uniformity and inner gas pressure for hot spark burning, and reduction of fuel-pusher mixture.

A principal disadvantage suffers when using a wetted foam fuel layer instead of a pure DT shell is an increase in ignition temperature,^[3] as shown in Fig. 6-2. The ignition temperature in this figure is defined as the temperature at which the alpha particle production rate equals to the bremsstrahlung radiation loss rate. This is an over-simplified view of the various factors controlling the ignition in an ICF target. On this basis, DT ignites as about 4.5 keV. A glass foam at density 0.1 g/cm³ has an ignition temperature of about 14 keV; a CH foam at density 0.05 g/cm³ ignites at about 7 keV.

Instead of such advantage of CRYFAT, no experimental data about implosion has been reported yet. When CRYFAT is considered to be a candidate for a reactor level target, it is essential to conduct an experiment using this target.

This chapter presents the first successful implosions of CRYFAT using the 10kJ GEKKO XII ($\lambda = 527$ nm) laser system.^[6] A variety of observations has been made to study laser target coupling in imploded plasmas, implosion dynamics, and thermo-nuclear fusion processes.

Experimentally areas covered in Section 6-3 include: (1) absorption and nonlinear laser interaction such as SRS and SBS (2) Implosion velocity and symmetry and (3) ion temperature, neutron yield, and fuel areal density of imploded core.

In Section 6-4 we discussed the preheat effects on implosion dynamics and thermo-nuclear fusion property comparing with one dimensional hydrodynamic simulation and simple models which are taken account of the experimental result with planar target as shown in Chapter 5. Finally we propose some ideas for efficient implosion with CRYFAT using simulation.

§6-2. Experimental Set up

Implosion experiments were performed using the 12-beam GEKKO XII laser facility. Laser condition is summarized on Table 6-1. Each 35 cm-diameter beam was focused onto a CRYFAT uniformly at an energy level of

Table 6-1. Laser conditions for the implosion experiments.

Wavelength	0.527 μm
Pulse Duration	1~1.3 nsec
Energy (12 beams)	5~10 kJ
Beam Energy Balance	1~2 %
Intensity on Target	$\sim 10^{14}$ W/cm ²
Irradiation Nonuniformity	~ 10 %

Table 6-2. Polystyrene foam sell conditions

Density	50 mg/cm ³
Sell Diameter	0.7~1 mm
Shell Thickness	20~50 μm
Shell Sphericity	> 90 %
Porous Size	$\phi = 3\sim 5$ μm $l = 5\sim 10$ μm
Shell Thickness Nonuniformity	< ± 5 %

5~10 kJ with a 1~1.3 nsec Gaussian-like temporal profile. Most of focusing condition was $D/R = -5$, where D was the distance between the beam waist and the target center, and R is the target radius. The minus sign indicates

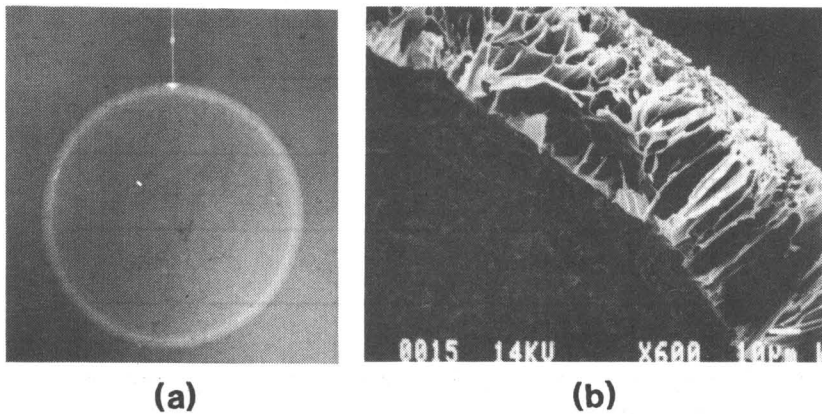


Fig. 6-3 (a)X-ray picture of a plastic foam shell target. (b)SEM picture of a plastic foam shell wall. Cells are several microns in diameter, and tend to be long in the radial direction.

the best focus point of the beam placed beyond the target. Incident laser intensity on target was several times 10^{14} W/cm². Beam energy balance was 1 - 2%. An intensity distribution at an equivalent target plane showed ± 30 % intensity modulation with a typical spatial scale length of 60 μ m.

A new system for fabricating CRYFATs was developed and was installed on the experimental vacuum chamber.^[7] A CH (plastic) foam target suspended with a 5 μ m ϕ stalk was dipped into liquid deuterium in a small quartz pot. The liquid deuterium was filled both in the cells of wall and the cavity in this way. In order to push out the liquid deuterium from cavity and fill only the cells of wall with it, we made use of boiling bubbles came out from the target. A heater surrounding the pot controlled the boiling. The filled liquid deuterium mass was measured using a resonance frequency of vibration of the stalk and shell target system.^[8] After those processes the surrounding deuterium gas was evacuated to a pressure of the triple point keeping the temperature of outside of pot at 5~7 °K in order to hold deuterium ice. The laser shot was performed after the fuel layer thickness was measured again and then the quick removal of the shroud following the evacuation of the residual gas. Note that in the above processes only a little amount (5%) of deuterium in target sublimates and the specific volume of the solid deuterium is smaller than that of the liquid.

Table 6-3. Diagnostics for implosion experiments.

Parameter	Diagnostics
I n t e r a c t i o n	
Absorption	A Set of Plasma Calorimeters
SBS	Spectrometer + Streak(S-20)
SRS	Spectrometer + Streak (S-1)
Implosion Dynamics	
Implosion Time & Velocity	X-ray Streak Camera
Implosion Symmetry & Velocity	X-ray Multi-framing Camera
Core Parameter	
Ion Temperature	Neutron Time of Flight
Number of Neutron Yield	Ag Activation & Scintillation Counters
Fuel Areal Density	Ratio of the Secondary-Nuclear-Reaction Neutrons

Polystyrene foam shells were fabricated by the phase separation method^[7]. Summarized on Table 6-2 are the conditions of used foam shells. Diameters and shell thickness of CRYFAT were 700~1000 μm and 25~40 μm , respectively. Porous sizes were typically several microns, but each cell is long in the radial direction. Shown in Fig. 6-3 are the typical cross sectional and SEM views of a foam shell. With the current target fabrication technique, the variation of the shell thickness remains still of the order of \pm

5 μ m. The observed radially oriented patterns of foam cells were formed during the crystalization process in a freeze-dry technique.

Diagnostics employed in the experiment were as follows and summarized on Table 6-3. A set of plasma calorimeters measured the absorbed fraction of the incident laser energy. Backscattered light was spectrally and temporally resolved to look for any sign of SBS and SRS as well as those energies were monitored as shown in Chapter 5. Time integrated images were taken for $\lambda=263$ nm (the second harmonic of the laser wavelength), $\lambda=351$ nm (the 3/2rd harmonic of the laser wavelength), and $\lambda=2.5$ nm (x rays). Implosion dynamics was monitored using an x-ray streak camera and x-ray framing camera. The number of neutrons was measured by Ag activation and scintillation counters while fuel ρR was estimated measuring the ratio of the secondary-nuclear-reaction neutrons to the primary (Secondary reaction method in DD fuel) ^[9]. The ion temperature was measured by the neutron time of flight method.

§6-3. Experimental Results

6-3-1. Laser interaction

Laser energy absorption was measured by 20 plasma calorimeters uniformly distributed on the inner wall of the vacuum chamber. Results are shown in Fig. 6-4, where 1-D simulation (HISHO) ^[10] and previous results with glass microballoons (GMB) ^[11] were also shown. In the simulation uniform irradiation ($D/R=-5$) condition with a flux limit of $f=0.3$ were assumed for CRYFATs[6]. As can be observed in the figure, results with CRYFATs show 40~50 % absorption at laser intensities of around several times 10^{14} W/cm², while CRYFATs with CMC overcoat layer (~ 5 μ m) show 50~60 % absorption. GMB results show absorption consistently higher than the CRYFAT due to the atomic number (Z) effect. Overall tendency of absorption with the pump intensity is in good agreement with the simulation results. Since in these simulation results nonlinear effect such as SRS or SBS is not included, it is indicative that absorption is fairly classical. In

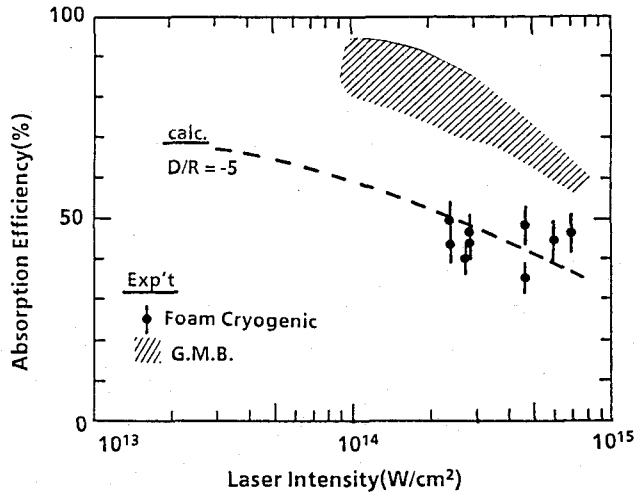


Fig. 6-4 Laser light absorption versus laser light intensity. The dotted line shows a result of 1-D HISHO simulation with $f=0.6$. The closed and open circles indicate CRYFATs without and with plastic overcoat. The hatched region indicates that previous experimental results with glass micro balloon targets. Laser energy was ~ 10 kJ with a 1 nsec Gaussian pulse at $\lambda_L = 527$ nm.

time resolved backscattered light spectroscopy, which will be shown in the following, there is no evidence of SBS observed.

In the experiment a density scale length (L_n) is inferred from time integrated pictures of both second ($\lambda = 263$ nm) and 3/2rd ($\lambda = 351$ nm) harmonic light. The second harmonic light is to come from the critical (n_c) region, while the 3/2rd light stems mainly from $n_c/4$ region. For a typical shot ($I_L = 3 \times 10^{14}$ W/cm², $E_L = 10$ kJ, and $\tau_L = 1$ nsec), L_n was estimated to be 80 μ m from the pictures, while the spot size was approximately equal to the target diameter (≈ 1 mm). Thus it may be assumed that plasmas produced for these shots are fairly one dimensional. With this L_n , a fraction due to classical absorption in a 1-D deuterium plasma can be calculated to be 50~60 % with an analytic model as ^[12]

$$\eta_{abs} = 1 - \exp \left[-\frac{8}{3} \frac{v_{ie}}{C_s L_n} \right], \quad (6-1)$$

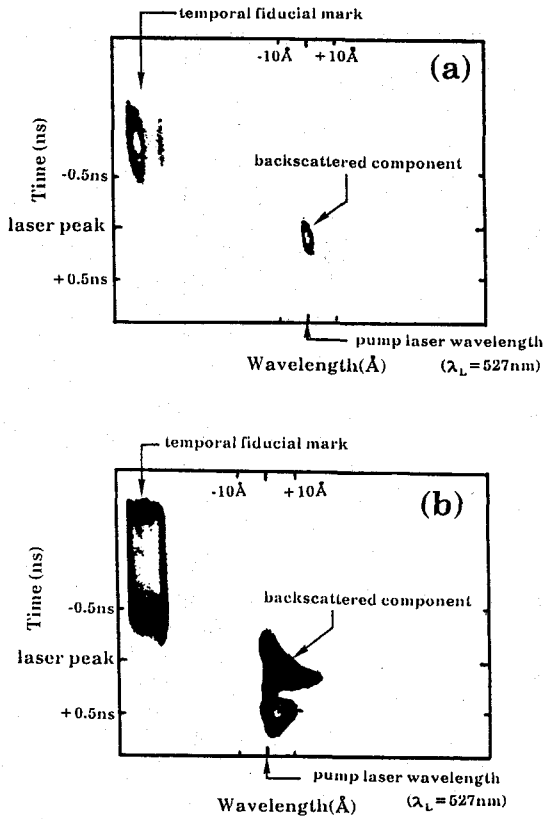


Fig. 6-5 (a) Time resolved backscattered spectrum from CRYFAT. The spectrum shows a red shift, indicating that the n_c region going inward with target compression. The order of the spectral broadening is similar to the amount of the spectral shift, indicating that the backscattered light has only a specular component.

(b) Time resolved backscattered spectrum from a foam shell target. The spectrum shows a very strong modulation in both time and wavelength. Actual spectral broadening becomes more than 100nm, which can be more clearly seen in Fig. 5-2(c).

where ν_{ie} is the electron ion collisional frequency. In this calculation a temperature $T_e = 750\text{--}800\text{ eV}$ at around n_c was used, which was estimated from charge collector signals. This estimation shows a slightly higher absorption, since effects of refraction are not included.

Time resolved backscattered light was temporally and spectrally resolved from one of twelve beams to monitor if there is any evidence of nonlinear scattering processes such as SBS and filamentation [13]. Detailed experimental set up was presented in Section 5-2. In Fig. 6-5, typical data of backscattered light are shown from CRYFAT (a) and a spherical foam shell target without any deuterium (b). One might expect that very strong SBS may occur for foam shell target and/or CRYFAT, since the surface of these targets are covered by porous materials and these structures may well work as initially-imposed density perturbations. Indeed we observed that SBS

from a foam shell target without D₂ was strongly modulated in both time and spectrum as shown in Fig. 6-5(b). The temporal oscillation was strongly correlated with both the spectral broadening and the spectrum of SRS, which has been seen clearly in Fig. 5-2(b) and discussed in Section 5-2. For CRTFAT in Fig. 6-5(a) the backscattered spectrum appeared to be fairly classical, showing only an acoustic broadening of the order of $\Delta\lambda/\lambda = 2C_s/C \approx 10^{-3}$. This small broadening is due to Doppler broadening^[14]. If this backscattered light includes a component of SBS, we should see a strong backward collimation and consequently see a large fraction of backscattered energy. The fraction of backscattered light was relatively small ($\leq 3\%$ of the total incident laser energy). We consider that the surface of CRYFAT could be covered by a liquid or solid layer of D₂ on the laser irradiation. Thus no more effect of porous appears in the backscattered spectrum. We can estimate a time history of the turning point using^[15]

$$\frac{\Delta\lambda}{\lambda} = 2 \left[-\frac{X_c}{C} - \frac{2(1-\ln 2)C_s}{C} \right], \quad (6-2)$$

which includes Doppler effects from both turning point and plasma flow. Since the backscattered light in the spherical illumination come mainly from the n_c region, we can have an absolute time history of the critical density (*i.e. we have a time fiducial for this set-up*).

In Fig. 6-6, a temporally resolved SRS spectrum is shown as well as x-ray streak camera picture. SRS light had its intensity peak right at the implosion. After the implosion there was still SRS continuing. Approximately two thirds of total SRS energy was before the implosion, while one third after the implosion. It is critical to note that the amount of SRS contributing to the degradation of the implosion is that before the laser peak, not after nor time integrated value. Time integrated values of SRS energy had been discussed in most of literatures, but it is always necessary to carry out time resolved SRS calorimetry and to compare SRS time history with the implosion time history.

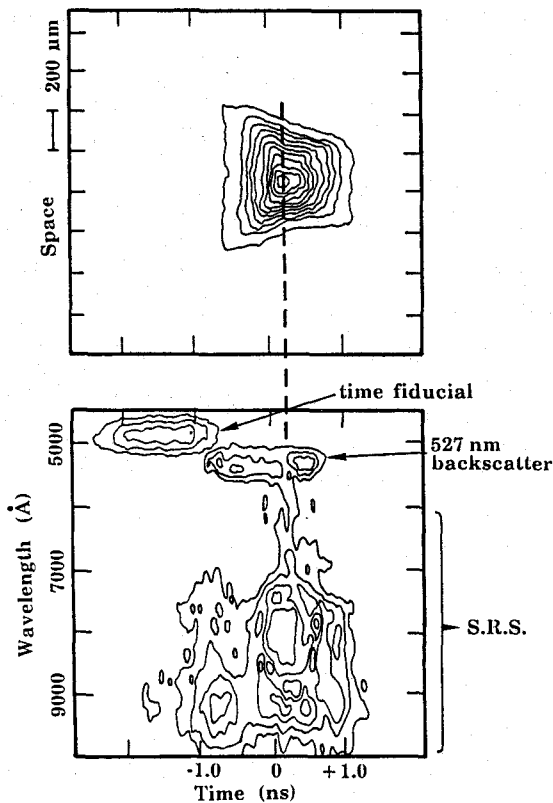


Fig. 6-6 Significance of SRS for implosion. Time resolved both SRS and imploding x-ray pictures show the temporal relation of each other. Two thirds of SRS occurred before the maximum compression.

6-3-2. Implosion dynamics

Figure 6-7 shows typical x-ray pinhole camera images for normal density CD shell target ($\rho = 1.1 \text{ g/cm}^2$, $Z = 3.5$), CRYFAT ($\rho = 0.2 \text{ g/cm}^2$, $Z = 1.2$), and plastic foam shell without D_2 ($\rho = 0.05 \text{ g/cm}^2$, $Z = 3.5$). Shell diameter was almost same to be $740 - 780 \text{ }\mu\text{m}\phi$. Areal density of foam shell without D_2 (0.2 mg/cm^2) was too low to be ablatively imploded, resulting that the shell was explosively imploded and x-ray emission was low level. On CD shell and CRYFAT the areal mass density was the same ($0.6 - 0.7 \text{ mg/cm}^2$) and both targets were ablatively imploded.

From these images the compressed core size of the CRYFAT ($230 \text{ }\mu\text{m}\phi$) was 1.5 times as large as that of normal density CD shell target ($150 \text{ }\mu\text{m}\phi$).

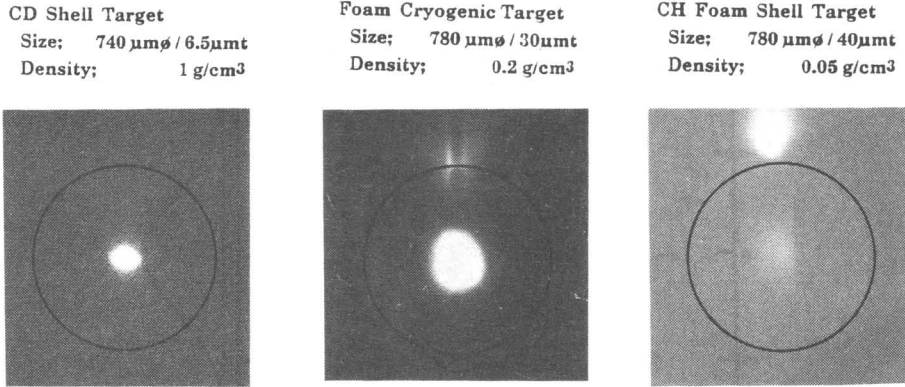


Fig. 6-7 Typical x-ray pinhole camera images for normal density CD shell target ($\rho = 1.1 \text{ g/cm}^3$, $Z = 3.5$), CRYFAT ($\rho = 0.2 \text{ g/cm}^3$, $Z = 1.2$), and plastic foam shell without D₂ ($\rho = 0.05 \text{ g/cm}^3$, $Z = 3.5$). Laser conditions: $E_L = 9 \text{ kJ}$, $\tau_L = 1 \text{ nsec}$, and $d/R = -5$.

Note here that x-ray emission size is not exactly equal to the core size because the emissivity strongly depends on the material, temperature, and density. However above difference (1.5 times) cannot be explained with emissivity difference. This difference of core size may be due to the differences of the initial density, shell thickness and/or target sphericity.

Assuming that the shell adiabatically expand with sound speed in inertial phase (from time t_i), the sound speed (C_s) when inner surface of shell reaches at the center (t_c) is approximately given by ^[16]

$$\zeta^2 + (1/3\beta - \zeta_i \beta^{1/3})\zeta - \zeta_i \beta^{1/3} = 0, \quad (6-3)$$

where $\zeta = C_s/V_a$, $\zeta_i = C_i/V_a$, and $\beta = 3\Delta r_i/R_i$. V_a , C_i , R_i . and Δr_i are implosion velocity, initial sound speed, diameter and shell thickness at t_i , respectively. Initial sound speed depends on shock heating and that in CRYFAT is about two times larger than CD shell from Eq. 2-9. Then the radius at t_c is

$$r_c = \frac{\zeta R_i + \Delta r_i}{1 + \zeta} \quad (6-4)$$

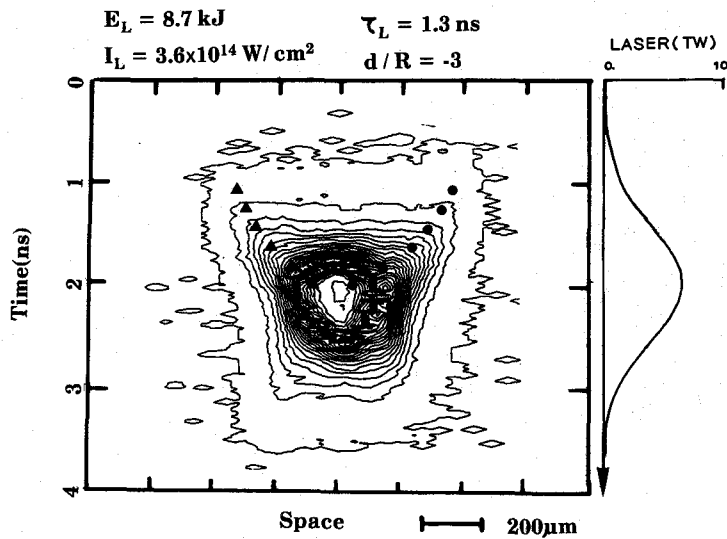


Fig. 6-8 Shell motion of imploded CRYFAT with x-ray streak camera having one dimensional spatial resolution. Iso intensity contours show and x-ray image of imploding CRYFAT. Triangles and circles indicate the ablation front from 1-D simulation with and without preheat. Experimental conditions: $I_L = 4 \times 10^{14} \text{ W/cm}^2$, $\tau_L = 1.3 \text{ nsec}$, and $770 \mu\text{m}\phi/30 \mu\text{m}^t$ target.

At the same areal mass density the implosion velocity is almost same assuming the absorption is the same. ζ of the CRYFAT is about two times larger than that of CD shell because of initial sound speed difference depending on the initial density. Δr_i of the CRYFAT is also several times (< 5) larger than that of CD shell. Thus the r_c of the CRYFAT will be about 1.8 times larger than that of CD shell. While this estimation may be too simple to give an exact core size, the final core size will depend on the initial thickness and density.

1-D simulation without hot electron preheat also indicates that the x-ray emission region of the CRYFAT is about 2.5 times larger than that of CD shell. However absolute value from 1-D simulation was much smaller than experimental results for both targets. This discrepancy may come from target sphericity, laser uniformity, fluid instability and/or preheat effect. The preheat effect is discussed in Section 6-4.

The implosion velocity was measured by an x-ray streak camera, whose typical image of CRYFAT is shown in Fig. 6-8. This image shows the one

dimensional spatial and time resolutions. The streak camera had no time fiducial and absolute time zero was determined within time jitter of streak camera by taking shots of 100 psec laser pulse duration. From this image the implosion velocity was $4 \pm 0.5 \times 10^7$ cm/s at $I_L = 4 \times 10^{14}$ W/cm² and $\tau_L = 1.3$ nsec (FWHM) with $770 \mu\text{m}\phi / 30 \mu\text{mt}$. 1-D simulation results are also predicted in Fig. 6-8; circles are ablation front without hot electron preheat and triangles are with preheat taking account of the experimental results with plane targets as mentioned in Sec. 5-4. While there is slightly difference in the implosion velocities with (4.5×10^7 cm/s) and without preheat (5×10^7 cm/s), the experimental result is in agreement with simulation results within measurable error.

Implosion symmetry was measured with an x-ray framing camera. Figures 6-9 (a) and (b) show the framing images of CRYFAT and normal density CD shell implosion properties at laser energy of 4.2 kJ on target, respectively. The areal density of both targets was same to be 0.9 - 1.0 mg/cm² (The thickness of CRYFAT and CD shell was 40-45 μmt and 8.3 μmt , respectively). This x-ray framing camera gave 9 channel images and had no time fiducial. Numbers on the right shoulder indicate the frame sequence. Time interval of each image was 170 psec and temporal exposurer response in each channel was 80 psec (FWHM) which was not square.^[17] Then If strong signals are input into a channel, some signals may appear in neighbor channels due to temporal tail of its response. X-ray spectral response depends on the gold cathode and Al-Be filter and obtaining signals were mainly 1 - 2 keV energy photon. Simulation indicates such photon energy imaging shell structure in Fig. 6-10 mostly is emitted from the area between the ablation front and critical point.

Both images for (a) CRYFAT and (b) CD shell indicate that the shell is imploded symmetrically and implosion dynamics is almost same. Implosion velocity was consistent with the results from the x-ray streak camera and the simulation. It should be noted that the center emission (pre-emission) appeared before the maximum compression even considering the problem of temporal shape of response. For the CRYFAT the pre-emission appeared more than 340 psec before the maximum compression. This time was much earlier than the time of normal density target. This early center emission is

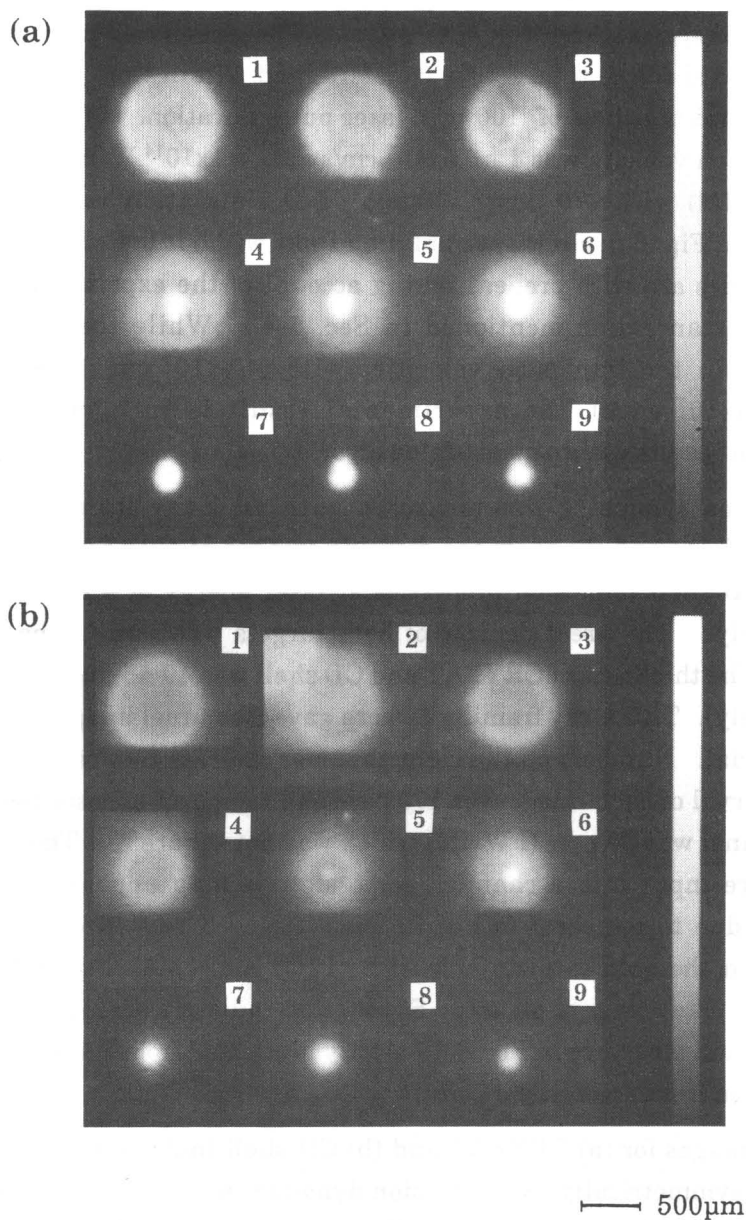


Fig. 6-9 Typical x-ray framing camera images of (a) CRYFAT and (b) normal density CD shell target. Numbers on right shoulder indicates the frame sequence. Time interval of each image is 170 psec and temporal exposur response is 80 psec (FWHM). Experimental conditions: $E_L = 4.2$ kJ, $\tau_L = 1$ nsec, and $\rho\Delta R = 0.9 \sim 1.0$ mg/cm².

explained as the effects of preheating and delayed arrival time of shock wave to the inner surface of the shell wall. Detailed explanation about this dynamics is in the following discussion.

6-3-3. Thermo-nuclear fusion property

Fig. 6-10 shows the ion temperature obtained by time of flight method.^[18] The ion temperature increases with decrease of target thickness. The target diameter was almost constant and the aspect ratio increased with decrease of target thickness. The implosion velocity (kinetic energy) increases with decrease the target thickness^[19] and ion temperature will also increase with decrease of thickness. Comparing with 1-D simulation, the ion temperature was almost same as the average of the inner four meshes. The inner four meshes correspond to a part of the precursor plasma.

The neutron yield and the fuel areal mass density (ρR) of the compressed core for CRYFATs are shown in Figs. 6-11 and 6-12. The experimental results for CRYFAT were almost same with those of normal density target at normal laser beam (without random phase plate). The maximum neutron yield and ρR were 8×10^8 DD neutrons and 10 mg/cm². 1-D hydrodynamic simulation (HISHO) results are also presented for solid and dotted lines with and without electron preheat, respectively. Either with or without preheat the simulation results are higher than experimental results. The neutron yields from simulation with and without preheat are 5 and 75 times as high as experimental results. ρR s from simulation with and without preheat are also from several to several hundred times as large as experimental results. Especially the discrepancy of ρR increases with decrease of target thickness. Even though the ρR from simulation with preheat is slightly reduced with decrease of target thickness because the inner region of shell tends to be preheated for thinner target, such discrepancy in thinner target cannot be explained by only preheat effect. These reduction of neutron yield and ρR may be caused by the degradation of the implosion symmetry. Shell implosion velocity or acceleration increases with initial aspect ratio i.e., decrease of target thickness, resulting thinner target will be sensitive to the fluid instability (Rayleigh-Taylor instability)^[20].

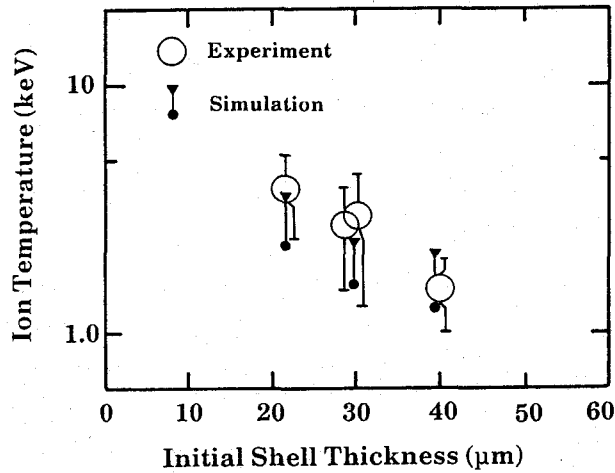


Fig. 6-10 The ion temperature obtained with neutron time of flight versus shell thickness. Closed circles indicate the simulation result with electron preheat.

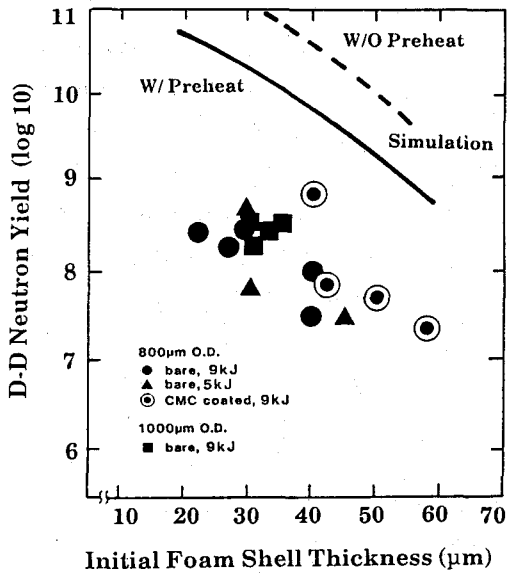


Fig. 6-11 Neutron yield as a function of shell thickness of CRYFAT. Solid line and broken line indicate the simulation results with and without electron preheat.

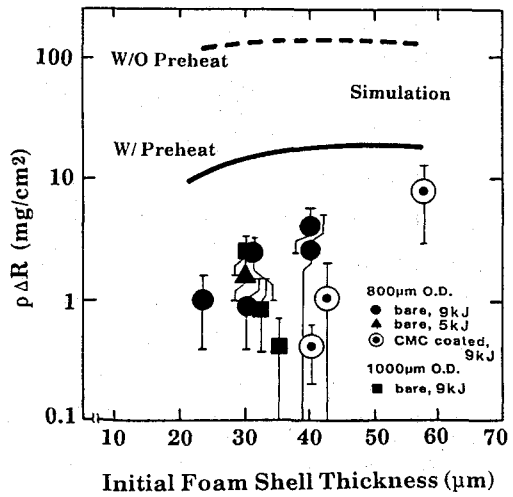


Fig. 6-12 Fuel areal mass density (ρR) of compressed core versus shell thickness. Solid line and broken line indicate the simulation results with and without electron preheat.

§6-4. Discussion

6-4-1. Implosion dynamics

We consider the preheat effect on implosion dynamics. Figures 6-13 (a) and (b) are the flow diagrams of CRYFAT without and with electron preheat. Laser light with the amount energy of 8 kJ is focused onto a $800\text{ }\mu\text{m}\phi / 40\text{ }\mu\text{m}$ target. Hot electron are artificially produced by resonance absorption. The temperature and the energy of hot electrons are 5 keV (average) and 20% of absorbed laser energy whose values are chosen to fit the preheating level to the experimental results with planar CRYFAT as mentioned in Section 5-4.

The implosion velocity with this preheat is 2.9×10^7 cm/s and 3.2×10^7 cm/s without preheat. If high energy electrons are produced at the laser irradiated side the absorbed energy is diffused to target inner region over the ablation front, resulting that the ablation pressure is reduced. Then the implosion velocity with hot electron preheat is slightly reduced compared with that without preheat.

Compressed core size with preheat is 2 to 3 times larger than that without preheat. The shell thickness in flight is also strongly different. The internal energy in shell increases with preheat and the shell expand with the speed depending on the internal energy. Then the precursor plasma is produced in the target by expanding inner surface of shell wall. This precursor plasma reaches the center at a few hundred psec before arriving of shell at the center. The pre-emission at the center as shown in Fig. 6-9 (a) will be influenced by this precursor plasma.

One approach to the data of the framing camera as in Fig. 6-9(a) is to compare with shell dynamics from theoretical functions which were established by previous fundamental experimental results (ablation pressure scaling to the laser intensity as determined in Sec. 5-3, shock breakthrough time measured in Secs. 5-3 and 5-4, and preheat performance obtained in Sec. 5-4). This approach has been tried with reasonable success. The procedure is carried out by formulating the equations of motion (the rocket equation, which arise from Newton's second law) using theoretical relations of

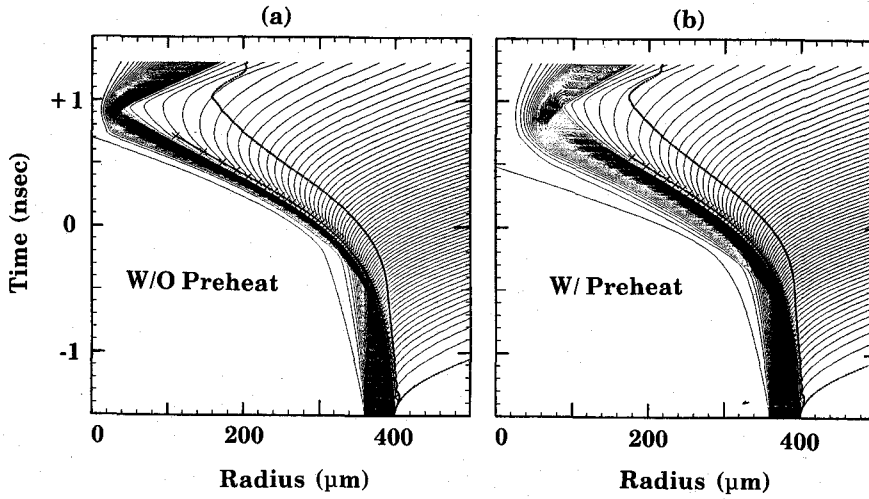


Fig. 6-13 Flow diagrams of CRYFAT with and without electron preheat. Condition: $E_L = 8 \text{ kJ } 800 \text{ } \mu\text{m}\phi / 40 \mu\text{m}$ target. Hot electrons are artificially produced by resonance absorption. The temperature and the energy of hot electrons are 5 keV (average) and 20% of absorbed laser energy whose values are chosen to fit the preheating level f to the experimental results with planar CRYFAT as mentioned in Section 5-4

$$M(t_n) \frac{dv_n}{dt} = -4\pi R(t_n)^2 P_a(t_n) \quad (6-4)$$

with

$$M(t_n) = M_0 - \int_{-\infty}^{t_n} 4\pi R(t)^2 \dot{m}(t) dt \approx M(t_{n-1}) - 4\pi R(t_n)^2 \dot{m}(t_n) \Delta t, \quad (6-5)$$

where $\Delta t = t_n - t_{n-1}$. $P_a(t)$, $\dot{m}(t)$, and $R(t)$ are ablation pressure, mass ablation rate, and shell radius, respectively. For quasi-acceleration model, it is reasonable assumption that $P_a(t)$, $\dot{m}(t)$, and $R(t)$ are constant between short time interval Δt (Here Δt was 100psec). Then the solution of Eq. 6-4 is the well-known equation

$$v(t_n) = \int_{-\infty}^{t_n} \frac{dv}{dt} dt \approx \frac{P_a(t_n)}{\dot{m}(t_n)} \ln \left[\frac{M_0}{M(t_n)} \right] \quad (6-6)$$

Thus the position of shell is obtained by integrating Eq. 6-6.

$$R_0 - R(t_n) = \int_{-\infty}^{t_n} v(t) dt \approx \sum_0^{n-1} v(t_n) \Delta t \quad (6-7)$$

The ablation pressure scaling to the time was used from the experimental results of x-ray backlighting method (Sec. 5-3) and maximum pressure from the experimental results of shock breakthrough method with planar CRYFAT (Sec. 5-4) as given by

$$P_a(t) = 20 \exp \left[-1.52 \left(\frac{t(\text{psec})}{800} \right)^2 \right] \quad (\text{Mbar}) \quad (6-8)$$

If the steady flow model is used in the time interval of Δt (100psec), the mass ablation rate is also obtained from the equation of mass and energy conservation describing the plasma flow as^[21]

$$P = 2 \rho_c c_0^2 \quad , \quad (6-9)$$

and

$$\dot{m} = \rho_c c_0 \quad , \quad (6-10)$$

where ρ_c and c_0 are critical density and the sound speed, respectively. Eqs. 6-9 and 6-10 give the mass ablation rate as

$$\dot{m}(t) = \left[\frac{\rho_c P_a(t)}{2} \right]^{1/2} = 4 \exp \left[-0.76 \left(\frac{t(\text{psec})}{800} \right)^2 \right] \quad (\times 10^5 \text{ g/cm}^2/\text{s}) \quad (6-11)$$

Thus the shell position is determined by Eq. 6-6, 6-8, and 6-11. The time beginning to move of target depends on the shock break through time. The

shock speed and shock front position are given by Eqs. 2-9 and 6-8 for strong shock wave. Ablation surface and its position are also determined by Eqs. 2-14, 6-8. After starting to move the shell, the coordinates of the ablation front is assumed to be on the shell movement.

The Shell expands with increasing of internal energy by preheat. Trajectory of the precursor plasma of inner surface in the shell wall depends on the preheat temperature or sound speed. Let us consider the motion of this inner surface by the centered rarefaction wave. From Euler's equation for plane coordinate in isentropic flow, the expansion plasma dynamics is solved by the self-similar solution [22]. Here exactly we have to solve the equation with the spherical coordinate. However if sound speed is not so much larger than shell implosion speed, the plane coordinate will be applied on the shell movement for quasi-steady state model (in short time i.e. $\Delta t = 100 \text{ psec}$). Then the self-similar solution gives the expansion speed v_x of a certain density (ρ_x) region as

$$v_{xn}(t_n) = |s| C_0(t_n) , \quad (6-12)$$

where $\rho/\rho_0 = (s+3)^3/64$. C_0 and ρ_0 are initial sound speed and density. The position of expanding plasma is

$$R_x(t_n) = \{R_0 - R(t_n)\} - \sum_0^{n-1} v_{xn}(t_n) \Delta t . \quad (6-13)$$

Figure 6- 14 shows the flow diagram of CRYFAT (the same laser and target conditions with those in Fig. 6-9(a)) obtained from 1-D simulation and above model taking account of experimental results of ablation pressure scaling, shock speed, and preheat level. The points of the expansion front and 1/10 times solid density region are shown for precursor plasmas. Above model estimations such as shell and precursor position are in good agreement with the simulation with electron preheat. The experimental points of shell and pre-emission time from an x-ray framing camera are also expressed in Fig. 6-14. Shell speed from the framing camera agrees well

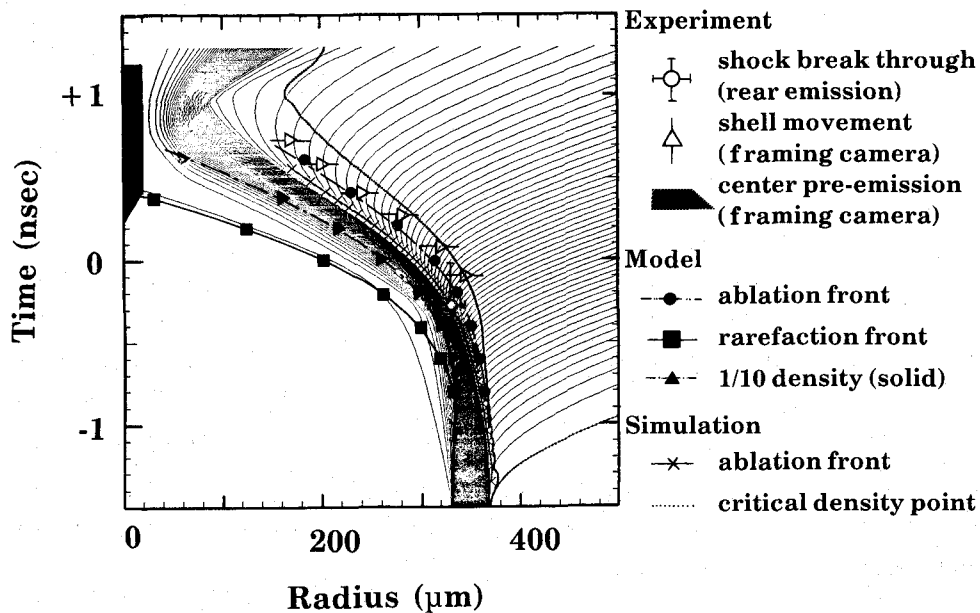


Fig. 6-14 Flow diagram of imploding CRYFAT obtained from 1-D simulation and analytical model at the same laser and target conditions with Fig. 4-9(a). Closed circles, squares, and closed triangles indicate the ablation front, rarefaction front, and 1/10 shell density from analytical model, respectively. The model was taken account of the fundamental experimental results (laser intensity scaling of ablation pressure in Sec. 5-3, shock breakthrough time in Secs. 5-3 and 5-4, and preheat performance in Sec. 5-4). Crosses are ablation front from the simulation. Simulation includes the electron preheat with the temperature of 5 keV and the 20% energy of absorbed laser energy. Open circle and triangles are experimental results of shock breakthrough time from the rear side emission and shell movement from x-ray framing camera. Shaded zone indicates the center preemission from the framing camera.

with the simulation result and model estimation. Pre-emission in the center appear near at the time when the precursor plasma reaches center. Hence the pre-emission in Fig. 6-10 is created by precursor plasma which strongly depends on the preheat.

6-4-2. Thermo-nuclear fusion property

In order to consider the thermalization in the core, we consider the energy conservation

$$\frac{1}{2} m v^2 + \frac{3}{2} k (T_i + T_e) = \frac{3}{2} k (T_{ef} + T_{if}) = \frac{3}{2} k \left(\frac{1}{\beta} + 1 \right) T_{if} , \quad (6-14)$$

where v , T_i , and T_e are the implosion speed, the ion and electron temperatures before compression(initial internal energy) and T_{if} and T_{ef} are the ion and electron temperatures after compression(final internal energy). The shell in the flight is isothermally heated then $T_i \approx T_e$. The kinetic energy in the shell transfer to the internal energy after compression i.e., the electron will be thermalized. Just at the time to reach center for shell we assume that the ion temperature is larger than electron temperature by thermalization factor β . Then Eq. 6-14 gives

$$\beta = \frac{k T_{if}}{\left\{ \frac{1}{2} m v^2 + 2k T_e \right\} - k T_{if}} . \quad (6-15)$$

For example at the implosion speed (v) of 4.2×10^7 cm/s the ion temperature (T_{if}) was about 2 keV. The electron temperature (T_e) just before arriving of first mesh at center is about 400-500 eV and 100-150 eV from the simulations with and without preheat, respectively. Then from Eq. 6-15 the thermalize factor is estimated to be 1.5~1.9 and 5.3~8.3 with and without preheat, respectively. If the preheat is large, energy in the target exists as internal energy, resulting that the core is thermalized to some degree and β becomes small. Either with or without preheat measured neutron may be yielded when the imploded core is not enough thermalized because the ion temperature is determined by neutron time of flight.

Figure 6-15 show the preheat effects on the temporal history and magnitude of ρR , neutron yield, and neutron production rate from the simulation. Experimental results do not correlate with simulation results

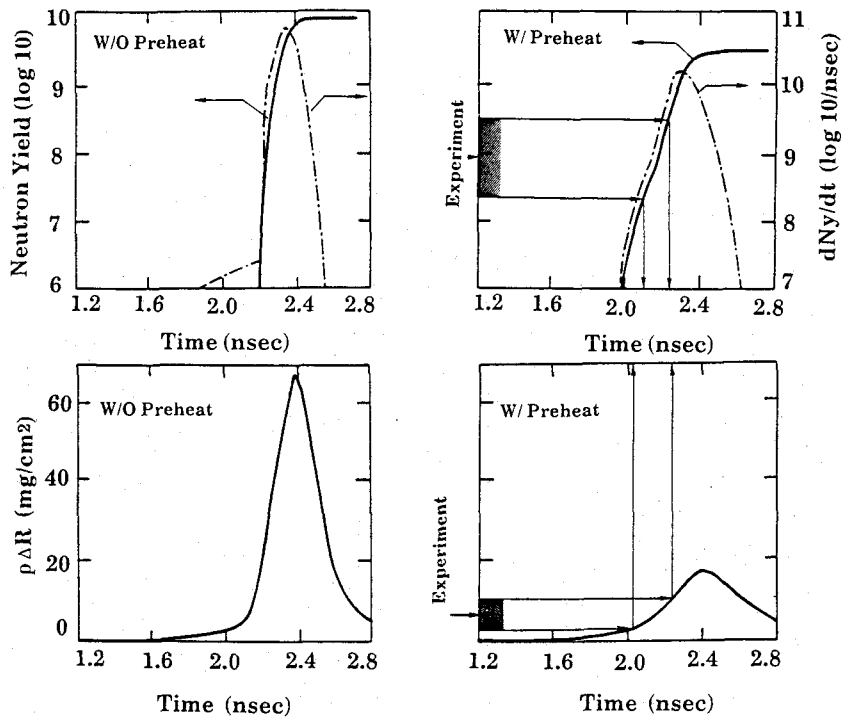


Fig. 6-15 Electron preheat effects to ρR , neutron yield, and neutron production rate from the simulation. Shaded zone indicates the experimental results.

without preheat. However with preheat there are temporal humps in the neutron yield and its production rate in simulation results. The humps are temporally corresponding to the time from inner first mesh arriving time at center to start of stagnation. Experimental results (ρR and neutron numbers) are in good agreement with the values at this hump. In this region the core is not enough thermalized and this agreement is consistent with discussion about ion temperature. In order to achieve better performance in thermo-nuclear fusion except for preheat effect, more symmetrical implosion will be necessary.

6-4-3. Ideas of efficient implosion with CRYFAT

Above experimental results indicates that the preheat by shock wave and high energy electron is important for implosion of CRYFAT.

Since the mass density of CRYFAT is significantly lower than those of the other solid materials, the laser ablation pressure generates a very strong shock wave to cause the shell disassembly when the ablation pressure rise rapidly. Therefore it is necessary to shape the pressure pulse tailoring. Without high energy electron preheat pressure pulse tailoring is simply estimated and controllable with laser pulse tailoring. For example to require the efficient implosion, the intensity ratio (maximum intensity to foot pulse intensity) is from 40 to 150.^[23] However in low-Z material we have to also note the high energy electron preheat as mentioned in Sec. 5-4.

There are several possibilities to satisfy above requirements using

- (1) short wavelength laser (high pressure and low electron temperature)
- (2) pulse tailoring (reduction of shock heating and additional acceleration)
- (3) higher-density ablator (reduction of shock heating)
- (4) higher-Z ablator or higher-Z shield (reduction of hot electron preheat).

Here to simplify the discussion we consider (2) and (3) in CRYFAT with hot electron preheat.

If there is an ablator layer of which density is sufficiently higher than the CRYFAT, the rarefaction wave on the ablator rear surface reduce the contact surface pressure, resulting the shock preheat is suppressed as mentioned in Sec.5-4 (CMC overcoated planar CRYFAT experiment). In order to avoid

Table 6-4. High density ablator effect on implosion performance

	T_s (shock)	$V_{imp.}$	ρR	N_y
Bare CRYFAT	18~20 eV	4.3×10^7 cm/s	17.6 mg/cm ²	2.6×10^{11}
CRYFAT+ High Density Ablator	14~15 eV	3.1×10^7 cm/s	17.9 mg/cm ²	2.7×10^{11}

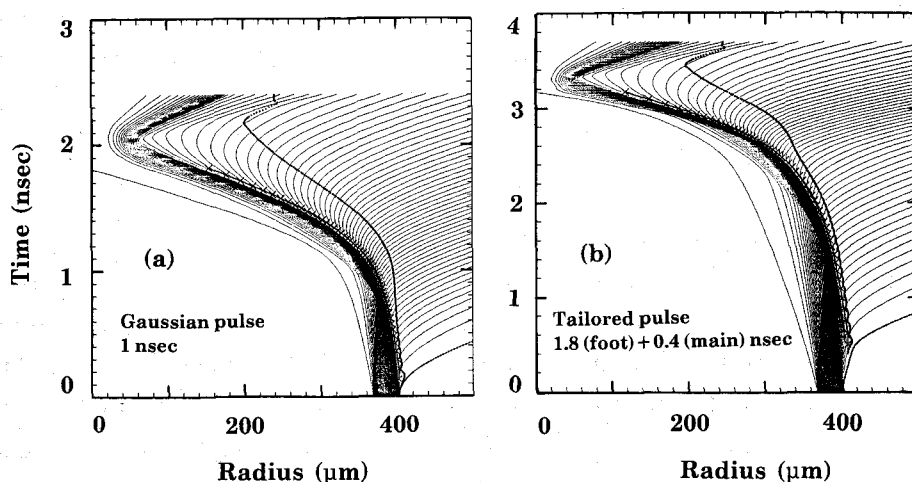


Fig. 6-16 Flow diagrams of imploding CRYFAT with Gaussian pulse (a) and tailored pulse (b). Total laser energy for both laser pulses is the same to be 700J×12. Gaussian laser pulse duration is 1 nsec (FWHM). Tailored pulse is composed of 500J×12/400psec(FWHM) and 200×12J/2.5nsec(FWHM) and the long pulse is delayed by 150 psec to the short pulse.

Table 6-5. Laser pulse shape dependence of implosion performance

	N _i (inflight) (×10 ²³ /cm ³)	V _{imp.} (cm/s)	T _i (keV)	ρR (mg/cm ²)	N _y (×10 ¹¹)
Goussian Pulse	1.3	4.3×10 ⁷	2~3	17.6	2.6
Tailored Pulse	2.2	4.5×10 ⁷	3.2~4.4	22.1	3.5

the differences of implosion dynamics due to absorption, hot electron preheat and hydrodynamic efficiency, we run the simulation with the same areal density CRYFATs (0.68mg/cm²). One of the simulations has been done with two same material (CRYFAT) and different density layer (for ablator 1.1g/cm³ (4μmt) and inner layer 0.2 g/cm³). Table 6-4 shows the shock

preheat temperature (T_s) at 600 psec before the laser peak, implosion velocity (V_i), ρR , and neutron yield (N_y). With a high density coat target, the shock preheat is reduced by shock attenuation at the boundary and implosion speed is also attenuated by the rarefaction. Therefore even though preheat is suppressed ρR and N_y are not so much improved.

Figure 6-16 and Table 6-5 shows the pulse dependences of implosion dynamics and core parameters with single (1 nsec FWHM) and two Gaussian pulses for tailored pulse. Double pulses are composed of 500Jx12/400psec(FWHM) and 200Jx12/2.5nsec(FWHM) and the long pulse is delayed by 150 psec to the short pulse. The shell with tailored pulse is imploded at a lower temperature and higher density states with implosion velocity higher compared with the single pulse. Shell thickness in flight including precursor plasmas becomes thinner with tailored pulse. As the results the thermo-nuclear property is improved.

While above simulation results may not be always optimized on laser and target condition, it will be useful to use an optimized layered target with tailored pulse. In addition to above simulation results, experimental results of CMC over-coated targets and low power shots are also some idea to reduce the preheat in the CRYFAT and to improve the implosion performance.

§6-5. Conclusion

In this chapter we present the first successful implosions of CRYFAT using the 10kJ GEKKO XII ($\lambda=530$ nm) laser system. A variety of observations has been made to study laser target coupling in imploded plasmas, implosion dynamics, and thermo-nuclear fusion processes.

Absorption was measured to be 40-50% at laser intensities of a few times 10^{14} W/cm² and SBS was found to be negligibly small.

Implosion dynamics of CRYFAT strongly depends on the preheat by shock wave and high energy electrons. We observed the pre-emission which appeared in earlier time before shell reaches center compared with normal

density target. This pre-emission will be due to the precursor plasmas produced by preheating by shock wave and high energy electrons.

Such preheat also affects the thermo-nuclear property. The maximum neutron yield and ρR were measured to be 8×10^8 DD neutrons and 10 mg/cm^2 with CRYFAT. The ρR and neutron yield were strongly reduced by preheat from simulation.

We have to reduce the preheat as well as to improve the implosion symmetry to achieve more efficient implosion. Using over-coated target and/or tailored laser pulse may be effective to suppress the preheat and efficiently implode the CRYFAT.

References

- [1] J. Nuckolls, L. Wood, A. Thiessen, and G. Zimmerman, *Nature* **239**, 139 (1972); K. A. Bruckner and S. Jorna, *Rev. Mod. Phys.* **46**, 325 (1974); R. E. Kidder, *Nucl. Fusion* **16**, 405 (1976).
- [2] R. E. Kidder, *Nucl. Fusion* **14**, 53 (1974); R. E. Kidder, *Nucl. Fusion* **19**, 223 (1979); S. M. Pollaine and J. D. Lindl, *Nucl. Fusion* **26**, 1719 (1986).
- [3] R. A. Sacks and D. H. Darling, *Nucl. Fusion* **27**, 447 (1987).
- [4] B. L. Haendler, R. C. Cook, L. M. Hair, F. M. Kong, and S. A. Ietts, *J. Vac. Sci. Technology A* **6**, 1894 (1988).
- [5] R. R. Johnson, F. J. Mayer, *Laser Interaction and Related Plasma Phenomena*, **4A**, 421 (1977).
- [6] T. Yamanaka, K. Nishihara, K. A. Tanaka, T. Norimatsu, M. Murakami, R. Kodama, Y. Kato, T. Jitsuno, M. Nakatsuka, S. Nakai, M. Nakai, and C. Yamanaka, *ECLIM '88, Madrid* (1988); *IQEC, Tokyo*, (1988).
- [7] T. Norimatsu, H. Katayama, T. Mano, M. Takagi, R. Kodama, K. A. Tanaka, Y. Kato, T. Yamanaka, S. Nakai, Y. Nishino, M. Nakai, and C. Yamanaka *J. Vac. Soc.* (1988).
- [8] H. Katayama, T. Norimatsu, Y. Kato, T. Yamanaka, and S. Nakai, *Appl. Phys. Lett.* **55**, (1989); H. Katayama, Ph. D. thesis, Osaka University (1990).
- [9] T. E. Blue and D. B. Harris, *Nucl. Sci. Eng.* **77**, 4463 (1981).
- [10] M. Murakami, and K. Nishihara, *Laser absorption in Cannonball targets for GEKKO XII system*, No. ILE-QPR-83-6, 1983, p.34, ILE, Osaka University, Osaka (1983).
- [11] H. Azechi, ILE, Osaka University (personal communication) 1988.
- [12] P. Mora, *Phys. Fluids* **25**, 1051 (1982).
- [13] K. Tanaka, L.M. Goldman, W. Seka, R. W. Short, and E. A. Williams, *Phys. Fluids*, **27**, 2960 (1984).
- [14] J. A. Tarvin and R. J. Schroeder, *Phys. Rev. Lett.* **47**, 341 (1981).
- [15] T. Dewandre, J. R. Albritton, and E. A. Williams, *Phys. Fluids* **24**, 528 (1981).

References

- [16] ILE Report on ICF reseach plan, KONGO Keikaku Kentosagyo Hokokusho, p. I-16 (1983) (unpublished).
- [17] M. Katayama, M. Nakai, and T. Yamanaka, Development of X-ray Framing Camera, No. ILE-QPR-88-25, 1988, p.42, ILE, Osaka University,. Osaka (1988).
- [18] M. Nakai, Ph. D. thesis, Osaka University (1985).
- [19] M. Murakami, K. Nishihara, and H. Takabe, *Laser and Partic Beams* **7**, 189 (1989).
- [20] J. H. Gardner and S. E. Bondner, *Phys. Fluids*, **29**, 2672 (1986).
- [21] R. Fabbro, C. Max, and E. Fabre, *Phys. Fluids* **28**, 1463 (1985).
- [22] Y. Zeldovich and Y. Raizer, *Physics of Shock Waves and High Temperature Hydrodynamic Phenomena* (Academic, New York, 1966).
- [23] K. Mima, H. Takabe, and S. Nakai, *Laser and Particle Beams* **7**, 249 (1989).

CONCLUSION

To complete this thesis, I summarize the results and discuss the significance of results that I obtained through our studies in this chapter. Studied was the energy transport for goal of efficient laser implosion of ICF target. Emphasized are laser driven shock wave, high energy electron transport, and x-ray transport.

In Chapter 3 energy transport were experimentally studied in UV-laser produced plasmas.

First studied was characteristic of x rays from laser-produced plasmas in various conditions (e.g. laser intensity, pulse duration, laser wavelength, target material, and plasma scalelength). The x-ray conversion efficiency in 263-nm laser produced Au plasmas could be as high as 80% for example.

Energy transport in UV laser produced plasmas was completed by comparing those in high-Z (Au) and medium-Z (Al) plasmas. Experiments with Al targets indicated that the energy transport mechanism could be primarily by the ablation front propagating at a slightly higher speed than the thermal conduction speed. For Au targets, the heating attributed to x radiation was clearly observed in addition to the heating by shock wave and thermal conduction. These results were reasonable with high x-ray conversion efficiency in higher atomic number plasmas produced by shorter wavelength laser.

However more effectively converted x rays may be able to preheat the cold high density region in high Z plasmas produced by UV laser. The choice for the optional driver wavelength depends on the a trade off between the increases in ablation rate and pressure and preheating due to increased x-ray generation.

In Chapter 4 radiative energy transport was experimentally studied in hot dense plasmas using laser-plasma x rays.

We obtained the experimental scaling of the x-ray heated electron temperature to x-ray intensity ($10^{12} \sim 10^{13}$ W/cm²) through XUV spectroscopy in order to give a basis of x-ray absorption for understanding the energy transport in x-ray heated plasmas. The obtained scaling was $T_e = 53 \cdot (I_x 10^{12} \text{ W/cm}^2)^{0.29}$ (eV).

X-ray energy transport was studied by measuring the temporal resolved x-ray spectra transmitted through the thin foil with double foil targets. In medium-Z plasmas (Al), ionization burn through has been clearly observed. Burn-through speed in Al was estimated to be 6×10^5 g/cm²/sec at the x ray intensity of 7.4×10^{12} W/cm². Penetration depth ($\rho \Delta R$) of radiative energy transport in Au is found to be 3-4 times larger than that in Al.

The obtained results and the discussion suggest that low-Z and medium-Z elements will easily become transparent to intense soft x rays by the ionization burn-through process. In a high-Z element strong radiative energy transport may take place through the successive processes of reemission and reabsorption. Both processes operate to that the inner part of the matter so efficiently that they may produce some difficulty in laser fusion scheme: the preheating of the fuel pellet.

In Chapter 5 we studied the energy transport by shock wave and electrons in low-Z and low-density target using mainly planar CRYFAT ($Z=1.2$, $\rho=0.2$ g/cm³).

Laser-driven shock wave in porous and low density material was studied using plastic foam target with an x-ray streak shadowgraphy. We observed clearly a shock formation in the porous targets, which was composed of two parts: a shock front and following a pile-up zone of multiple shock waves. The pile-up zone followed a thermodynamic condition closer to the adiabat than the shock front.

The energy transport in low-Z and low-density target was studied with planar CRYFAT. It was found that low-density and low-Z target such as

CRYFAT was sensitive to the preheating due to high energy electrons and also shock heating. The preheat preceding of shock heating was due to high energy electrons whose source temperature and energy was 6 keV and $10 \pm 5\%$ of absorbed laser energy, respectively. The high energy electron causing the preheat was mainly due to the nonlocal effect i.e, high energy tail of thermal electron distribution. The preheating by shock and high energy electrons were suppressed to 50% by overcoating of higher-Z and higher-density material on laser irradiated side.

In low-Z and low-density target, such strong electron preheat and shock heating may produce some difficulty in efficient laser implosion: preheating of the fuel.

In Chapter 6 we present the first successful implosions of CRYFAT using the 10kJ GEKKO XII ($\lambda = 527$ nm) laser system.

Implosion dynamics of CRYFAT strongly depends on the preheat by shock wave and high energy electron as mentioned in Chap. 5. The thermo-nuclear property such as pR and neutron yield was also affected by such preheat. The measured maximum neutron yield and pR were 8×10^8 DD neutrons and 10 mg/cm² with CRYFAT.

We have to reduce the preheat as well as to improve the implosion symmetry for more efficient implosion. Using over-coated target and/or tailored laser pulse may be effective to suppress the preheat.

The findings in this thesis about energy transport will contribute to the suppression of preheat in the ICF target to achieve highly efficient laser implosion.

Acknowledgements

The author would like to express gratitude to Professor T. Yamanaka for his excellent guidance throughout his research at the Course of Electrical Engineering and the Institute of Laser Engineering , Osaka University, Osaka, Japan.

He would like to acknowledge Professor S. Nakai, the director of the Institute of Laser Engineering for the encouragement of this study.

He wishes to thank to Professor Emeritus C. Yamanaka who strongly impressed on me the interest and mission of this study.

He is deeply grateful to Assistant Professor K. A. Tanaka for his invaluable advice and continuous encouragement throughout this investigation.

He is indebted to Professors R. Aoki, K. Matsuura, Y. Murakami, J. Shirafuji, A. Hiraki, Y. Suzuki, K. Tsuji, Y. Kato, E. Kuroda, and T. Nakajima at the Course of Electrical Engineering. He is also indebted to Professors Emeritus Y. Inuishi, H. Kinoshita, and K. Fujii.

He is grateful to Professors M. Yokoyama, K. Mima, Y. Izawa, and K. Nishihara at the Institute of Laser Engineering. He would like to thank to Dr. T. Mochizuki (former-Professor) who initiated him into experimental studies on laser produced plasmas.

His grateful thanks are to Associate Professors T. Sasaki, N. Nakajima, M. Yamanaka, Y. Kitagawa, M. Nakatsuka, Assistant Professors K. Yoshida, H. Azechi, T. Jitsuno, T. Norimatsu, H. Takabe, Associate Researcher H. Nishimura, H. Miyanaga, H. Daido, S. Miyamoto, H. Niki, E. Fujiwara, S. Sakabe, H. Shiraga, M. Nakai, K. Okada(Kinki Univ.), Dr. A. Nishiguchi and all the members of the MT, M, Target fabrication, Laser operation, and Computer groups

He would like to specially acknowledge the members of the Mp 4 (former-GPIV, M6) group.

He is grateful to everyone who provided assistance during various stages of this research.

List of Works

Publications in Journals:

- (1) *"Energy confinement effect on soft x-ray generation in 0.53- μ m laser heated cavity target."*
J. Appl. Phys., (1986), **59**, 2332.
K. Okada, T. Mochizuki, N. Ikeda, M. Hamada, M. Mineo, R. Kodama, and C. Yamanaka.
- (2) *"Soft x-ray emission from ω_0 , $2\omega_0$, and $4\omega_0$ laser-produced plasmas."*
J. Appl. Phys., (1986), **59**, 3050.
R. Kodama, K. Okada, N. Ikeda, M. Mineo, K. A. Tanaka, T. Mochizuki, and C. Yamanaka.
- (3) *"Increased x-ray emission in keV range from laser-produced plasma with use of prepulse."*
Rev. Laser Eng., (1986), **14**, 378.
R. Kodama, T. Mochizuki, K. A. Tanaka, and C. Yamanaka.
- (4) *"Laser plasma x-ray source using cryogenic target of inert atomic element."*
Rev. Laser Eng., (1986), **14**, 975.
T. Mochizuki, R. Kodama, and C. Yamanaka.
- (5) *"Enhancement of keV x-ray emission in laser-produced plasmas by a weak prepulse laser."*
Appl. Phys. Lett., (1987), **50**, 720.
R. Kodama, T. Mochizuki, K. A. Tanaka, and C. Yamanaka.
- (6) *"Experimental evidence of ionization burn-through and absorption resonance in radiative energy transport in hot dense matters."*
Phys. Rev. A, (1987), **36**, 3279.
T. Mochizuki, K. Mima, N. Ikeda, R. Kodama, H. Shiraga, K. A. Tanaka, and C. Yamanaka.
- (7) *"Population inversion in laser-produced plasmas stagnating on a radiative coolant of solid density."*
Opt. Lett., (1987), **12**, 990.
R. Kodama, and T. Mochizuki.

- (8) "Energy transport in aluminum targets irradiated by a 263-nm laser."
Appl. Phys. Lett., (1988), 52, 786.
A. Yamauchi, K. A. Tanaka, R. Kodama, M. Kado, T. Yamanaka,
T. Mochizuki, S. Nakai, and C. Yamanaka.
- (9) "Enhancement of soft x-ray emission using prepulse with 2ω and 4ω laser
plasmas."
J. Appl. Phys., (1988), 63, 1787.
K. A. Tanaka, A. Yamauchi, R. Kodama, M. Kado, T. Mochizuki,
T. Yamanaka, S. Nakai, and C. Yamanaka.
- (10) "Measurements of electron temperature in x-ray heated plasmas."
Phys. Rev. A, (1988), 37, 3622.
R. Kodama, M. Kado, K. A. Tanaka, A. Yamauchi, T. Mochizuki,
T. Yamanaka, S. Nakai, and C. Yamanaka.
- (11) "Optimized Design and its Characteristics of Schwartzschild Type Soft
X-Ray Microscope."
Jpn. J. Opts., (1988), 17, 234.
M. Kado, K. A. Tanaka, R. Kodama, A. Yamauchi, T. Mochizuki,
T. Yamashita, T. Yamanaka, S. Nakai, and C. Yamanaka.
- (12) "Fabrication of a cryogenic foam target for inertial confinement fusion
experiments."
J. Vac. Sci. Technol. A, (1988), 6, 3144.
T. Norimatsu, H. Katayama, T. Mano, M. Takagi, R. Kodama,
K. A. Tanaka, Y. Kato, T. Yamanaka, S. Nakai, Y. Nishino, M. nakai,
and C. Yamanaka.
- (13) "Experimental study on energy transport in thin Al and Au foil
irradiated with 263nm laser."
J. Appl. Phys., (1989), 65, 5068.
K. A. Tanaka, A. Yamauchi, R. Kodama, T. Mochizuki, T. Yabe,
T. Yamanaka, and S. Nakai.
- (14) "Energy transport experiments at Institute of Laser Engineering,
Osaka University."
Laser and Part. Beams, (1989), .
K. A. Tanaka, Y. Kato, S. Nakai, H. Shiraga, T. Yabe, T. Yamanaka,
T. Endo, and R. Kodama.
- (15) "Time-resolved measurements of laser-induced shock waves in CD

porous targets."

(to be published in Phys. of Fluids B).

R. Kodama, K. A. Tanaka, M. Nakai, T. Norimatsu, K. Nishihara,
T. Yamanaka, and S. Nakai.

- (16) *"Energy transport in laser-produced low-Z plasmas."*

(to be submitted to Phys. Rev. A)

R. Kodama, et al.

Proceedings:

- (1) *"Laser plasma x-ray source for lithography."*

Proceedings of SPIE, (1987), 773, 246.

T. Mochizuki, R. Kodama, C. Yamanaka, and H. Aritome.

- (2) *"Computer simulation of population inversion and the x-ray lasing of H-like aluminum by electron heat conduction cooling in stagnated plasmas."*

Proceedings in short wavelength conf., (1987), (Springer-Verlag), 284.

K. Nishihara, M. Kuboyama, R. Kodama, and T. Mochizuki.

- (3) *"Experimental studies of x-ray generation and its characteristics in laser-produced plasmas."*

Proceedings in short wavelength conf., (1987), (Springer-Verlag), 265.

K. A. Tanaka, R. Kodama, A. Yamauchi, M. Kado, T. Mochizuki,
T. Yamanaka, S. Nakai, and C. Yamanaka.

- (4) *"Experimental study and application of laser-produced plasmas in two-plate target."*

Proceedings in short wavelength conf., (1987), (Springer-Verlag), 245.

R. Kodama, K. A. Tanaka, T. Mochizuki.

- (5) *"Schwartzschild X-ray Microscope."*

X-ray Microscopy in Biology and Medicine, (1988),

K. A. Tanaka, T. Yamanaka, M. Kado, R. Kodama, S. Nakai, and
K. Yamashita.

- (6) *"High Brightness, Pulsive X-ray Source from Laser Produced Plasmas."*

X-ray Microscopy in Biology and Medicine, (1988),

K. A. Tanaka, T. Yamanaka, R. Kodama, and S. Nakai.

- (7) *"Soft X-ray Microscopy in Laser Plasmas."*
 Proceedings of SPIE, (1989).
 K. A. Tanaka, M. Kado, R. Kodama, M. Ohtani, S. Kitamoto,
 T. Yamanaka, K. Yamashita, and S. Nakai.

International Conference:

As first author:

- (1) *"X-ray emissions from stagnated plasmas between two plates created by 0.53- μ m laser light."*
 6th APS topicalconf. on atomic processes in high temperautre plasmas,
 Santa Fe, New Mexico, U.S.A., Oct. 1-6 (1987).
- (2) *"Experimental study and application of laser-produced plasmas in two-plate target."*
 International Sympo. on Short Wavelength Laser and their Applications,
 Univ. Osaka, Japan, Nov. 12-15 (1987).
- (3) *"Energy trarnsport in Laser-Produced Low-Z Plasmas."*
 31 APS annual meeting of the Division of Plasma Physics Anaheim,
 California, U.S.A., Nov.,13-17 (1989).

As coauthor:

- (1) *"Laser Acceleration of Electrons of Up To -Mev Energies by Gekko XII Laser System."*
 6th International Conf. on High-Particle Beams, Kobe, Japan, (1986).
- (2) *"Intense Soft X-Ray Generation and its Energy Transport in Short Wavelength Laser-Produced Plasmas."*
 16th Anomalous Absorption Conf., Lake Lezerne, N.Y. U.S.A., July 13-18 (1986).
- (3) *"Measurements of Scatter Light and Absorption Processes in Cavity Structured Target."*
 16th Anomalous Absorption Conf., Lake Lezerne, N.Y. U.S.A., July 13-18 (1986).
- (4) *"Experimental Evidence of Ionization Burn-through and Absorption Resonance in Radiation Energy Transport in Solid Density Plasmas."*
 10th International Conf. on Atomic Physics (ICAP), Tokyo, Japan, Aug. 25-29 (1986).
- (5) *"Laser plasma x-ray source for lithography."*
 SPIE, (1987).
- (6) *"Computer simulation of population inversion and the x-ray lasing of H-like alminum by electron heat conduction cooling in stagnated plasmas."*
 International Sympo. on Short Wavelength Laser and their Applications,
 Univ. Osaka, Japan, Nov. 12- (1987).
- (7) *"Experimental studies of x-ray generation and its characteristics in laser-produced plasmas."*

- International Sympo. on Short Wavelength Laser and their Applications,
Univ. Osaka, Japan, Nov. 12- (1987).
- (8) "*Implosion Experiments of Cryogenic Foam target.*"
IQEC, Tokyo, Japan, June (1988).
 - (9) "*High Brightnes, Pulsive X-ray Source from Laser Produced Plasmas.*"
Satellite meeting of international conf. on Synchrotron radiation
instrumentation X-ray Microscopy, Jichi Medical School, Tochigi, Japan,
Aug. 26-27 (1988).
 - (10) "*Schwarlzschild X-ray Microscope.*"
Satellite meeting of international conf. on Synchrotron radiation
instrumentation X-ray Microscopy, Jichi Medical School, Tochigi, Japan,
Aug. 26-27 (1988).
 - (11) "*Energy transport experiments at Institute of Laser Engineering, Osaka
University.*"
Japan-US seminar on Generation and application of Hot Dense Laser
Plasmas, Hawaii, U.S.A., Aug. 8-12 (1988).
 - (12) "*Schwarlzschild X-ray Microscope.*"
SPIE, Paris, France, Apr. 25-28 (1989).
 - (13) "*High Density Compression of Hollow-Shell target by GEKKO XII and
Laser Fusion Research at ILE, Osaka University.*"
International Workshop on Laser Interaction and Related Plasma
Phenomena, Monterey, U.S.A. Nov. 6-10 (1989).

Domestic conference:

As first author:

- (1) "*Characterization of X-ray Emission from UV-laser Produced Plasmas.*"
Annual Meeting of the Laser Society of Japan, Osaka University, Jan. 29
(1985).
- (2) "*Fundamental Process of X-ray Driven Implosion by Laser Light.*"
Spring Meeting of the Electrical Society of Japan, Nagoya University,
Apr. 4 (1985).
- (3) "*Characterization of Laser Plasma X Rays (II) -enhancement of keV x-ray
conversion efficiency by prepulse laser-.*"
Autumn Meeting of the Japan Applied Physical Society, Hokkaido
University, Sept. 27 (1986).
- (4) "*Interaction Between Laser-produced Plasma and Solid Matter (I)
-characteristic of x-ray emission and its application for XUV laser-.*"
Autumn Meeting of the Japan Physical Society, Kansai Gakuin
University, Sept. 28 (1986).
- (5) "*Interaction Between Laser-produced Plasma and Solid Matter
-Characteristic of XUV Emission-.*"
Annual Meeting of the Laser Society of Japan, Osaka University, Jan. 30
(1987).

- (6) *"Interaction Between Laser-produced Plasma and Solid Matter (II)
-production of population inversion-."*
Spring Meeting of the Japan Physical Society, Nagoya University, Mar.
27 (1987).
- (7) *"Foam Cryogenic Target Implosion (VI) -shock wave-."*
Spring Meeting of the Japan Physical Society, Nippon University, Apr. 1
(1988).
- (8) *"Foam Cryogenic Target Implosion (III)
-energy transport in low-density target-."*
Autumn Meeting of the Japan Physical Society, Hiroshima University,
Oct. (1988).
- (9) *"Experiment of Foam Cryogenic Target Implosion -energy transport-."*
Annual Meeting of the Laser Society of Japan, Osaka Int. Center, Jan.
(1989).
- (10) *"Implosion of Foam Cryo. Target IV -Energy transport-."*
Spring Meeting of the Japan Physical Society, Tokai University
Sagami School, Mar. 31 (1989).
- (11) *"Implosion of Foam Cryo. Target IV -Energy transport-."*
Autumn Meeting of the Japan Physical Society, Kagoshima
University, Oct. 4 (1989).

